Robert Harald Rogne

Observer Design For Fault-Tolerant Dynamic Positioning Using MEMS Inertial Sensors

Thesis for the degree of Philosophiae Doctor

Trondheim, March 2017

Norwegian University of Science and Technology
Faculty of Information Technology and Electrical Engineering
Department of Engineering Cybernetics

NTNU
Norwegian University of
Science and Technology

NTNU
Norwegian University of Science and Technology

Thesis for the degree of Philosophiae Doctor

Faculty of Information Technology and Electrical Engineering
Department of Engineering Cybernetics

ISBN 978-82-326-2244-3 (printed version)
ISBN 978-82-326-2245-0 (electronic version)
ISSN 1503-8181

ITK-report: 2017-9-W

Doctoral theses at NTNU, 2017:86

Printed by Skipnes Kommunikasjon as

Observer Design For Fault-Tolerant Dynamic Positioning Using MEMS Inertial Sensors

Robert Harald Rogne

To my loving family

Summary

The contribution of this disseration is threefold. First, it provides insight into the use of a certain type of nonlinear observers (NLO) for platform independent position, velocity and attitude estimation, exemplified by an unmanned aerial vehicle (UAV) and an anchor handling tug supply (AHTS) vessel. Second, it considers methods for fault detection and isolation for various sensors: Accelerometers, angular rate sensors, gyrocompasses and position reference systems. Third, it discusses application of the topics above in dynamic positioning systems. The NLOs are based on the principle of reference and measurement vectors for attitude estimation, and may or may not be aided by a separate translational motion observer in feedback interconnection. The work is presented through the findings of six separate chapters, each based on a single journal or conference article.

The first chapter considers global navigation satellite system (GNSS) and inertial navigation system (INS) integration in general, presenting methods for loose and tight integration, GNSS error models, and experimental results using a UAV. The experimental results using NLOs are compared to a real time kinematic GNSS solution, and they show unsurprisingly that a tightly coupled integration solution is superior.

The second chapter covers the use of NLO-based INS on an AHTS vessel. The first topic is attitude and heave estimation, where two distinct versions of the aforementioned NLOs are compared to each other, and to an extended Kalman filter (EKF)-based solution. Also, two MEMS-based inertial measurement units (IMUs) from different manufacturers are used in the testing: the ADIS16485 and the STIM300. The difference between the NLO versions is whether or not they are aided by position measurements. The EKF represents the classic way of attitude estimation in navigation, and the NLOs handle themselves well in comparison, with the aided NLO coming out on top. No tangible variation is found between the two IMUs for attitude estimation, while for heave estimation the ADIS16485 is preferable, owing to a better accelerometer. The second topic of the chapter is

dead reckoning, where the NLO-based INS has to calculate heading and position without aiding in two separate tests. For heading the results are very promising for the STIM300, drifting only one degree in the heading estimate after one hour. For position, it is found that both MEMS IMUs cannot provide an adequate and independent position estimate performance wise, while they might well be used to increase navigation fault tolerance.

The third chapter deals with a redundant IMU configuration, presenting two alternatives for combining IMUs together for performance and fault detection and isolation (FDI). Alternative 1 is based on the classic parity space method, while alternative 2 uses quaternion-based weighting. Considering performance, they are basically equal, both improving upon the results from the previous chapter, especially for heave estimation and dead reckoning. However, in a fault case for an angular rate sensor in the IMU, alternative 2 is evidently the best solution.

The fourth and fifth chapter both investigate the same topic, namely FDI in the sensors and systems aiding the NLOs. A selection of NLO variants are evaluated in an FDI context, and it is revealed that in order to successfully detect position reference faults, the attitude estimation should preferably be completely independent from the position measurements. A new attitude estimator with virtual aiding is proposed. Algorithms for FDI are also presented, where one is found in the literature and applied in a novel way to detect slow drifts. Faults in both position reference systems and gyrocompasses are sufficiently dealt with. Note, on the contrary to the previous chapters, these chapters encompass mainly simulation results.

The sixth and final chapter based on an article, attempts to bring the newfound knowledge of previous results together, to provide a novel approach of assembling a dynamic positioning (DP) system. New sensor structures are considered, and a case is made to revise today's DP classification and testing, and move towards new ideas in system- and risk-based thinking allowing integrated INS a place in DP.

The conclusion of the thesis is that using NLOs with MEMS IMUs has great potential for navigation, in DP and otherwise. With the IMU's small size and the NLO's low computational demands and model-less approach, the combination of the two is truly platform independent. Using the methods described in this work may improve the performance and fault tolerence of any navigation system.

Preface

This thesis is the main outcome of my efforts to earn the degree of philosophiae doctor (PhD) at the Norwegian University of Science and Technology (NTNU). The work was carried out at the Centre for Autonomous Marine Operations and Systems (NTNU AMOS) and the Department of Engineering Cybernetics (ITK), and supported by the Research Council of Norway and Rolls–Royce Marine through the Centres of Excellence funding scheme and the MAROFF programme, grant numbers, 223254 and 225259 respectively. The Research Council of Norway is acknowledged as the main sponsor of NTNU AMOS. The work has been completed under the supervision of Professor Tor Arne Johansen (ITK, NTNU) and Professor Thor I. Fossen (ITK, NTNU).

Acknowledgments

First and foremost, I would like to express my sincere gratitude to my supervisor Tor Arne Johansen, firstly for having faith in me before enrollment, secondly for the continued, unwavering support and excellent follow-up during my time as a PhD candidate, and thirdly for sharing with me what seems to be an infinite source of knowledge and time for his PhD students.

I would also like to thank my co-supervisor Thor I. Fossen for his inspiration and motivation, always being energetic and accomodating lively discussion, both academic and otherwise.

My deepest thanks also goes out to my colleague Torleiv H. Bryne for wonderful cooperation and invaluable consultation and backing. I'm not sure how this would have turned out without him.

Furthermore, I would like to acknowledge Rolls-Royce Marine with employees Ivar Ihle, Jann Peter Strand and others for very useful industrial input and fruitful meetings, and for making the experiments possible.

Also, the staff at the Department of Engineering Cybernetics deserves recognition: The administrative staff for keeping things running smoothly, and the technical staff for great help during experiments. Besides the staff, my fellow PhD students at the same department and AMOS have my thanks for providing a terrific working environment, and being great company on conference travels!

On the more "unprofessional" level, I would like to give thanks to my friends, for providing relief from my doctoral work through hikes, parties, beers on the pub, various GNSS-based mobile games, PC-gaming and more. I won't mention anyone by name in fear of leaving someone out by accident, but if you are reading this while neither being all that into control engineering, nor a member of my family, you are probably one of them.

I would like to thank my parents Eva and Harald, both of whom former seafarers, for providing me with the tools for making it this far in life, and instilling in me the interest for the sea. Recognition is also warranted for my sister Mona, for being the generous and caring person that she is.

Finally, I sincerely thank those closest to me — my dear daughters Alexandra and Sophia, and my significant other Mette — for being the cornerstone of my life. Your support matters immensely.

If you feel left out at this point, I'm truly sorry. This one goes out to you!

Once again, thank you all!

Robert H. Rogne

Contents

Abbreviations

6-DOF six-degree-of-freedom.

AHRS attitude and heading reference systems.

AHTS anchor handling tug supply.

ARS angular rate sensor.

CAE cumulative absolute error.

dGNSS differential global navigation satellite systems (GNSS).

DP dynamic positioning.

DR dead reckoning.

ECEF earth-centered, earth-fixed.

ECI earth-centered inertial.

EKF extended Kalman filter.

FDI fault detection and isolation.

FOG fiber optic gyroscope.

GES global exponentially stability.

GNC guidance, navigation and control.

GNSS global navigation satellite systems.

GPS Global Positioning System.

HIL hardware-in-the-loop.

HPR hydroacoustic position reference.

HRG hemispherical resonator gyroscope.

IMO International Maritime Organization.

IMU inertial measurement unit.

INS inertial navigation system.

KF Kalman filter.

LOS line-of-slight.

LPF low pass filter.

LTV linear-time varying.

MEKF multiplicative extended Kalman filter.

MEMS micro-electro-mechanical systems.

NED north east down.

NLO nonlinear observer.

PosRef position reference.

PSD power spectral destiny.

PVA position, velocity and attitude.

RLG ring laser gyroscope.

RMS root mean square.

RTK real time kinematic.

TMO translational motion observer.

UAV unmanned aerial vehicle.

USGES uniformly semiglobal exponentially stability.

VRU vertical reference unit.

VVR virtual vertical reference.

Nomenclature

$\boldsymbol{q}_a^b$ Unit quaternion from frame $\{a\}$ to frame $\{b\}$.

$\boldsymbol{R}_a^b$ Rotation matrix from frame $\{a\}$ to frame $\{b\}$.

$\{i\}$ Inertial coordinate frame.

$\{e\}$ Earth-centered, earth-fixed coordinate frame.

$\{n\}$ North-east-down coordinate frame.

$\{t\}$ Tangent coordinate frame.

$\{b\}$ BODY coordinate frame.

ϕ Roll angle.

θ Pitch angle.

ψ Yaw angle.

μ Latitude on the WGS-84 ellipse.

λ Longitude on the WGS-84 ellipse.

h Height over the WGS-84 ellipse.

$\boldsymbol{p}_{bc}^a$ Position vector of frame $\{c\}$ relative frame $\{b\}$ decomposed in frame $\{a\}$.

$\boldsymbol{v}_{bc}^a$ Linear velocity vector of frame $\{c\}$ relative frame $\{b\}$ decomposed in frame $\{a\}$.

$\boldsymbol{f}_{bc}^a$ Specific force of frame $\{c\}$ relative frame $\{b\}$ decomposed in frame $\{a\}$.

$\boldsymbol{\omega}_{bc}^{a}$ Angular velocity of frame $\{c\}$ relative frame $\{b\}$ decomposed in frame $\{a\}$.

$\boldsymbol{g}_{b}^{a}$ Gravity vector decomposed in frame $\{a\}$.

1

Introduction

Ever since mankind set its sight on the open seas, it has yearned to travel across and discover new horizons. In the days of yonder, this was a perilous task, and many a brave seaman's life has been lost to the waves. Not only because of daunting storms, but also as a result of not knowing the vessel's actual position and path, wandering into dangerous areas and striking hidden reefs. Untrustworthy, dubious or even unavailable, by today's standards, means of navigation meant that traveling by sea was only for the bold and adventurous. As time passed however, more and more equipment became available to the seafarers. Sextants and accurate clocks made it possible to manually obtain, measure and calculate the position on Earth. In addition, by estimating your heading and speed, and knowing from where you came, you could calculate your current position in a process referred to as *dead reckoning*. More recently, motion sensors, rotation sensors, computers and electronic navigational aids have all but automated the navigation process.

The term navigation comes from the Latin words *navis* and *agere*, which translates to "ship" and "to drive". In colloquial conversation, navigation today is used broadly, meaning everything from moving around, finding one's way in an unknown environment, determining a vessel's position, or even using a web browser on the internet. However, navigation as a scientific modern field of study, usually pertains to the ascertainment of position, velocity and orientation of some body relative to a reference point, and is applied to all types of vehicles such as aircraft, ship, submarines and cars.

In this work, inertial navigation systems (INS) using nonlinear observers lay the foundations for a fault-tolerant and efficient way of determining position, velocity and attitude (PVA), independent of vehicle platform, while the main focus is on ships and dynamic positioning operations. Micro-electro-mechanical systems (MEMS)-based inertial sensors providing acceleration and angular rates are employed. These sensors are typically mounted directly to the vehicle's hull in a strapdown way, providing independent estimates of the translational and ro-

tational motion of the craft in using dead reckoning techniques. They are too inaccurate to maintain position by themselves, and must therefore be assisted by navigational aids providing a non-drifting position reference, the most prevalent of which are the global navigation satellite systems (GNSS), and in particular the Global Positioning System (GPS). GPS is the sole position reference system utilized in the experimental setups of this dissertation. As of now, most MEMS IMUs are also not accurate enough to provide a true-north heading reference without the assistance of other sensors. For environments without magnetic disturbances, built-in magnetometers in many IMUs will supply the INS with a heading reference, given the local magnetic field of your location. For ships, gyrocompasses are the established sources for heading reference. Gyrocompasses may either be mechanical with physical self-alignment to true north, or based on some other principle like fiber optics, ring lasers or resonance.

Position and attitude correction of the INS is generally done with an estimator or observer, and the extended Kalman Filter (EKF) is the time-honored method which has been in use for five decades. More recently, nonlinear observers have become more frequent, and they form the basis for the INSs presented in this thesis.

1.1 Dynamic Positioning

A dynamically positioned (DP) vessel is, according to classification society DNV GL (2013), "*a vessel which automatically maintains its position and heading (fixed location or predetermined track) exclusively by means of thruster force*". The goal of DP is to keep the vessel stationary, or within an acceptable zone (see Fig. 1.1), and it makes use of position references, vessel sensors, propellers and thrusters to achieve this goal. A DP system consists of a power system, a thruster system and a DP-control system, where the latter comprises (DNV GL, 2013):

1. dynamic positioning control computers
2. sensor system
3. display system
4. operator panels
5. positioning reference system
6. associated cabling and cable routing

Fig. 1.2 shows a typical DP vessel and its components. The topics of this thesis cover points 1, 2 and 5, delving into the subject of navigation. In DP Classes 2 and 3, requirements dictate that the vessel must possess three independent position reference (PosRef) systems and have triple redundancy in vessel sensors

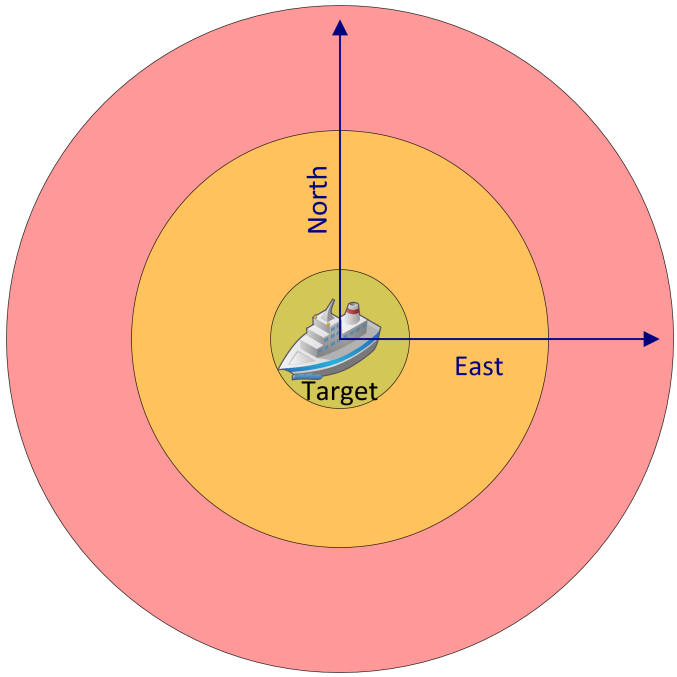

Figure 1.1: DP simplified concept.

(International Maritime Organization (1994); DNV GL (2013); American Bureau of Shipping (2013)). At the open seas, common posref systems include

- taut wire
- hydro-acoustic systems
- global navigation satellite systems, such as GPS, GLONASS and Galileo
- laser and radar based systems

The main vessel sensors are gyrocompasses and vertical reference units, two types of inertial sensors. The requirements in redundancy are there to improve safety and obtain resilience in single-fault scenarios, but the requirement realization is not without challenges. Sections 1.2 and 1.3 presents some basic material on some of these position references and vessel sensors.

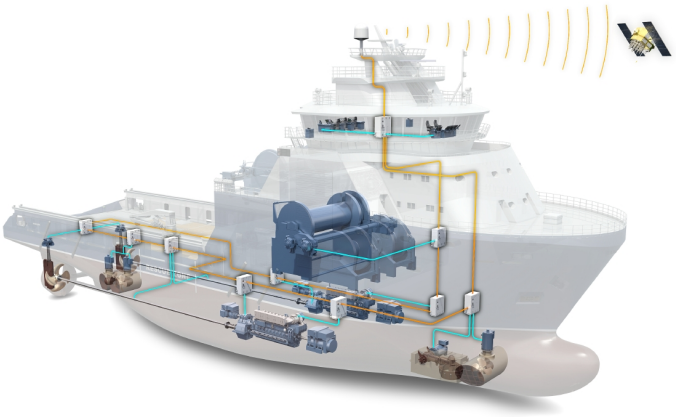

Figure 1.2: A anchor handling tug supply DP vessel. Courtesy of Rolls-Royce Marine AS.

1.2 Position References

INS can be aided by a number of sensors and position reference systems such as radio-, radar- laser-, hydroacoustic- and satellite-based systems, see Fig 1.3. The latter type has the benefit of world-wide coverage, and are known as Global Navigation Satellite System (GNSS), the most famous of which is GPS. However, these systems are exposed to both natural degradation and deliberate outages. Natural degradation can be caused by signal distortion from reflection of nearby objects, known as multipath, loss of signal due to sun storms or loss of line of sight to the satellite. Deliberately outages can be because of signal jamming. The other systems are often in the need of an external aid or reference. For the examples given above we have clump weights and transponders on the sea bed (taut wire and hydro-acoustic, respectively), and platforms or other vessels with mirrors and/or various kinds of transmitters for laser, radio and radar. When the waters are too deep, or operations carry the vessel away from the required equipment, the position references cannot be applied, leaving us only with the GNSS and possibly hydroacoustic option. Relying on more instances of one type of system only can put the safety promised by the redundancy at risk due to common failure modes. In an incident study (Chen and Moan, 2005) cited by Chen et al. (2008), *"six incidents are classified as drive-off, while five of these six incidents were initiated due to erroneous position data from DGPSs"*. Also , determining which position reference is providing the most accurate position is difficult.

In addition to the questionable redundancy, there is the unavoidable question of cost. More equipment means higher cost, and since adding more position reference systems of the same type does not automatically enhance performance, the cost can

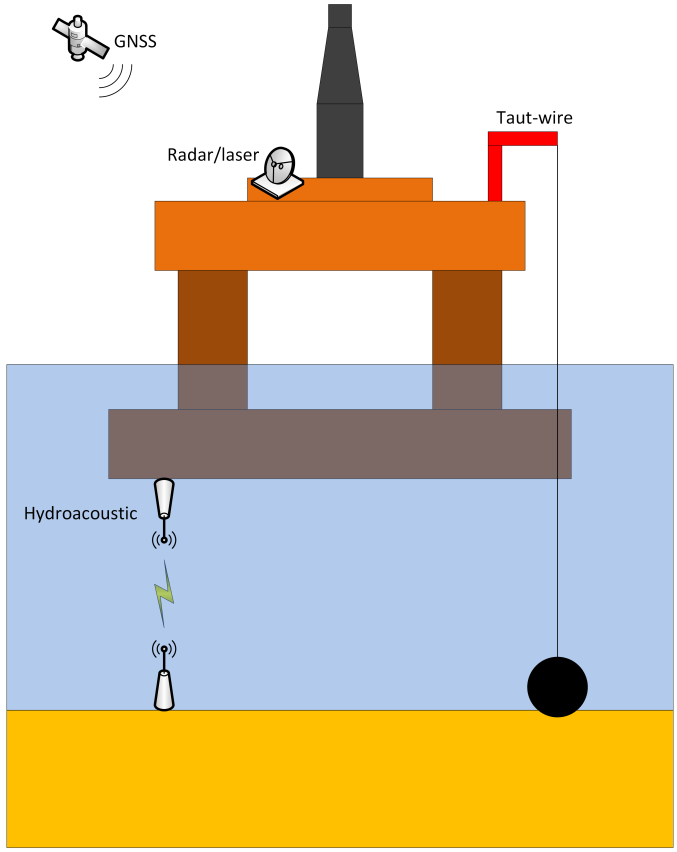

Figure 1.3: Some position reference systems commonly used in DP, here displayed on a semi-submersible.

be considered superfluous. In order to increase the quality of position references, both in terms of performance and fault detection and isolation, especially for faults that are not abrupt, an inertial measurement unit (IMU) can be applied. IMUs typically measure linear accelerations and angular velocities. In this case, IMUs can serve as a technically independent system, providing position information through the integration of accelerometer data, and attitude through the angular rate sensor.

1.3 Inertial Sensors

During loss of position reference, good dead reckoning capabilities is crucial for the INS to provide accurate PVA estimates to the user, or to enable the INS's abilities to detect errors in the aiding sensors.

Inertial sensors have been vital in the foundation for automatic control of ships since the first operational gyrocompass was introduced by Anschutz in 1907, and the ballistic compass by Sperry three years later. Since then, the gyrocompass based on gimbal inertial sensor technology and physical self-alignment, has been established as the main source of heading information on ships and free floaters. Other types of gyrocompasses also exist, the primary ones being fiber optic gyroscopes (FOG), hemispherical resonant gyroscopes (HRG) and ring laser gyroscopes (RLG) (Armenise et al., 2010) all being inertial navigation systems (INS) applied to estimate heading. In contrast to the gyrocompass, a full INS applies tri-axial accelerometer and angular rate measurements to estimate three-degree-of-freedom position, velocity and attitude (PVA) via dead reckoning.

A type of inertial sensor receiving increasing amounts of attention, in both academia and the industry, is based on MEMS technology. In present day MEMS IMUs are integrated with software to provide the ship with motion sensing capabilities, in particular on ships equipped with a DP system, often referred to as a vertical reference unit (VRU) (Ingram et al., 1996). They also go by the names Vertical Reference Systems and Motion Reference Units. VRUs outputs roll, pitch and sometimes heave estimates. Ballasting systems and lever arm compensation of position reference system measurements on a ship are the main application areas of the roll and pitch estimates as of today. Heave estimates are of interest in heave compensation of cranes (Fig. 1.4) or drill floors during marine operation in waves, in heave displacement control of high-speed surface effect ships and for on-board decision support systems for e.g. weather monitoring. MEMS inertial sensors have gone through a substantial development in the last decades, Barbour et al. (2011), increasing their performance, and lowering costs for prospective INS producers. An IMU measures linear accelerations and angular velocities. These measurements are related to position and attitude through double and single integration, respectively, in a dead reckoning fashion.

While IMUs are not in widespead use in the DP industry as of today, the idea of using an IMU in conjunction with a position reference system is not new (Paturel, 2004; Berntsen, 2007; Vik and Fossen, 2001; Russell, 2012; Carter, 2011). The idea of fully integrated INSs in DP was proposed in an industrial context almost 20 years ago (Vickery, 1999). However, most of the literature focus their efforts on combining inertial sensors with a single posref system for performance reasons. Carter (2011) proposed that INS should be applied with GNSS to improve the performance of the DP system, and in Berntsen (2007) the main aspiration was to filter a hydroacoustic system before being applied as a pure position reference in the DP system. The notion of utilizing an IMU for improving redundancy has been proposed (Blanke, 2005; Stephens et al., 2008; Carter, 2011; Russell, 2012), but has had limited impact as of yet.

Many of the high-end integrated INS products for DP are subjected to export restrictions, limiting the market potential and increasing the cost of installation due

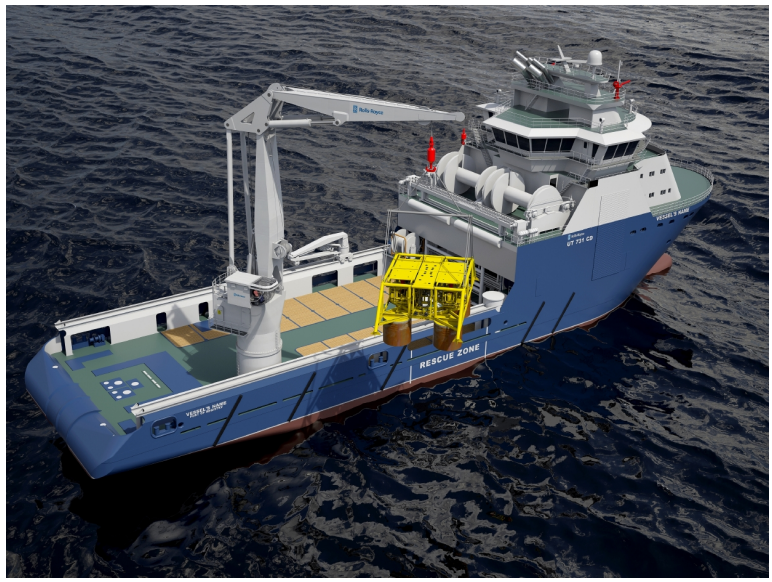

Figure 1.4: A ship with a crane. Courtesy of Rolls-Royce Marine AS.

to a possibly lengthy approval process before installation. Up to present time such solutions have all applied high-end IMUs, with FOG- or RLG-based angular rate sensors. MEMS-based IMUs are significantly less expensive and rarely subjected to export restrictions, which in it self motivates the investigation of applying these at the core of the onboard INS. This is also paving the way for low-cost or cost-effective MEMS-based INS on a variety of ships from fishery vessels to bulk and tank ships.

The low adoption of IMUs in DP so far could be due to the lack of sensors with justifiable cost vs. performance ratio. Yet, with the advent of low-cost, MEMS-based sensors with ever increasing performance, today's and tomorrow's IMUs may enliven the industry's enthusiasm, providing motivation for further research on the topic. With promising performance for a low cost, MEMS IMUs are on the way to become ubiquitous, finding themselves in a range of applications including mobile phones, remote controlled toys, automobiles, UAVs, munitions and human motion capturing equipment, basically anything that moves. However, MEMS IMUs are not yet adequate for use in unaided INS, suffering from noise and systematic errors such as biases and drifts.

1.4 Observers for Position Reference and INS Integration

INS corrections are usually performed using an estimator, where the extended Kalman filter (EKF) has traditionally been the applied estimator, and it has been

covered in the literature for at least five decades (Maybeck, 1979; Titterton and Weston, 2004; Farrell, 2008; Grewal et al., 2013; Groves, 2013). Fig. 1.5 shows the basic concept of an aided INS, where the navigation computer is where the EKF, or other estimation methods, are implemented.

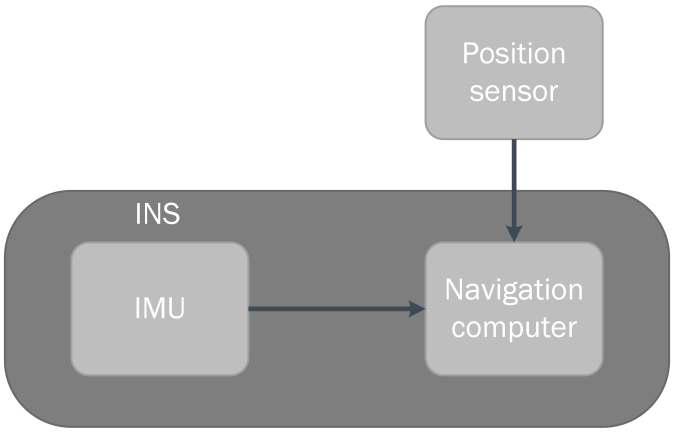

Figure 1.5: Aided INS structure.

From consumer grade to automotive and tactical grade, the advancement of MEMS IMUs over the last three decades, and the sudden availability of low-cost IMUs has motivated research on nonlinear attitude observers such as Salcudean (1991); Vik and Fossen (2001); Mahony et al. (2008); Hua (2010); Hua et al. (2014, 2016); Grip et al. (2012a, 2013, 2015); Batista et al. (2011, 2012a,b). A good attitude estimate is of great importance when integrating the IMUs acceleration output for use in an observer for position and velocity. To obtain high quality estimates of the attitude, one may employ the angular velocities from the IMU, together with vector measurements in the inertial frame such as acceleration and compasses in a sensor fusion scheme. Nonlinear observers (NLOs) for attitude estimation have also been integrated with position and velocity sensors resulting in a complete INS providing estimates of position, velocity and attitude. The work of Grip et al. (2012a), which builds upon Mahony et al. (2008), includes position reference aiding, both for position and velocity estimation and for aiding the attitude estimates themselves, based on the theory of Grip et al. (2012b). Examples of such results are Grip et al. (2013, 2015) where a three-degree-of-freedom position measurement is assumed available. Furthermore, Bryne et al. (2014, 2015b) have tailored the result of Grip et al. (2013) for marine surface navigation by replacing the need for a vertical measurement, as navigation aid, from PosRefs (GNSS or hydroacoustics) with a virtual vertical reference (VVR) measurement. Other examples of nonlinear observers that includes the estimation of position and velocity are Morgado et al. (2011); Batista et al. (2010, 2013, 2014), where the focus is mainly on underwater

vehicles.

Using inertial sensors, one could provide heave estimates. Examples of heave estimation based on such sensors, using both linear and nonlinear methods, are presented in Godhavn (1998); Küchler et al. (2011); Richter et al. (2014); Bryne et al. (2014, 2015b). Godhavn (1998) and Richter et al. (2014) are based on linear bandpass filtering, while Bryne et al. (2014) is applying NLOs to estimate heave. In Bryne et al. (nd), a more sophisticated method evolving from Bryne et al. (2014) is used, estimating wave motion parameters and employing these in the estimator.

The type of NLOs that will be employed in this work have, unlike the extended Kalman filter (EKF), proven semiglobal exponential stability (Mahony et al., 2008; Grip et al., 2013; Bryne et al., 2014). NLOs have the benefit of having explicit stability properties guaranteeing robustness. Similar stability properties are difficult to obtain using standard attitude estimators based on the extended Kalman filter (Farrell, 2008; Groves, 2013), the multiplicative extended Kalman filter (MEKF) such as (Markley, 2003), the unscented Kalman filter (UKF) (Julier and Uhlmann, 2004) or the particle filter (PF) (Djuric et al., 2003), which are all based on approximate minimum variance filtering. Consequentially, we have some guarantees for robustness and convergence regardless of initialization. Additionally, since we do not need to propagate any Riccati equations as for the EKF, NLOs have the potential for being less of a computational burden, which is very beneficial on small platforms.

The developed literature covering EKF for integrated inertial navigation, (Titterton and Weston, 2004; Farrell, 2008; Grewal et al., 2013; Groves, 2013), focuses strongly on the modeling and estimation of systematic errors such as ionospheric and tropospheric impact on satellite navigation accuracy, and bias and drift properties of inertial sensors. In contrast, NLOs typically make no explicit assumptions on the attributes of such errors, except typically including "constant parameter" augmentations to estimate the gyro biases, (Salcudean, 1991; Vik and Fossen, 2001; Mahony et al., 2008; Hua, 2010; Batista et al., 2011, 2012c; Grip et al., 2012a, 2013, 2015). However, it is clear that the deterministic modeling framework underlying the NLOs could allow some frequency-dependent characterization of sensor errors to be included. By doing so, the accuracy of INS aided by position reference is potentially increased.

1.5 Fault Tolerance

Blanke et al. (2006) defines a *fault* in a dynamic system as "*a deviation of the system structure or the system parameters from the nominal system*". Faults may present themselves in all sorts of manners and in all parts of a system, i.e. sensor loss or malfunction, electrical shortage and actuator blockage. This work considers only fault occuring in, or in connection to, sensors.

According to Blanke et al. (2006), there are three diagnostic steps regarding fault-tolerant control:

- Fault detection
- Fault isolation
- Fault identificaion and estimation

First, in fault detection, it is decided whether or not a fault has appeared, and if so, the time of the fault. Second, fault isolation determines which component is faulty or the location of the fault. Finally, actions may be take to identify the fault's magnitude and severity. Primarily, this work focuses on the first two steps, fault detection and isolation (FDI), simply excluding the faulty component.

1.5.1 FDI in Sensors and Reference Systems

For FDI in inertial units, a method based on the generalized likelihood ratio test, Willsky and Jones (1976), has prevailed for decades. The ratio is based on the likelihood given that the data fits under one model (failure) or another (non-failure). In the adaptation for inertial sensors, the classical discrete methods Daly et al. (1979); Sturza (1988), and for the continuous case Medvedev (1995), employ parity equations to generate residuals, upon which the FDI is based. The admitted inaccuracies of MEMS IMUs prove to be a challenge when applying classical methods for FDI on inertial sensors, Guerrier et al. (2012); Waegli et al. (2008), so Guerrier et al. (2012) has proposed an improved method based on Mahalanobis distance with promising results. FDI in INS using NLOs have up to this day received limited attention, except for results such as Bryne et al. (2015a). However, the focus has not been on IMU faults, but primarily rather on faults in aiding sensors.

The diagnostic steps of finding outliers, jumps and wild points in sensors is relatively easy and well established, see e.g. (Gustafsson, 2012, Ch. 7.6). In Bryne et al. (2015a), a triple redundant position reference system in tandem with an INS based on NLOs was employed, and by using sensor weighting position reference faults presenting themselves as outliers and drifts could be detected, isolated and estimated. Zhao and Skjetne (2014) presents a method for fault detection and diagnosis using particle filters, for faults occuring as bias, drifts and outliers. Blanke (2005) discusses diagnosis and fault tolerence in station keeping, not only for sensors, but the entire control system through graph-based analysis. In a DP industrial context, Carter (2011) suggests using an INS to detect faults in the navigation system. For tightly coupled integration strategies, other strategies may be used, such as Receiver Autonomous Integrity Monitoring, known as RAIM, presented in e.g. (Groves, 2013, Ch. 17.4).

1.6 Overview of the Thesis

1.6.1 Organization

The rest of the thesis' chapters present work from different articles completed during the PhD fellowship. The Chapter 3 covers GNSS/INS in general, with experimental results from an unmanned aerial vehicle. The rest of the thesis considers dynamic positioning vessels, where Chapters 4 and 5 use full-scale experimental data collected on a DP vessel in the Norwegian sea during normal operation. Chapters 6 and 7 are simulation studies on position and heading reference fault detection and isolation, while Chapter 8 is an attempt to gather the threads of the results of this thesis and joint work with fellow PhD student Torleiv H. Bryne.

Papers included in thesis

The following papers are included in this thesis, in order of appearance:

- Bryne, T. H., Hansen, J. M., Rogne, R. H., Sokolova, N., Fossen, T. I., and Johansen, T. A. (2017a). Nonlinear observers for integrated INS/GNSS navigation – implementation aspects. *IEEE Control Systems Magazine*. To Appear.
- Rogne, R. H., Bryne, T. H., Fossen, T. I., and Johansen, T. A. (n.d.b). Strapdown inertial navigation on ships using mems sensors and nonlinear observers. *IEEE Transactions On Control System Technology*. Submitted for publication
- Rogne, R. H., Bryne, T. H., Fossen, T. I., and Johansen, T. A. (n.d.a). Redudant MEMS-based inertial navigation using nonlinear observers. *ASME Journal of Dynamic Systems, Measurement and Control*. Submitted for publication.
- Rogne, R. H., Johansen, T. A., and Fossen, T. I. (2015). On attitude observers and inertial navigation for reference system fault detection and isolation in dynamic positioning. In *Proc. European Control Conference (ECC)*, Linz, Austria.
- Rogne, R. H., Bryne, T. H., Johansen, T. A., and Fossen, T. I. (2016b). Fault detection in lever-arm-compensated position reference systems based on nonlinear attitude observers and inertial measurements in dynamic positioning. In *Proc. of the American Control Conference*, Boston, MA.
- Bryne, T. H., Rogne, R. H., Fossen, T. I., and Johansen, T. A. (2017b). Inertial Sensors for Risk-Based Redundancy in Dynamic Positioning, In *Proc. of the 36th International Conference on Ocean, Offshore & Arctic Engineering*, Trondheim, Norway. To Appear.

1.6.2 Other papers

In addition, I have also authored or contributed to:

- Rogne, R. H., Johansen, T. A., and Fossen, T. I. (2014). Observer and IMU-based detection of faults in position reference systems and gyrocompasses with dual redundancy in dynamic positioning. *In Proc of the IEEE Conference on Control Applications (CCA)*, Antibes, France.
- Bryne, T. H., Rogne, R. H., Fossen, T. I., and Johansen, T. A. (2016). Attitude and heave estimation for ships using mems-based inertial measurements using MEMS-based inertial measurements. In *Proc. of the 10th IFAC Conference on Control Applications in Marine Systems*, Trondheim, Norway.
- Rogne, R. H., Bryne, T. H., Fossen, T. I., and Johansen, T. A. (2016a). MEMS-based inertial navigation on dynamically positioned ships: Dead reckoning. In *Proc. of the 10th IFAC Conference on Control Applications in Marine Systems*, Trondheim, Norway.
- Bryne, T. H., Rogne, R. H., Fossen, T. I., and Johansen, T. A. (n.d.). A virtual vertical reference concept for integrated inertial navigation at the sea surface. *Control Engineering Practice*. Submitted for publication.

1.6.3 Contribution of the thesis

The main contribution of this thesis is threefold: Firstly, it presents experimental and simulation results for a class of nonlinear PVA observers employing IMUs, illustrating what performance can be achieved with these for two very different vehicles. Secondly, it considers fault tolerance in light of these observers, presenting novel ways to exploit them in order to increase robustness of the navigation system. Thirdly, it discusses applications of the topics above in dynamic positioning.

Each of the Chapters 3 to 8, which are based on separate articles, have their own distinct contributions.

Chapter 3 GNSS/INS Integration: This chapter considers the implementation of complete position, velocity and attitude (PVA) estimators using nonlinear observers. First, a formulation of time-varying gains for estimating position, velocity and some auxiliary states in a nonlinear observer is completed, on the basis of a time-varying Riccati-equation. Then, we investigate GNSS error models for dynamic noise characteristics. Also, discrete updates for multi-rate and asynchronous measurements in estimation of position, velocity and attitude are taken into account. Finally an experimental verification of methods using data collected from a UAV flight mission is conducted.

Chapter 4 INS on Ships: This chapter's contribution concerns full-scale verification of nonlinear observers for ships using MEMS IMUs. Comparisons are

made against industry standard hardware and software for the estimation of attitude and heave. In addition, a dead reckoning test is performed to study how the unaided INS manages over time, both for position and heading in separate test. A discussion regarding ship vibrations is undertaken, and the output of vibration isolated IMUs are compared to non-isolated ones.

Chapter 5 Redundant INS: Here we build upon the previous chapter using the same dataset, but utilize more IMUs in a redundant setup. Two alternative strategies for combining inertial sensors are presented and compared, one based on the classic parity space method and the other on quaternion averaging. The same tests as in Chapter 4 are performed, and also some IMUs fault cases are examined.

Chapter 6 Position and Heading Reference Fault Detection and Isolation: The main contribution of this chapter is the comparison of three state-of-the-art estimators, with focus on use in FDI. Two of the attitude observers are aided by position reference, while the third is not. All observers are put in cascade with a separate translational motion observer aided by GNSS that is used for detection and isolation of faults in said system. The stability of the cascade is analyzed, and simulations of two FDI cases on a ship are performed for position and heading reference fault.

Chapter 7 Position Reference FDI with Lever-Arm Compensation: This chapter has a twofold contribution: A three-stage observer for dynamic positioning vessels, estimating position, velocity and attitude with proven stability properties, taking into account lever arm compensation of position reference signals. A VRU providing attitude and heave is inherent in the observer's design. The second part is the fault detection of position measurements with slowly emerging faults, using established fault-diagnosis techniques and the observer structure posed.

Chapter 8 INS in Fault-Tolerant Dynamic Positioning: Based on the experiences of previous work, we propose an alternative sensor configuration to the state of the art of current DP class notations. Using MEMS IMUs in an INS, recommendations are made to replace existing sensors such as wind sensors and dedicated VRUs, while improving the fault detection capabilities of position reference systems in cases where only dual-redundancy can be achieved.

2

Notation, and some Kinematics

This chapter covers some of the notations and formulation used throughout this work, and may be repeated in the separate chapters for convenience.

2.1 General Mathematical Notations

- The Euclidean vector norm and the induced matrix norm are denoted $\|\cdot\|_2$ and $\|\cdot\|$, respectively.
- Gaussian white noise n with mean μ and variance σ^2 is given as $n \sim (\mu, \sigma^2)$.
- The scalar exponential function is denoted $\mathrm{e}^{(\cdot)}$, while the matrix exponential function is denoted $\mathbf{e}^{(\cdot)}$.
- The $n \times n$ identity matrix is denoted $\boldsymbol{I}_n$.
- A block diagonal matrix is given by $\boldsymbol{M} = \mathrm{blockdiag}(\boldsymbol{M}_1, \boldsymbol{M}_2, \ldots, \boldsymbol{M}_n)$ for square matrices M_j.
- The transpose of a vector or a matrix is denoted with $(\cdot)^\intercal$.
- $\boldsymbol{S}(\cdot) \in SS(3)$ represents the skew symmetric matrix such that $\boldsymbol{S}(z_1)z_2 = z_1 \times z_2$ for two vectors $z_1, z_2 \in \mathbb{R}^3$.
- $z = (z_1; z_2; \ldots; z_n)$ denotes a vector of stacked column vectors $z_1, z_2, \ldots z_n$.
- $\otimes$ represents the Hamiltonian quaternion product.
- For a vector $z \in \mathbb{R}^3$, we denote by $\bar{z}$ the quaternion with zero real part and vector part z, that is $\bar{z} = (0; z)$.
- The right Moore-Penrose pseudo inverse is denoted $(\cdot)^\dagger$.

- The sinc function is defined as

$$\operatorname{sinc}(\alpha) := \begin{cases} 1 & \text{for } \alpha = 0 \\ \frac{\sin(\alpha)}{\alpha} & \text{otherwise,} \end{cases} \tag{2.1}$$

  for an angle α.

2.2 Attitude Representation

A general rotation matrix describing the rotation between two given frames $\{a\}$ and $\{b\}$ and is denoted $\boldsymbol{R}_a^b \in SO(3)$. Euler angles and the unit quaternion are two different ways of representing orientiation or attitude. The main purpose of the former is illustrative purposes, for showing how the attitude evolves over time in plots, given that is the most recognizable for a human. The unit quaternion on the other hand is used in the estimation procedures.

2.2.1 Euler angles

The roll, pitch and yaw angles are denoted ϕ, θ and ψ, together with their angular rates p, q and r in compliance with the SNAME (1950) notations. From Fossen (2011, Ch. 2) and the references therein, the rotation matrix $\boldsymbol{R}_b^n$ may be expressed with them in the following way:

$$\boldsymbol{R}_b^n = \begin{pmatrix} \mathrm{c}\theta\mathrm{c}\psi & -\mathrm{c}\phi\mathrm{s}\psi + \mathrm{s}\phi\mathrm{s}\theta\mathrm{c}\psi & \mathrm{s}\phi\mathrm{s}\psi + \mathrm{s}\theta\mathrm{c}\phi\mathrm{c}\psi \\ \mathrm{c}\theta\mathrm{s}\psi & \mathrm{c}\phi\mathrm{c}\psi + \mathrm{s}\psi\mathrm{s}\theta\mathrm{s}\phi & -\mathrm{s}\phi\mathrm{c}\psi + \mathrm{c}\phi\mathrm{s}\psi\mathrm{s}\theta \\ -\mathrm{s}\theta & \mathrm{s}\phi\mathrm{c}\theta & \mathrm{c}\phi\mathrm{c}\theta \end{pmatrix} \in SO(3), \tag{2.2}$$

where $\mathrm{s}\cdot := \sin(\cdot)$, $\mathrm{c}\cdot := \cos(\cdot)$.

2.2.2 Unit quaternion

In addition to Euler angles and the rotation matrix, the rotation between $\{a\}$ and $\{b\}$ may be represented using the unit quaternion $\boldsymbol{q}_a^b = (s, \boldsymbol{r}^\intercal)^\intercal$ where $s \in \mathbb{R}^1$ is the scalar part of the quaternion and $\boldsymbol{r} \in \mathbb{R}^3$ is the vector part. A unit quaternion's conjugate is defined as $\boldsymbol{q}_a^{b*} = (s, -\boldsymbol{r}^\intercal)^\intercal$. For the unit quaternion $\boldsymbol{q}_a^b \in \mathcal{Q}$, we have that

$$\mathcal{Q} := \left\{ \boldsymbol{q} | \boldsymbol{q}^\intercal \boldsymbol{q} = 1,\ \boldsymbol{q} = (s, \boldsymbol{r}^\intercal)^\intercal \right\}.$$

The rotation matrix $\boldsymbol{R}(\boldsymbol{q}_a^b) := \boldsymbol{R}_a^b$ can be obtained from the unit quaternion, $\boldsymbol{q}_a^b$ using

$$\boldsymbol{R}(\boldsymbol{q}_a^b) = \boldsymbol{I}_3 + 2s\boldsymbol{S}(\boldsymbol{r}) + 2\boldsymbol{S}^2(\boldsymbol{r}), \tag{2.3}$$

Fossen (2011, Eq. 2.56) and the reference therein.

Consequently, Euler angles may be obtained from $\boldsymbol{q}_a^b$ by relating these through the rotation matrix

$$\boldsymbol{R}(\boldsymbol{q}_a^b) = \boldsymbol{R}_a^b(\phi, \theta, \psi) = \begin{pmatrix} R_{11} & R_{12} & R_{13} \\ R_{21} & R_{22} & R_{23} \\ R_{31} & R_{32} & R_{33} \end{pmatrix}, \tag{2.4}$$

such that

$$\phi = \arctan2(R_{32}, R_{33}), \tag{2.5}$$

$$\theta = -\arcsin(R_{32}) = -\arctan\left(\frac{R_{31}}{\sqrt{1 - R_{31}^2}}\right), \quad \text{for } \theta \neq \pm 90^\circ \tag{2.6}$$

$$\psi = \arctan2(R_{31}, R_{11}). \tag{2.7}$$

The unit quaternion rate of change, $\dot{\boldsymbol{q}}_a^b$, may be expressed in numerous ways. Different notations are used in this thesis, and they are all equivalent. One of them takes the form of

$$\dot{\boldsymbol{q}}_a^b = \boldsymbol{T}(\boldsymbol{q}_a^b)\boldsymbol{\omega}_{ba}^a, \tag{2.8}$$

where

$$\boldsymbol{T}(\boldsymbol{q}) = \frac{1}{2}\begin{pmatrix} -\boldsymbol{r} \\ s\boldsymbol{I}_3 + \boldsymbol{S}(\boldsymbol{r}) \end{pmatrix} = \frac{1}{2}\begin{pmatrix} -r_1 & -r_2 & -r_3 \\ s & -r_3 & r_2 \\ r_3 & s & -r_1 \\ -r_2 & r_1 & s \end{pmatrix}, \tag{2.9}$$

similar to Fossen (2011, Ch. 2.2.2). An alternative representation is

$$\dot{\boldsymbol{q}}_a^b = \boldsymbol{q}_a^b \otimes \begin{pmatrix} 0 \\ \boldsymbol{\omega}_{ba}^a \end{pmatrix}, \tag{2.10}$$

and a third

$$\dot{\boldsymbol{q}}_a^b = \boldsymbol{q}_a^b \otimes \bar{\boldsymbol{\omega}}_{ba}^a, \tag{2.11}$$

strongly resembling the previous.

2.3 Navigation Related Notations

In this work, coordinate frames are represented as $\{\cdot\}$, where the $\cdot$ is exchanged with some letter depending on the frame. All vectors representing a state of the navigating vehicle is generally presented using the notation

$$\boldsymbol{z}_{bc}^a \in \mathbb{R}^3, \tag{2.12}$$

where a vector $\boldsymbol{z}$, to frame $\{c\}$, relative $\{b\}$, decomposed in $\{a\}$. An overview of variables used to describe position, velocity and attitude (PVA) is found in Table. 2.1.

Table 2.1: Navigation related notations

Type	**Notation**
Position vector	$\boldsymbol{p}^{\star}_{\star\star} \in \mathbb{R}^3$
Linear velocity vector	$\boldsymbol{v}^{\star}_{\star\star} \in \mathbb{R}^3$
Specific force vector	$\boldsymbol{f}^{\star}_{\star\star} \in \mathbb{R}^3$
Angular velocity vector	$\boldsymbol{\omega}^{\star}_{\star\star} \in \mathbb{R}^3$
Gravity vector	$\boldsymbol{g}^{\star}_{b} \in \mathbb{R}^3$
Rotation matrix	$\boldsymbol{R}^{\star}_{\star} \in SO(3)$
Unit quaternion	$\boldsymbol{q}^{\star}_{\star} \in \boldsymbol{Q}$
Latitude	$\mu \in [-\pi, \pi]$
Longitude	$\lambda \in [-\pi, \pi]$
Height	$h \in \mathbb{R}^1$

3

GNSS/INS Integration

This chapter is based on Bryne et al. (2017a).

3.1 Introduction

This chapter considers the NLOs of Grip et al. (2013) and Johansen and Fossen (2015), which are based on complementary filtering for attitude estimation, Mahony et al. (2008), in combination with a linear approach to design a translational motion observer (TMO), Grip et al. (2012b), which in turn is used to estimate the position, linear velocity and specific force. In applied usage, NLOs are immature, in particular related to implementation aspects and handling imperfect measurements with different errors, resolution and sample rates. In addition to present implementation related aspects of the NLO, further re-design is addressed to answer the research questions presented above. The basis for this work include linear methods for exact discretization of the translational motion part of the observer, error model augmentation, and the methods in Hua et al. (2014); Fossen (2011) for discretization, tuning and multi-rate implementation of the attitude observer.

Since NLOs are commonly designed using nonlinear stability theory in continuous time, a challenge is how to best discretize the observer dynamics and how to manage measurements that may have different sampling rates, may be asynchronous, or delayed. For the complementary filter (Mahony et al., 2008), applied to attitude estimation, some answers are given in Hua et al. (2014). For the update of position and velocity estimates, the best practice appears to be use of a corrector–predictor algorithm (Fossen, 2011, Ch. 11.3.4), similar to the propagation update steps in a Kalman filter (KF), (Brown and Hwang, 2012, Ch. 4.2). Similar ideas can be used to deal with delayed measurements, when the delay is known, Hansen et al. (2015); Khosravian et al. (2014, 2015). Still, a systematic study on discrete-time implementation has not been made in the context of NLOs.

In the works of Salcudean (1991); Vik and Fossen (2001); Mahony et al. (2008); Hua (2010); Batista et al. (2012c); Grip et al. (2012a, 2013, 2015), fixed observer feedback gains are sufficient to achieve certain stability properties, which guarantee a high degree of robustness. A relevant question, also when comparing NLOs to estimators such as the MEKF and minimum energy filters (Zamani et al., 2013), whose global stability properties are difficult to guarantee, is whether a fixed gain strategy incurs a loss of estimation accuracy in steady-state or transient conditions. If so, an other question needs to be resolved; that is how nonlinear or time-varying gains can be synthesized to achieve significantly better performance of NLOs compared to applying a fixed-gain approach.

Based on the above, the main contributions of this chapter are:

- A linear time-varying (LTV) representation of the observer error dynamics is exploited to formulate a time-varying Riccati equation to select time-varying gains in the update of velocity and position estimates (as well as some auxiliary variable estimates).
- Strategies originally developed for the Kalman filter are exploited in handling sequential single-measurement updates to accommodate multi-rate and asynchronous measurements in estimation of position, velocity and attitude based on direct observer implementations.
- Inclusion of GNSS error models in order to take into account the dynamic noise characteristic of GNSS observables.
- Experimental verification of the presented methods using data collected during a unmanned aerial vehicle (UAV) test flight mission.

3.1.1 Organization

The chapter is organized by first presenting the necessary mathematical notations and definitions. Then, the kinematic modeling, which the INSs are based upon, and the respective inertial sensor models are presented. After that, an overview of the nonlinear observer structures are presented before going into detail by presenting the attitude observer. The presentation follows with the two TMOs, estimating the position, linear velocity and specific forces. The TMO required for the loosely coupled integration scheme is presented first, then the tightly coupled GNSS/INS integration scheme is presented, both with the respective GNSS noise and error models. The experimental verification of the presented methods and algorithms concludes the chapter.

3.1.2 Application example

With new emerging technologies, the commercial market for unmanned aerial vehicles (UAV) is growing rapidly. These types of aircraft perform a multitude of

task, including surveillance, scientific measurements, environmental monitoring and wildlife mapping, and inherently require an accurate, precise, lightweight and small-size navigation solution. A photograph of a Penguin B fixed-wing UAV is shown in Fig. 3.1, and its technical specifications are included in Table 3.1.

Figure 3.1: Penguin B unmanned aerial vehicle (UAV) in flight. Photo: Jakob M. Hansen.

Table 3.1: Penguin B Unmanned Aerial Vehicle (UAV) Technical Specifications

Engine type:	Gasoline
Wingspan:	3.3 m
Length:	2.27 m
MTOW:	21.5 kg
Endurance:	5+ hours
Cruise speed:	28 m/s
Max level speed:	36 m/s

In flight, high resolution PVA and temporal information must be provided by the navigation system for the UAV and its operator to safely and accurately control the vehicle and georeference the payload sensor data in order to fulfill the mission objective. At an altitude of 200 m, a 1° error in roll corresponds to approximately 3.5 m georeferencing error on the ground, and a 100 ms timing error results in a 3 m error at a speed of 30 m/s. Also, position information obtained from a

typical commercial grade GNSS receiver only provide position data at 1–5 Hz, while the dynamics of the craft are much faster than that. Hence, even though GNSS solutions are improving, there are still issues, prompting the employment of integrated GNSS/INS to conduct UAV missions. Moreover, attitude information is also not available using only one GNSS antenna, meaning that this has to be estimated using integrated GNSS/INS. Fig. 3.2 presents the flight path of a UAV test flight, conducted from Eggemoen, Norway.

In the setup used for experimental validation, the UAV is equipped with an ADIS 16488 inertial measurement unit (IMU) measuring specific force, rotation rate and magnetic field of the vehicle at 410 Hz. For more on IMUs, see section "Inertial and magnetic measurements". Additionally a u-Blox LEA-6T GNSS receiver supplies computed position as well as pseudoranges at 5 Hz. The sensors are synchronized using a microcontroller in order to accurately timestamp the measurements. Engine induced vibrations are significant and can typically be seen as a signal of magnitude close to 1 m/s^2 at 70 Hz on the accelerometer measurements.

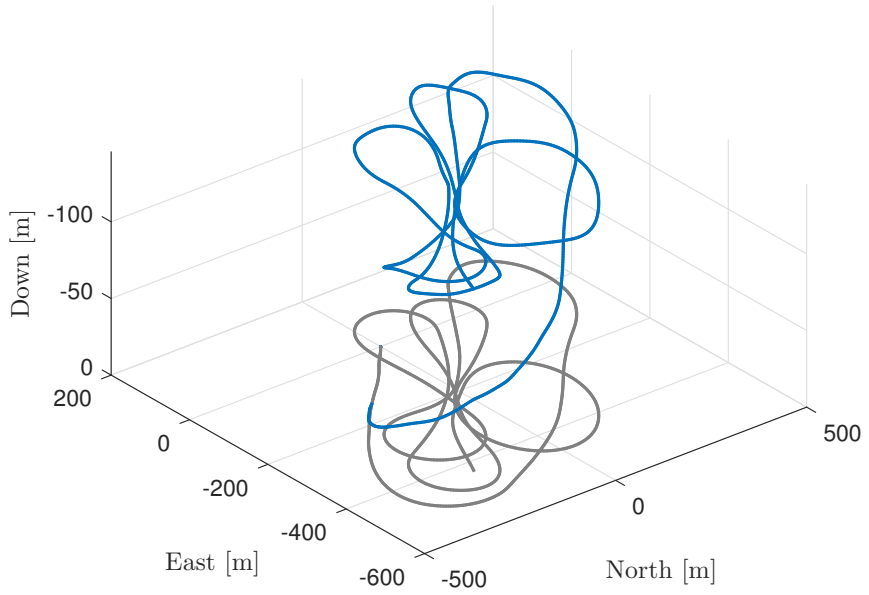

Figure 3.2: Flight path. The flight path using a Penguin B Unmanned Aerial Vehicle (UAV) is shown. Takeoff of the UAV is used as the origin. The flight path is shown in blue, while the ground track is shown in gray.

3.1.3 Notation and preliminaries

The Euclidean vector norm is denoted as $\|\cdot\|_2$. The column vector $(z_1; z_2)$ describes the vector z_1 stacked over the vector z_2. The set $\mathcal{I}_k$ is a set containing the indices of available measurements at time $t = k \cdot T$ where T indicates the sampling interval and k is the time index. $E[\cdot]$ denotes statistical expectation, while the matrix exponential function is denoted $e^{(\cdot)}$. The identity matrix of dimension n is denoted $\boldsymbol{I}_n$, and $\boldsymbol{0}_{n\times n}$ symbolizes a $n \times n$ matrix of zeros, or just $\boldsymbol{0}$ where the dimensions are implicitly given by the context. To simplify the notation, usually the time dependency is implicitly given.

A unit quaternion $\boldsymbol{q} = (s_q; \boldsymbol{r}_q)$ with $||\boldsymbol{q}||_2 = 1$ consists of a real part $s_q \in \mathbb{R}$ and a vector part $\boldsymbol{r}_q \in \mathbb{R}^3$. For a vector $\boldsymbol{x} \in \mathbb{R}^3$, with transpose $\boldsymbol{x}^\intercal$, we denote by $\bar{\boldsymbol{x}}$ the quaternion with zero real part and vector part $\boldsymbol{x}$, that is $\bar{\boldsymbol{x}} = (0; \boldsymbol{x})$. The Hamiltonian quaternion product is given by $\otimes$, the vector cross product is denoted $\times$, and for a vector $\boldsymbol{x} \in \mathbb{R}^3$ we define the skew-symmetric matrix

$$\boldsymbol{S}(\boldsymbol{x}) = \begin{pmatrix} 0 & -x_3 & x_2 \\ x_3 & 0 & -x_1 \\ -x_2 & x_1 & 0 \end{pmatrix},$$

with $\boldsymbol{x} = (x_1; x_2; x_3)$. A block diagonal matrix $\boldsymbol{M}$ is indicated with

$$\boldsymbol{M} = \text{blockdiag}\,(\boldsymbol{M}_1, \boldsymbol{M}_2, \ldots, \boldsymbol{M}_n)$$

for some square matrices $\boldsymbol{M}_1, \boldsymbol{M}_2, \ldots, \boldsymbol{M}_n$. The Moore-Penrose pseudo inverse is denoted $\dagger$. The sinc function is defined as

$$\text{sinc}(\alpha) := \begin{cases} 1 & \text{for } \alpha = 0 \\ \frac{\sin(\alpha)}{\alpha} & \text{otherwise,} \end{cases} \tag{3.1}$$

for an angle α. Gaussian white noise n with mean μ and variance σ^2 is given as $n(\mu, \sigma^2)$.

Superscript indexes are used to indicate the coordinate system in which a given vector is decomposed, thus $\boldsymbol{x}^a_{bc}$ and $\boldsymbol{x}^b_{bc}$ refers to the same vector $\boldsymbol{x}$ decomposed in the coordinate systems indexed by $\{a\}$ and $\{b\}$, respectively. The rotation between these coordinate systems may be represented by a quaternion $\boldsymbol{q}^b_a$. The corresponding rotation matrix is denoted $\boldsymbol{R}(\boldsymbol{q}^b_a)$. The rate of rotation of the coordinate system indexed by $\{b\}$ with respect to $\{a\}$, decomposed in $\{c\}$, is denoted $\boldsymbol{\omega}^c_{ab}$.

In the following, $\{e\}$ denotes the earth-centered, earth-fixed (ECEF) coordinate system, $\{b\}$ the vehicle BODY-fixed coordinate system, and $\{i\}$ the earth-centered inertial (ECI) coordinate system.

3.1.4 Discretization and measurements samples

For the discrete-time implementation, the discretization interval T and a discrete time index k are utilized such that the continuous time variable t is related to T

and k with $t = kT$ (for a constant T).

At a given index k all valid measurements at time $t = kT$ are contained in the measurements set $\mathcal{I}_k$ of measurements. If the i'th measurement is available and valid, this is indicated by $i \in \mathcal{I}_k$. The opposite case is denoted as $i \notin \mathcal{I}_k$.

3.2 Modeling

3.2.1 Kinematic model

The rigid body kinematic model follows from Grip et al. (2013) and Britting (1971),

$$\dot{\boldsymbol{p}}^e_{eb} = \boldsymbol{v}^e_{eb}, \tag{3.2}$$

$$\dot{\boldsymbol{v}}^e_{eb} = -2\boldsymbol{S}(\boldsymbol{\omega}^e_{ie})\boldsymbol{v}^e_{eb} + \boldsymbol{f}^e_{ib} + \boldsymbol{g}^e_b(\boldsymbol{p}^e_{eb}), \tag{3.3}$$

$$\dot{\boldsymbol{q}}^e_b = \frac{1}{2}\boldsymbol{q}^e_b \otimes \bar{\boldsymbol{\omega}}^b_{ib} - \frac{1}{2}\bar{\boldsymbol{\omega}}^e_{ie} \otimes \boldsymbol{q}^e_b, \tag{3.4}$$

where $\boldsymbol{p}^e_{eb}, \boldsymbol{v}^e_{eb}, \boldsymbol{f}^e_{ib} \in \mathbb{R}^3$ are position, linear velocity and specific force in the ECEF frame, respectively.

The attitude of the vehicle is represented by a unit quaternion $\boldsymbol{q}^e_b$. It represents the rotation from BODY to ECEF, and $\boldsymbol{\omega}^b_{ib}$ represents the rotation rate of BODY with respect to ECI, while $\boldsymbol{\omega}^e_{ie} = (0; 0; \omega_{ie})$, where ω_{ie} represents the Earth's rotation rate, which is assumed to be constant. Equivalently, by representing the attitude as a rotation matrix, (3.4) is realized as

$$\dot{\boldsymbol{R}}^e_b = \boldsymbol{R}^e_b \boldsymbol{S}(\boldsymbol{\omega}^b_{ib}) - \boldsymbol{S}(\boldsymbol{\omega}^e_{ie})\boldsymbol{R}^e_b. \tag{3.5}$$

The known vector $\boldsymbol{g}^e_b(\boldsymbol{p}^e_{eb})$ denotes the plumb-bob gravity vector, which is a function of the vehicle's position decomposed in the ECEF frame and is obtained with a gravity model.

3.2.2 Inertial and magnetic measurements

The inertial sensor model is chosen based upon strapdown technology, that is an IMU fixed to the BODY frame

$$\boldsymbol{f}^b_{\text{IMU}} = \boldsymbol{f}^b_{ib} + \boldsymbol{\varepsilon}^b_f, \tag{3.6}$$

$$\boldsymbol{\omega}^b_{\text{IMU}} = \boldsymbol{\omega}^b_{ib} + \boldsymbol{b}^b_{\text{gyro}} + \boldsymbol{\varepsilon}^b_\omega, \tag{3.7}$$

$$\dot{\boldsymbol{b}}^b_{\text{gyro}} = \boldsymbol{\varepsilon}^b_b, \tag{3.8}$$

where $\boldsymbol{f}^b_{ib} = \boldsymbol{R}^b_e \left(\boldsymbol{a}^e_{ib} - \boldsymbol{g}^e_b(\boldsymbol{p}^e_{eb})\right)$, with $\boldsymbol{a}^e_{ib}$ being the acceleration relative the Earth measured by the IMU and where $\boldsymbol{b}^b_{\text{gyro}}$ denotes the gyro/angular rate bias. Accelerometer drift and biases are assumed to be compensated for using offline and

online calibration methods such as (Grip et al., 2012a, Sec. VI). Reference information about the heading may be obtained using a magnetometer that measures

$$m^b_{\text{mag}} = m^b + \varepsilon^b_m. \tag{3.9}$$

The variables ε^b_* represent measurement errors. Alternative sensors for providing heading information are compasses or GNSS-based heading obtained from multiple receiver measurements and a known baseline between the receivers.

With the kinematic vehicle model together with inertial and magnetic measurement models presented, the following section introduces the integration of GNSS and inertial measurements.

3.3 Nonlinear Observer for Integrated GNSS/INS Navigation

3.3.1 Overview

The two most common GNSS/INS integration techniques are known in the navigation literature as loosely coupled and tightly coupled integration, and are described below.

With loosely coupled integration the receiver's measurements of position, and sometimes velocity, are fused with the inertial measurements. When applying this integration strategy, the GNSS position and velocity measurements are given as $\boldsymbol{p}^e_{\text{GNSS}} = \boldsymbol{p}^e_{eb} + \boldsymbol{\delta}_p$ and $\boldsymbol{v}^e_{\text{GNSS}} = \boldsymbol{v}^e_{eb} + \boldsymbol{\delta}_v$ where $\boldsymbol{\delta}_*$ represents the errors and noise. These are calculated by the receiver, in the ECEF frame, either with a Least Squares estimator or by using an EKF (Groves, 2013, Ch. 9.4).

With a tightly coupled integration strategy, the raw GNSS observables, pseudorange and Doppler range-rate, are utilized as aiding measurements by relating these to the inertial measurements using (3.2)–(3.4). Here, the pseudorange and range-rate measurements are denoted y_i and v_i, respectively, representing measurements from the i-th satellite out of m satellites in view. These measurements are determined based on the knowledge of satellite position and velocity, denoted $\boldsymbol{p}^e_{eb_i}$ and $\boldsymbol{v}^e_{eb_i}$, calculated with the help of broadcasted satellite ephemeris.

An advantage of the loosely coupled approach is the ease of implementation as the receiver takes care of all considerations about satellite constellation and integrity of the raw GNSS observables. On the other hand this also entails that only complete solutions can be used, whereas the tight integration approach can use a few raw GNSS observables that would be insufficient for a standalone solution. A disadvantage of tightly coupled integration is that not all receivers grants access to the raw GNSS observables, Groves (2013). Moreover, the implementation and tuning of GNSS/INS integration is more straight forward with loosely coupled integration than with tightly coupled integration due to pseudorange measurements with different elevation angles may have considerably different noise characteristics. On the other hand, integrity monitoring is easier with tightly coupled inte-

gration in the range domain compared to its counterpart in the position domain since erroneous pseudorange measurements may be excluded while maintaining GNSS aiding. If a GNSS fault in loosely coupled integration is detected, GNSS aiding is lost until the fault has been remedied.

A schematic overview of the difference between the two integration strategies, applying the same NLO for attitude determination, is shown in Fig. 3.3. Two key features are obtained using the NLO in feedback interconnection with the TMO as depicted in Fig. 3.3; The first feature is that the attitude is estimated without linearization, in contrast to KF-based techniques, making the attitude observer robust to initialization errors allowing for large initial attitude errors. The second, is that the attitude observer is utilizing the estimated specific force in the navigation frame provided by the TMO as reference vector when calculating attitude corrections. The latter feature is particularly useful when the navigation system is accelerated.

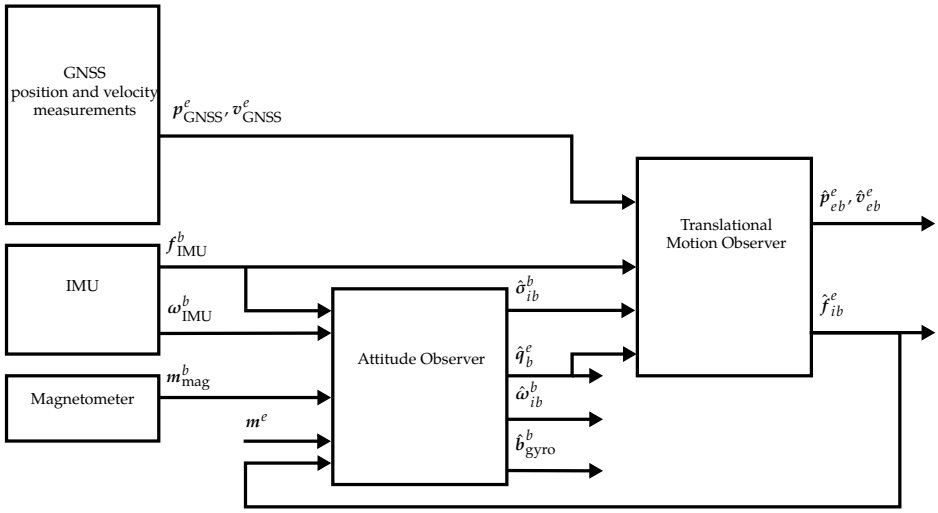

(a) Loosely coupled GNSS/INS integration

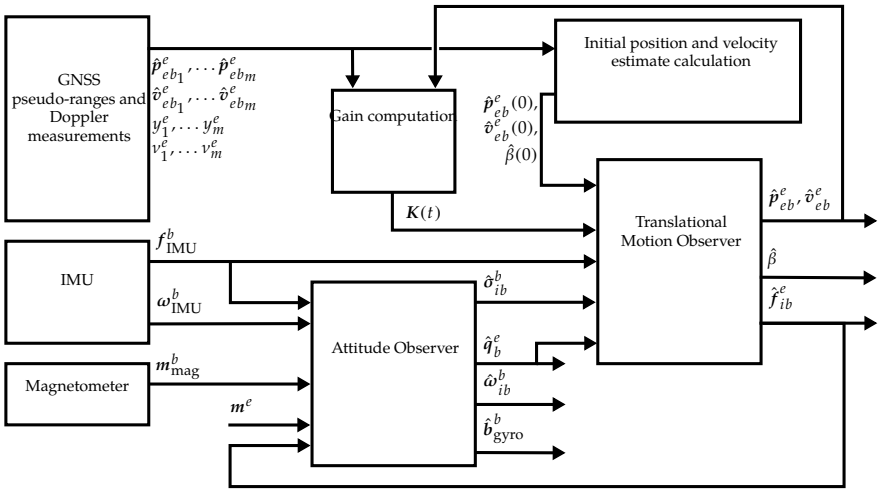

(b) Tightly coupled GNSS/INS integration. An algebraic pseudo-range solver is used to initialize the translational motion observer

Figure 3.3: Feedback-interconnected observer structures. An overview of the two feedback-interconnected observer structures used for integration of global navigation satellite systems (GNSS) and the inertial navigation system (INS) is presented. Fig. 3.3a shows the loosely coupled INS/GNSS integration. With loosely coupled integration there exists a standalone GNSS solution used as aiding for estimation of position and velocity. Fig. 3.3b shows the tightly coupled INS/GNSS integration. With this integration scheme, the position and velocity solution is obtained using GNSS pseudorange and Doppler range-rate measurements in combination with the inertial measurement unit (IMU) readings. With both integration techniques, the nonlinear attitude observer provides the translational motion observer (TMO) with the quaternion $\hat{q}^e_b$ and injection term $\hat{\sigma}$, while the TMO provides the attitude observer with the estimate of the specific force $\hat{f}^e$.

3.4 Attitude Observer

The proposed loosely and tightly coupled GNSS/INS integration schemes, are both dependent on the nonlinear attitude observer. The latter is presented in detail in this section, where discretization prior to implementation, also is discussed.

The attitude observer used is based on Mahony et al. (2008) and Grip et al. (2012a, 2013), employing complementary filtering,

$$\dot{\hat{\boldsymbol{q}}}_b^e = \frac{1}{2}\hat{\boldsymbol{q}}_b^e \otimes \left(\bar{\boldsymbol{\omega}}_{\text{IMU}}^b - \bar{\hat{\boldsymbol{b}}}_{\text{gyro}}^b + \bar{\hat{\boldsymbol{\sigma}}}_{ib}^b\right) - \frac{1}{2}\bar{\boldsymbol{\omega}}_{ie}^e \otimes \hat{\boldsymbol{q}}_b^e, \tag{3.10}$$

$$\dot{\hat{\boldsymbol{b}}}_{\text{gyro}}^b = \text{Proj}\left(-k_I \hat{\boldsymbol{\sigma}}_{ib}^b, \|\hat{\boldsymbol{b}}_{\text{gyro}}^b\|_2 \leq M_{\hat{b}}\right), \tag{3.11}$$

$$\begin{aligned}\hat{\boldsymbol{\sigma}}_{ib}^b &= k_1 \boldsymbol{f}_{\text{IMU}}^b \times \boldsymbol{R}(\hat{\boldsymbol{q}}_b^e)^\intercal \text{sat}_{M_f}(\hat{\boldsymbol{f}}_{ib}^e) \\ &\quad + k_2 \boldsymbol{m}_{\text{mag}}^b \times \boldsymbol{R}(\hat{\boldsymbol{q}}_b^e)^\intercal \boldsymbol{m}_{eb}^e,\end{aligned} \tag{3.12}$$

where $\bar{\boldsymbol{x}} = (0; \boldsymbol{x})$, k_1, k_2, k_I are gains. k_I is the gain of the gyro/angular rate bias estimator, giving an integral effect in the NLO, whereas Proj$(\cdot)$ is a projection operator ensuring that the gyro/angular rate bias is bounded, $\|\hat{\boldsymbol{b}}_{\text{gyro}}^b\|_2 \leq M_{\hat{b}}$. See Grip et al. (2013) for details. The injection term $\hat{\boldsymbol{\sigma}}_{ib}^b$ is utilized to correct the attitude and compensate for the gyro bias in (3.10), by estimating it in (3.11), with the goal of obtaining an estimate of $\boldsymbol{\omega}_{ib}^b$ with $\hat{\boldsymbol{\omega}}_{ib}^b = \boldsymbol{\omega}_{\text{IMU}}^b - \hat{\boldsymbol{b}}_{\text{gyro}}^b$. The injection $\hat{\boldsymbol{\sigma}}_{ib}^b$ is based on comparing the measured vectors in the BODY frame, here specific force and magnetic field from the accelerometer and the magnetometer, respectively, with the corresponding reference vector in the ECEF frame, rotated to the BODY frame using $\boldsymbol{R}(\hat{\boldsymbol{q}}_b^e)$. If there are discrepancies between the two, the nonlinear injection term $\hat{\boldsymbol{\sigma}}_{ib}^b$ acts as an angular velocity in (3.10) to compensate for this error. The reference vectors in question are $\boldsymbol{m}_{eb}^e$, being the Earth's magnetic field and assumed to be known, and the estimated specific force $\hat{\boldsymbol{f}}_{ib}^e$. Moreover, $\text{sat}_{M_f}(\cdot)$ is a saturation operator, such that specific force estimate remains bounded, $\|\hat{\boldsymbol{f}}_{ib}^e\|_2 \leq M_f$. As in Grip et al. (2013), $\hat{\boldsymbol{f}}_{ib}^e$ is obtained from the TMO, presented later on, which offers an accurate estimate also when the vehicle is accelerated. This is beneficial, compared to assuming that $\boldsymbol{f}_{ib}^e \approx -\boldsymbol{g}_b^e(\hat{\boldsymbol{p}}_{eb}^e)$, where the gravity component $\boldsymbol{g}_b^e$ is obtained with a gravity model based on the estimated position $\hat{\boldsymbol{p}}_{eb}^e$, an assumption that holds only when the vehicle in question is not exposed to acceleration for prolonged periods of time. More vector measurement/reference pairs may be added to (3.12) depending on the application. A minimum of two colinear vectors are required in order to guarantee convergence regardless of the vehicle trajectories. The injection term $\hat{\boldsymbol{\sigma}}_{ib}^b$ is calculated in a way that resembles how the linearized attitude error enters the measurement matrix when using the quaternion-based MEKF, Markley (2003), algorithm to estimate the attitude.

3.4.1 Alternative implementation of the injection term and continuous-time gain selection

There exist other alternatives than (3.12) to construct the vector measurement/reference pairs. Normalized versions of $\boldsymbol{m}^b_{\text{mag}}$, $\boldsymbol{m}^e_{eb}$, $\boldsymbol{f}^b_{\text{IMU}}$ and $\text{sat}_{M_f}(\hat{\boldsymbol{f}}^e_{ib})$ can be implemented using

$$\underline{\boldsymbol{f}}^b = \frac{\boldsymbol{f}^b_{\text{IMU}}}{\|\boldsymbol{f}^b_{\text{IMU}}\|}, \qquad \underline{\boldsymbol{m}}^b = \frac{\boldsymbol{m}^b_{\text{mag}}}{\|\boldsymbol{m}^b_{\text{mag}}\|},$$
$$\underline{\boldsymbol{f}}^e = \frac{\text{sat}_{M_f}(\hat{\boldsymbol{f}}^e_{ib})}{\|\text{sat}_{M_f}(\hat{\boldsymbol{f}}^e_{ib})\|}, \quad \underline{\boldsymbol{m}}^e = \frac{\boldsymbol{m}^e_{eb}}{\|\boldsymbol{m}^e_{eb}\|}.$$

By doing so, the gains k_1 and k_2 can be viewed as cut-off frequencies of a complementary filter as described in Mahony et al. (2008); Hua et al. (2014) with the same unit as the angular velocity $\boldsymbol{\omega}^b_{\text{IMU}}$ in (3.12) since the vector pairs become dimensionless. This means that for motion with frequencies above k_1 (rad/s), the rate gyro is the primary sensor used for estimating the attitude in the directions excited by the first reference vector, while for lower frequencies, the first reference vector correction dominates. Similarly k_2 essentially determines the cut-off frequency for use of low-frequency information from the second reference vector. Furthermore, the construction of vector pairs may be additionally extended, inspired by the TRIAD algorithm, Black (1964), by crossing the k-th vector pair with the previous vector pair, making the vectors in each frame perpendicular to each other. Hence, the new vectors $\underline{\boldsymbol{v}_1}^b$, $\underline{\boldsymbol{v}_1}^e$, $\underline{\boldsymbol{v}_2}^b$ and $\underline{\boldsymbol{v}_2}^e$ take the form of,

$$\underline{\boldsymbol{v}_1}^b = \underline{\boldsymbol{f}}^b, \quad \underline{\boldsymbol{v}_2}^b = \underline{\boldsymbol{f}}^b \times \underline{\boldsymbol{m}}^b,$$
$$\underline{\boldsymbol{v}_1}^e = \underline{\boldsymbol{f}}^e, \quad \underline{\boldsymbol{v}_2}^e = \underline{\boldsymbol{f}}^e \times \underline{\boldsymbol{m}}^e,$$

resulting in $\hat{\boldsymbol{\sigma}}^b_{ib}$ becoming,

$$\hat{\boldsymbol{\sigma}}^b_{ib} = k_1 \underline{\boldsymbol{v}_1}^b \times \boldsymbol{R}(\hat{\boldsymbol{q}}^e_b)^\intercal \underline{\boldsymbol{v}_1}^e + k_2 \underline{\boldsymbol{v}_2}^b \times \boldsymbol{R}(\hat{\boldsymbol{q}}^e_b)^\intercal \underline{\boldsymbol{v}_2}^e, \tag{3.13}$$

with the possibility to increase the attitude estimation performance compared to using (3.12).

Alternatively, a linearization of the complementary attitude filter is provided in (Hua et al., 2014, Eq. (37)), and may be used to develop an optimal gain selection algorithm given the noise covariances.

3.4.2 Discretization of the attitude observer

The rate gyro measurements are integrated at a high rate $f = 1/T$, updating the attitude estimates whenever a new angular rate measurement is available, as in

Hua et al. (2014). If T is small enough to assume that $\hat{\omega}(t)$ remains constant between samples, the exact discretization of the kinematic equation (3.10), is obtained using

$$\hat{\boldsymbol{q}}_b^e[k] = \boldsymbol{e}^{\left(\frac{T}{2}\boldsymbol{\Omega}(\hat{\boldsymbol{\omega}}[k])\right)}\boldsymbol{e}^{\left(-\frac{T}{2}\bar{\boldsymbol{\Omega}}(\boldsymbol{\omega}_{ie}^e)\right)}\hat{\boldsymbol{q}}_b^e[k-1], \tag{3.14}$$

where

$$\begin{aligned}
\hat{\boldsymbol{\omega}}[k] &= \boldsymbol{\omega}_{\text{IMU}}^b[k] - \hat{\boldsymbol{b}}_{\text{gyro}}^b[k-1] + \hat{\boldsymbol{\sigma}}_{ib}^b[k], \\
\boldsymbol{\Omega}(\boldsymbol{\omega}) &= \begin{pmatrix} 0 & -\boldsymbol{\omega}^\intercal \\ \boldsymbol{\omega} & -\boldsymbol{S}(\boldsymbol{\omega}) \end{pmatrix}, \quad \bar{\boldsymbol{\Omega}}(\boldsymbol{\omega}) = \begin{pmatrix} 0 & -\boldsymbol{\omega}^\intercal \\ \boldsymbol{\omega} & \boldsymbol{S}(\boldsymbol{\omega}) \end{pmatrix}, \\
\boldsymbol{e}^{\left(\frac{T}{2}\boldsymbol{\Omega}(\boldsymbol{\omega})\right)} &= \cos\left(\frac{T}{2}\|\boldsymbol{\omega}\|_2\right)\boldsymbol{I}_4 \\
&\quad + \frac{T}{2}\operatorname{sinc}\left(\frac{T}{2}\|\boldsymbol{\omega}\|_2\right)\boldsymbol{\Omega}(\boldsymbol{\omega}),
\end{aligned}$$

and

$$\begin{aligned}
\boldsymbol{e}^{\left(-\frac{T}{2}\bar{\boldsymbol{\Omega}}(\omega)\right)} &= \left(\cos\left(\frac{T}{2}\|\boldsymbol{\omega}\|_2\right)\boldsymbol{I}_4 \right. \\
&\quad \left. + \frac{T}{2}\operatorname{sinc}\left(\frac{T}{2}\|\boldsymbol{\omega}\|_2\right)\bar{\boldsymbol{\Omega}}(\boldsymbol{\omega})\right)^{-1}.
\end{aligned}$$

According to Hua et al. (2014), the expressions $\cos(\cdot)$ and $\operatorname{sinc}(\cdot)$ can, in practice, be approximated for by their first- or second-order approximation or by using a lookup table to increase the computational efficiency of (3.14). After (3.14) is calculated, re-normalization of $\hat{\boldsymbol{q}}_b^e$ is carried out to account for numerical round-off errors,

$$\hat{\boldsymbol{q}}_b^e[k] = \frac{\hat{\boldsymbol{q}}_b^e[k]}{\|\hat{\boldsymbol{q}}_b^e[k]\|}. \tag{3.15}$$

The gyro bias estimate can be updated using exact integration of (3.11) as

$$\hat{\boldsymbol{b}}_{\text{gyro}}^b[k] = \hat{\boldsymbol{b}}_{\text{gyro}}^b[k-1] - T\,k_I\,\hat{\boldsymbol{\sigma}}_{ib}^b[k], \tag{3.16}$$

where a projection algorithm, such as that of Grip et al. (2012a), is straightforward to add. In this implementation, one or both terms in $\hat{\boldsymbol{\sigma}}[k]$ is not included if there is no valid vector measurement available at time index k. To ensure that the cut-off frequency, chosen for each measurement vector, maps from continuous to discrete time, $\hat{\boldsymbol{\sigma}}_{ib}^b[k]$ is implemented as

$$\hat{\boldsymbol{\sigma}}_{ib}^b[k] = \hat{\boldsymbol{\sigma}}_{ib,1}^b[k] + \hat{\boldsymbol{\sigma}}_{ib,2}^b[k], \tag{3.17}$$

such that if $i = 1 \in \mathcal{I}_k$, then $\hat{\sigma}_1[k]$ is implemented by

$$\hat{\boldsymbol{\sigma}}_{ib,1}^b[k] = \frac{\delta t_{\text{acc}}}{T}k_1\,\underline{\boldsymbol{v}_1}^b[k] \times \boldsymbol{R}(\hat{\boldsymbol{q}}_b^e[k-1])^\intercal\,\underline{\boldsymbol{v}_1}^e[k], \tag{3.18}$$

else $\hat{\boldsymbol{\sigma}}^b_{ib,1}[k] = \mathbf{0}_{3\times1}$. If $i = 2 \in \mathcal{I}_k$, then

$$\hat{\boldsymbol{\sigma}}^b_{ib,2}[k] = \frac{\delta t_{\text{mag}}}{T} k_2 \, \underline{\boldsymbol{v}_2}^b[k] \times \boldsymbol{R}(\hat{\boldsymbol{q}}^e_b[k-1])^\intercal \underline{\boldsymbol{v}_2}^e[k], \tag{3.19}$$

else $\hat{\boldsymbol{\sigma}}^b_{ib,2}[k] = \mathbf{0}_{3\times1}$. δt_{acc} and δt_{mag} denote the time intervals since the previous valid accelerometer and magnetometer measurements were available, respectively. This ensures that gains and bandwidth of the respective vector measurements are independent of sampling frequency and only decided by the continuous-time cut-off frequencies k_1 and k_2. Typically, the specific force measurement is available at the same rate as the rate gyro readings such that $\delta t_{\text{acc}} = T$. In this case

$$\hat{\boldsymbol{\sigma}}^b_{ib,1}[k] = k_1 \, \underline{\boldsymbol{v}_1}^b[k] \times \boldsymbol{R}(\hat{\boldsymbol{q}}^e_b[k-1])^\intercal \underline{\boldsymbol{v}_1}^e[k],$$

if $i = 1 \in \mathcal{I}_k$. This implementation strategy assumes that a valid specific force measurement is available when a new magnetometer measurement is available due to the cross product of normalized vectors embedded in the implementation of $\hat{\boldsymbol{\sigma}}^b_{ib,2}[k]$.

The described implementation strategy, for nonlinear and potentially low-rate injection terms is in compliance with the corrector-predictor scheme presented in (Fossen, 2011, Ch. 11.3.4) and allows for k_1, k_2 and k_I to be time-varying.

With the attitude estimator defined, the following two sections present the loosely and tightly coupled TMOs in detail.

3.5 Loosely Coupled Translation Motion Observer

The TMO presented first is used together with the attitude observer to perform the loosely coupled GNSS/INS integration. In addition to the algorithm itself, conditions for stability, and gain selection are presented. Discretization and implementation considerations are also covered.

For loosely coupled GNSS/INS integration, the TMO is obtained from Grip et al. (2013),

$$\begin{aligned}\dot{\hat{\boldsymbol{p}}}^e_{eb} &= \hat{\boldsymbol{v}}^e_{eb} + \vartheta \boldsymbol{K}^0_{pp}(\boldsymbol{p}^e_{\text{GNSS}} - \hat{\boldsymbol{p}}^e_{eb}) \\ &\quad + \boldsymbol{K}^0_{vp}(\boldsymbol{v}^e_{\text{GNSS}} - \hat{\boldsymbol{v}}^e_{eb}),\end{aligned} \tag{3.20}$$

$$\begin{aligned}\dot{\hat{\boldsymbol{v}}}^e_{eb} &= -2\boldsymbol{S}(\boldsymbol{\omega}^e_{ie})\hat{\boldsymbol{v}}^e_{eb} + \hat{\boldsymbol{f}}^e_{ib} + \boldsymbol{g}^e_b(\hat{\boldsymbol{p}}^e_{eb}) \\ &\quad + \vartheta^2 \boldsymbol{K}^0_{pv}(\boldsymbol{p}^e_{\text{GNSS}} - \hat{\boldsymbol{p}}^e_{eb}) \\ &\quad + \vartheta \boldsymbol{K}^0_{vv}(\boldsymbol{v}^e_{\text{GNSS}} - \hat{\boldsymbol{v}}^e_{eb}),\end{aligned} \tag{3.21}$$

$$\begin{aligned}\dot{\boldsymbol{\xi}}^e_{ib} &= -\boldsymbol{R}(\hat{\boldsymbol{q}}^e_b)\boldsymbol{S}(\hat{\boldsymbol{\sigma}}^b_{ib})\boldsymbol{f}^b_{\text{IMU}} \\ &\quad + \vartheta^3 \boldsymbol{K}^0_{p\xi}(\boldsymbol{p}^e_{\text{GNSS}} - \hat{\boldsymbol{p}}^e_{eb}) \\ &\quad + \vartheta^2 \boldsymbol{K}^0_{v\xi}(\boldsymbol{v}^e_{\text{GNSS}} - \hat{\boldsymbol{v}}^e_{eb}),\end{aligned} \tag{3.22}$$

$$\hat{\boldsymbol{f}}^e_{ib} = \boldsymbol{R}(\hat{\boldsymbol{q}}^e_b)\boldsymbol{f}^b_{\text{IMU}} + \boldsymbol{\xi}^e_{ib}. \tag{3.23}$$

The rotation matrix $\boldsymbol{R}(\hat{\boldsymbol{q}}_b^e)$ is obtained from the standard formula $\boldsymbol{R}(\hat{\boldsymbol{q}}_b^e) = \boldsymbol{I}_3 + 2s_q\boldsymbol{S}(r_q) + 2\boldsymbol{S}^2(\boldsymbol{r}_q)$. The state $\boldsymbol{\xi}_{ib}^e$ is an auxiliary parameter/state, necessary to assist the estimation of the specific force $\boldsymbol{f}_{ib}^e$, motivated by the analysis in Grip et al. (2012b) applied in Grip et al. (2013, 2015). This state couples the rotational and translational motions, facilitating precise attitude estimation also when the vehicle is accelerated. The feedback of $\hat{\boldsymbol{f}}_{ib}^e$ from the TMO to the attitude observer requires stability analysis leading to some restrictions on the observer gains, that are discussed next.

3.5.1 Stability conditions

The TMO for loosely coupled integration can now be written as a continuous-time linear system,

$$\dot{\hat{\boldsymbol{x}}}^* = \boldsymbol{A}^*\hat{\boldsymbol{x}}^* + \boldsymbol{B}^*\boldsymbol{u}^* + \boldsymbol{D}^*(t, \hat{\boldsymbol{x}}^*) + \boldsymbol{K}^*(\boldsymbol{y} - \boldsymbol{C}^*\hat{\boldsymbol{x}}^*), \tag{3.24}$$

with the state, input and output, defined respectively as

$$\begin{aligned}
\hat{\boldsymbol{x}}^* &:= (\hat{\boldsymbol{p}}_{eb}^e; \hat{\boldsymbol{v}}_{eb}^e; \boldsymbol{\xi}_{ib}^e),\\
\boldsymbol{u}^* &:= (\boldsymbol{f}_{\text{IMU}}^b; -\boldsymbol{S}(\hat{\boldsymbol{o}}_{ib}^b)\boldsymbol{f}_{\text{IMU}}^b),\\
\boldsymbol{y} &:= (\boldsymbol{p}_{\text{GNSS}}^e; \boldsymbol{v}_{\text{GNSS}}^e),
\end{aligned}$$

and with the matrices,

$$\begin{aligned}
\boldsymbol{A}^* &= \begin{pmatrix} \boldsymbol{0}_{3\times3} & \boldsymbol{I}_3 & \boldsymbol{0}_{3\times3} \\ \boldsymbol{0}_{3\times3} & \boldsymbol{0}_{3\times3} & \boldsymbol{I}_3 \\ \boldsymbol{0}_{3\times3} & \boldsymbol{0}_{3\times3} & \boldsymbol{0}_{3\times3} \end{pmatrix},\\
\boldsymbol{B}^* &= \begin{pmatrix} \boldsymbol{0}_{3\times3} & \boldsymbol{0}_{3\times3} \\ \boldsymbol{R}(\hat{\boldsymbol{q}}_b^e) & \boldsymbol{0}_{3\times3} \\ \boldsymbol{0}_{3\times3} & \boldsymbol{R}(\hat{\boldsymbol{q}}_b^e) \end{pmatrix},\ \boldsymbol{D}^*(t, \hat{\boldsymbol{x}}^*) = \begin{pmatrix} \boldsymbol{0}_{3\times1} \\ \boldsymbol{g}_b^e(\hat{\boldsymbol{p}}_{eb}^e) - 2(\boldsymbol{\omega}_{ie}^e)\hat{\boldsymbol{v}}_{eb}^e \\ \boldsymbol{0}_{3\times1} \end{pmatrix},\\
\boldsymbol{C}^* &= \begin{pmatrix} \boldsymbol{I}_3 & \boldsymbol{0}_{3\times3} & \boldsymbol{0}_{3\times3} \\ \boldsymbol{0}_{3\times3} & \boldsymbol{I}_3 & \boldsymbol{0}_{3\times3} \end{pmatrix},\\
\boldsymbol{K}^* &= \begin{pmatrix} \boldsymbol{K}_{pp} & \boldsymbol{K}_{vp} \\ \boldsymbol{K}_{pv} & \boldsymbol{K}_{vv} \\ \boldsymbol{K}_{p\xi} & \boldsymbol{K}_{v\xi} \end{pmatrix} = \begin{pmatrix} \vartheta\boldsymbol{K}_{pp}^0 & \boldsymbol{K}_{vp}^0 \\ \vartheta^2\boldsymbol{K}_{pv}^0 & \vartheta\boldsymbol{K}_{vv}^0 \\ \vartheta^3\boldsymbol{K}_{p\xi}^0 & \vartheta^2\boldsymbol{K}_{v\xi}^0 \end{pmatrix},
\end{aligned}$$

such that the system $(\boldsymbol{A}^*, \boldsymbol{B}^*, \boldsymbol{C}^*)$ is both controllable and observable.

For the nominal case when there are no sensor errors or noise, the uniform semiglobal exponential stability (USGES) of the feedback interconnection of the attitude and translational motion observers is established in Grip et al. (2013) under the following conditions:

- The two attitude reference vectors are not colinear. This is satisfied if there exists a constant $c_{\text{obs}} > 0$ such that $||\boldsymbol{m}_{eb}^e \times \hat{\boldsymbol{f}}_{ib}^e||_2 \geq c_{\text{obs}}$ or $||\underline{\boldsymbol{v}_1}^e \times \underline{\boldsymbol{v}_2}^e||_2 \geq$

c_{obs}. Temporary violation of this assumption can be tolerated since the attitude estimate can be updated using only the angular rate measurements for shorter periods of time.

- Attitude observer parameters satisfy $k_1, k_2 \geq k_P$ for some $k_P > 0$ and $k_I > 0$.
- The constant gains in the matrix

$$\boldsymbol{K}^0 = \begin{pmatrix} \boldsymbol{K}^0_{pp} & \boldsymbol{K}^0_{vp} \\ \boldsymbol{K}^0_{pv} & \boldsymbol{K}^0_{vv} \\ \boldsymbol{K}^0_{p\xi} & \boldsymbol{K}^0_{v\xi} \end{pmatrix},$$

of the TMO can be chosen arbitrarily provided that the linear error dynamics matrix $\boldsymbol{A}^* - \boldsymbol{K}^0\boldsymbol{C}^*$ is Hurwitz, and $\vartheta \geq \vartheta^*$, where $\vartheta^* \geq 1$ is sufficiently large, Grip et al. (2013). The intuitions behind a large ϑ is that it implies that the estimate of $\hat{\boldsymbol{f}}^e$ is dominated by the GNSS measurement such that the attitude estimation errors do not lead to a large error in $\hat{\boldsymbol{f}}^e_{ib}$, which could otherwise destabilize the attitude observer.

The practical implication of the USGES stability properties is the robustness to arbitrarily large initialization errors in both position and attitude since no linearization is needed in the nonlinear attitude estimator.

3.5.2 Continuous-time gain selection

The gain conditions of Grip et al. (2013), reviewed above, are of limited practical use since they are general and sufficient (not always necessary) conditions where a non-conservative bound ϑ^* may be difficult to find. Moreover, ϑ^* also depends on the attitude observer gains k_1, k_2, k_I. In a practical approach to tuning, the gains in the matrix $\boldsymbol{K}_0$ of the TMO may be tuned using a minimum-variance estimation criterion by taking into account the influences of noises on its measurements. This is done by choosing $\vartheta = 1$ and

$$\boldsymbol{Q}^* = \text{blockdiag}(\boldsymbol{S}_f, \boldsymbol{S}_{\hat{o}f}), \qquad R = \text{blockdiag}(\boldsymbol{S}_p, \boldsymbol{S}_v),$$

as input and output noise covariance matrices, respectively. Regarding $\boldsymbol{R}$, the matrices $\boldsymbol{S}_p$ and $\boldsymbol{S}_v$ represent the covariance matrices of the position and velocity measurement noise components $\boldsymbol{\varepsilon}_p$ and $\boldsymbol{\varepsilon}_v$, respectively. In practice the GNSS position and velocity measurements are time-varying and correlated as the user position estimates are used to determine the user-to-satellite line-of-sight (LOS) vector in the velocity computation procedure. An alternative can then be to include cross terms $\boldsymbol{S}_{pv}$ and $\boldsymbol{S}_{vp}$ such that

$$\boldsymbol{R} = \begin{pmatrix} \boldsymbol{S}_p & \boldsymbol{S}_{pv} \\ \boldsymbol{S}_{vp} & \boldsymbol{S}_v \end{pmatrix}, \quad \boldsymbol{S}_{pv} = \boldsymbol{S}_{vp}.$$

The covariance matrices $\boldsymbol{S}_f$ and $\boldsymbol{S}_{\hat{o}f}$ are obtained from the accelerometer's measurement noise by $\boldsymbol{S}_f = \boldsymbol{E}[\boldsymbol{\varepsilon}_f \boldsymbol{\varepsilon}_f^\intercal]$ and $\boldsymbol{S}_{\hat{o}f} = \boldsymbol{E}[\boldsymbol{S}(\hat{\boldsymbol{o}})\boldsymbol{\varepsilon}_f \boldsymbol{\varepsilon}_f^\intercal \boldsymbol{S}^\intercal(\hat{\boldsymbol{o}})]$. The latter term goes to a steady-state value when the attitude estimates has converged.

A gain matrix that gives an approximately minimum variance estimate is given by the Riccati equation solution $\boldsymbol{P}^* = (\boldsymbol{P}^*)^\intercal > 0$ motivated by the fact that the TMO's error dynamics are identical to the time-scaled error dynamics of the Kalman-Bucy filter Kalman and Bucy (1961)

$$\boldsymbol{K}^0 = \boldsymbol{P}^*(\boldsymbol{C}^*)^\intercal \boldsymbol{R}^{-1}, \tag{3.25}$$

$$\begin{aligned} \frac{1}{\vartheta}\dot{\boldsymbol{P}}^* = {} & \boldsymbol{A}^*\boldsymbol{P}^* + \boldsymbol{P}^*(\boldsymbol{A}^*)^\intercal + \boldsymbol{B}^*\boldsymbol{Q}^*(\boldsymbol{B}^*)^\intercal \\ & - \boldsymbol{P}^*(\boldsymbol{C}^*)^\intercal \boldsymbol{R}^{-1}\boldsymbol{C}^*\boldsymbol{P}^*. \end{aligned} \tag{3.26}$$

One reason for (3.24)–(3.26) only being an approximate minimum variance estimator is that $\hat{\boldsymbol{q}}_b^e$ and $\hat{\boldsymbol{o}}$ are correlated with $\boldsymbol{f}_{\text{IMU}}^b$. Therefore the accelerometer's noise $\boldsymbol{\varepsilon}_f$ and the accompanying covariance $\boldsymbol{S}_f$ are correlated with $\boldsymbol{B}^*$. The result of (Johansen and Fossen, 2015, Lemma 6) shows that it is possible to choose ϑ independently from $\boldsymbol{P}^*$, using the time-varying Riccati equation (3.26) such that the USGES stability properties posed in Grip et al. (2013) still hold when calculating the gains with (3.25)–(3.26). However, choosing $\vartheta > 1$ is suboptimal with respect to the minimum variance optimization problem the Kalman-Bucy filter solves. In addition, the covariance matrix $\boldsymbol{S}_{\hat{o}f}$, associated with $\boldsymbol{\xi}$, is not necessarily straight forward to determine since $\boldsymbol{S}(\hat{o})$ is correlated with $\boldsymbol{\varepsilon}_f^b$. These terms are also further correlated with $\boldsymbol{R}(\hat{\boldsymbol{q}}_b^e)$. As an alternative, ad hoc tuning of $S_{\hat{o}f}$ can be considered. By always choosing $\boldsymbol{S}_{\hat{o}f}$ larger than zero, the gains associated with the state $\boldsymbol{\xi}_{ib}^e$ never become zero, guaranteeing stability.

The TMO realization presented above can be referred to as a *direct filter* or *total state* implementation in the navigation literature, (Farrell, 2008, Ch. 7.4). In practice, this means that the filter's Riccati equation (3.26) is implemented at the frequency of the IMU and that the aiding sensors are used to correct the INS when available. As a result, for high integration frequencies, the computational burden might be considerable. Therefore, more computationally efficient alternatives are desirable, while still maintaining time-varying gains. This is possible to achieve since the time-varying dynamics of (3.26) is slowly-varying.

3.5.3 Example

To study the effects of the gain synthesis suggested for the feedback-interconnected observer above, inertial sensors and position measurements with white Gaussian noise are simulated, and both fixed and time-varying gain schemes are applied to the observers. This is a simplification, made for illustrative purposes, since in general both position and inertial sensors provide measurements containing noise with colored spectral content. The results are transformed to north-east-down

(NED) coordinates. Conversion from ECEF to NED coordinates is performed by first acquiring the estimated latitude $\hat{\mu}$ and longitude $\hat{l}$ from the position estimate $\hat{\boldsymbol{p}}^e_{eb}$ for instance in closed form with Vermeille (2004). This information is then used to rotate the ECEF estimates to NED with the quaternion $\hat{\boldsymbol{q}}^e_n = \hat{\boldsymbol{q}}_\mu \otimes \hat{\boldsymbol{q}}_l$, where $\hat{\boldsymbol{q}}_\mu = (\cos((\hat{\mu}+\pi/2)/2), 0, \sin((\hat{\mu}+\pi/2)/2), 0)^\intercal$ and $\hat{\boldsymbol{q}}_l = \left(\cos(\hat{l}/2), 0, 0, -\sin(\hat{l}/2)\right)^\intercal$.

The respective transient performance is shown in Figs. 3.4–3.6 implemented with IMU noise characteristics $\boldsymbol{\varepsilon}_\omega \sim n(0, 0.0025^2)$ and $\boldsymbol{\varepsilon}_f \sim n(0, 0.05^2)$ using position as the only aiding TMO measurement. The GNSS noise characteristics where realized using $\boldsymbol{\varepsilon}_p \sim (\varepsilon_{p_n}; \varepsilon_{p_e}; \varepsilon_{p_d})$ with $\varepsilon_{p_n} \sim n(0, 1.1^2)$, $\varepsilon_{p_e} \sim n(0, 1.1^2)$, and $\varepsilon_{p_d} \sim n(0, (1.5 \cdot 1.1)^2)$ such that the GNSS is less accurate in the vertical component after converting to NED.

The fixed-gain synthesis is done with $\vartheta = 1$ and the algebraic Riccati equation,

$$\begin{aligned} &\boldsymbol{A}^*\boldsymbol{P}^* + \boldsymbol{P}^*(\boldsymbol{A}^*)^\intercal + \boldsymbol{B}^*\boldsymbol{Q}^*(\boldsymbol{B}^*)^\intercal \\ &- \boldsymbol{P}^*(\boldsymbol{C}^*)^\intercal \boldsymbol{R}^{-1}\boldsymbol{C}^*\boldsymbol{P}^* = \boldsymbol{0}. \end{aligned} \tag{3.27}$$

For both observers, the TMOs were synthesized using $\boldsymbol{S}_f = 0.05^2 \cdot \boldsymbol{I}_3$, $\boldsymbol{S}_{\delta f} = 0.5 \cdot 0.05^2 \cdot \boldsymbol{I}_3$ and $\boldsymbol{S}_p = \text{blockdiag}(1.1 \cdot \boldsymbol{I}_2, 1.65^2)$, after converting from ECEF to NED coordinates, with initial NED position and attitude error of $\tilde{\boldsymbol{p}}^n_{nb}(0) = (10, -7, 4)^\intercal$ m and $\tilde{\phi}(0) = 10$, $\tilde{\theta}(0) = 7$, $\tilde{\psi}(0) = -10$ degrees, respectively. The attitude gains where chosen as $k_1 = k_2 = 0.5$, $k_I = 0.01$. In the time-varying filter implementation the initial covariance $\boldsymbol{P}(0)$ was chosen as $\boldsymbol{P}(0) = \text{blockdiag}(10^2 \cdot \boldsymbol{I}_3, \boldsymbol{I}_3, \boldsymbol{I}_3)$. A third case was also run with higher attitude gains $k_1 = k_2 = 20$ during the first 100 seconds, together with the time-varying TMO solution. The transient performance obtained is based on simulated sensors at rest.

The transient performance of the position, velocity and attitude errors is improved using the time-varying Kalman filter to synthesize the TMO as seen in Figs. 3.4–3.6. As indicated, in Fig. 3.6 by improving the TMO's estimates, improvements in the attitude convergence properties are also obtained. The fastest attitude covariance properties are witnessed with both a time-varying TMO and higher prescribed initial attitude gains as seen in Fig. 3.6. What also can be seen from Figs. 3.4–3.5, is that the convergence properties of the position and velocity estimates are not improved by time-varying attitude gains. It can also been seen in Figs. 3.4–3.6 that the estimates have to fully converged at 100 seconds. This is due to the gyro bias estimates have not yet fully converged to the true gyro biases.

3.5.4 Position space GNSS error models

The position and velocity measurements provided by the GNSS receiver's least squares estimator or EKF are subjected to time-varying errors inflicted by three main effects; Satellite errors, signal propagation errors and receiver errors (Grewal et al., 2013, Ch. 7).

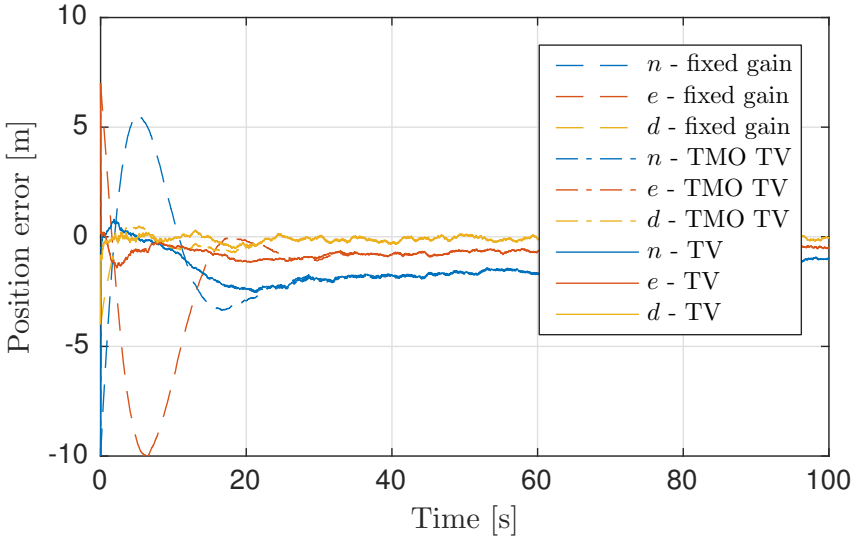

Figure 3.4: Position estimation error. The position errors obtained with the steady-state Kalman gain are presented with dash lines. The position errors obtained with the translational motion observer (TMO) applying a time-varying Kalman gain are shown using dash-dot lines. The error in position obtained when both the TMO and the attitude observer applied time-varying gains is shown using solid lines. The results indicate that using a TMO with time-varying gains toghter with an attitude observer prescribed with high initial gains accelerates the convergence of the position estimates to the true position.

The GNSS position and velocity errors can be characterized by their spectral contents. Using spectral factorization and a state-space realization of the resulting filtered white noise processes for loosely coupled integration leads to an m-th order linear error model on the form

$$\dot{\boldsymbol{z}} = \boldsymbol{F}\boldsymbol{z} + \boldsymbol{G}\boldsymbol{n}, \qquad \boldsymbol{\delta} = \boldsymbol{H}\boldsymbol{z} + \boldsymbol{\varepsilon}_{pv}, \tag{3.28}$$

where $\boldsymbol{\delta} = (\boldsymbol{\delta}_p; \boldsymbol{\delta}_v) \in \mathbb{R}^6$ represents the position and velocity errors, and $\boldsymbol{\varepsilon}^e_{pv} \in \mathbb{R}^6$ and $\boldsymbol{n} \in \mathbb{R}^6$ are vectors with unity white noise where $\boldsymbol{n} \sim (0, 1)$ and $\boldsymbol{\varepsilon}^e_{pv} \sim (0, \sigma^2_{pv})$. Hence, the receiver outputs position and velocity estimates $\boldsymbol{p}^e_{\text{GNSS}} = \boldsymbol{p}^e_{eb} + \boldsymbol{\delta}_p$ and $\boldsymbol{v}^e_{\text{GNSS}} = \boldsymbol{v}^e_{eb} + \boldsymbol{\delta}_v$, respectively. The model (3.28), related to the GNSS position measurements can be chosen to be a first-order Gauss-Markov process Rankin (1994); Mohleji and Wang (2010). By defining $\boldsymbol{z} := (\boldsymbol{z}_p; \boldsymbol{z}_v)$, the dynamic GNSS position error is represented by the system

$$\dot{\boldsymbol{z}}_p = \boldsymbol{F}_p\boldsymbol{z}_p + \boldsymbol{G}_p\boldsymbol{n}_p, \qquad \boldsymbol{\delta}_p = \boldsymbol{H}_p\boldsymbol{z}_p + \boldsymbol{\varepsilon}_p, \tag{3.29}$$

with $\boldsymbol{F}_p = -\boldsymbol{T}_p^{-1}$, where $\boldsymbol{T}_p$ is the correlation time constant. $\boldsymbol{G}_p$ is chosen equal to the appropriate standard deviation of the driving noise.

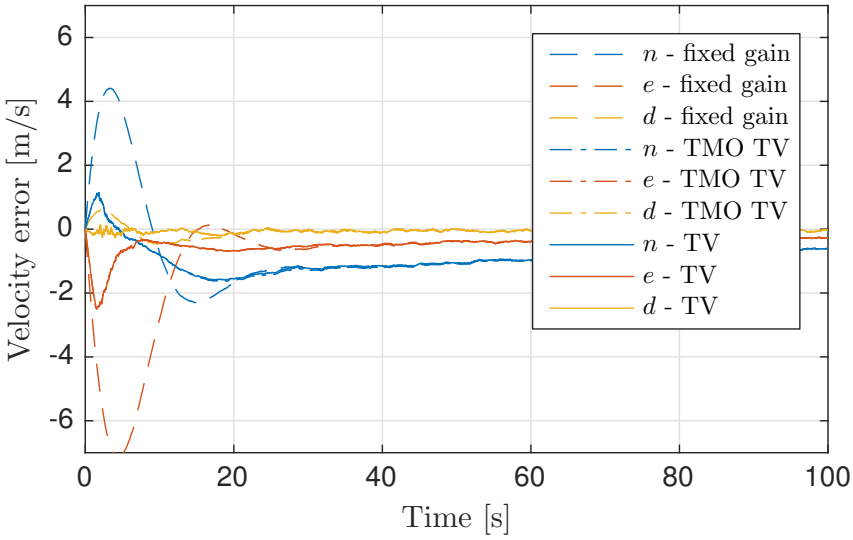

Figure 3.5: Velocity estimation error. The velocity errors obtained with the steady-state Kalman gain are presented with dash lines. The velocity errors obtained with the translational motion observer (TMO) applying a time-varying Kalman gain are shown using dash-dot lines. The error in velocity obtained when both the TMO and the attitude observer applied time-varying gains is shown using solid lines. The results indicate that using a TMO with time-varying gains, with or without an attitude observer prescribed with high initial gains, accelerates the convergence of the velocity estimates to the true velocity compared to the fixed-gain solution.

It is evident that even though the GNSS velocity measurements can be very precise (RMS error of down to 0.1 m/s), these also contain some dynamic errors, depending on satellite geometry and the resulting effects on measurement precision. Moreover, for the dynamic error of the GNSS velocity measurement can be represented by

$$\dot{\boldsymbol{z}}_v = \boldsymbol{F}_v \boldsymbol{z}_v + \boldsymbol{G}_v \boldsymbol{n}_v, \quad \boldsymbol{\delta}_v = \boldsymbol{H}_v \boldsymbol{z}_v + \boldsymbol{\varepsilon}_v. \tag{3.30}$$

By choosing $\boldsymbol{F}_v = -\boldsymbol{T}_v^{-1}$ where $\boldsymbol{T}_v$ is the assumed correlation time and $\boldsymbol{G}_v$ corresponds to the standard deviation of the driving noise (3.30), the steady-state covariance of the Gauss-Markov processes $\boldsymbol{z}_p$ and $\boldsymbol{z}_v$ become

$$\boldsymbol{P}_{z_p}(\infty) = -\frac{1}{2}\boldsymbol{F}_p^{-1}\boldsymbol{G}_p\boldsymbol{G}_p^\intercal, \quad \boldsymbol{P}_{z_v}(\infty) = -\frac{1}{2}\boldsymbol{F}_v^{-1}\boldsymbol{G}_v\boldsymbol{G}_v^\intercal, \tag{3.31}$$

respectively for sufficiently long measurement periods since $\boldsymbol{F}_p = \boldsymbol{F}_p^\intercal$, $\boldsymbol{F}_v = \boldsymbol{F}_v^\intercal$. For higher-order models $\boldsymbol{P}_{z_\star}(\infty)$ is obtained by solving

$$\boldsymbol{F}_\star \boldsymbol{P}_{z_\star} + \boldsymbol{P}_{z_\star}\boldsymbol{F}_\star^\intercal + \boldsymbol{G}_\star\boldsymbol{G}_\star^\intercal = \boldsymbol{0}_{l\times l}, \tag{3.32}$$

where $\star$ is a placeholder for p or v and l being the dimension of $F_\star$.

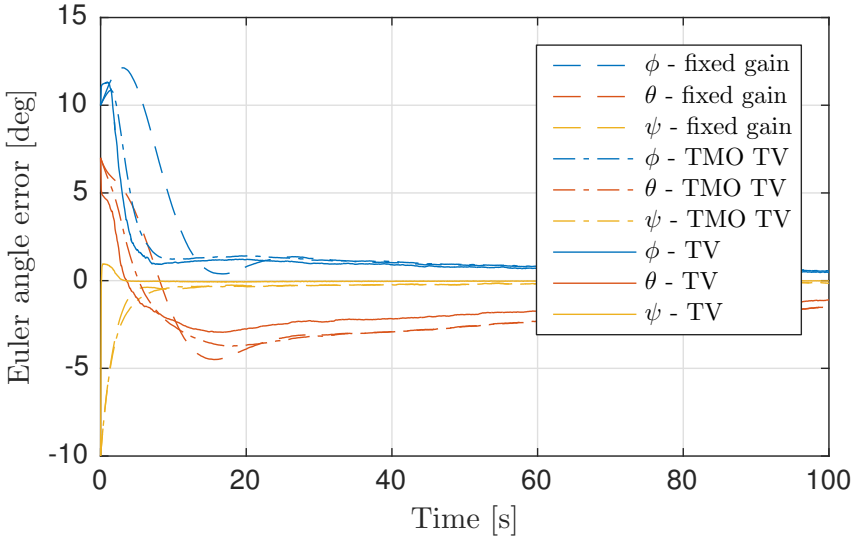

Figure 3.6: Attitude estimation error. The attitude error is presented applying Euler angles as attitude representation. The attitude errors obtained in feedback interconnection with the translational motion observer (TMO) using a steady-state Kalman gain are presented with dash lines. The attitude errors obtained in connection with the TMO applying a time-varying Kalman gain are shown using dash-dot lines. The attitude error obtained when both the TMO and the attitude observer applied time-varying gains is shown using solid lines. The results indicate that using a TMO with time-varying gains in feedback interconnection with an attitude observer prescribed with high initial gains accelerates the convergence of the attitude estimates to the true attitude.

3.5.5 Augmented TMO for loosely coupled integration including GNSS error models

To account for colored GNSS measurement noise, the TMO is augmented with an estimator of the noise dynamics

$$\begin{aligned}\dot{\hat{z}} = \boldsymbol{F}\hat{z} + \boldsymbol{K}_{pz}(\boldsymbol{p}^e_{\text{GNSS}} - \hat{\boldsymbol{p}}^e_{eb} - \hat{\boldsymbol{\delta}}_p) \\ + \boldsymbol{K}_{vz}(\boldsymbol{v}^e_{\text{GNSS}} - \hat{\boldsymbol{v}}^e_{eb} - \hat{\boldsymbol{\delta}}_v),\end{aligned} \tag{3.33}$$

such that the augmented state vector becomes $\boldsymbol{x} = (\boldsymbol{x}^*; \boldsymbol{z})$ which is leads to

$$\dot{\boldsymbol{x}} = \boldsymbol{A}\boldsymbol{x} + \boldsymbol{B}_1\boldsymbol{u}^* + \boldsymbol{B}_2\boldsymbol{n} + \boldsymbol{D}, \tag{3.34}$$

and the corresponding TMO

$$\dot{\hat{\boldsymbol{x}}} = \boldsymbol{A}\hat{\boldsymbol{x}} + \boldsymbol{B}_1\boldsymbol{u}^* + \boldsymbol{D}(t, \hat{\boldsymbol{x}}) + \boldsymbol{K}(\boldsymbol{y} - \boldsymbol{C}\hat{\boldsymbol{x}}), \tag{3.35}$$

where the augmented system is defined by

$$\boldsymbol{A} = \begin{pmatrix} \boldsymbol{A}^* & \boldsymbol{0}_{9\times l} \\ \boldsymbol{0}_{m\times 9} & \boldsymbol{F} \end{pmatrix}, \qquad \boldsymbol{C} = \begin{pmatrix} \boldsymbol{C}^*, \boldsymbol{H} \end{pmatrix},$$
$$\boldsymbol{B}_1 = \begin{pmatrix} \boldsymbol{B}^* \\ \boldsymbol{0}_{l\times 6} \end{pmatrix}, \qquad \boldsymbol{B}_2 = \begin{pmatrix} \boldsymbol{0}_{9\times l} \\ \boldsymbol{G} \end{pmatrix},$$
$$\boldsymbol{B} = \begin{pmatrix} \boldsymbol{B}_1 & \boldsymbol{B}_2 \end{pmatrix}, \quad \boldsymbol{D}(t, \hat{\boldsymbol{x}}) = \begin{pmatrix} \boldsymbol{D}^*(t, \hat{\boldsymbol{x}}) \\ \boldsymbol{0}_{l\times 1} \end{pmatrix},$$
$$\boldsymbol{K} = \begin{pmatrix} \boldsymbol{K}^* \\ \boldsymbol{K}_z \end{pmatrix},$$

and where $\boldsymbol{B}$ is used to calculate $\boldsymbol{K} = \vartheta \boldsymbol{L}_\vartheta^{-1} \boldsymbol{K}^0 \boldsymbol{E}_\vartheta$ from the augmented equivalent of (3.25)–(3.26), that is

$$\boldsymbol{K}^0 = \boldsymbol{P}\boldsymbol{C}^\intercal \boldsymbol{R}^{-1}, \tag{3.36}$$
$$\frac{1}{\vartheta}\dot{\boldsymbol{P}} = \boldsymbol{A}\boldsymbol{P} + \boldsymbol{P}\boldsymbol{A}^\intercal + \boldsymbol{B}\boldsymbol{Q}\boldsymbol{B}^\intercal - \boldsymbol{P}\boldsymbol{C}^\intercal \boldsymbol{R}^{-1}\boldsymbol{C}\boldsymbol{P}, \tag{3.37}$$

with

$$\boldsymbol{L}_\vartheta = \text{blockdiag}\left(\boldsymbol{I}_3, \frac{1}{\vartheta}\boldsymbol{I}_3, \frac{1}{\vartheta^2}\boldsymbol{I}_3, \boldsymbol{I}_{l_p}, \frac{1}{\vartheta}\boldsymbol{I}_{l_v}\right), \tag{3.38}$$
$$\boldsymbol{E}_\vartheta = \boldsymbol{C}\boldsymbol{L}_\vartheta \boldsymbol{C}^\dagger. \tag{3.39}$$

Moreover, l is the degrees of freedom of the Gauss-Markov process and the dimension of $\boldsymbol{G}$ relating the driving noise $\boldsymbol{n}$ to the augmented state $\boldsymbol{z}$. l_p and l_v are the respective dimensions of the GNSS position and velocity error models. If only the position measurement is corrupted by colored noise, $l := 3$ resulting in $\boldsymbol{L}_\vartheta = \text{blockdiag}\left(\boldsymbol{I}_3, 1/\vartheta \cdot \boldsymbol{I}_3, 1/\vartheta^2 \cdot \boldsymbol{I}_3, \boldsymbol{I}_l\right)$. However, if this is also applicable for the velocity measurement, $l := 6$ with the spectral factorization chosen above. The pair $(\boldsymbol{A}, \boldsymbol{C})$ can be shown to always be observable for any $\boldsymbol{T}_p, \boldsymbol{T}_v > 0$ when the chosen spectral factorization results in a first-order Gauss-Markov process since

$$\text{rank}(\boldsymbol{O}) = 9 + l, \tag{3.40}$$

where

$$\boldsymbol{O} = \left(\boldsymbol{C}; \boldsymbol{C}\boldsymbol{A}; \ldots; \boldsymbol{C}\boldsymbol{A}^{9+l-1}\right), \tag{3.41}$$

hence satisfying Kalman's rank condition of observability of linear time-invariant systems, Kalman and Bucy (1961). With this state-space augmentation, and by defining $\boldsymbol{Q} = \text{blockdiag}\,(\boldsymbol{Q}^*, \boldsymbol{I}_l)$, the TMO is realized using (3.35) where the gain can be obtained using (3.36)–(3.37).

3.5.6 Example continued: Effects of colored GNSS noise

GNSS position and velocity measurements contain colored noise components.To illustrate the effect of the colored noise on the GNSS/INS integration performance, induced by (3.28), a GNSS receiver is simulated, at high latitude, where the measurement is given in the NED frame, $\boldsymbol{p}^n_{\text{GNSS}} = \boldsymbol{p}^n_{nb} + \boldsymbol{z}_p + \boldsymbol{\varepsilon}_p$ and $\boldsymbol{v}^n_{\text{GNSS}} = \boldsymbol{v}^n_{nb} + \boldsymbol{z}_v + \boldsymbol{\varepsilon}_v$ and the model parameters are chosen as $\boldsymbol{F} = \text{blockdiag}(\boldsymbol{F}_p, \boldsymbol{F}_v)$ and $\boldsymbol{G} = \text{blockdiag}(\boldsymbol{G}_p, \boldsymbol{G}_v)$ with

$$\begin{aligned}
&\boldsymbol{F}_p = -1/T_p \cdot \boldsymbol{I}_3, \boldsymbol{F}_v = -1/T_v \cdot \boldsymbol{I}_3,\\
&\boldsymbol{G}_p = \text{diag}(1.2, 0.7, 2),\\
&\boldsymbol{G}_v = \text{diag}(1, 1, 2).
\end{aligned}$$

The time constant of the position error was chosen to be $T_p = 1100$ s as in Rankin (1994), (Beard and McLain, 2012, Ch 7.5), while the time constant for the velocity was chosen as $T_v = 2$ s. The latter was chosen based on the assumption that the GNSS velocity measurements, obtained from the receiver, primarily are based on the Doppler range-rate measurements. The time constant related to these can be much smaller than for the noise embedded in the C/A code-based pseudoranges. This is due to the GNSS carrier phase and code observables being affected differently by various error sources. Furthermore, with this choice of $\boldsymbol{G}$, it is taken into account that the horizontal measurements are more accurate than the vertical counterparts and that the eastern measurements are more precise than the northern at higher latitudes using GPS. The chosen noise and bias parameters related to the simulated inertial sensors are equal to those presented in the previous simulation example.

The motion simulated is of a small UAV flying in a circular motion with a speed 25 m/s and with a constant altitude of 150 meters over ground. The UAV is flying with a constant yaw rate with a roll angle and pitch angles of $\phi = -3$ and $\theta = 2$ degrees, respectively. The north-east motion in shown in Fig. 3.7.

Case 1: Only GNSS Position measurement available: This first case is simulated with only position measurements available.

Figs. 3.8–3.9 show the position estimation error and performance of the GNSS colored noise estimation. It is obvious that even though $\text{rank}\,(\boldsymbol{O}) = 12$, such that the pair $(\boldsymbol{A}, \boldsymbol{C})$ is observable, the GNSS transient error is not captured by the model augmentation. Due to the stochastic properties, in this case, the system $(\boldsymbol{A}, \boldsymbol{C})$ is only weakly observable as indicated by the estimation error covariance $\boldsymbol{P}$. Fig. 3.10, based on the stationary estimation error covariance $\boldsymbol{P}(\infty)$ shows the error ellipsis, with 95% confidence interval, illustrating that the states associated with the colored GNSS noise are highly correlated with the position error. Hence, it can be expected that the position covariance is close to that of (3.31), the Gauss-Markov process describing the colored noise.

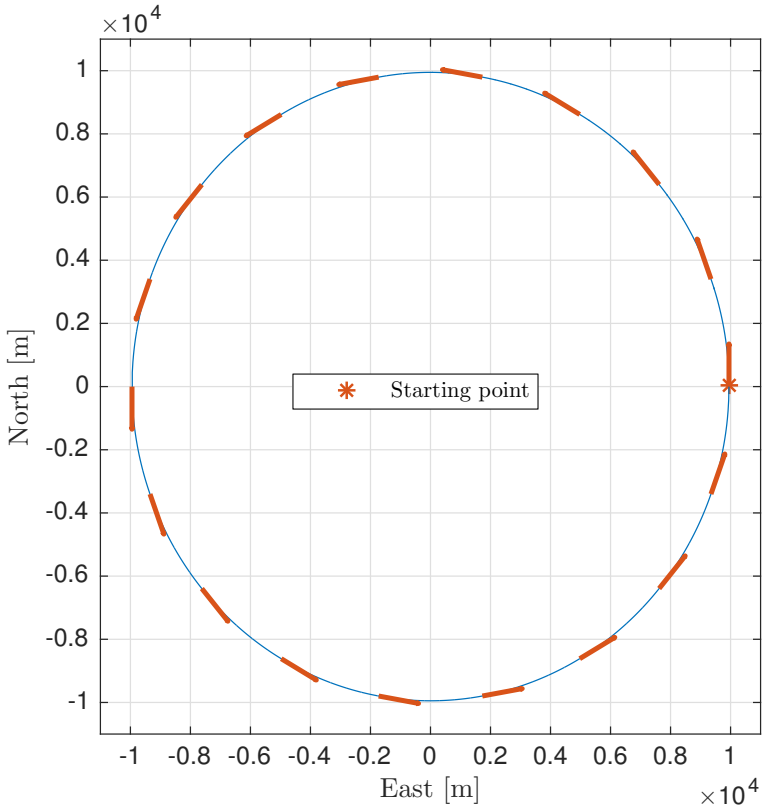

Figure 3.7: Overview of the simulated horizontal unmanned aerial vehicle (UAV) motion. The motion simulated is a circle with radius of 10 000 meters, where the initial heading of the UAV was zero. The chosen simulated UAV speed was 25 m/s. The blue circle indicates the UAV motion, while the red arrows depicts the heading of the UAV at fixed intervals.

Case 2: GNSS position measurements together and a velocity measurement with white noise: In this case, unrealistic GNSS velocity measurements are added, containing the true velocity and only corrupted with white noise for illustrative purposes.

Figs. 3.11–3.12 show the position estimation error and performance of the GNSS colored noise estimation error when the velocity measurements, only corrupted with white noise, are added as an aiding measurements in the TMO. The deterministic observability properties are still the same with rank 12, however the performance has increased significantly. Hence, now the TMO is able to track the colored GNSS position error to a large extent. This is reflected in Fig. 3.11 where the position estimation error is reduced compared to the performance shown in Fig. 3.8.

Case 3: GNSS position and velocity measurements containing colored noise: In this last

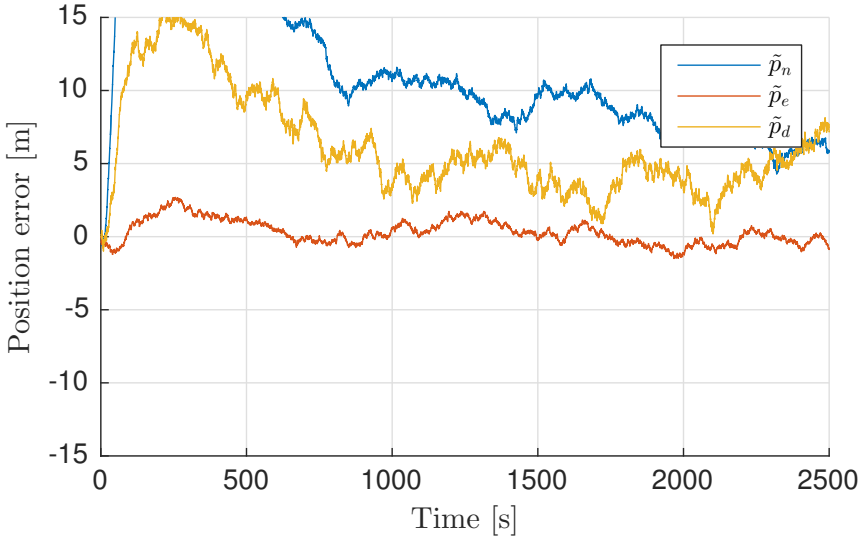

Figure 3.8: Case 1, position estimation error. The position estimation error obtained in simulation when applying global navigation satellite systems (GNSS) position measurements containing colored noise.

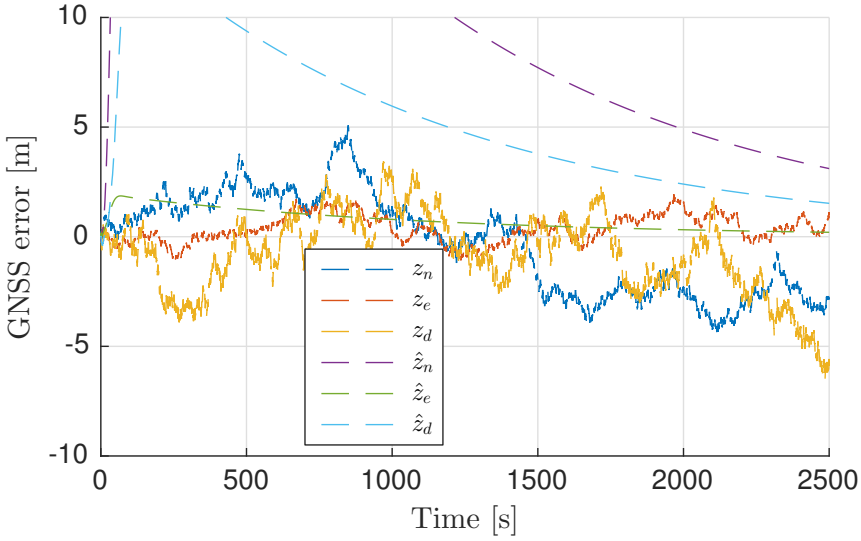

Figure 3.9: Case 1, global navigation satellite systems (GNSS) error state estimates. The true GNSS error states (colored noise) are shown in blue, red and yellow, respectively. The corresponding respective estimates are presented in purple, green and light blue. It can be seen that the translational motion observer fails in estimating the colored GNSS correctly.

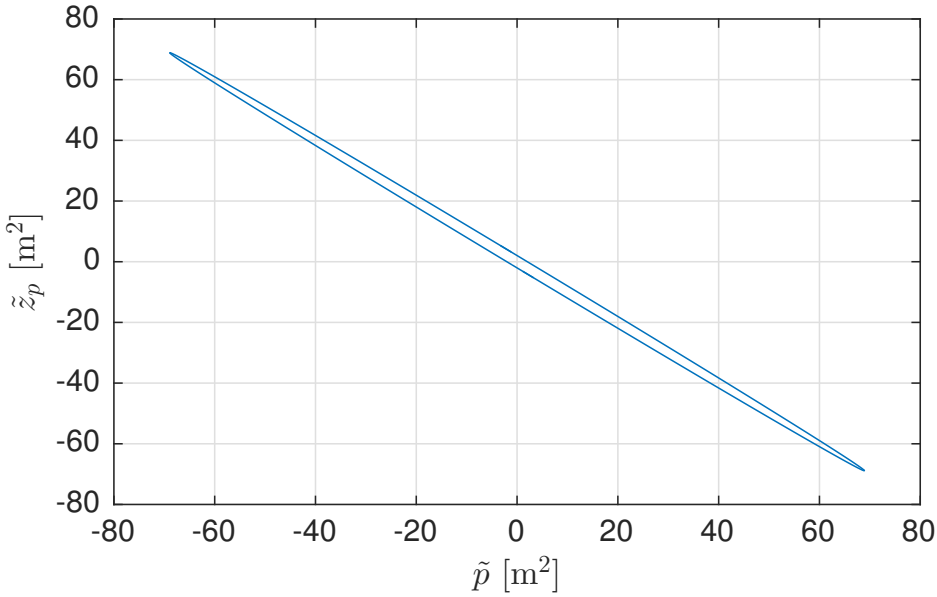

Figure 3.10: Case 1, error ellipsis of the north position estimation error and the corresponding colored noise estimate of the position measurement. The error ellipsis presented shows that the position estimation error and the colored GNSS noise estimation error are significantly correlated. This indicate that the translational motion observer struggles to separate the colored noise from the true position. Similar ellipsis are also obtainable for the East and Down axes.

case, a more realistic GNSS velocity measurement is used, having some dynamic error such that $\boldsymbol{v}^n_{\text{GNSS}} = \boldsymbol{v}^n_{nb} + \boldsymbol{z}_v + \boldsymbol{\varepsilon}_v$, as described earlier, where $\boldsymbol{z}_v$ is generated as a Gauss-Markov process with time constant $T_v = 2$. Related to case 2 only minor differences are seen considering Figs. 3.13–3.14 compared to Figs. 3.11–3.12. The augmented observer structure of (3.35) is able to utilize the velocity measurements with colored noise, hence improving the position accuracy compared to Case 1 and Figs. 3.8–3.9. Even though the absolute position error is reduced compared to Case 1, the covariance of the estimation error still indicates the same problem; the TMO may still struggle to distinguish the colored noise of the position measurements from the true position as seen in Fig. 3.15 showing the error ellipsis of $\boldsymbol{P}(\infty)$, where the cross correlation between the $\tilde{\boldsymbol{p}^n_{nb}}$ and $\tilde{\boldsymbol{z}}_p$ still is significant, however reduced compared to case 1 where only the position measurements were used.

Discussion:
The reason why the augmented observer, applying loosely coupled GNSS/INS integration, (3.35), struggles to separate the true position from the slowly-varying colored GNSS noise is the relatively high noise in the IMUs accelerometers. Since the rotated accelerometer noise is integrated twice in the TMO, the TMO gains are

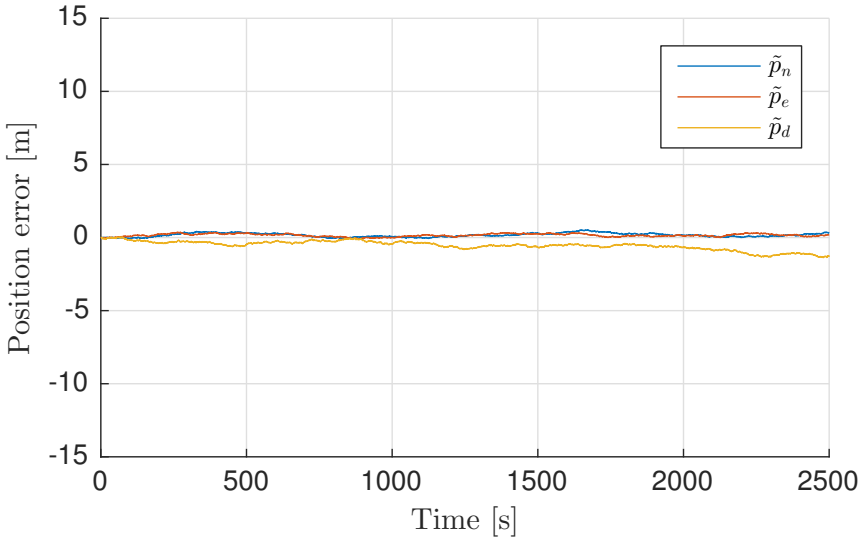

Figure 3.11: Case 2, position estimation error. The position estimation error obtained in simulation when applying global navigation satellite systems (GNSS) position measurements containing colored noise together with GNSS velocity measurements containing white noise. The estimation accuracy is better with velocity measurements corrupted by white noise compared to solely applying position measurements.

synthesized, using (3.36)–(3.37), such that the uncertainty in the position estimate is minimized and by that stabilizing the observer. Hence, the gains, in practice, become so large that the position estimate in the observer tracks the slowly-varying colored GNSS noise. To illustrate this, a Bode diagram, related to the northern position estimation error and the GNSS errors from Case 1 is shown in Fig. 3.16. The transfer functions shown, are the IMU noise $\boldsymbol{\varepsilon}_f^n$ rotated to the NED frame, to the position estimation error $\boldsymbol{p}_{nb}^{\tilde{n}} = \boldsymbol{p}_{nb}^n - \hat{\boldsymbol{p}}_{nb}^n$, the transfer function from the GNSS measurement error $\boldsymbol{\delta}_p = \boldsymbol{H}_p \boldsymbol{z}_p + \boldsymbol{\varepsilon}_p$ to the position estimation error, and the transfer function from the input of the GNSS colored noise model $\boldsymbol{n}_p$ to the output of the model $\boldsymbol{z}_p$. These are denoted

$$\frac{\tilde{\boldsymbol{p}}}{\boldsymbol{\varepsilon}_f^b} = \boldsymbol{h}_{\text{INS}}(s), \tag{3.42}$$

$$\boldsymbol{h}_{\text{INS}}(s) = \bar{\boldsymbol{C}} \left(s\boldsymbol{I}_3 - (\boldsymbol{A}^* - \boldsymbol{K}^* \boldsymbol{C}^*) \right)^{-1} \boldsymbol{B}^*, \tag{3.43}$$

and

$$\frac{\tilde{\boldsymbol{p}}}{\boldsymbol{\delta}_p} = \boldsymbol{h}_{\text{PosErr}}(s), \tag{3.44}$$

$$\boldsymbol{h}_{\text{PosErr}}(s) = \bar{\boldsymbol{C}} \left(s\boldsymbol{I}_3 - (\boldsymbol{A}^* - \boldsymbol{K}^* \boldsymbol{C}^*) \right)^{-1} K^* \boldsymbol{C}^*, \tag{3.45}$$

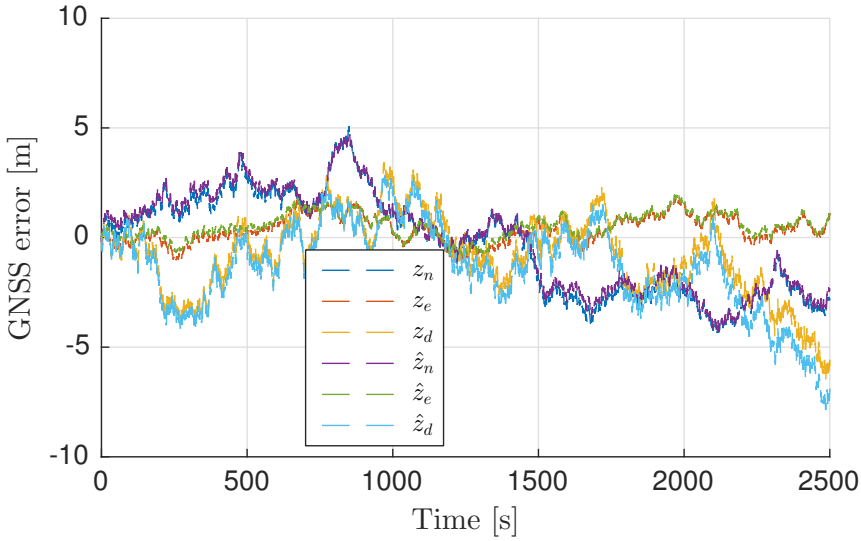

Figure 3.12: Case 2, global navigation satellite systems (GNSS) error state estimates. The true GNSS error states (colored noise), associated with position, are shown in blue, red and yellow, respectively. The corresponding respective estimates are presented in purple, green and light blue. It can be seen that the translational motion observer estimates the colored GNSS error more accurate after the velocity measurements were introduced.

where $\bar{C} = (I_3, \mathbf{0}_{3\times3}, \mathbf{0}_{3\times3})$ and

$$\frac{z_p}{n_p} = h_{\mathrm{CN}}(s), \tag{3.46}$$

$$h_{\mathrm{CN}}(s) = I_3 \left(sI_3 - (F_p)\right)^{-1} G_p, \tag{3.47}$$

respectively. It is evident from Fig. 3.16 that the INS has higher bandwidth than the GNSS colored noise. This is due to the gains synthesis obtained from (3.36)–(3.37) is emphasizing the correction of the position estimate significantly more than the update of corresponding GNSS error state. As a result, the estimated position tracks the colored noise contained in the GNSS position measurements regardless of the model augmentation.

The results from Case 3 indicate that velocity measurements are beneficial to improve the position estimation accuracy, using loosely coupled GNSS/INS integration. However, the parameters representing the colored noise characteristics are time-varying and difficult to know in general. These are highly receiver dependent, and dependent on the user's location on Earth with respect to satellite geometry, elevation of the satellites, the ionosphere, and whether the Doppler observables are utilized in the GNSS's receiver estimator. In particular, knowledge on how the velocity measurements are calculated is difficult to know using off-the

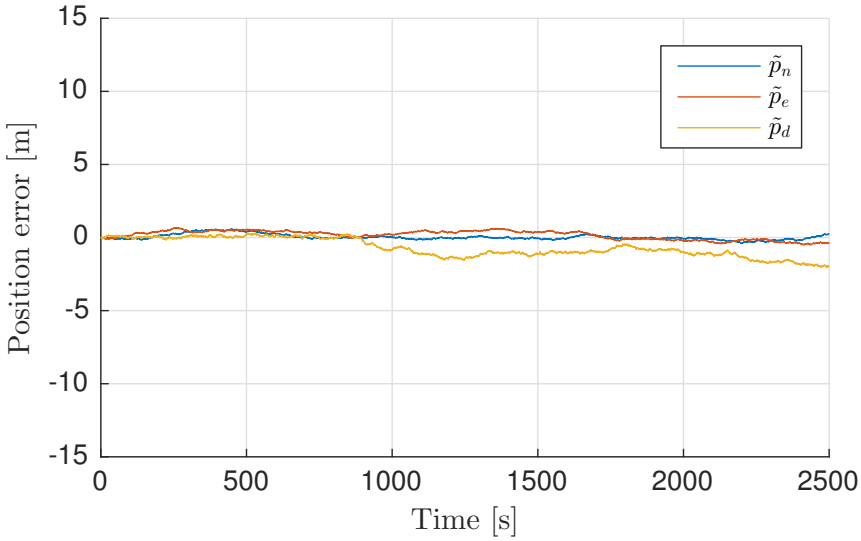

Figure 3.13: Case 3, position estimation error. The position estimation error obtained in simulation when applying global navigation satellite systems (GNSS) position and velocity measurements containing colored noise. The estimation accuracy is better with velocity measurements compared to solely applying position measurements, however, still worse than applying a velocity measurement only corrupted by white noise.

shelf equipment. Typically, the current position estimate is used in the velocity estimation process to determine user-to-satellite LOS vectors or to estimate the receiver's velocity without the Doppler measurement, yielding that the position information is being accounted for twice in the GNSS/INS observer. Knowing the cross correlation between the position and velocity measurements are of utmost importance in such situations. If not known, using only the position measurements may be advised.

3.5.7 Discretization of TMO

The main principle for the discrete-time implementation is to approximate the continuous time behavior despite the finite data rate. It implies that the estimates are only updated when the output measurements contained in the injection terms are valid, and otherwise integrate the model using measured inputs at their highest available update rate. Measurement updates can be processed sequentially by a KF, assuming the measurements are uncorrelated such that the $\boldsymbol{R}$ matrix is diagonal, with benefits for processing structure and complexity (Groves, 2013; Farrell, 2008). Due to the close relationship between (3.36)–(3.37) and the KF, a similar strategy can be applied also for NLOs. The TMO (3.35) is straightforward to discretize due

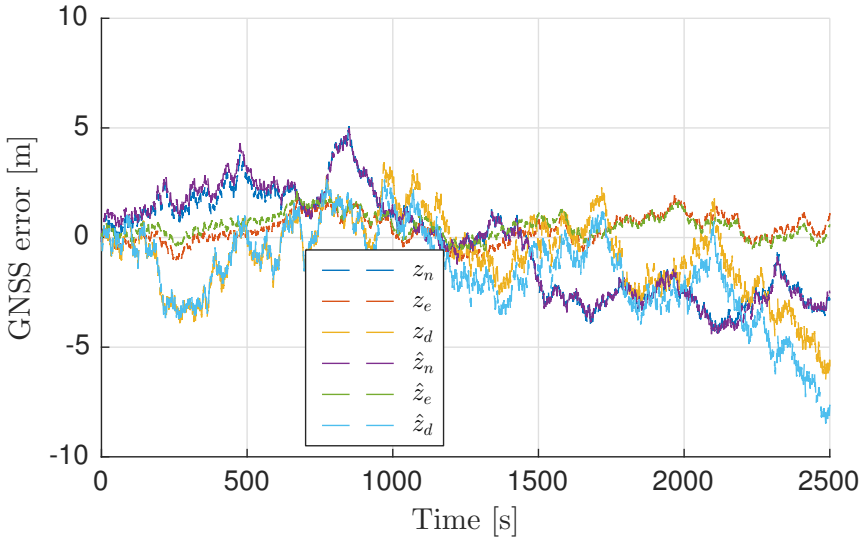

Figure 3.14: Case 3, global navigation satellite systems (GNSS) error state estimates. The true GNSS error states (colored noise), associated with position, are shown in blue, red and yellow, respectively. The corresponding respective estimates are presented in purple, green and light blue. It can be seen that the translational motion observer estimates the colored GNSS error more accurate with velocity measurements than without, however, not as accurate as when the velocity measurements only were corrupted with white noise.

to its linearity and the simple $\boldsymbol{A}$-matrix, allowing for exact discretization of the unforced dynamics. In particular, the one-step ahead predicted state, $\boldsymbol{x}^-$ can be computed by

$$\begin{aligned}\boldsymbol{x}^-[k+1] = \boldsymbol{e}^{\boldsymbol{A}T}\boldsymbol{x}^+[k] \\ + \int_{kT}^{(k+1)T} \boldsymbol{e}^{\boldsymbol{A}\left((k+1)T-\tau\right)}\boldsymbol{B}_1(\tau)\boldsymbol{u}^*(\tau)\,\mathrm{d}\tau \\ + \int_{kT}^{(k+1)T} \boldsymbol{e}^{\boldsymbol{A}\left((k+1)T-\tau\right)}\boldsymbol{D}(\tau)\mathrm{d}\tau,\end{aligned} \tag{3.48}$$

from the estimate $\boldsymbol{x}^+[k]$, where

$$\boldsymbol{A}_d = \boldsymbol{e}^{\boldsymbol{A}T} = \begin{pmatrix} \boldsymbol{I}_3 & T\boldsymbol{I}_3 & \frac{T^2}{2}\boldsymbol{I}_3 & \boldsymbol{0}_{3\times l} \\ \boldsymbol{0}_{3\times 3} & \boldsymbol{I}_3 & T\boldsymbol{I}_3 & \boldsymbol{0}_{3\times l} \\ \boldsymbol{0}_{3\times 3} & \boldsymbol{0}_{3\times 3} & \boldsymbol{I}_3 & \boldsymbol{0}_{3\times l} \\ \boldsymbol{0}_{l\times 3} & \boldsymbol{0}_{l\times 3} & \boldsymbol{0}_{l\times 3} & \boldsymbol{e}^{\boldsymbol{F}T} \end{pmatrix}, \tag{3.49}$$

based on the model parameters of (3.35). Assuming the specific force input, the rotation matrix and the gravity vector are constant between the sampling

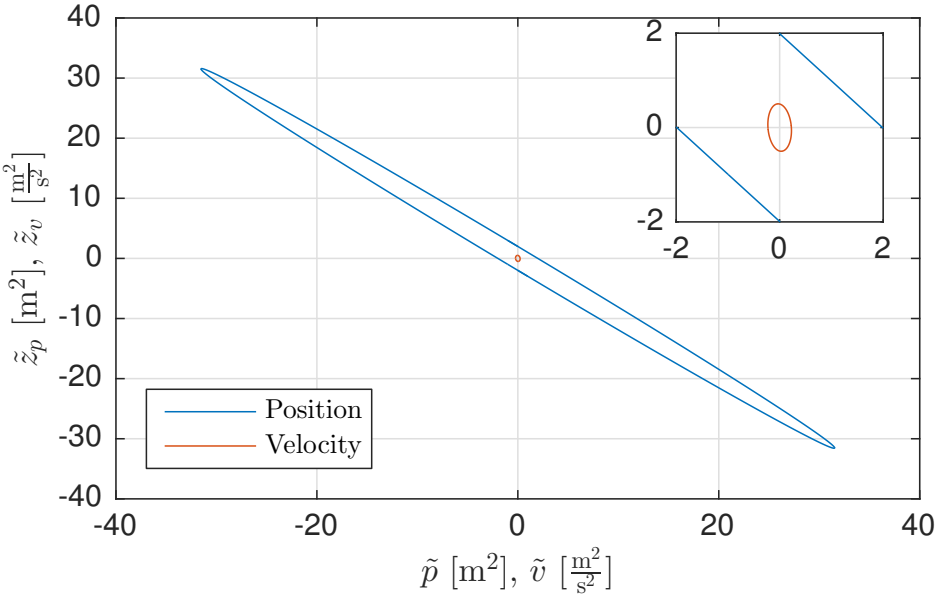

Figure 3.15: Case 3, error ellipsis of the north position and velocity estimation error and the corresponding colored noise estimate of the position and velocity measurement. The error ellipsis associated with position is shown in blue, while error ellipsis associated the velocity is shown red. The error position ellipsis shows that the position estimation error and the colored global navigation satellite system noise estimation error still are significantly correlated, however, the correlation is significantly reduced by introducing the velocity measurement. Regarding the velocity estimation error and the velocity colored noise, the correlation is significantly smaller the compared to the position equivalent.

intervals, $\boldsymbol{f}^b_{\text{IMU}}(t) = \boldsymbol{f}^b_{\text{IMU}}[k]$, $\boldsymbol{R}(t) = \boldsymbol{R}(\boldsymbol{q}^e_b[k])$ and $\boldsymbol{g}^e(\hat{\boldsymbol{p}}^e(t)) = \boldsymbol{g}^e(\hat{\boldsymbol{p}}^e[k])$, for

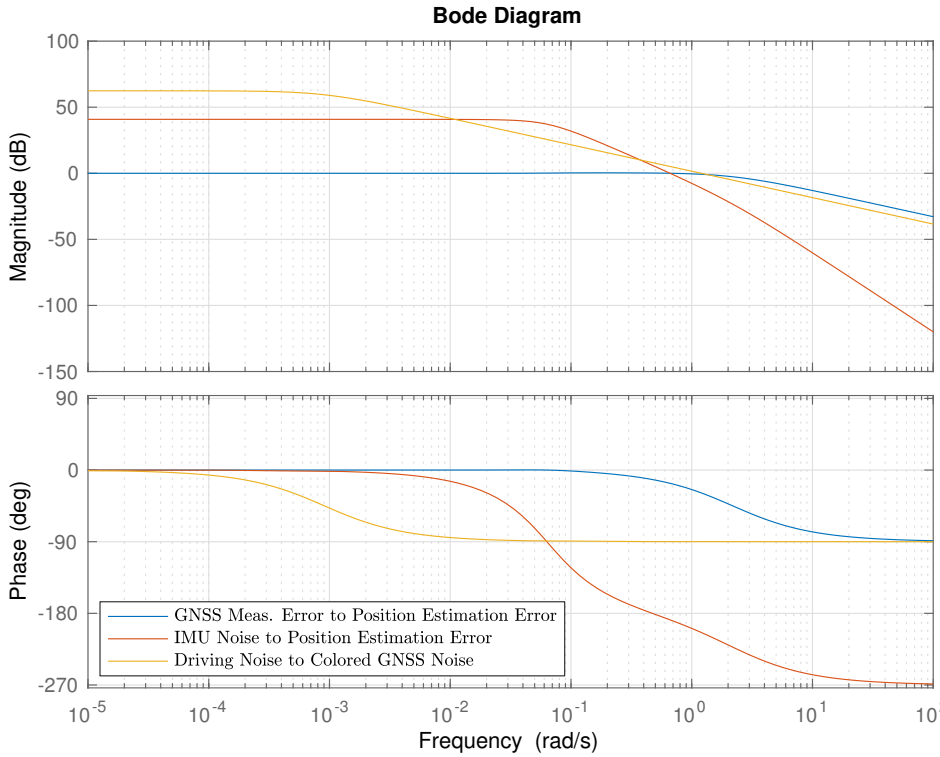

Figure 3.16: Bode plot. Three bode plots are shown; the transfer function from the GNSS measurements error to the position measurement error is shown in blue, the transfer function from the IMU noise to the position estimation error is shown in red and the transfer function from the driving noise of the global navigation satellite system (GNSS) error model to the colored GNSS position noise model output is shown in yellow. From the three frequency responses, the conclusion is that the bandwidth of the navigation system is higher than the slowly-varying colored noise component embedded in the GNSS position measurements. Due to this, the observer struggles to estimate the GNSS's colored noise correctly.

$t \in [kT, (k+1)T)$, the definitions follows from (3.48)

$$\boldsymbol{B}_{d,1}[k] := \begin{pmatrix} \frac{T^2}{2}\boldsymbol{R}(\hat{\boldsymbol{q}}_b^e[k]) & \frac{T^3}{6}\boldsymbol{R}(\hat{\boldsymbol{q}}_b^e[k]) \\ T\boldsymbol{R}(\hat{\boldsymbol{q}}_b^e[k]) & \frac{T^2}{2}\boldsymbol{R}(\hat{\boldsymbol{q}}_b^e[k]) \\ \boldsymbol{0}_{3\times 3} & T\boldsymbol{R}(\hat{\boldsymbol{q}}_b^e[k]) \\ \boldsymbol{0}_{l\times 3} & \boldsymbol{0}_{l\times 3} \end{pmatrix},$$

$$\boldsymbol{B}_{d,2}[k] := \begin{pmatrix} \boldsymbol{0}_{9\times l} \\ \boldsymbol{F}^{-1}\left(\boldsymbol{e}^{\boldsymbol{F}T} - \boldsymbol{I}_l\right)\boldsymbol{G} \end{pmatrix},$$

$$\boldsymbol{B}_d[k] = \begin{pmatrix} \boldsymbol{B}_{d,1}[k] & \boldsymbol{B}_{d,2}[k] \end{pmatrix},$$

$$\boldsymbol{D}_d[k] := \begin{pmatrix} \frac{T^2}{2}(\boldsymbol{g}_b^e(\hat{\boldsymbol{p}}[k]) - 2\boldsymbol{S}(\boldsymbol{\omega}_{ie}^e)\boldsymbol{v}_{eb}^e[k]) \\ T(\boldsymbol{g}_b^e(\hat{\boldsymbol{p}}[k]) - 2\boldsymbol{S}(\boldsymbol{\omega}_{ie}^e)\boldsymbol{v}_{eb}^e[k]) \\ \boldsymbol{0}_{3\times 3} \\ \boldsymbol{0}_{l\times 3} \end{pmatrix}.$$

Then, the state estimate can be recursively propagated by iterating through the time update

$$\begin{aligned} \boldsymbol{x}^-[k+1] &= \boldsymbol{A}_d[k]\boldsymbol{x}^+[k] + \boldsymbol{B}_{d,1}[k]\boldsymbol{u}^*[k] + \boldsymbol{D}_d[k], \\ \boldsymbol{P}^-[k+1] &= \boldsymbol{A}_d[k]\boldsymbol{P}^+[k]\boldsymbol{A}_d^\intercal[k] + \boldsymbol{B}_d[k]\boldsymbol{Q}_d[k]\boldsymbol{B}_d^\intercal[k], \end{aligned}$$

many times as necessary. $\boldsymbol{Q}_d$ can be approximated as $\boldsymbol{Q}_d = \boldsymbol{Q} \cdot T$. Alternatively, the term $\boldsymbol{B}_d[k]\boldsymbol{Q}_d[k]\boldsymbol{B}_d^\intercal[k]$ can be replaced with $\bar{\boldsymbol{Q}}_d$ calculated by using van Loan's method (Brown and Hwang, 2012, p. 126), from van Loan (1978).

If all measurements in the vector $\boldsymbol{y}[k]$ were available at time index k, a gain matrix $\boldsymbol{K}_d[k]$ can be calculated in the same way as the discrete-time KF, Farrell (2008); Groves (2013)

$$\boldsymbol{K}_d[k] = \boldsymbol{P}^-[k]\boldsymbol{C}^\intercal[k]\left(\boldsymbol{C}[k]\boldsymbol{P}^-[k]\boldsymbol{C}^\intercal[k] + \boldsymbol{R}[k]\right)^{-1},$$

and the updated estimate could be obtained as

$$\begin{aligned} \hat{\boldsymbol{x}}^+[k] &= \boldsymbol{x}^-[k] + \boldsymbol{K}_d[k]\left(\boldsymbol{y}[k] - \boldsymbol{C}[k]\boldsymbol{x}^-[k]\right), \\ \boldsymbol{P}^+[k] &= (\boldsymbol{I}_{9+l} - \boldsymbol{K}_d[k]\boldsymbol{C}[k])\boldsymbol{P}^-[k]. \end{aligned}$$

If measurements with indices in the set $\mathcal{I}_k$ are available at time index k, they can be proceed sequentially as follows, Farrell (2008); Groves (2013). First, use the propagated estimate and covariance,

$$\begin{aligned} \hat{\boldsymbol{x}}^+[k] &\leftarrow \boldsymbol{x}^-[k], \\ \boldsymbol{P}^+[k] &\leftarrow \boldsymbol{P}^-[k], \end{aligned}$$

as the starting point for the update loop. Then, for each $i \in \mathcal{I}_k$, where $\mathcal{I}_k$ is set of aiding measurements available at time $t = kT$ in time, loop through the updates

$$\begin{aligned}
\boldsymbol{K}_{d,i}[k] &\leftarrow \boldsymbol{P}^{+}[k]\boldsymbol{C}_i^{\intercal}[k]/(\boldsymbol{C}_i[k]\boldsymbol{P}[k]\boldsymbol{C}_i[k]^{\intercal} + \boldsymbol{R}_{ii}[k]), \\
\hat{\boldsymbol{x}}^{+}[k] &\leftarrow \hat{\boldsymbol{x}}^{+}[k] + \boldsymbol{K}_{d,i}[k]\left(\boldsymbol{y}_i[k] - \boldsymbol{C}_i[k]\hat{\boldsymbol{x}}^{+}[k]\right), \\
\boldsymbol{P}^{+}[k] &\leftarrow (\boldsymbol{I}_{9+m} - \boldsymbol{K}_{d,i}[k]\boldsymbol{C}_i[k])\boldsymbol{P}^{+}[k],
\end{aligned}$$

where $\boldsymbol{C}_i$ is the i-th row of the matrix $\boldsymbol{C}$, and R_{ii} is the i-th diagonal element of the matrix $\boldsymbol{R}$. As a result, such implementation yields a corrector-predictor effect where the measurement update is bypassed for all $i \notin \mathcal{I}_k$ corresponding to $\boldsymbol{K}_{d,i}[k] = 0$. A practical consequence is that the elements of the covariance $\boldsymbol{P}[k]$ associated with $i \notin \mathcal{I}_k$, at a given point in time k, increases due to the positive definite process noise covariance matrix $\boldsymbol{Q}_d[k]$ in the time update. Furthermore, for low-frequency measurement updates, the resulting effect is that these are emphasized more at each measurement correction, when available, than high rate measurements. In comparison, the corrector-predictor algorithm of (Fossen, 2011, Ch. 11.3.4), for fixed-gain observers, is realized with an explicit time-scale separation where the gain associated with the low-rate measurement i is multiplied with the rate ratio, of the observer relative the aiding sensor, similar to that done in the presentation of the attitude observer discretization.

3.5.8 Time delay

If the measurements, typically GNSS and/or magnetometer, Hansen et al. (2015), used in the NLO experiences a significant time delay, the resetting of the INS state may be a delayed state estimate at the time with index $k - j$ corresponding to the time of validity of the measurement delayed with j samples relative to current time. In this case the INS also contains a "fast-forward" function to rapidly compute the current state estimate based on intermediate IMU measurements. Efficient implementation methods are given in Khosravian et al. (2014, 2015) for such problems.

3.6 Tightly Coupled Translational Motion Observer

This section introduces the TMO for tightly coupled GNSS/INS integration in detail. The main difference between the loosely and tightly coupled integration is that the aiding sensor information from GNSS changes from the position domain to range domain.

An observer for tightly coupled GNSS/INS integration was presented by Johansen and Fossen (2015) where an altered version of the TMO for the loosely coupled observer, (3.20)–(3.23), was introduced. In Johansen and Fossen (2015), the TMO was integrated with the same attitude observer as presented earlier.

Tightly coupled integration utilize the raw GNSS observables, range and range-rate (Doppler) measurements, to alter the TMO injection terms from the position domain to the range domain. The range measurements $\boldsymbol{y}_i$ can either be pseudoranges, obtained with C/A or other code-phase techniques, or with carrier-phase based ranges, where the subscript i indicate measurements from the ith satellite. The range-rate measurement is the Doppler frequency $\boldsymbol{\nu}_i$ here measured in meters per second.

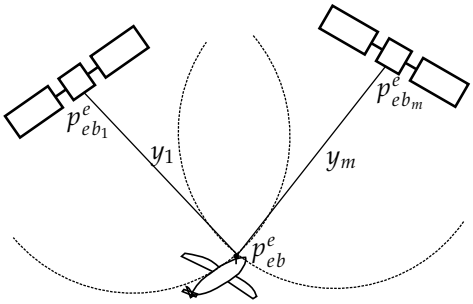

Figure 3.17: Concept illustration of the ranging done in global navigation satellite systems (GNSS). The receiver position is denoted $\boldsymbol{p}^e_{eb}$, while the satellite positions are denoted $\boldsymbol{p}^e_{eb_i}$, where $i \in [1, \ldots, m]$. The position of the GNSS receiver may be located anywhere along the circles with radius y_i and origin $\boldsymbol{p}^e_{eb_i}$. Because of this, the (pseudo)ranges y_i relate to position of the receiver p^e nonlinearly. The figure is a simplification. With pseudoranges $y_i = \varrho_i + \beta$, where $\varrho_i = \|\boldsymbol{p}^e_{eb} - \boldsymbol{p}^e_{eb_i}\|_2$ are the geometric distances between the receiver and the satellites and β being the receiver's clock error multiplied with the speed of light, the nonlinearities become hyperbolic for $\beta > 0$, not circular as indicated.

The range and range-rate measurements are subject to disturbances and errors represented by, for instance, the clock range error
$beta$ between the atomic satellite clocks and the less accurate receiver clock. Even a small error in timing can have a large impact as it is multiplied with the speed of light. It is therefore vital that β is estimated in the observer. Other disturbances on the satellite measurements include ionospheric and tropospheric disturbances which delay the signals due to obstructions in the signal path. Such disturbances can be opposed by a dual frequency receiver where a ionospheric-free linear combination of the two frequency measurements (for instance GPS L1 and L2) can be formed. The drawbacks of this approach is the higher cost of receiver and antenna and the increase in noise on the linear combination due to amplification of multipath and receiver noise. Another approach is to utilize a dual receiver configuration where the satellite measurements are differenced with measurements at a known location close by, thereby cancelling the delays. In Hansen et al. (2016) observers using single- and double-differenced measurements are proposed using an observer structure similar to the one presented here.

Assuming measurements from at least four satellites ($m \geq 4$) are available, the TMO takes the form of

$$\dot{\hat{\boldsymbol{p}}}^e_{eb} = \hat{\boldsymbol{v}}^e_{eb} + \sum_{i=1}^{m} \left(\boldsymbol{K}_i^{pp} e_{y,i} + \boldsymbol{K}_i^{pv} e_{v,i} \right), \tag{3.50}$$

$$\begin{aligned} \dot{\hat{\boldsymbol{v}}}^e_{eb} = &-2\boldsymbol{S}(\boldsymbol{\omega}^e_{ie})\hat{\boldsymbol{v}}^e_{eb} + \hat{\boldsymbol{f}}^e_{ib} + \boldsymbol{g}^e_b(\hat{\boldsymbol{p}}^e_{eb}) \\ &+ \sum_{i=1}^{m} \left(\boldsymbol{K}_i^{vp} e_{y,i} + \boldsymbol{K}_i^{vv} e_{v,i} \right), \end{aligned} \tag{3.51}$$

$$\begin{aligned} \dot{\boldsymbol{\xi}}^e_{ib} = &-\boldsymbol{R}(\hat{\boldsymbol{q}}^e_b)\boldsymbol{S}(\hat{\boldsymbol{\sigma}}^b_{ib})\boldsymbol{f}^b_{\text{IMU}} \\ &+ \sum_{i=1}^{m} \left(\boldsymbol{K}_i^{\xi p} e_{y,i} + \boldsymbol{K}_i^{\xi v} e_{v,i} \right), \end{aligned} \tag{3.52}$$

$$\hat{\boldsymbol{f}}^e_{ib} = \boldsymbol{R}(\hat{\boldsymbol{q}}^e_b)\boldsymbol{f}^b_{\text{IMU}} + \boldsymbol{\xi}^e_{ib}, \tag{3.53}$$

$$\dot{\hat{\beta}} = \sum_{i=1}^{m} \left(K_i^{\beta p} e_{y,i} + K_i^{\beta v} e_{v,i} \right). \tag{3.54}$$

The observer structure of (3.50)–(3.54) is similar to the loosely coupled equivalent (3.20)–(3.23), however it has different injection terms and it includes estimation of the clock error parameter β accounting for synchronization errors between the satellites' and receiver clocks. The clock bias error is the reason why at least four, and not three, satellites are required to calculate the three position coordinates from the pseudoranges. The error is expressed as a time-varying range: $\beta := c\Delta_c$, where c is the speed of light and Δ_c is the clock error. However, due to the injection signals $e_{y,i}$ $e_{v,i}$ some colored noise is going to be embedded in β over time. As indicated by (3.54), β is assumed constant in the deterministic observer design; $\dot{\beta} = 0$. Incorporating this with a minimum variance optimization criterion, similar to (3.36)–(3.37), this model might be considered as a Wiener process, $\dot{\beta} = n_c$, in the tuning process, where n_c is considered to be Gaussian white noise with variance σ_c^2 representing the drift rate of the receiver's clock. Hence, the time-varying dynamics of β is captured by the TMO through the injection terms obtained using the raw GNSS observables.

The injection terms of the observer, based on pseudo-range and range-rate measurements, are driven by the errors $e_{y_i} := y_i - \hat{y}_i$ and $e_{v,i} := v_i - \hat{v}_i$, with the estimated measurements

$$\hat{y}_i = \hat{\varrho}_i + \hat{\beta}, \tag{3.55}$$

$$\hat{v}_i = \left(\frac{\hat{p}^e_{eb} - p^e_{eb_i}}{\hat{\varrho}_i} \right)^{\mathsf{T}} \left(\hat{v}^e_{eb} - v^e_{eb_i} \right), \tag{3.56}$$

where the position and velocity of the ith satellite are denoted $\boldsymbol{p}^e_{eb_i}$ and $\boldsymbol{v}^e_{eb_i}$. The estimated geometric distance between satellite and receiver is given as $\hat{\varrho}_i =$

$\|\hat{\boldsymbol{p}}^e_{eb} - \boldsymbol{p}^e_{eb_i}\|_2$. The estimation errors are defined as $\tilde{\boldsymbol{p}}^e_{eb} := \boldsymbol{p}^e_{eb} - \hat{\boldsymbol{p}}^e_{eb}$, $\tilde{\boldsymbol{v}}^e_{eb} := \boldsymbol{v}^e_{eb} - \hat{\boldsymbol{v}}^e_{eb}$, and $\tilde{\beta} := \beta - \hat{\beta}$. When estimating the satellite measurements and geometric distance, the position and velocity of the satellites are assumed known. This assumption is satisfied by using the updated ephemeris data to determine position and velocity of the visible satellite.

Similar to (3.35) the observer (3.50)–(3.54) can be written

$$\dot{\hat{\boldsymbol{x}}} = \boldsymbol{A}\hat{\boldsymbol{x}} + \boldsymbol{B}\boldsymbol{u} + \boldsymbol{D}(t, \hat{\boldsymbol{x}}) + \boldsymbol{K}(\boldsymbol{y} - \boldsymbol{h}(\hat{\boldsymbol{x}})), \tag{3.57}$$

however with a nonlinear observation vector $h(\hat{x})$, and the matrices,

$$\boldsymbol{A} = \text{blockdiag}(\boldsymbol{A}^*, 0), \quad \boldsymbol{B} = \begin{pmatrix} \boldsymbol{B}^* \\ \boldsymbol{0}_{1\times 3} \end{pmatrix},$$

$$\boldsymbol{D}(t, \hat{x}) = \begin{pmatrix} \boldsymbol{0}_{3\times 1} \\ \boldsymbol{g}^e_b(\hat{\boldsymbol{p}}^e_{eb}) - 2(\boldsymbol{\omega}^e_{ie})\hat{\boldsymbol{v}}^e_{eb} \\ \boldsymbol{0}_{3\times 1} \\ 0 \end{pmatrix},$$

where the linearized $\boldsymbol{C}$ matrix,

$$\boldsymbol{C} = \left.\frac{\delta h}{\delta x}\right|_{x=\hat{x}}, \tag{3.58}$$

takes the form of

$$\boldsymbol{C} = \begin{pmatrix} \frac{\left(\hat{\boldsymbol{p}}^e_{eb} - \boldsymbol{p}^e_{eb_1}\right)^\intercal}{\hat{\varrho}_1} & \boldsymbol{0}_{1\times 3} & \boldsymbol{0}_{1\times 3} & 1 \\ \vdots & \vdots & \vdots & \vdots \\ \frac{\left(\hat{\boldsymbol{p}}^e_{eb} - \boldsymbol{p}^e_{eb_m}\right)^\intercal}{\hat{\varrho}_m} & \boldsymbol{0}_{1\times 3} & \boldsymbol{0}_{1\times 3} & 1 \\ \frac{\left(\hat{\boldsymbol{v}}^e_{eb} - \boldsymbol{v}^e_{eb_1}\right)^\intercal}{\hat{\varrho}_1} & \frac{\left(\hat{\boldsymbol{p}}^e_{eb} - \boldsymbol{p}^e_{eb_1}\right)^\intercal}{\hat{\varrho}_1} & \boldsymbol{0}_{1\times 3} & 0 \\ \vdots & \vdots & \vdots & \vdots \\ \frac{\left(\hat{\boldsymbol{v}}^e_{eb} - \boldsymbol{v}^e_{eb_m}\right)^\intercal}{\hat{\varrho}_m} & \frac{\left(\hat{\boldsymbol{p}}^e_{eb} - \boldsymbol{p}^e_{eb_m}\right)^\intercal}{\hat{\varrho}_m} & \boldsymbol{0}_{1\times 3} & 0 \end{pmatrix}, \tag{3.59}$$

when using GNSS pseudorange and range-rate measurements. The time-varying $\boldsymbol{C}$ matrix consists of estimated LOS vectors describing the direction from rover to each satellite. As the distance between rover and satellites is large compare to the relative velocity, the LOS vectors are slowly time-varying. As illustrated in Fig. 3.17 the pseudoranges relate to the position $\boldsymbol{p}^e_{eb}$ nonlinearly. Hence, the linerization (3.58) is necessary to obtain $\boldsymbol{C}$. If the $\boldsymbol{C}$ matrix is applied to the augmented version of (3.26) with $\boldsymbol{A}$ and $\boldsymbol{B}$ to obtain $\boldsymbol{P}(t)$, the observer gain can be calculated as

$$\boldsymbol{K} = \vartheta \boldsymbol{L}_\vartheta^{-1} \boldsymbol{K}^0 \boldsymbol{E}_\vartheta, \tag{3.60}$$

with

$$\boldsymbol{K}^0 = \boldsymbol{P}\boldsymbol{C}^\intercal \boldsymbol{R}^{-1}, \tag{3.61}$$

and

$$\boldsymbol{L}_\vartheta = \text{blockdiag}\left(\boldsymbol{I}_3, \frac{1}{\vartheta}\boldsymbol{I}_3, \frac{1}{\vartheta^2}\boldsymbol{I}_3, \frac{1}{\vartheta^4}\right), \tag{3.62}$$

$$\boldsymbol{E}_\vartheta = \boldsymbol{C}\boldsymbol{L}_\vartheta \boldsymbol{C}^\dagger. \tag{3.63}$$

The conditions for (3.50)–(3.63) are satisfied when four or more pseudoranges are available (except in degenerate configurations), thereby ensuring observability of the system (Johansen and Fossen, 2015). In contrast to the loosely coupled GNSS/INS integration, the feedback interconnection of (3.50)–(3.54) with the attitude observer, is only locally exponentially stable, with respect to position and velocity initialization errors, since the $\boldsymbol{C}$ matrix is based on linearization of the pseudorange and Doppler measurement equations about the estimated position and velocity. Accurate initialization procedures are easily applied, Johansen and Fossen (2015), so this is not a significant problem in practice.

To accommodate colored noise, when applying tightly coupled integration, the $\boldsymbol{R}$ matrix can be increased in an ad hoc manner. An example using such strategy, is designing a tuning rule based on the elevation angle of each satellite in view, (Groves, 2013, Ch. 9.4.2.4). By doing this, it is possible to weight pseudoranges from low elevation satellites less than measurements from high elevation satellites (with high elevation satellites, the GNSS signal travels through less atmosphere compared to the signals from the low elevation satellites and therefore has less errors).

3.6.1 Augmented TMO for tightly coupled integration including clock error model

Above, the clock error was modelled in range space as $\beta = c \cdot \Delta_c$ with Δ_c being the clock error. This can be extended further by considering that Δ_c is dependent on the clock frequency error, such that β is no longer considered as a constant, but expressed with a state space model with a constant clock frequency error f_{clock} such that $\ddot{\beta} = 0$, see (Farrell, 2008, Ch. 8.4.3.2), (Groves, 2013, Ch 9.4.2.3):

$$\begin{pmatrix} \dot{\beta} \\ \dot{f}_{\text{clock}} \end{pmatrix} = \begin{pmatrix} 0 & 1 \\ 0 & 0 \end{pmatrix} \begin{pmatrix} \beta \\ f_{\text{clock}} \end{pmatrix} + \begin{bmatrix} 0 \\ n_f \end{bmatrix}, \tag{3.64}$$

where n_f is the driving process noise assumed to be white. By introducing the additional clock error state, (3.54) in the TMO is replaced by

$$\dot{\hat{\beta}} = \hat{f}_{\text{clock}} + \sum_{i=1}^{m} \left(K_i^{\beta p} e_{y,i} + K_i^{\beta v} e_{v,i} \right), \tag{3.65}$$

$$\dot{\hat{f}}_{\text{clock}} = \sum_{i=1}^{m} \left(K_i^{fp} e_{y,i} + K_i^{fv} e_{v,i} \right). \tag{3.66}$$

By doing this, (3.57) is augmented accordingly. With this augmentation, the C-matrix of (3.59), in (3.26), is replaced with C_{aug}, given as

$$\boldsymbol{C}_{\text{aug}} = \begin{pmatrix} \boldsymbol{C} & \boldsymbol{C}_{\text{f}} \end{pmatrix}, \tag{3.67}$$

where $\boldsymbol{C}_{\text{f}} = (\boldsymbol{0}_{m\times 1}; \boldsymbol{I}_{m\times 1})$. The standard deviation of the white noise n_f ought to be chosen small (less than 0.02 m/s as proposed in (Farrell, 2008, Ch. 8.4.3.2)). However, by modeling of the clock bias as (3.64), compared to $\dot{\beta} = 0$ as done in Johansen and Fossen (2015), only minor effects (centimeter level) on the estimation of β were observed. Therefore major effects on the position and velocity estimates cannot be expected with this augmentation. Also with this clock error model, it is necessary to take into account that noncompensated common residuals of the time-varying errors due to signal delays, in the ionosphere and troposphere or stemming from multipath, may be embedded in β and f_{clock} since these are the only nuisance parameters related to the GNSS in this TMO.

3.7 Experimental Results

This section presents a comparison of the performance of the discussed observer structures using experimental data collected during a UAV mission.

Experimental verification of the presented observers is carried out using flight data from a UAV test flight, to verify the observers under realistic conditions with fast dynamics. The UAV used is a fixed wing Penguin B UAV configured as listed in Table 3.1 in the Application example. The dataset used here has a length of approximately 22 minutes with a flight part consisting of multiple circles and figures-of-eight over an area of one square kilometer.

During the flight, a stationary GNSS receiver of the same type was placed at a known location to serve as base station for a real time kinematic (RTK) positioning solution. The RTK position was computed by the open source software package RTKLIB (2013), where the position is obtained using carrier-phase positioning, with a fixed or float integer ambiguity solution, indicating decimeter accuracy (Groves, 2013). The RTK position is used as reference when comparing the performance of the loosely and the tightly coupled observer structures. The base station also logged the transmitted satellite ephemeris data, used to calculate the satellites' positions and velocities. RTK is a type of differential GNSS.

The loosely and tightly coupled observers are compared. To guarantee a fair comparison, the standalone GNSS position solution used in the loosely coupled integration is based on the tightly coupled observer using solely the pseudoranges as observables. Hence, no IMU is used to generate this aiding position solution.

The tuning parameters for the observers are gathered in the $\boldsymbol{Q}$ and $\boldsymbol{R}$ matrices for gain selection. For the loose integration, the matrices are:

$$\boldsymbol{Q}_l = \text{blockdiag}(\boldsymbol{0}_{3\times3}, 10^{-10} \cdot \boldsymbol{I}_3, 2.5 \cdot 10^{-3}), \boldsymbol{R}_l = \text{blockdiag}(2.5 \cdot \boldsymbol{I}_3).$$

For the tightly coupled integration, the tuning matrices are:

$$\boldsymbol{Q}_t = \text{blockdiag}(\boldsymbol{Q}_l, 1), \boldsymbol{R}_t = \text{blockdiag}(1 \cdot \boldsymbol{I}_m).$$

The observers use the same constant attitude estimator gains: $k_I = 0.004$, $k_1 = 0.25$, and $k_2 = 0.75$.

The comparison of the observers are seen in Fig. 3.18, depicting the position estimation error. Fig. 3.19 shows the estimated attitude, while Fig. 3.20 displays the estimated gyro bias. The position estimation is evaluated in terms of root-mean-square error (RMSE) and standard deviation (STD) relative to the RTK solution and summarized in Table 3.2.

As presented above, tuning of the $\boldsymbol{Q}$ matrix associated with the velocity state is based on statistics describing the accelerometer's noise characteristics. These can either be based on the data collected or from a data sheet. For a standalone GNSS solution (IMU not used), tuning of the $\boldsymbol{Q}$ matrix reduces to an ad hoc procedure based on the assumed host-vehicle dynamics. (Groves, 2013, Ch. 9.4) recommends 1^2 m/s^2, 10^2 m/s^2 and 100^2 m/s^2 for pedestrian, automotive and military aircraft, respectively associated with the velocity state.

Table 3.2: Navigation performance comparison

	RMSE (x,y,z) [m]			STD (x,y,z) [m]		
Tightly coupled	3.412	3.341	1.106	1.067	0.561	1.005
No IMU	4.541	3.732	2.184	2.951	1.756	2.065
Loosely coupled	4.442	3.818	2.264	2.836	1.868	2.177

As seen in Fig 3.18, the tightly coupled GNSS/INS integration strategy provides the position estimates with smallest variation and also the smallest deviation from the RTK positioning solution. This statement is backed up by Table 3.2. The difference between a standalone GNSS solution and loosely coupled integration seems less evident from Fig. 3.18 and Table 3.2. This is however expected, taking into account the simulation results related to the loosely coupled GNSS/INS integration and the estimation of colored GNSS noise presented earlier. The benefit of loosely coupled integration, relative not using an IMU at all, is however

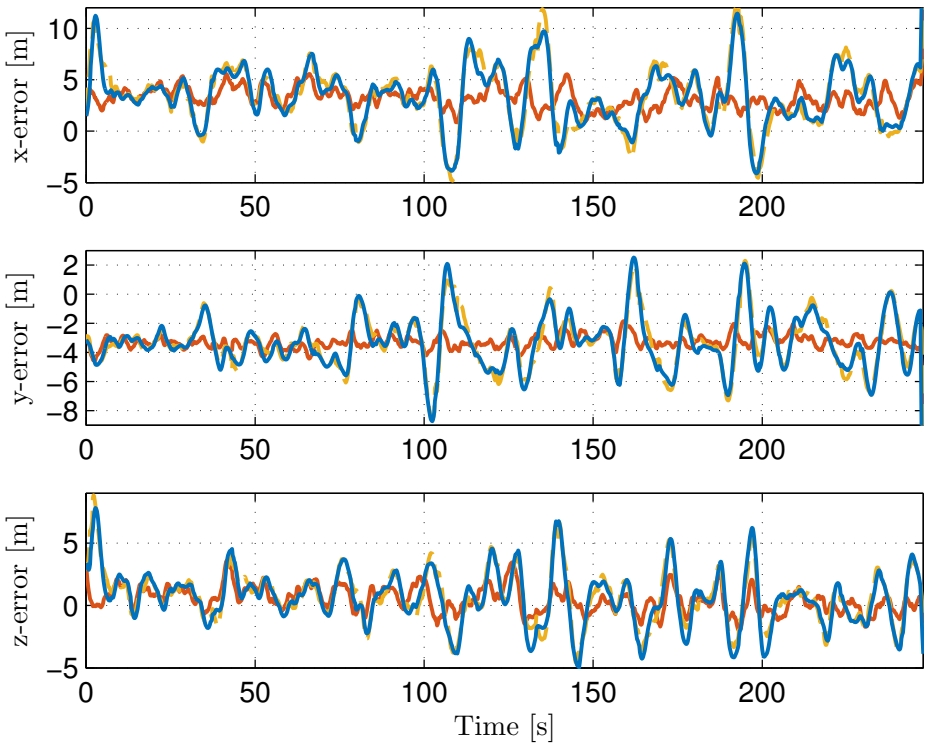

Figure 3.18: Position estimation error. The results are presented in the earth-centered, earth-fixed (ECEF) frame relative the real time kinematic (RTK) global navigation satellite System (GNSS) positioning solution. The result obtained using loosely coupled integration is shown in blue, the result obtained using tightly coupled integration is shown in red, while the standalone GNSS solution is presented in yellow. These results indicate that tightly coupled integration of inertial and GNSS measurements yield more accurate position estimation compared to loosely coupled integration and standalone GNSS when applying satellite-based navigation based on the standard GNSS positioning service.

evident in Fig. 3.21. The loosely coupled solution provides a smoother estimate than the standalone GNSS solution and is hence more suitable to be used in an autopilot that operate at high sampling rate. The INS also provides fault tolerance when GNSS fails or is degraded. Moreover, one large benefit of loosely coupled GNSS/INS, relative to a standalone GNSS solution, is that the attitude estimates also are obtained with high accuracy.

As mentioned, the most accurate and precise position estimates relative to the RTK solution are obtained with the tightly coupled integration strategy. Since the pseudoranges are directly fused with the inertial measurements, instead of calculating the GNSS position before using this as aid in loosely coupled integration,

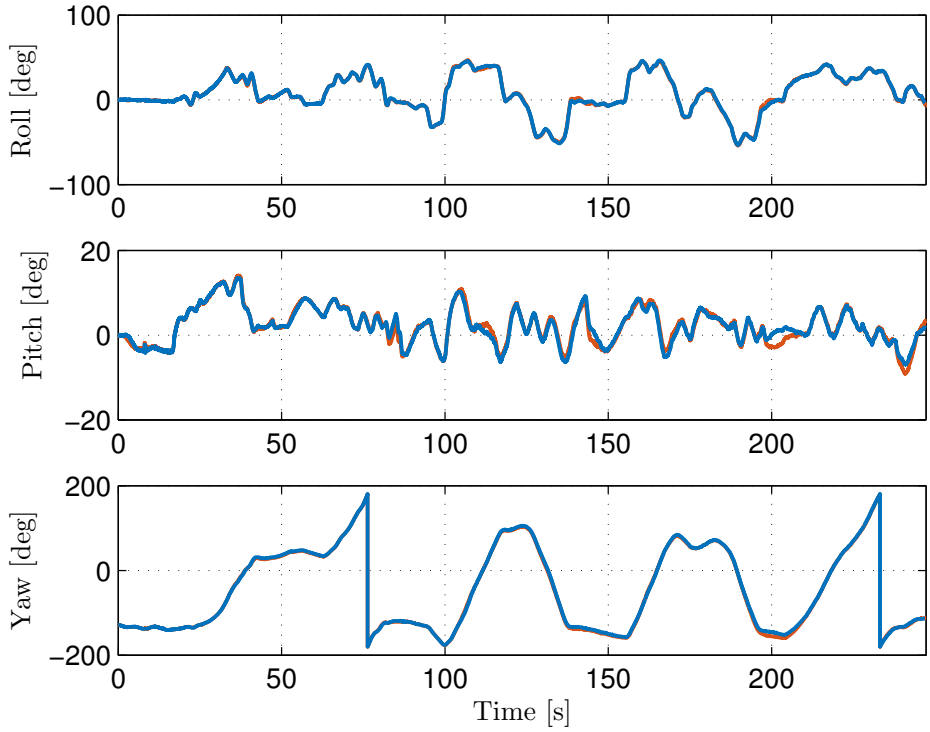

Figure 3.19: Attitude estimation. The results are presented using Euler angles as attitude representation. The estimate obtained using loosely coupled integration is shown in blue, while the estimate obtained using tightly coupled integration is shown in red. The standalone GNSS navigation solution did not provide attitude estimates.

more of the colored noise, embedded in the GNSS pseudoranges, is captured by the receiver's clock bias estimate. This is possible since the acceleration measurements are available between GNSS samples. Hence, every new position and clock error calculation, made by the observer, is based on the current predicted position between GNSS samples using inertial data rather than using a 0.2 to 1 second old estimate obtained at the previous GNSS update. This point however, is mainly relevant for low-cost GNSS receivers, as higher grade receivers can output raw data at frequencies of 20 Hz or more. A contributing factor to the performance differences of the two integration schemes may also be due to the 5 Hz GNSS update. By sampling the GNSS that fast, more of the pseudorange measurements can become correlated in time compared to using 1 Hz position calculation. If differential GNSS is utilized, more accurate position estimates can be obtained for both integration schemes.

The attitude estimates obtained with both loosely and tightly coupled integra-

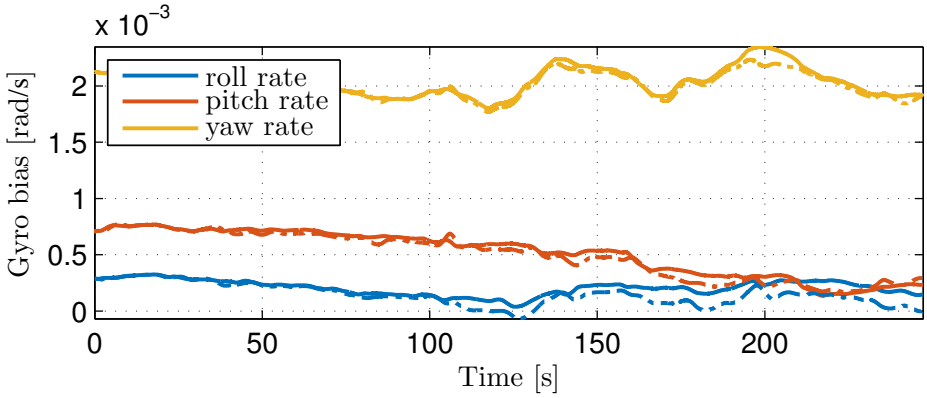

Figure 3.20: Gyro bias estimation. The result obtained using loosely coupled integration is shown with dotted lines, while the result obtained using tightly coupled integration is shown with solid lines.

tion are mostly similar except from a few significant differences. These differences are most likely due to the attitude estimate $\hat{\boldsymbol{q}}_b^e$ has two components, the unit quaternion from BODY to NED $\boldsymbol{q}_b^n$ and the unit quaternion from NED to ECEF $\boldsymbol{q}_n^e$ and how the GNSS information enters the TMOs. The latter quaternion $\boldsymbol{q}_n^e$ is in principle a horizontal position estimate containing information of the craft's latitude and longitude. Therefore, the attitude estimates from the two integration strategies may differ as a result of the difference in how the position information enters the TMO due to the feedback interconnection with the attitude observer and the TMO through the auxiliary state $\boldsymbol{\xi}_{eb}^e$. This again will also affect the gyro bias estimation, seen in Fig. 3.20, and therefore explaining that the estimates obtain using tightly coupled GNSS/INS integration resulted in more steady estimates compared to applying loosely coupled integration.

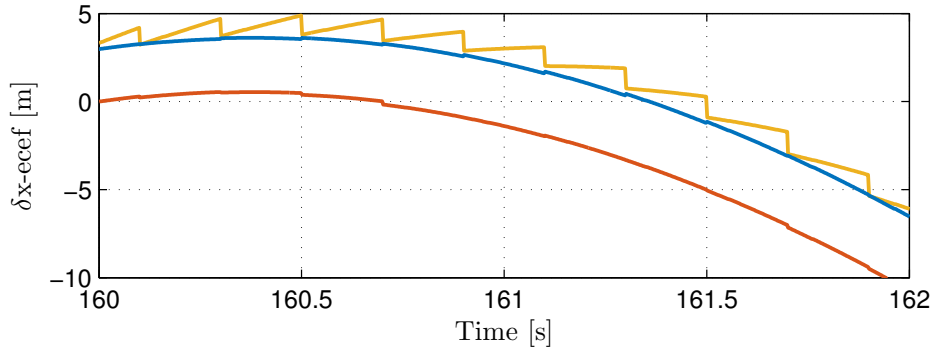

Figure 3.21: Normalized position error. The results are related to the real time kinematic (RTK) global navigation satellite system (GNSS) positioning solution between 160 and 162 seconds of flight. The error relative the RTK solution applying the loosely coupled integration is shown in blue and the error relative the RTK solution applying the tightly coupled integration is shown in red, while the error relative RTK using pure GNSS positioning is shown in yellow. The error relative RTK is smallest applying tightly coupled integration. The error using loosely coupled integration and pure GNSS is of similar magnitude, however, the integrated solution is smoother than pure GNSS since inertial data is available between GNSS samples.

3.8 Conclusion

Accurate and precise position, velocity and attitude estimates are needed in numerous areas such as the automotive, robotics, marine and aircraft applications. The need for computationally efficient and robust algorithms achieving this is growing due to a wide-spread interest in unmanned platforms, such as unmanned aerial vehicles, with potential limited computational power available. This need can be met by applying nonlinear feedback-interconnected observers for integrated GNSS/INS navigation with known stability properties.

The experimentally verified simulation results, using data collected during a unmanned aerial vehicle flight, show that the estimation of translational motion (position and velocity) benefits from a minimum-variance-like implementation applying the Riccati equation. Using such an implementation strategy, compared to a fixed-gain strategy, accelerates the observers convergence. This is also reflected in the attitude estimates due to the feedback-interconnection relating the two observers.

The attitude estimates are obtained with an exponentially stable and computationally efficient observer based on complementary filtering and vector measurements. In contrast to the Kalman filter, this is not a stochastic method, but based on the desired observer bandwidth and nonlinear stability theory.

The results presented here indicate that tightly coupled GNSS/INS integration

outperforms loosely coupled integration when considering position accuracy. By fusing the pseudorange measurements directly with the inertial data, more of the colored noise embedded in the pseudoranges is captured by the receiver's clock error estimate, compared to that achieved with the augmented loosely coupled integration scheme posed.

The attitude estimates obtained with both loosely and tightly coupled integration are mostly similar. Differences are possibly due to the different amount of colored noise being fed from the respective translational motion observer to the attitude observer.

Accuracy of the loosely and tightly coupled integration schemes can be increased by applying pseudorange corrections using differential GNSS, carrier-phase smoothed pseudoranges or dual-frequency solutions canceling the ionospheric delay at the expense of increased noise.

4

INS on Ships

This chapter is based on Rogne et al. (ndb).

4.1 Introduction

Inertial sensors are not of course unknown on a ship, with the venerable gyrocompass well established as a source for heading, and the VRU as an essential vessel sensor for DP. This chapter investigates the addition of MEMS IMUs for use in a more general way, implementing a fully integrated INS aided by position reference systems and gyrocompasses utilizing nonlinear observer theory.

The main contributions of this chapter are on full-scale verification of different NLOs for attitude estimation for ships, comparing two low-cost MEMS IMUs. The results are acquired by comparing the estimation result to well-proven industrial sensor systems providing roll, pitch and heave measurements for marine surface vessels. Furthermore, a method of evaluating the aggregate performance of one's navigation solution (combination of sensor quality and algorithm) is to evaluate the INS through dead reckoning. The verification consist of:

- Applying two NLOs —Mahony et al. (2008) and Bryne et al. (2015b) — for ship attitude estimation.
- Applying the NLOs and IMUs during two operation conditions: DP and turning maneuvers.
- Evaluation of heave estimation performance using a virtual vertical reference (VVR) signal, Bryne et al. (2014, 2015b).
- Testing the potential of the underlying fault-tolerance properties of the integrated INS solutions by evaluating the DR capabilities of the IMU-and-estimator combinations.

In addition a short discussion regarding vibrations and other high-frequency motion picked up by the MEMS sensors is provided, and some ways to reduce or mitigate, or even take advantage of these effects.

Parts of this chapter is based on the preliminary work found in Bryne et al. (2016) and Rogne et al. (2016a). The work has been expanded with new tuning to better reflect performance achievable with NLOs, low-pass filtering of IMU signals, comparison with extended Kalman filter, applying the VVR to a new observer, and an analysis of vibration and mechanical noise afflicting the IMUs.

4.2 Preliminaries

4.2.1 Notation

The Euclidean vector norm is denoted $\|\cdot\|_2$. The $n \times n$ identity matrix is denoted $\boldsymbol{I}_n$, while the transpose of a vector or a matrix is denoted with $(\cdot)^\intercal$. Coordinate frames are denoted with $\{\cdot\}$. $\boldsymbol{S}(\cdot) \in SS(3)$ represents the skew symmetric matrix such that $\boldsymbol{S}(z_1)z_2 = z_1 \times z_2$ for two vectors $z_1, z_2 \in \mathbb{R}^3$. $z = (z_1; z_2; \ldots; z_n)$ denotes a vector of stacked column vectors $z_1, z_2, \ldots z_n$. In addition, $z^a_{bc} \in \mathbb{R}^3$ denotes a vector z, to frame $\{c\}$, relative $\{b\}$, decomposed in $\{a\}$. Moreover, $\otimes$ denotes the Hamiltonian quaternion product. $(\cdot)^\dagger$ denotes the right Moore-Penrose pseudoinverse

The rotation matrix from the given frame $\{a\}$ to the given frame $\{b\}$ is denoted $\boldsymbol{R}^b_a \in SO(3)$. $\boldsymbol{\omega}^a_{ab} \in \mathbb{R}^3$ is an angular velocity of $\{b\}$ relative $\{a\}$, decomposed in $\{a\}$. Similar to the rotation matrix, the rotation between $\{a\}$ to $\{b\}$ may be represented using the unit quaternion $\boldsymbol{q}^b_a = (s, \boldsymbol{r}^\intercal)^\intercal$ where $s \in \mathbb{R}^1$ is the real part of the quaternion and $\boldsymbol{r} \in \mathbb{R}^3$ is the vector part. Roll, pitch and yaw are denoted ϕ, θ and ψ, respectively, in compliance with the SNAME notations.

4.2.2 Coordinate reference frames

In this chapter four reference frames are employed; The earth-centered inertial (ECI) frame, the earth-centered, earth-fixed (ECEF) frame, a tangent frame equivalent of an earth-fixed north-east-down (NED) frame, and the BODY reference frame, denoted $\{i\}$, $\{e\}$, $\{t\}$ and $\{b\}$, respectively (see Fig. 4.1). ECI is an assumed inertial frame following the Earth as it orbits around the sun, where the x-axis points towards vernal equinox, the z-axis is pointing along the Earth's rotational axis and the y-axis completes the right hand frame. As for the ECEF frame, the x-axis points towards the zero meridian, the z-axis points along the Earth's rotational axis, while the y-axis completes the right hand frame. The Earth's rotation rate $\omega_{ie} = 7.292115 \cdot 10^{-5}$ rad/s is given by the WGS-84 datum. It is decomposed in the ECEF and NED frame as

$$\boldsymbol{\omega}^e_{ie} = \begin{pmatrix} 0 \\ 0 \\ 1 \end{pmatrix} \omega_{ie}, \quad \boldsymbol{\omega}^t_{ie} = \begin{pmatrix} \cos(\mu) \\ 0 \\ -\sin(\mu) \end{pmatrix} \omega_{ie}, \tag{4.1}$$

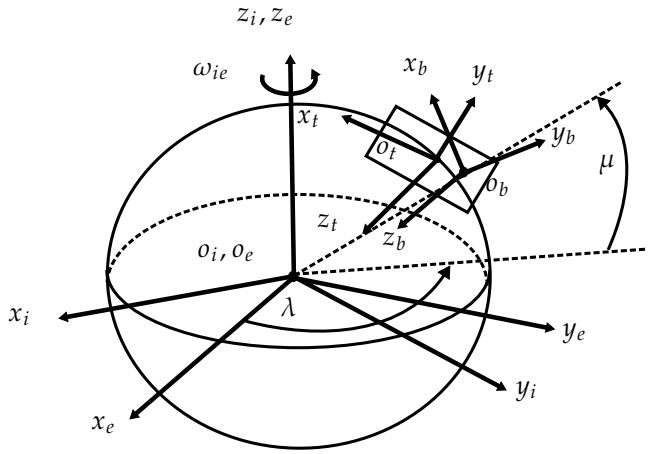

Figure 4.1: Definitions of the BODY, NED (tangent), ECEF and ECI reference frames.

where μ is the latitude on the Earth. The longitude is denoted λ. Moreover, the navigation frame is a local Earth-fixed tangent frame, {t}, where the x-axis points towards north, the y-axis points towards east, and the z-axis points downwards. The BODY frame is fixed to the vessel. The origin of {b} is located at the nominal center of gravity of the vessel. The x-axis is directed from aft to fore, the y-axis is directed to starboard and the z-axis points downwards.

4.2.3 Kinematic strapdown equations

The attitude representation most comprehensible for the user is the attitude between the BODY and the NED or tangent frame. This is also the most intuitive representation for control and lever arm compensation purposes. Using a rotation matrix representation, the attitude kinematics are given as

$$\dot{\boldsymbol{R}}_b^t = \boldsymbol{R}_b^t \left(\boldsymbol{S}(\boldsymbol{\omega}_{ib}^b) - \boldsymbol{S}(\boldsymbol{\omega}_{it}^b) \right), \tag{4.2}$$

or equivalently,

$$\dot{\boldsymbol{q}}_b^t = \frac{1}{2} \boldsymbol{q}_b^t \otimes \begin{pmatrix} 0 \\ \boldsymbol{\omega}_{ib}^b \end{pmatrix} - \frac{1}{2} \begin{pmatrix} 0 \\ \boldsymbol{\omega}_{it}^t \end{pmatrix} \otimes \boldsymbol{q}_b^t, \tag{4.3}$$

using the unit quaternion attitude representation. $\boldsymbol{\omega}_{it}^b = \boldsymbol{R}_t^b \boldsymbol{\omega}_{it}^t$ is the angular rate of navigation frame relative the inertial frame where $\boldsymbol{\omega}_{it}^t$ is given as

$$\boldsymbol{\omega}_{it}^t = \boldsymbol{\omega}_{ie}^t + \boldsymbol{\omega}_{et}^t = \boldsymbol{\omega}_{ie}^t, \tag{4.4}$$

since a tangent frame representation of the strapdown equations is chosen, resulting in $\boldsymbol{\omega}_{en}^t = \boldsymbol{0}_{3\times 1}$. Moreover, $\boldsymbol{\omega}_{ib}^b$ is the angular rate of the navigating object relative the inertial frame, decomposed in $\{b\}$. Furthermore, from (Fossen, 2011,

Eq. (2.56)) and reference therein, the rotation matrix $\boldsymbol{R}(\boldsymbol{q}_b^t) := \boldsymbol{R}_b^t$ is obtained from $\boldsymbol{q}_b^t$ using

$$\boldsymbol{R}(\boldsymbol{q}_b^t) = \boldsymbol{I}_3 + 2s\boldsymbol{S}(\boldsymbol{r}) + 2\boldsymbol{S}(\boldsymbol{r}). \tag{4.5}$$

When using the tangent frame as the navigation frame, the rotational and translational motion is related with

$$\dot{\boldsymbol{p}}_{tb}^t = \boldsymbol{v}_{tb}^t, \tag{4.6}$$

$$\dot{\boldsymbol{v}}_{tb}^t = -2\boldsymbol{S}(\boldsymbol{\omega}_{ie}^t)\boldsymbol{v}_{tb}^t + \boldsymbol{R}_b^t\boldsymbol{f}_{ib}^b + \boldsymbol{g}_b^t, \tag{4.7}$$

where $\boldsymbol{p}_{tb}^t \in \mathbb{R}^3$ is the position, relative a defined origin of the tangent frame, $\boldsymbol{p}_{tb}^t(0) := \boldsymbol{0}_{3\times1}$ based on $\mu(0)$ and $\lambda(0)$. Furthermore, $\boldsymbol{v}_{tb}^t \in \mathbb{R}^3$ is the linear velocity. It follows that $\boldsymbol{g}^t(\mu, \lambda) \in \mathbb{R}^3$ is the local gravity vector which may be obtained using a gravity model based on the vessel's latitude and longitude. $\boldsymbol{f}_{ib}^b = (\boldsymbol{R}_b^t)^\intercal(\boldsymbol{a}_{ib}^t - \boldsymbol{g}_b^t) \in \mathbb{R}^3$ is the specific force decomposed in {b}, where $\boldsymbol{a}_{ib}^t$ is the accelerations decomposed in the tangent frame, measured by the IMU. Moreover, (4.6)–(4.7) can be further extended for marine surface craft with the auxiliary variable $p_{tb,I}^t$. The augmentation, first applied in Bryne et al. (2014), is motivated by the fact that the mean vertical position of the vessel is zero over time since the wave-induced motion of the craft in heave oscillates about the mean sea surface. From Bryne et al. (2015b) and references therein we may write:

$$p_{tb,I}^t = \lim_{T\to\infty} \frac{1}{T} \int_0^T p_z^t(t)\mathrm{d}t = 0. \tag{4.8}$$

Based on (4.8) we augment the strapdown equations (4.6)–(4.7) by introducing $p_{tb,I}^t$ as a state with

$$\dot{p}_{tb,I}^t = p_{tb,z}^t, \tag{4.9}$$

by integrating the vertical (down) position associated with the heave motion.

4.3 IMU and Ship Sensor Configuration

4.3.1 IMU and error sources

An strapdown IMU is a sensor unit measuring tri-axial angular velocity and tri-axial specific force of the unit in BODY frame relative the inertial frame,

$$\boldsymbol{f}_{\text{IMU}}^b = \left(f_x^b; f_y^b; f_z^b\right), \quad \boldsymbol{\omega}_{\text{IMU}}^b = \left(\omega_x^b; \omega_y^b; \omega_z^b\right),$$

where the subscripts x, y and z, denote the forward, starboard and downwards axes, respectively, in the BODY frame. In addition to the specific forces and angular velocity, each measurement is contaminated with sensor biases, errors and noise. Sensor errors may consist of nonlinearity, scale factors, cross-coupling

and g-sensitivity errors, where the latter only effects the angular rate sensor's reading. In additional to internal noise sources, external noise may arise due to e.g. electrical and magnetic interference or stem from mechanical sources in the form of vibrations. We assume that error sources related to sensor nonlinearity, scale factors, misalignment, cross-coupling and g-sensitivity are compensated for in calibration by the manufacturer, or are otherwise neglectable. Sensor biases may also be calibrated for by the manufacturer or compensated for by in-silico temperature sensors. For a summary on IMU error sources, see (Groves, 2013, Ch. 4.4). For more detailed information on inertial sensors and inertial sensor errors, (Titterton and Weston, 2004, Ch. 4–8) may be advised.

Nevertheless, some time-varying bias instability and run-to-run instability is often present with MEMS IMUs. Therefore, we model the angular rate and accelerometer measurements as

$$\boldsymbol{\omega}^b_{\text{IMU}} = \boldsymbol{\omega}^b_{ib} + \boldsymbol{b}^b_{\text{gyro}} + \boldsymbol{w}^b_{\text{gyro}}, \tag{4.10}$$

$$\boldsymbol{f}^b_{\text{IMU}} = \boldsymbol{f}^b_{ib} + \boldsymbol{b}^b_{\text{acc}} + \boldsymbol{w}^b_{\text{acc}}, \tag{4.11}$$

where $\boldsymbol{\omega}^b_{ib}$ and $\boldsymbol{f}^b_{ib}$ are the true angular rates and specific forces, respectively. Moreover, the respective sensors biases are denoted $\boldsymbol{b}^b_{\text{gyro}}$ and $\boldsymbol{b}^b_{\text{acc}}$, while $\boldsymbol{w}^b_{\text{gyro}}$ and $\boldsymbol{w}^b_{\text{acc}}$ represent the sensor noise and vibration induced noise contained in the respective measurements. Both the angular rate/gyro and accelerometer biases are assumed slowly time-varying,

$$\dot{\boldsymbol{b}}^b_{\text{gyro}} = \boldsymbol{w}^b_{b,\text{gyro}}, \quad \dot{\boldsymbol{b}}^b_{\text{acc}} = \boldsymbol{w}^b_{b,\text{acc}}, \tag{4.12}$$

where $\boldsymbol{w}^b_{b,\text{gyro}}$ and $\boldsymbol{w}^b_{b,\text{acc}}$ represent small variations in the biases (zero mean).

4.3.2 Ship sensor configuration

Several IMUs were installed on an offshore vessel operating in the Norwegian sea, equipped with a Rolls-Royce Marine DP system, see Appendix A for more details. The ship in question is owned and operated by Farstad Shipping. In this chapter we will present results obtained using ADIS16485 and STIM300 MEMS IMUs. The sensor configuration used in aided strapdown INS on board the offshore vessel, based on the kinematic formulation of (4.3), (4.6)–(4.7), (4.9) for fusing IMU, compass, GNSS and VVR measurements, was:

- 1x differential GNSS position measurement, $\boldsymbol{p}^t_{\text{GNSS}} = (p^t_x, p^t_y)^\intercal$ at 1 Hz (we only use horizontal position).
- VVR: $p^t_{tb,I} = 0$, for all $t \geq 0$. By using the VVR, other vertical references based on ranging with reduced precision due to the vertical ranging geometry, such as with GNSS-based and hydroacoustic-based PosRefs are avoided. For more details on the VVR measurement principle, see Bryne et al. (2015b).

- 2x IMUs (ADIS16485 and STIM300) providing
  - Tri-axial angular rate measurements, $\boldsymbol{\omega}^b_{\text{IMU}}$
  - Tri-axial accelerometer-based specific force measurements, $\boldsymbol{f}^b_{\text{IMU}}$

  both interfaced at 1000 Hz.
- Yaw measurements from a triple-redundant gyrocompass solution, ψ_c, at 5 Hz.

The IMU measurements are filtered with a 6th order low-pass Butterworth filter with a cutoff frequency of 5 Hz.

In addition, we use roll (ϕ) and pitch (θ) signals for comparison, obtained from a VRU at 5 Hz, see Tab. 4.1 for specifications from the manufacturer. The specifications of the IMUs installed on the offshore vessel are presented in Tab. 4.2.

Table 4.1: VRU Specification

	Static roll and pitch	**Dynamic roll and pitch**	**Heave**
RMS error	0.02°	0.02°	5 cm or 5%

Table 4.2: IMU specifications from manufacturer

	ADIS16485	**STIM300**
In-run Gyro Rate Bias Stability	6.25 $\frac{\text{deg}}{\text{h}}$	0.5 $\frac{\text{deg}}{\text{h}}$
Angular Random Walk	0.3 $\frac{\text{deg}}{\sqrt{\text{h}}}$	0.15 $\frac{\text{deg}}{\sqrt{\text{h}}}$
In-run Accelerometer Bias Stability	0.032 mg	0.05 mg
Velocity Random Walk	0.023 $\frac{\text{m/s}}{\text{h}}$	0.06 $\frac{\text{m/s}}{\text{h}}$

4.3.3 Effect of sensor biases and mounting errors on the attitude estimation

The IMU sensor biases has a direct effect on the attitude estimates. The gyro bias influences the attitude dynamically, implying that the unit rotates slower or faster than what is physically happening. The accelerometer biases affect the attitude estimation statically. As stated in e.g. (Fossen, 2011, Ch. 11), roll and pitch angles

may be obtained in static conditions using accelerometers or inclinometers,

$$\phi = \tan^{-1}\left(\frac{f^b_{\text{IMU},y}}{f^b_{\text{IMU},z}}\right), \tag{4.13}$$

$$\theta = -\tan^{-1}\left(\frac{f^b_{\text{IMU},x}}{\sqrt{{f^b_{\text{IMU},y}}^2 + {f^b_{\text{IMU},z}}^2}}\right), \tag{4.14}$$

making the initialization of roll and pitch (known as leveling) susceptible to accelerometer biases. Similar to accelerometer bias, mounting errors also contribute to static roll and pitch errors. Tab. 4.3 describe how the different IMU noise and error sources affect the attitude estimation.

Table 4.3: Main error sources effecting the attitude estimation

Error source	Effect on attitude estimate
Gyro bias	Dynamic
Accelerometer bias	Static
Mounting errors	Static
Vibration	Dynamic

Similar to using accelerometers in static condition, also using them as measurement vectors in the attitude estimation of (4.15)–(4.16) may be problematic since the angular rate sensor biases and accelerometer biases are not mutually uniformly observable, (Farrell, 2008, Ch. 11.9). However, in most situations it is the only option to obtain a roll and pitch like reference. The theory of Grip et al. (2012a, 2013) assumes zero accelerometer bias or that it is possible to compensate for it by estimation, subject to an additional persistent excitation requirement. Accelerometer bias compensation for the attitude estimation, using the bias estimate $\bar{\boldsymbol{b}}^b_{\text{acc}}$, can be done statically based on calibration results or by online estimation. In this work we are applying constant accelerometer bias compensation obtained in port, based on the VRU references available, prior to the attitude observer verification scenarios. As presented in Bryne et al. (2016), static accelerometer bias compensation proved successful for at least several days after the initial calibration due to the in-run stable accelerometers available.

4.4 Nonlinear Observers

In this section we will compare two nonlinear attitude observers with Grip et al. (2013); Bryne et al. (2015b) and without Mahony et al. (2008) aiding from a translational motion observer. An overview of the observer structure is presented in Fig. 4.2. Both attitude observers are based on the kinematics of (4.3) and the gyro

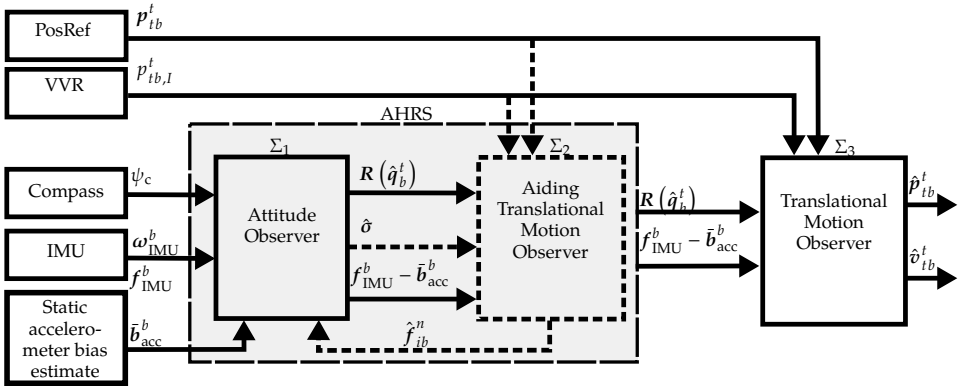

Figure 4.2: Observer structure. Depending on configuration, the attitude and heading reference system (AHRS) may be aided by a TMO, itself aided by PosRefs and VVR measurements.

bias model of (4.12) resulting in the observer equations,

$$\Sigma_1 : \begin{cases} \dot{\hat{\boldsymbol{q}}}_b^t = \frac{1}{2}\hat{\boldsymbol{q}}_b^t \otimes \begin{pmatrix} 0 \\ \hat{\boldsymbol{\omega}}_{ib}^b \end{pmatrix} - \frac{1}{2}\begin{pmatrix} 0 \\ \boldsymbol{\omega}_{it}^t \end{pmatrix} \otimes \hat{\boldsymbol{q}}_b^t, & \text{(4.15a)} \\ \hat{\boldsymbol{\omega}}_{ib}^b = \boldsymbol{\omega}_{\text{IMU}}^b - \hat{\boldsymbol{b}}_{\text{gyro}}^b + \hat{\boldsymbol{\sigma}}_{ib}^b, & \text{(4.15b)} \\ \dot{\hat{\boldsymbol{b}}}_{\text{gyro}}^b = \text{Proj}\left(\hat{\boldsymbol{b}}_{\text{gyro}}^b, -k_I \hat{\boldsymbol{\sigma}}_{ib}^b\right), & \text{(4.15c)} \end{cases}$$

where the gain k_I is associated with the gyro bias estimation, and Proj denotes the gyro bias projection algorithm of Grip et al. (2012a) and the reference therein. The algorithm imposes a bound on $\hat{\boldsymbol{b}}_{\text{gyro}}^b$ to a compact set. The difference between the two observers lies in the injection term, $\hat{\boldsymbol{\sigma}}_{ib}^b$, given as

$$\hat{\boldsymbol{\sigma}}_{ib}^b = k_1 \underline{\boldsymbol{v}}_1^b \times \boldsymbol{R}(\hat{\boldsymbol{q}}_b^t)^\intercal \underline{\boldsymbol{v}}_1^t + k_2 \underline{\boldsymbol{v}}_2^b \times \boldsymbol{R}(\hat{\boldsymbol{q}}_b^t)^\intercal \underline{\boldsymbol{v}}_2^t, \tag{4.16}$$

where $\underline{\boldsymbol{v}}_1^b$ and $\underline{\boldsymbol{v}}_2^b$ are the measurement vectors and $\underline{\boldsymbol{v}}_1^t$ and $\underline{\boldsymbol{v}}_2^t$ are the reference vectors, calculated using

$$\underline{\boldsymbol{v}}_1^b = \underline{\boldsymbol{f}}^b, \quad \underline{\boldsymbol{v}}_2^b = \underline{\boldsymbol{f}}^b \times \underline{\boldsymbol{c}}^b,$$
$$\underline{\boldsymbol{v}}_1^t = \underline{\boldsymbol{f}}^t, \quad \underline{\boldsymbol{v}}_2^t = \underline{\boldsymbol{f}}^t \times \underline{\boldsymbol{c}}^t.$$

An overview of the main differences of NLO A and B can be found in Tab. 4.4. For both, $\underline{\boldsymbol{c}}^b = (\cos(\psi_c), -\sin(\psi_c), 0)^\intercal$ and $\underline{\boldsymbol{c}}^t = (1, 0, 0)^\intercal$ as posed in Bryne et al. (2014). Both $\underline{\boldsymbol{c}}^b$ and $\underline{\boldsymbol{c}}^t$ are naturally normalized. By using normalized measurement/reference vector pairs, the gains k_1 and k_2 can be considered as the NLO's complimentary filter cut-off frequencies. Hence, for motion frequencies higher than k_1 and k_2, the angular rate measurements are the primary source of attitude information, while for frequencies lower than k_1 and k_2, the respective measurement vectors are the primary source of attitude information.

Table 4.4: NLO reference vectors configuration

	Vector $\underline{c}^t$	Vector $\underline{f}^t$
NLO A	Unit vector North	$-\boldsymbol{g}_b^t/\|\|-\boldsymbol{g}_b^t\|\|_2$
NLO B	Unit vector North	$\hat{\boldsymbol{f}}_{ib}^t/\|\|\hat{\boldsymbol{f}}_{ib}^t\|\|_2$ through feedback from VVR and PosRef injection

4.4.1 Nonlinear attitude observer A

For attitude observer A, $\hat{\boldsymbol{\sigma}}_{ib,A}^b$ is implemented with $\underline{f}^b$ and $\underline{f}^t$ based on the injection term of Mahony et al. (2008) choosing

$$\underline{f}^b = \frac{\boldsymbol{f}_{\text{IMU}}^b - \bar{\boldsymbol{b}}_{\text{acc}}^b}{\|\boldsymbol{f}_{\text{IMU}}^b - \bar{\boldsymbol{b}}_{\text{acc}}^b\|_2}, \quad \underline{f}^t = \frac{-\boldsymbol{g}_b^t}{\|-\boldsymbol{g}_b^t\|_2}, \tag{4.17}$$

where the local gravity vector is utilized as reference vector based on the assumption that the specific force in the navigation frame is dominated by $-\boldsymbol{g}_b^t$.

4.4.2 Nonlinear attitude observer B

Regarding attitude observer B, the reference vector $\underline{f}^t$, in the calculation of $\hat{\boldsymbol{\sigma}}_{ib,B}^b$ is chosen as

$$\underline{f}^t = \frac{\text{sat}_{M_f}(\hat{\boldsymbol{f}}_{ib}^t)}{\|\text{sat}_{M_f}(\hat{\boldsymbol{f}}_{ib}^t)\|_2}, \tag{4.18}$$

where $\hat{\boldsymbol{f}}_{ib}^t$ is estimated using a modified version of the feedback-interconnected observer framework Grip et al. (2013), using the translational motion observers (TMO) of Bryne et al. (2014, 2015b), where the VVR aiding concept is applied. Moreover, by providing the specific force estimate $\hat{\boldsymbol{f}}_{ib}^t$, to Σ_1, the attitude estimate is potentially more accurate when the vessel is accelerated than it is when using $-\boldsymbol{g}_b^t$ as reference vector. $\hat{\boldsymbol{f}}_{ib}^t$, provided to attitude observer B, is estimated using the TMO Σ_2 (see Fig. 4.2 and below), which has injection from a PosRef in addition to the VVR measurement. The TMO used to estimate $\hat{\boldsymbol{f}}_{ib}^t$ used by NLO B takes the

form of

$$\Sigma_2 : \begin{cases} \dot{\hat{p}}^t_{tb,I} = \hat{p}^t_{tb,z} + \vartheta K_{p_I p_I} \tilde{p}^t_{tb,I}, & (4.19a) \\ \dot{\hat{\boldsymbol{p}}}^t_{tb} = \hat{\boldsymbol{v}}^t_{tb} \\ \qquad + \vartheta^2 \begin{pmatrix} \mathbf{0}_{2\times 1} \\ K_{pp_I} \end{pmatrix} \tilde{p}^t_{tb,I} + \vartheta \begin{pmatrix} \boldsymbol{K}_{pp} \\ 0 \quad 0 \end{pmatrix} \tilde{\boldsymbol{p}}^t_{tb}, & (4.19b) \\ \dot{\hat{\boldsymbol{v}}}^t_{tb} = -2\boldsymbol{S}(\boldsymbol{\omega}^t_{ie})\boldsymbol{v}^t_{tb} + \hat{\boldsymbol{f}}^t_{ib} + \boldsymbol{g}^t_b \\ \qquad + \vartheta^3 \begin{pmatrix} \mathbf{0}_{2\times 1} \\ K_{vp_I} \end{pmatrix} \tilde{p}^t_{tb,I} + \vartheta^2 \begin{pmatrix} \boldsymbol{K}_{vp} \\ 0 \quad 0 \end{pmatrix} \tilde{\boldsymbol{p}}^t_{tb}, & (4.19c) \\ \dot{\hat{\boldsymbol{\xi}}}^t_{ib} = -\boldsymbol{R}(\hat{\boldsymbol{q}}^t_b)\boldsymbol{S}(\hat{\boldsymbol{\sigma}}^b_{ib}) \left(\boldsymbol{f}^b_{\text{IMU}} - \bar{\boldsymbol{b}}^b_{\text{acc}} \right) \\ \qquad + \vartheta^4 \begin{pmatrix} \mathbf{0}_{2\times 1} \\ K_{\xi p_I} \end{pmatrix} \tilde{p}^t_{tb,I} + \vartheta^3 \begin{pmatrix} \boldsymbol{K}_{\xi p} \\ 0 \quad 0 \end{pmatrix} \tilde{\boldsymbol{p}}^t_{tb}, & (4.19d) \\ \hat{\boldsymbol{f}}^t_{ib} = \boldsymbol{R}(\hat{\boldsymbol{q}}^t_b) \left(\boldsymbol{f}^b_{\text{IMU}} - \bar{\boldsymbol{b}}^b_{\text{acc}} \right) + \hat{\boldsymbol{\xi}}^t_{ib}, & (4.19e) \end{cases}$$

where $\tilde{p}^t_{tb,I} = p^t_{tb,I} - \hat{p}^t_{tb,I}$, $\tilde{\boldsymbol{p}}^t_{tb} = \boldsymbol{p}^t_{\text{GNSS}} - (\hat{p}^t_{tb,x}, \hat{p}^t_{tb,y})^\intercal$. $K_{[\cdot]p_I}$ and $\boldsymbol{K}_{[\cdot]p}$ are fixed gains, while $\vartheta \geq 1$ is a tuning parameter used to guarantee stability. Since the VVR provides $p^t_I = 0$ for all $t \geq 0$, the vertical estimates of Σ_2 are self contained regardless of GNSS precision and accuracy or GNSS position fix. The gains may be chosen such that the feedback interconnection $\Sigma_1 - \Sigma_2$ possesses uniform semiglobal exponential stability (Bryne et al., 2015b).

In state space form, the TMO is represented as:

$$\dot{\hat{\boldsymbol{x}}}_a = \boldsymbol{A}_a \hat{\boldsymbol{x}}_a + \boldsymbol{B}_a \boldsymbol{u}_a + \vartheta \boldsymbol{L}^{-1}_\vartheta \boldsymbol{K}_a \boldsymbol{E}_\vartheta \left(\boldsymbol{y} - \boldsymbol{C}\hat{\boldsymbol{x}}_a \right) + \boldsymbol{D}_a \tag{4.20}$$

with the state-space, measurements and input vectors

$$\begin{aligned} \hat{\boldsymbol{x}}_a &= \left(\hat{p}^t_{tb,I}; \hat{\boldsymbol{p}}^t_{tb}; \hat{\boldsymbol{v}}^t_{tb}; \hat{\boldsymbol{\xi}}^t_{ib} \right), \\ \boldsymbol{y} &= \left(p^n_I; \boldsymbol{p}^t_{\text{GNSS}} \right), \\ \boldsymbol{u} &= \left(\boldsymbol{f}^b_{\text{IMU}} - \bar{\boldsymbol{b}}^b_{\text{acc}}; -\boldsymbol{S}(\hat{\boldsymbol{\sigma}}^b_{ib})(\boldsymbol{f}^b_{\text{IMU}} - \bar{\boldsymbol{b}}^b_{\text{acc}}) \right), \end{aligned}$$

and matrices and vectors,

$$
\begin{aligned}
\boldsymbol{A}_a &= \begin{pmatrix} 0 & \begin{pmatrix} 0 & 0 & 1 \end{pmatrix} & \boldsymbol{0}_{1\times 3} & \boldsymbol{0}_{1\times 3} \\ \boldsymbol{0}_{3\times 1} & \boldsymbol{0}_{3\times 3} & \boldsymbol{I}_3 & \boldsymbol{0}_{3\times 3} \\ \boldsymbol{0}_{3\times 1} & \boldsymbol{0}_{3\times 3} & \boldsymbol{0}_{3\times 3} & \boldsymbol{I}_3 \\ \boldsymbol{0}_{3\times 1} & \boldsymbol{0}_{3\times 3} & \boldsymbol{0}_{3\times 3} & \boldsymbol{0}_{3\times 3} \end{pmatrix}, \\
\boldsymbol{B}_a &= \begin{pmatrix} \boldsymbol{0}_{1\times 3} & \boldsymbol{0}_{1\times 3} \\ \boldsymbol{0}_{3\times 3} & \boldsymbol{0}_{3\times 3} \\ \boldsymbol{R}(\hat{\boldsymbol{q}}_b^t) & \boldsymbol{0}_{3\times 3} \\ \boldsymbol{0}_{3\times 3} & \boldsymbol{R}(\hat{\boldsymbol{q}}_b^t) \end{pmatrix}, \\
\boldsymbol{C}_a &= \begin{pmatrix} \boldsymbol{I}_3 & \boldsymbol{0}_{3\times 7} \end{pmatrix}, \\
\boldsymbol{D}_a &= \begin{pmatrix} 0; & \boldsymbol{0}_{3\times 1}; & -2\boldsymbol{S}(\boldsymbol{\omega}_{ie}^t)\boldsymbol{v}_{tb}^t + \boldsymbol{g}_b^t; & \boldsymbol{0}_{3\times 1} \end{pmatrix}, \\
\boldsymbol{K}_a &= \begin{pmatrix} K_{p_I p_I} & \boldsymbol{0}_{1\times 2} \\ \boldsymbol{0}_{2\times 1} & \boldsymbol{K}_{pp} \\ K_{pp_I} & \boldsymbol{0}_{1\times 2} \\ \boldsymbol{0}_{2\times 1} & \boldsymbol{K}_{vp} \\ K_{vp_I} & \boldsymbol{0}_{1\times 2} \\ \boldsymbol{0}_{2\times 1} & \boldsymbol{K}_{\xi p} \\ K_{\xi p_I} & \boldsymbol{0}_{1\times 2} \end{pmatrix}, \\
\boldsymbol{L}_\vartheta &= \text{blockdiag}\left(1, \frac{1}{\vartheta}\boldsymbol{I}_3, \frac{1}{\vartheta^2}\boldsymbol{I}_3, \frac{1}{\vartheta^3}\boldsymbol{I}_3\right), \\
\boldsymbol{E}_\vartheta &= \boldsymbol{C}_a \boldsymbol{L}_\vartheta \boldsymbol{C}_a^\dagger,
\end{aligned}
$$

where $\boldsymbol{E}_\vartheta$ satisfies $\boldsymbol{E}_\vartheta \boldsymbol{C}_a = \boldsymbol{C}_a \boldsymbol{L}_\vartheta$ such that the semiglobal exponential stability follows from Bryne et al. (2014).

4.4.3 Translational motion observer

Even though the gyro and accelerometer biases are not mutually uniformly observable, (Farrell, 2008, Ch. 11.9), without the vessel accelerating and rotating, some accelerometer bias compensation has to be performed in order to obtain an INS with reasonable DR capabilities. For $\Sigma_1 - \Sigma_2$, a fixed pre-compensated accelerometer bias $\bar{\boldsymbol{b}}_{\text{acc}}^b$ is applied for attitude estimation. However, some accelerometer errors may be present owing to some in-run bias instability, w.r.t. Tab. 4.2. To atone for this, we create a new TMO including an estimate of the residual accelerometer bias $\hat{\boldsymbol{b}}_{\text{acc}}^b$, inspired by the observer of (Fossen, 2011, Ch. 11.5.1). Observer Σ_3 for additional accelerometer bias estimation can be described as follows:

$$
\dot{\hat{\boldsymbol{x}}} = \boldsymbol{A}\hat{\boldsymbol{x}} + \boldsymbol{B}\boldsymbol{u} + \boldsymbol{K}\left(\boldsymbol{y} - \boldsymbol{C}\hat{\boldsymbol{x}}\right) + \boldsymbol{D} \tag{4.21}
$$

with $\hat{\boldsymbol{x}} = \left(p^t_{tb,I}; \hat{\boldsymbol{p}}^t_{tb}; \hat{\boldsymbol{v}}^t_{tb}; \hat{\boldsymbol{b}}^b_{\text{acc}}\right)$,
$\boldsymbol{y} = \left(p^n_I; \boldsymbol{p}^t_{\text{GNSS}}\right)$ and $\boldsymbol{u} = \boldsymbol{f}^b_{\text{IMU}} - \bar{\boldsymbol{b}}^b_{\text{acc}}$, resulting in

$$\boldsymbol{A} = \begin{pmatrix} 0 & \begin{pmatrix} 0 & 0 & 1 \end{pmatrix} & \boldsymbol{0}_{1\times3} & \boldsymbol{0}_{1\times3} \\ \boldsymbol{0}_{3\times1} & \boldsymbol{0}_{3\times3} & \boldsymbol{I}_3 & \boldsymbol{0}_{3\times3} \\ \boldsymbol{0}_{3\times1} & \boldsymbol{0}_{3\times3} & \boldsymbol{0}_{3\times3} & -\boldsymbol{R}(\hat{\boldsymbol{q}}^t_b) \\ \boldsymbol{0}_{3\times1} & \boldsymbol{0}_{3\times3} & \boldsymbol{0}_{3\times3} & \boldsymbol{0}_{3\times3} \end{pmatrix},$$

$$\boldsymbol{B} = \begin{pmatrix} \boldsymbol{0}_{1\times3} \\ \boldsymbol{0}_{3\times3} \\ \boldsymbol{R}(\hat{\boldsymbol{q}}^t_b) \\ \boldsymbol{0}_{3\times3} \end{pmatrix},$$

$$\boldsymbol{C} = \begin{pmatrix} \boldsymbol{I}_3 & \boldsymbol{0}_{3\times7} \end{pmatrix},$$

$$\boldsymbol{D} = \begin{pmatrix} 0; & \boldsymbol{0}_{3\times1}; & -2\boldsymbol{S}(\boldsymbol{\omega}^t_{ie})\boldsymbol{v}^t_{tb} + \boldsymbol{g}^t_b; & \boldsymbol{0}_{3\times1} \end{pmatrix},$$

Considering $\boldsymbol{R}(\hat{\boldsymbol{q}}^t_b)$ as an external signal to Σ_3, $\boldsymbol{A}$ is treated as time-varying and the TMO's error dynamics is rendered exponentially stable by employing a Riccati-equation and gain similar to the Kalman-Bucy filter Kalman and Bucy (1961),

$$\boldsymbol{K} = \boldsymbol{P}\boldsymbol{C}^\intercal \boldsymbol{R}^{-1}, \tag{4.22}$$

$$\dot{\boldsymbol{P}} = \boldsymbol{A}\boldsymbol{P} + \boldsymbol{P}\boldsymbol{A}^\intercal - \boldsymbol{K}\boldsymbol{R}\boldsymbol{K}^\intercal + \boldsymbol{G}\boldsymbol{Q}\boldsymbol{G}. \tag{4.23}$$

$\boldsymbol{Q}$ and $\boldsymbol{R}$ are covariance matrices chosen according to sensor noise and desired tuning, see Section 4.5. Furthermore,

$$\boldsymbol{G} = \begin{pmatrix} \boldsymbol{0}_{1\times3} & \boldsymbol{0}_{1\times3} \\ \boldsymbol{0}_{3\times3} & \boldsymbol{0}_{3\times3} \\ \boldsymbol{R}(\hat{\boldsymbol{q}}^t_b) & \boldsymbol{0}_{3\times3} \\ \boldsymbol{0}_{3\times3} & \boldsymbol{I}_3 \end{pmatrix}, \tag{4.24}$$

such that the process noise associated with the accelerometer in $\boldsymbol{Q}$ is related to the navigation frame, $\{t\}$, through $\boldsymbol{R}(\hat{\boldsymbol{q}}^t_b)$. The actual implementation of the observer is done in discrete time, as in for instance Bryne et al. (2017a), using the discrete time versions of the Riccati equation and Kalman gain.

4.5 Observer tuning

For Σ_1 we used the gains $k_1 = 0.1, k_2 = 0.1, k_I = 0.05$.

For Σ_2, the parameter $\vartheta = 1$ was chosen. For the gains $K_{[\cdot]p_I}$ and $\boldsymbol{K}_{[\cdot]p}$, we employed the continuous-time steady-state Riccati equation, similar to the Kalman-Bucy filter Kalman and Bucy (1961), and akin to Σ_3,

$$\begin{aligned} \boldsymbol{K}_a &= \boldsymbol{P}_{a,\infty}\boldsymbol{C}_a^\intercal \boldsymbol{R}_a^{-1} \\ \boldsymbol{0} &= \boldsymbol{A}_a\boldsymbol{P}_{a,\infty} + \boldsymbol{P}_{a,\infty}\boldsymbol{A}_a - \boldsymbol{K}_a\boldsymbol{R}_a\boldsymbol{K}_a^\intercal + \boldsymbol{B}_a\boldsymbol{Q}_a\boldsymbol{B}_a \end{aligned}$$

using the following covariance matrices for process and measurement noise

$$\begin{aligned}\boldsymbol{Q}_a &= \text{blockdiag}(0.1^2\boldsymbol{I}_3, 0.15^2\boldsymbol{I}_3),\\ \boldsymbol{R}_a &= \text{diag}(35^2, 2^2\boldsymbol{I}_2),\end{aligned}$$

where the first element of $\boldsymbol{Q}_a$ is the variance associated with the input $\boldsymbol{f}^b_{\text{IMU}}$, and the second element is associated with the cross product of $\hat{\boldsymbol{\sigma}}$ and $\boldsymbol{f}^b_{\text{IMU}}$ as seen in (4.19d). The first element of $\boldsymbol{R}_a$ is a value representing VVR measurement uncertainty, and the second element is the GNSS horizontal measurement variance. This results in the following gains:

$$\begin{aligned}K_{p_I p_I} &= 0.6368,\\ K_{pp_I} &= 0.2028, \boldsymbol{K}_{pp} = 0.7950\boldsymbol{I}_2,\\ K_{vp_I} &= 0.0378, \boldsymbol{K}_{vp} = 0.3160\boldsymbol{I}_2,\\ K_{\xi p_I} &= 0.0035, \boldsymbol{K}_{\xi p} = 0.0612\boldsymbol{I}_2.\end{aligned}$$

For Σ_3 we chose the following covariance matrices to go with the Riccati equation:

$$\begin{aligned}\boldsymbol{Q} &= \text{blockdiag}(0.1^2\boldsymbol{I}_3, 0.001^2\boldsymbol{I}_3).\\ \boldsymbol{R} &= \text{diag}(20^2, 2^2\boldsymbol{I}_2).\end{aligned}$$

As for Σ_2, the first element of $\boldsymbol{Q}$ is the variance associated with $\boldsymbol{f}^b_{\text{IMU}}$, but the second element is the process noise of the $\hat{\boldsymbol{b}}^b_{\text{acc}}$ state. $\boldsymbol{R}$ represents exactly the same as $\boldsymbol{R}_a$, albeit tuned a bit differently for the VVR measurement.

All matrices are tuned in continuous time, and then converted to discrete time equivalents in the actual implementation, see for instance Bryne et al. (2017a) for methods for discretization.

4.6 Full-scale testing: Attitude estimation

In this section, we present the results of the attitude estimation using two distinct attitude observers and two particular MEMS IMUs, during two different operations undertaken by the offshore vessel. The first operation is station keeping during DP. The second is a maneuvering operation, where the vessel changes heading while surging forward. Plots of the respective path tracks over two hours are shown in Fig. 4.3. The attitude estimation is evaluated using the mean error, root-mean-square error (RMSE) and cumulative absolute error (CAE) metrics, using the onboard VRU and gyrocompass as reference. Also, a comparison with the output of NavLab Gade (2004) is provided. NavLab is a navigation software suite based on the Extended Kalman Filter, and has been applied in industry and defense on a wide range of systems, maritime and otherwise. The metrics for all estimators were evaluated for the last 90 minutes of the data set.

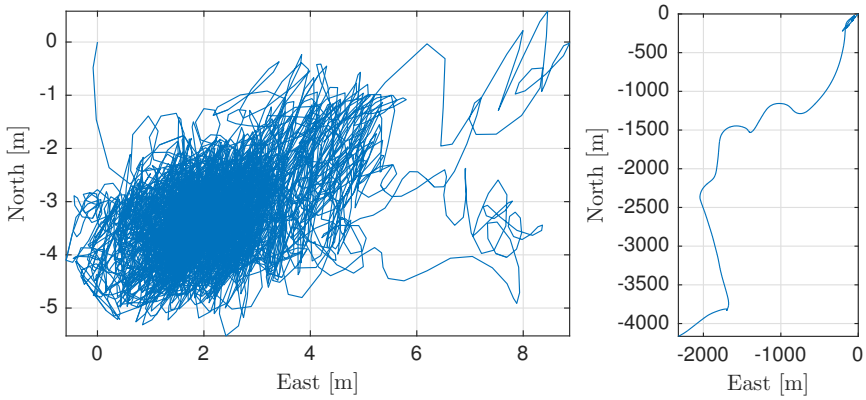

(a) Dynamic Positioning (b) Turning

Figure 4.3: Two operational situations used to evaluate the attitude estimation performance. The path track is obtained from the on-board GNSS.

Table 4.5: Attitude error statistics using NLO A in DP

	ADIS16485	**STIM300**
Roll mean error [deg]	0.0036	0.0003
Pitch mean error [deg]	0.0090	0.0070
Roll RMSE [deg]	0.1113	0.1151
Pitch RMSE [deg]	0.1080	0.1071
Roll CAE [deg]	2361.8	2442.7
Pitch CAE [deg]	2254.9	2239.7

4.6.1 DP

An excerpt of the attitude estimates obtained using the STIM300 IMU and NLO B in DP is shown in Fig. 4.4a. The estimation errors relative the VRU and gyrocompass measurements over two hours are shown in Fig. 4.4b. The statistics obtained using NLO A as attitude estimator in DP are presented in Tab. 4.5. Similar statistics obtained using NLO B and NavLab, are presented in Tab. 4.6 and 4.7

Results

From Tabs. 4.5–4.7 one can see that the choice of estimator to perform the attitude estimation in DP is more important than the choice of sensor, atleast when it comes to our selection of IMUs. It is evident from the results that both the RMSE and CAE is improved using NLO B and NavLab compared to the results obtained with NLO A. This is particularly noticeable in roll. The mean errors are approximately

Table 4.6: Attitude error statistics using NLO B in DP

	ADIS16485	**STIM300**
Roll mean error [deg]	-0.0007	-0.0044
Pitch mean error [deg]	0.0047	0.0016
Roll RMSE [deg]	0.0363	0.0299
Pitch RMSE [deg]	0.0670	0.0649
Roll CAE [deg]	759.80	628.99
Pitch CAE [deg]	1406.0	1357.5

Table 4.7: Attitude error statistics using Navlab in DP.

	ADIS16485	**STIM300**
Roll mean error [deg]	-0.0193	-0.0094
Pitch mean error [deg]	0.0463	0.0063
Roll RMSE [deg]	0.0417	0.0287
Pitch RMSE [deg]	0.0813	0.0628
Roll CAE [deg]	881.89	610.79
Pitch CAE [deg]	1731.1	1233.3

the same, where the differences are on such a scale that the practical effects of such errors, for instance in lever arm compensation, are negligible. For NavLab, larger differences are observed between the IMUs than is the case for the NLOs. This could mean that the tuning of NavLab is more sensitive to sensor changes.

4.6.2 Maneuvering

The statistics obtained using attitude NLO A during the turning maneuvers are presented in Tab. 4.8. Similar statistics obtained using NLO B and NavLab are presented in Tab. 4.9 and in Tab. 4.10, respectively.

Results

Comparable results to what were obtained in DP, are achieved during the maneuvers as shown in Tabs. 4.8–4.10. NLO B and NavLab outperforms NLO A considering RMSE and CAE in roll and pitch, but not as much as in the DP case. As opposed to the DP case, NavLab yielded virtually no difference in output between the two sensors.

Table 4.8: Attitude error statistics using NLO A during turning maneuvers

	ADIS16485	**STIM300**
Roll mean error [deg]	-0.0089	-0.0134
Pitch mean error [deg]	-0.0245	-0.0041
Roll RMSE [deg]	0.1102	0.1122
Pitch RMSE [deg]	0.1161	0.1139
Roll CAE [deg]	2442.6	2484.0
Pitch CAE [deg]	2638.6	2582.6

Table 4.9: Attitude error statistics using NLO B during turning maneuvers

	ADIS16485	**STIM300**
Roll mean error [deg]	-0.008	-0.0115
Pitch mean error [deg]	-0.0188	0.0022
Roll RMSE [deg]	0.0870	0.0848
Pitch RMSE [deg]	0.1113	0.1193
Roll CAE [deg]	1636.3	1575.8
Pitch CAE [deg]	2446.2	2500.2

Table 4.10: Attitude error statistics using Navlab during turning maneuvers

	ADIS16485	**STIM300**
Roll mean error [deg]	-0.0345	-0.0301
Pitch mean error [deg]	0.0311	0.0081
Roll RMSE [deg]	0.0847	0.0817
Pitch RMSE [deg]	0.1078	0.1154
Roll CAE [deg]	1613.3	1433.3
Pitch CAE [deg]	2135.6	2123.5

4.6.3 High-speed turning

We do not generate statistics for yaw estimation error, as this is somewhat meaningless exercise considering that the gyrocompass, which is our only reference for heading, is also aiding our attitude observers. However, Fig. 4.5 illustrates what happens during a sharp turn. The estimation error increases, most likely because of the IMU gyro's greater dynamic range compared to that of the mechanical gyrocompass.

4.6.4 Discussion

The results obtained during the two vessel operations gave approximately similar results for both IMUs. The two different NLOs however provided varied results when compared to the onboard VRUs. Since injection from the respective accelerometers and the gyrocompass heading were enabled during the entire test, the mean attitude estimation error is primarily dependent on the vector measurement/reference pairs. Signals with frequencies below the NLO's internal cut-off frequencies, k_1 and k_2, affects the attitude estimates through the measurement vectors. Hence, the mean error over time is dependent on measurement vector sensor bias, not the angular rate measurement biases. Since both IMUs gave approximately the same performance, one can assume that the accelerometer biases are highly in-run stable in the environment they were located, considering that is was three days between the end of the bias compensation done in port and the beginning of the second vessel operation presented.

During both test cases, the attitude estimation errors compared to the VRU were smaller using NLO B, compared to using NLO A, particularly in roll. The latter NLO has a static specific force injection, (see Sec. 4.4 and Tab. 4.4) using $-\boldsymbol{g}_b^t$ as reference vector. $-\boldsymbol{g}_b^t$ is not equal to $\boldsymbol{f}_{ib}^t$, even in DP, due to the wave-induced motions of the vessel. The positive effect of using $\hat{\boldsymbol{f}}_{ib}^t$ as reference vector is considerable, as expected from the results of Bryne et al. (2015b), due to the kinematic coupling between roll, pitch and heave obtained using VVR as vertical reference in TMO Σ_2. The performance of NLO B was comparable to what we achieved with NavLab. In contrast to the Kalman filter, the NLOs used here are not designed with optimality in mind, as in minimum variance, but rather stability and guarantees of convergence. Still, we managed to get similar stationary performance for attitude estimation compared to an EKF-based solution of NavLab. This reaffirms previous results on GNSS/INS-integration using NLOs Grip et al. (2015).

When turning, larger yaw errors can be observed compared to when the ship is in station keeping. Fig. 4.5 shows an example of NLO yaw estimate and error during a sharp turn with high forward speed. The estimate from the NLO starts leading the gyrocompass quite a bit, but is ultimately "corrected" because of aiding. This is due to the slow dynamics of the gyrocompass during sharp turns, such that the angular rate measurements from the IMUs about the BODY z-axis is the primary source of yaw information for turns with rate faster than k_2. Hence, larger discrepancies between the NLOs and the gyrocompass is expected in dynamic conditions, underlining that the MEMS IMU is more capable of capturing this motion than the traditional gyrocompass.

It should also be emphasized that we compared the NLOs' performance to the VRU's equivalent signals and not to absolute truth, revisit Tab. 4.1 for the VRU specifications. Hence, there may exist situations where the NLOs provide more accurate estimates than the VRU.

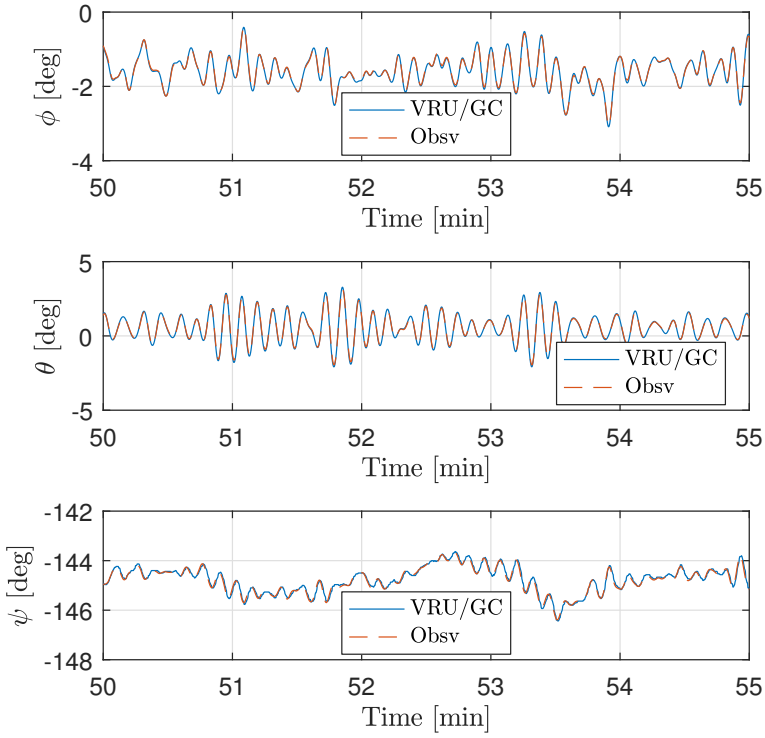

(a) Attitude estimates.

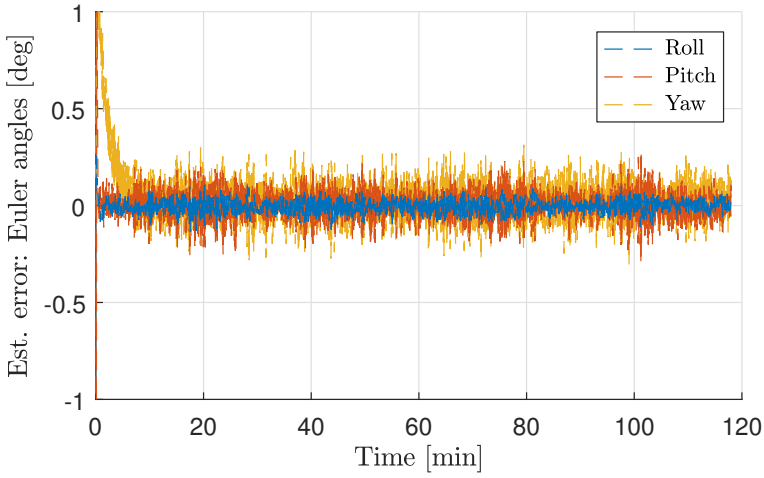

(b) Attitude estimation error.

Figure 4.4: Heading estimation in high-speed turning using gyrocompass as aiding

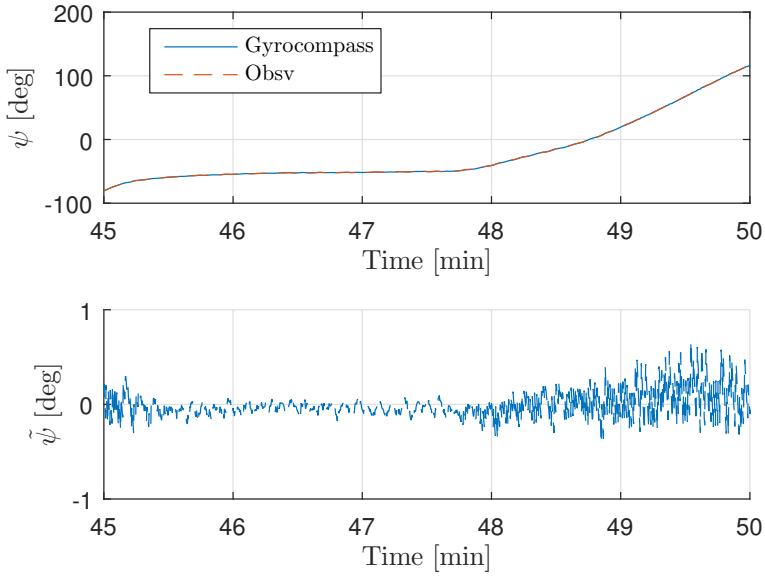

(a) Yaw estimation and estimation error.

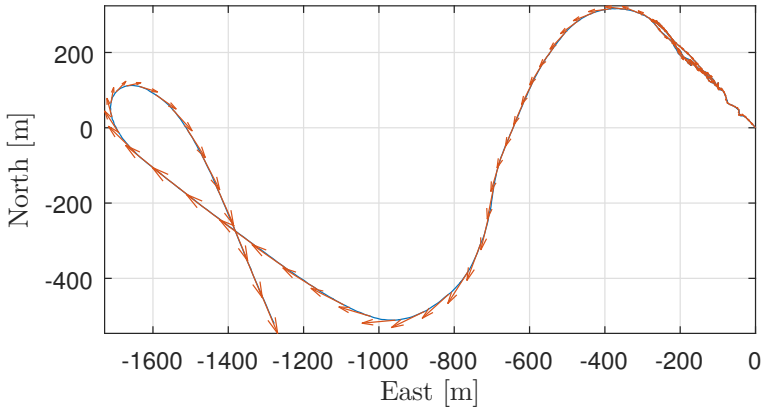

(b) XY plot. Arrows indicate velocity.

Figure 4.5: Heading estimation in high-speed turning using gyrocompass as aiding

4.7 Full-scale testing: Heave

4.7.1 DP

A selection of the heave estimates obtained using the STIM300 and Σ_2 and Σ_3 is shown in Fig. 4.6. The heave estimation error statistics obtained using the same

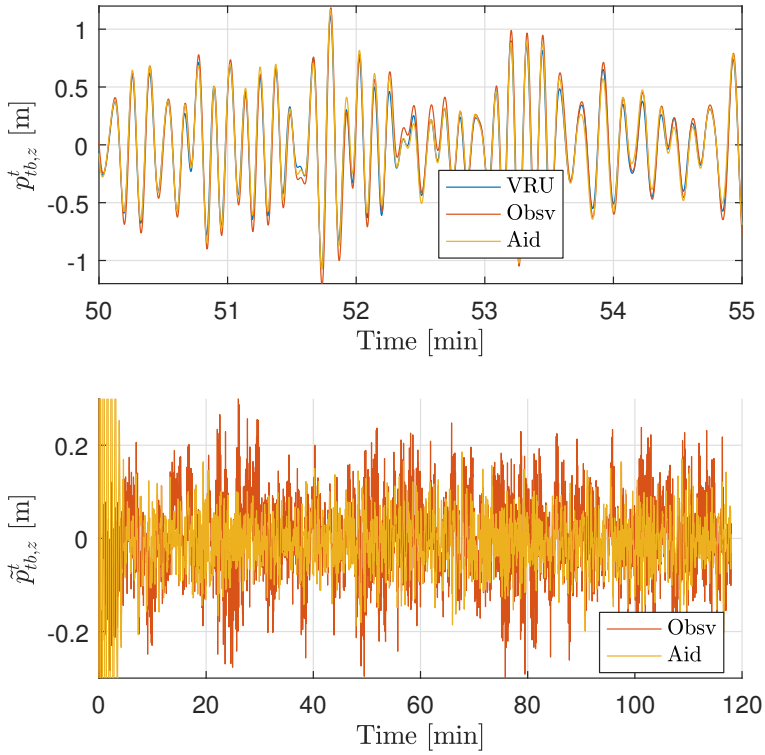

Figure 4.6: Heave estimation and error in DP using Σ_2 (yellow) and Σ_3 (red) vs. the onboard VRU (blue)

observers are presented in Tabs. 4.11–4.12.

Table 4.11: Heave error statistics using Σ_2 in DP

	ADIS16485	**STIM300**
Mean heave error [cm]	-0.6511	-0.6005
RMSE heave [cm]	5.7766	10.523
CAE heave [m]	1215.0	2207.3

Table 4.12: Heave error statistics using Σ_3 in DP

	ADIS16485	**STIM300**
Mean heave error [cm]	0.2288	0.1339
RMSE heave [cm]	8.0644	10.274
CAE heave [m]	1706.2	2112.6

Table 4.13: Heave error statistics using Σ_2 during turning maneuvers

	ADIS16485	**STIM300**
Mean heave error [cm]	-0.2982	-0.2689
RMSE heave [cm]	6.3318	9.8799
CAE heave [m]	1462.5	2275.0

Table 4.14: Heave error statistics using Σ_3 during turning maneuvers

	ADIS16485	**STIM300**
Mean heave error [cm]	0.3831	0.7008
RMSE heave [cm]	8.5277	12.308
CAE heave [m]	1907.4	2699.1

4.7.2 Maneuvering

The heave estimation error statistics obtained during the turning maneuvers using the Σ_2 and Σ_3 are presented in Tab. 4.13 and Tab. 4.14, respectively.

4.7.3 Discussion

Considering the heave estimation performance, this appears to be better when using the ADIS16485 as IMU. Between Σ_2 and Σ_3, there appears to be some differences in favor of Σ_2. While the attitude estimates showed practically no difference between the IMUs, the use of ADIS16485 gave better heave estimates than obtained with STIM300, with the method used. This might be due to the ADIS16485's accelerometer having better velocity-random walk characteristics than the STIM300. Also, it should be mentioned that the STIM300 unit provided by Sensonor, is an engineering sample. Such units are made for testing and do not necessarily fulfill all of the specifications in the datasheet under all environmental conditions. Therefore, we cannot guarantee that the results obtained is representative for a commercially available STIM300. Generally for the heave estimation results, they might be improved with a tuning emphasizing heave specifically, or using alternative algorithms, such as in Bryne et al. (nd).

4.8 Full-scale testing of DR capability in DP with MEMS IMUs

In this section, the evaluation of the DR properties in light of fault detection using the ADIS16485 and STIM300 is presented. The DR performance evaluation is carried out with data collected in a DP operation whose GNSS track is shown in Fig. 4.3a.

First, the heading DR performance when using the IMUs available is discussed, and illustrated with an example. Then, the position DR performance during the particular DP operation is evaluated, applying both IMUs and NLO A with Σ_3. The resulting DR statistics are based on a collection of estimation runs.

4.8.1 Heading angle DR capabilities

The heading angle DR capabilities using the IMUs available were found to be in compliance with the IMUs' angular rate specifications, presented in Tab. 4.2. A total of 60 one-hour-long heading DR evolutions of the absolute yaw angle error

$$|\tilde{\psi}| = |\psi_c - \hat{\psi}|, \tag{4.25}$$

compared to the ship gyrocompass measurements for both sensors, are shown in Fig. 4.7. The DR was carried out with NLO B, by disabling the observer injection from the gyrocompass by setting $k_2 = 0$, after an observer initialization time of 15 minutes. In addition, the average DR error, of the 60 runs, is highlighted in Fig. 4.7. Examples of typical angular rate bias estimates are shown in Fig. 4.8, exhibiting that the STIM300's biases are more stable than those of the ADIS16485.

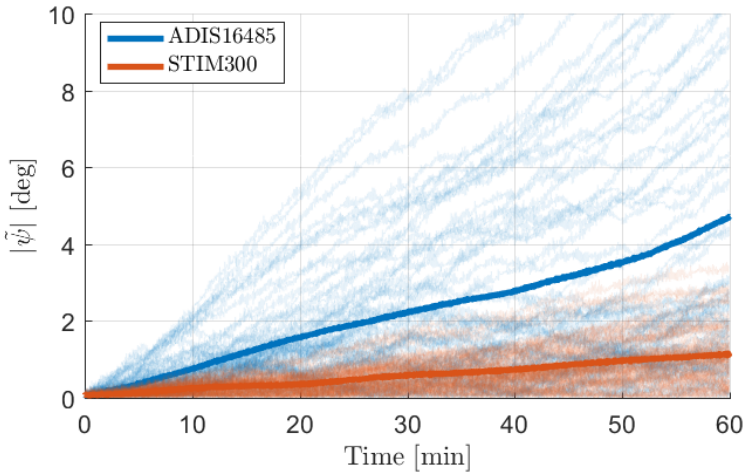

Figure 4.7: DR performance in yaw obtained using the ADIS16485 and STIM300 IMUs. Highlighted evolution indicates average DR error.

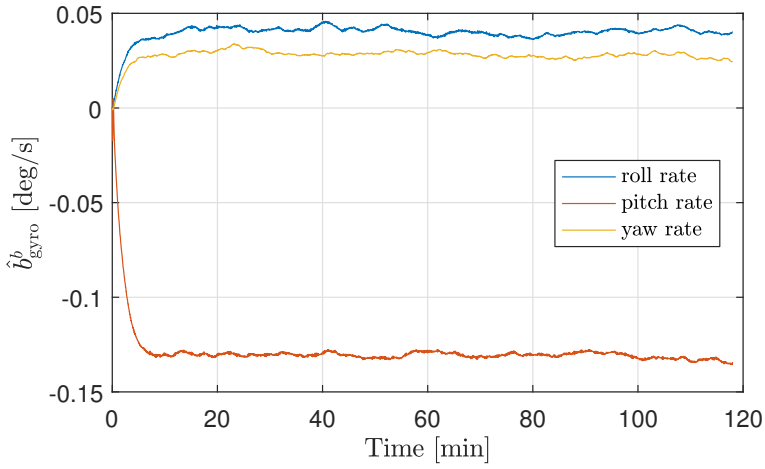

(a) Typical angular rate bias estimates of the ADIS16485.

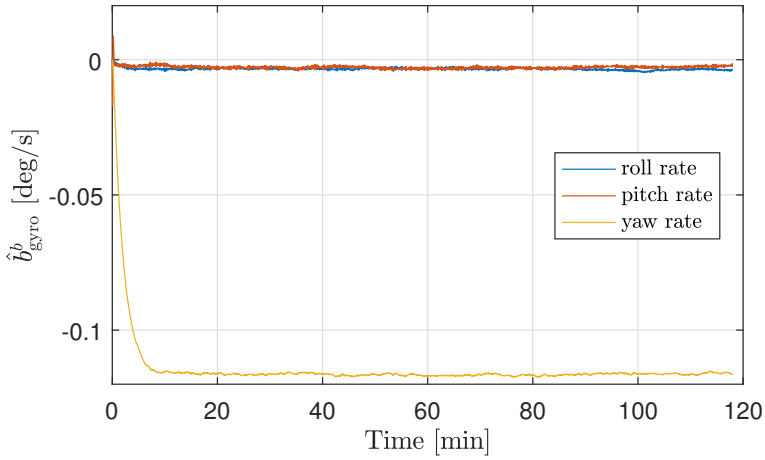

(b) Typical angular rate bias estimates of the STIM300.

Figure 4.8: Angular rate bias estimates.

4.8.2 Position DR capabilities

Evaluation of the DR capabilities in position is similar yet more elaborate than for heading since the theoretical growth of errors are a combination of higher order terms, (Groves, 2013, Ch. 5.7), as opposed to linear growth for heading. In order to obtain statistically significant results related to the position drift while performing DR, each combination of IMU and NLO was evaluated 60 times (using different data sets) by comparing the DR errors accumulated when disabling GNSS feedback at selected intervals. The DR evaluation is done by taking the norm of the difference between the horizontal components of $\boldsymbol{p}^t_{\text{GNSS}}$ and $\hat{\boldsymbol{p}}^t_{\text{GNSS}}$, defined

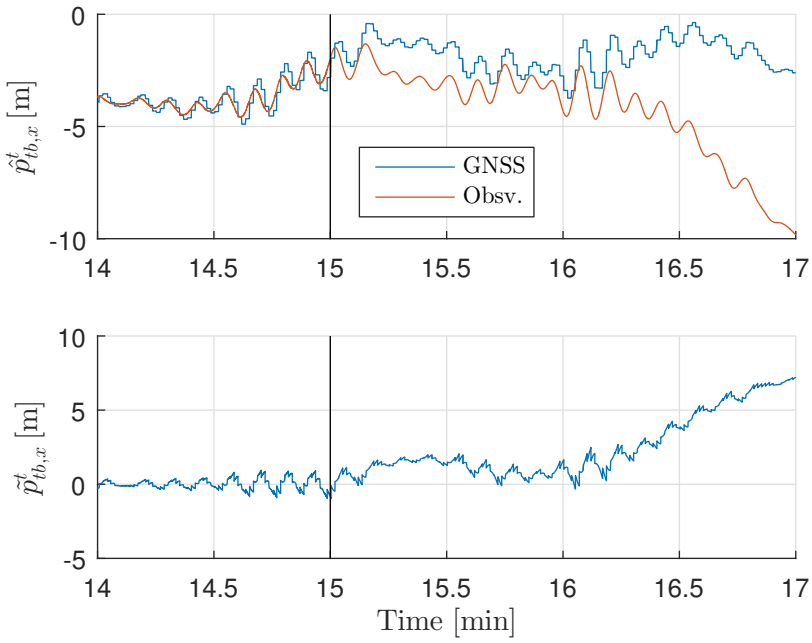

Figure 4.9: Example of DR run with prior bias estimation, where feedback from GNSS is cut after 15 minutes (indicated by vertical line)

$\tilde{\boldsymbol{p}}^t_{\text{GNSS}} := \boldsymbol{p}^t_{\text{GNSS}} - \hat{\boldsymbol{p}}^t_{\text{GNSS}}$ where,

$$\hat{\boldsymbol{p}}^t_{\text{GNSS}} = \hat{\boldsymbol{p}}^t_{tb} + \boldsymbol{R}(\hat{\boldsymbol{q}}^t_b)\boldsymbol{r}^b_b, \tag{4.26}$$

and where $\boldsymbol{r}^b_b$ is the lever arm from the IMU to the GNSS antenna position such that

$$\begin{aligned} \|\tilde{\boldsymbol{p}}^t_{\text{GNSS}}\|_2 &= \|\boldsymbol{p}^t_{tb} + \boldsymbol{R}^t_b\boldsymbol{r}^b_b - \hat{\boldsymbol{p}}^t_{tb} - \boldsymbol{R}(\hat{\boldsymbol{q}}^t_b)\boldsymbol{r}^b_b\|_2, \\ &= \|\tilde{\boldsymbol{p}}_{tb} + \left(\boldsymbol{R}^t_b - \boldsymbol{R}(\hat{\boldsymbol{q}}^t_b)\right)\boldsymbol{r}^b_b\|_2. \end{aligned} \tag{4.27}$$

For position DR, only NLO A is to be considered. This is because of NLO B's dependency on PosRef for improving attitude estimates. In a dead reckoning case, one would have to cut the feedback interconnection and use the same reference vector as for NLO A, effectively making the NLOs the same. For the dead reckoning test, an accelerometer bias average estimate based on the last minute of the $\hat{\boldsymbol{b}}^b_{\text{acc}}$ state is used. This is to account for any short term fluctuations of the accelerometer bias and GNSS imprecisions. The same could be achieved by tuning the matrices $\boldsymbol{Q}$ and $\boldsymbol{R}$ differently, at the expense of estimator convergence time. Fig. 4.9 displays an example of a DR run with ADIS16485. The position estimate starts drifting immediately after feedback is cut at $t = 15$ min. Fig. 4.10 shows the aggregated

Table 4.15: Position DR error statistics

	ADIS16485	**STIM300**
Mean error [m] 1 min	4.3014	3.2885
Mean error [m] 5 min	35.125	25.762
Mean error [m] 10 min	102.12	83.927
Min error [m] after 10 min	11.639	3.0962
Max error [m] after 10 min	264.03	231.74
RMSE [m] after 10 min	115.74	96.141

Table 4.16: Position DR error statistics without accelerometer bias estimation

	ADIS16485	**STIM300**
Mean error [m] 1 min	4.6148	3.9820
Mean error [m] 5 min	54.037	56.2560
Mean error [m] 10 min	211.89	218.51
Min error [m] after 10 min	76.464	120.83
Max error [m] after 10 min	359.18	362.18
RMSE [m] after 10 min	220.24	224.94

Table 4.17: Position DR error statistics without filtering IMU data

	ADIS16485	**STIM300**
Mean error [m] 1 min	4.7580	4.3560
Mean error [m] 5 min	38.588	44.631
Mean error [m] 10 min	112.07	139.51
Min error [m] after 10 min	4.1972	26.919
Max error [m] after 10 min	244.97	350.30
RMSE [m] after 10 min	125.25	159.93

drift errors over 10 minutes, after PosRef injection is disabled, applying NLO A and Σ_3 for both the ADIS16485 and the STIM300 IMU.

The statistical results based on the 60 DR runs are presented in Tab. 4.15. Results for the DR without the residual bias estimation in Σ_3 is presented in Fig. 4.11 and Tab. 4.16. Finally, results for the unfiltered IMUs are shown in Tab. 4.17.

4.8.3 Discussions

Heading DR

It is evident, with regards to Fig. 4.8, that the gyro bias estimates using the STIM300 is smoother and more in-run stable than those found using the ADIS16485, result-

ing in the performance difference seen in Fig. 4.7. This is in compliance with the sensor specifications presented in Tab. 4.2. The asymptotic angular rate bias estimation performances seen in Fig. 4.8, is representative of what is seen from run to run.

Position DR

As seen from Tab. 4.15 and Fig. 4.10, one of the main conclusions from the six times 60 DR runs performed over the data sets collected during DP is that using the STIM300 results in better DR performance than using the ADIS16485. Interestingly enough, for the unfiltered data of Tab. 4.17 the opposite conclusion is reached. According to specifications, the ADIS16485 has the better accelerometer, while the STIM300 contains a superior angular rate sensor. One could speculate that by removing the white noise of the accelerometer through filtering, the errors induced by angular rate sensors become more important. In any case, from looking at the results of Tab. 4.16 and Fig. 4.11 one can see that estimating the accelerometer biases as in (4.21) clearly works.

The results indicate a large spread of DR errors over 10 minutes, and this might be due to noise, mechanical disturbance such as vibration, or insufficient tuning of the observers. Time synchronization of signals is also an issue, as the GNSS and gyrocompasse signals were acquired from a system separate from the IMUs' signal acquisition, with an unknown, albeit small, delay.

Considering the quality of the results obtained compared to the results in Paturel (2004), using either of the two MEMS-based IMUs available in this work gave worse results than in Paturel (2004) where an INS with a FOG gyro was applied. In the results presented in Paturel (2004), a position accuracy during GNSS outage stayed within GNSS accuracy for a period exceeding two and a half minutes. The mean position drift after a 50 seconds GNSS outage was less than half a meter. These results are considerably better than the approximately 3-5 meters error obtained after one minute DR for both MEMS IMUs. However, in Paturel (2004) only 10 runs are presented, making a definite statistical comparison difficult due to the few DR trajectories presented. The FOG-based INS product in question is currently advertised to have a 20 m error with a 50 % circular error probability after five minutes of unaided navigation, whereas we obtain approximately 25 meters averaged error in the same time frame for STIM300.

As depicted in Fig. 4.10, a MEMS-based INS may provide relatively stable position estimates (around four meters error) for half a minute, without PosRef injection. From a fault-tolerance perspective, such as Rogne et al. (2016b) and Chapters 6–7, the results obtained here indicate what kind of PosRef errors one might detect based on MEMS IMUs. For instance a PosRef drift of 10 centimeters per second results in a PosRef error of 3 meters after half a minute, which might be possible to detect with the results obtained, considering the average DR error is two meters with either of the two IMUs. Moreover, in the situation of PosRef failure

during DP, if four meters is an acceptable error margin, 30 seconds is available to the DP operator to decide whether the operation should be aborted or not. This might be sufficient time for PosRef recovery e.g. if tracking is reestablished with one or more satellites, resulting in a complete GNSS solution.

The DR performance is not only dependent on the sensor biases, but also on the velocity-random walk and the sensed vibrations on the ship. Integrating these over time, results in a large error even when averaging them out using high-rate integration (1000 Hz). Regarding tuning, more emphasis on tuning for a DR application may accomplish better results. Here, the tuning is geared towards attaining the smallest errors in attitude and heave compared to the onboard VRU. Also, time-synchronization errors between our IMUs and the on-board GNSS may result in small errors in velocity and specific force at the time of disabling GNSS injection, resulting in a steeper error slope than otherwise obtained if the position and inertial measurements were synchronized. As for the attitude and heave estimation, it is also difficult to conclude with certainty that the results found using the STIM300 are representative since we used an engineering sample.

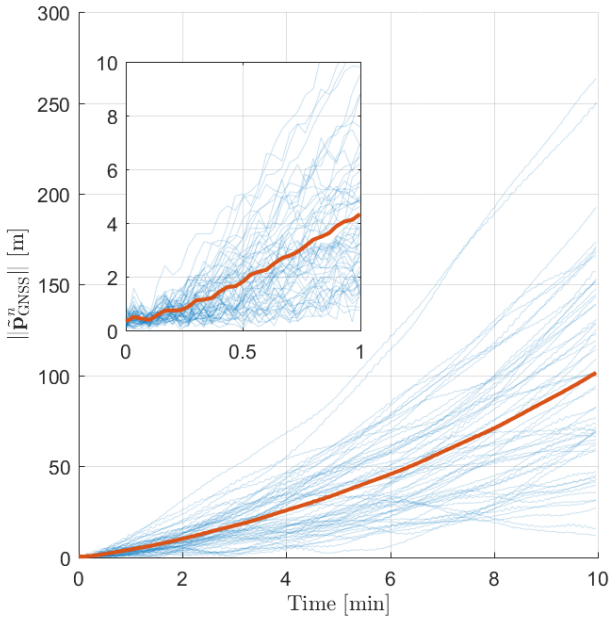

(a) DR errors obtained with ADIS16485.

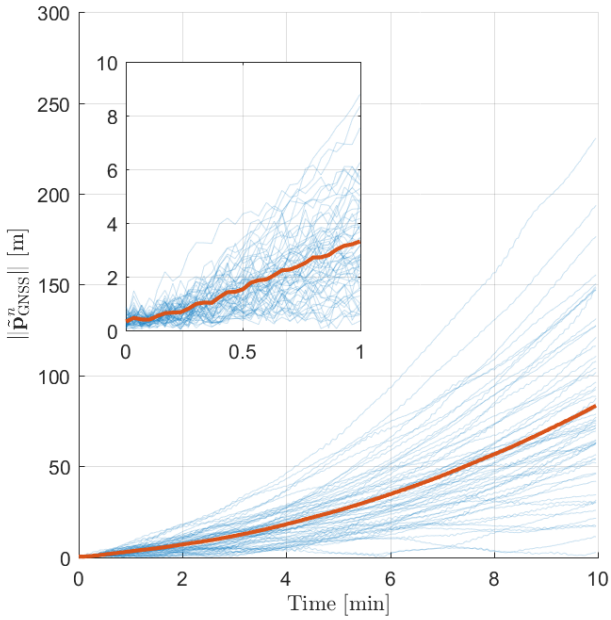

(b) DR errors obtained with STIM300.

Figure 4.10: Aggregated DR error over 60 runs using NLO A. Red indicates the mean DR error.

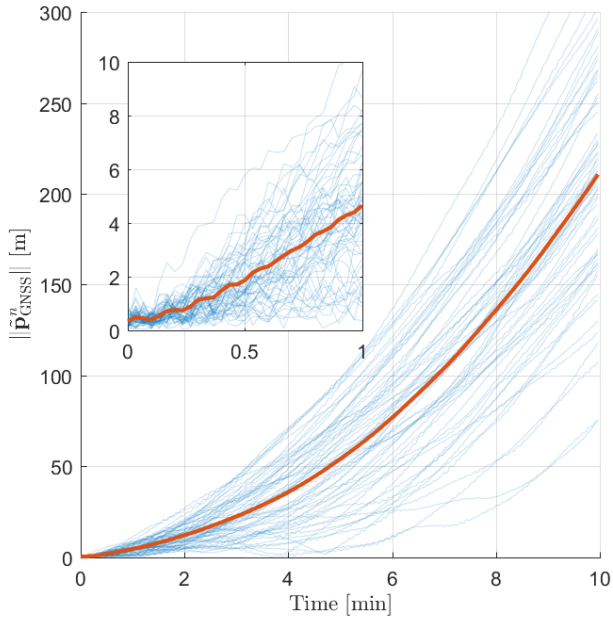

(a) DR errors obtained with ADIS16485.

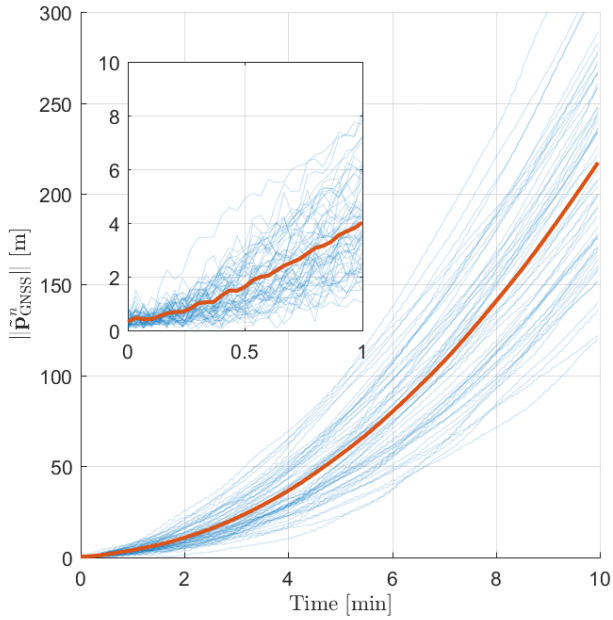

(b) DR errors obtained with STIM300.

Figure 4.11: Aggregated DR error over 60 runs using NLO A, and no bias estimation in Σ_3. Red indicates the mean DR error.

4.9 Full-scale testing: Vibrations and high-rate MEMS-based INS

4.9.1 Vibrations

During the experiments, we had one ADIS16485 situated on a vibration-isolated plate supported by four Vibrachoc 7002 dampers, and one of the same type mounted without vibration dampers. These two will be referred to as ADIS1 and ADIS2 respectively in the following. Fig. 4.12 shows the difference of the raw measurement in the time domain between these two IMUs, during the DP operation. As we can see, a lot of external noise has been attenuated by the vibration isolation, especially for the accelerometer. For the gyro on the other hand, there is still a lot of noise present. This is reflected also by the frequency domain plot in Figs. 4.13, where we can see that there are a lot of unwanted frequencies for the ADIS1 in the range of 10-100 Hz. Fig. 4.13 is from the DP-operation depicted in Fig. 4.3a and Fig. 4.14 is from steaming at ten knots. Whereas there is nothing much above 100 Hz for the ADIS1, there are many high frequency components on the ADIS2. Common for both IMUs, to the far left just above zero Hz one can find the ship motion, and the main engine rotations starts showing up at around 12 Hz, particularly evident for ADIS1. The increased response below 100 Hz for ADIS1 could stem from resonance motion induced by the vibration isolated plate. Regardless, looking at the attitude estimate statistics coming from using each of the IMUs in Tab. 4.18, there is not that much of a difference, owing to our high integration rate of 1000 Hz averaging out the noise components. The results from the vibration isolated sensor are nonetheless still somewhat better, and we can see that applying the same filter to both IMUs does not yield the same outcome in the end. There is however significant improvement to be had by low-pass filtering.

Table 4.18: Attitude error statistics for vibration isolation in DP.

D: Damped. UD: undamped. LPF: low-pass filtered.

	D	**D+LPF**	**UD**	**UD+LPF**
Roll mean error [deg]	-0.0017	-0.0007	-0.0028	0.0014
Pitch mean error [deg]	0.0040	0.0047	-0.0076	-0.0179
Roll RMSE [deg]	0.0490	0.0363	0.0685	0.0484
Pitch RMSE [deg]	0.0968	0.0670	0.1017	0.0750
Roll CAE [deg]	1002.3	759.80	1437.0	1021.5
Pitch CAE [deg]	1980.1	1406.0	2071.8	1564.0

A simple result that comes from observing Figs. 4.13–4.14, is that different modes of operation could, in theory, be identified on the basis of the frequency signatures. In addition, the higher frequency components might contain interest-

ing information from a machinery diagnosis point of view. Whether one wants to keep all the frequency components depends consequently on one's application beyond traditional navigation use, but with filters implemented in software more flexibility is achieved in this regard.

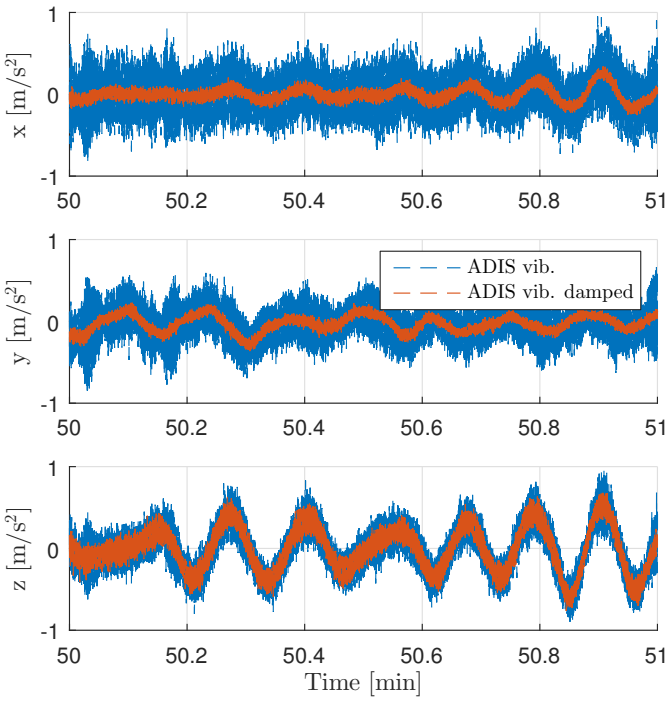

(a) Accelerometer raw measurements.

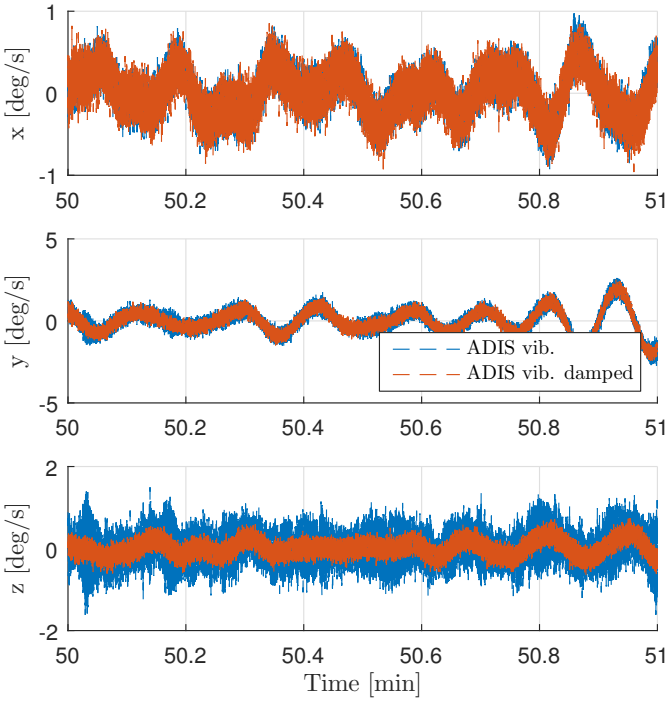

(b) Gyro raw measurements.

Figure 4.12: ADIS measurements, vibration isolated (red) and not (blue) in DP.

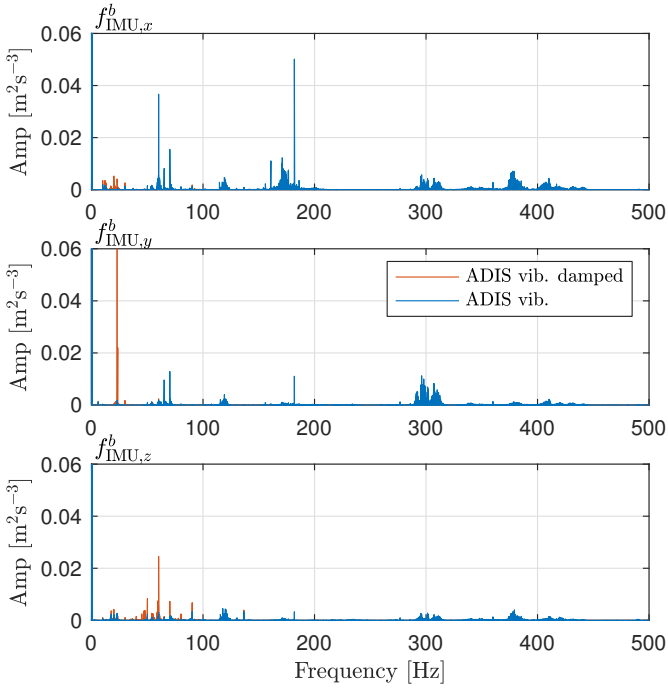

(a) Accelerometer.

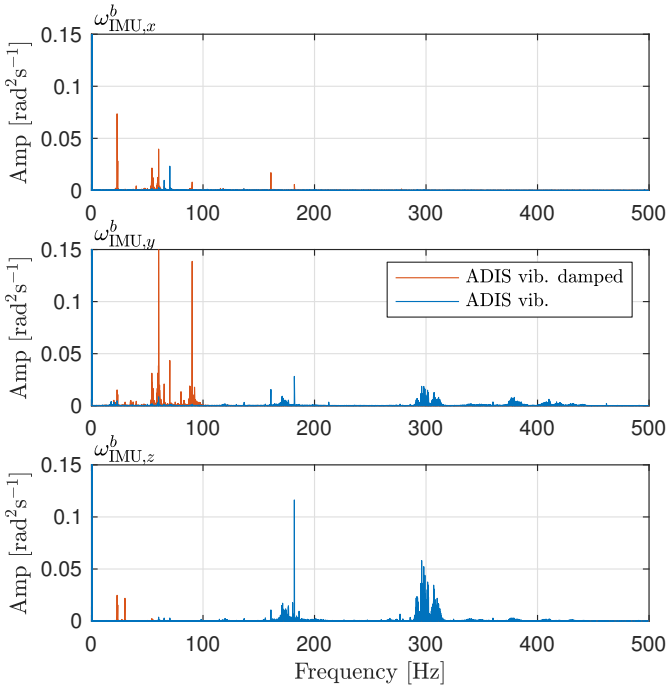

(b) Gyro.

Figure 4.13: Power spectral density estimate of IMU measurements, vibration isolated (red) and not (blue) in DP.

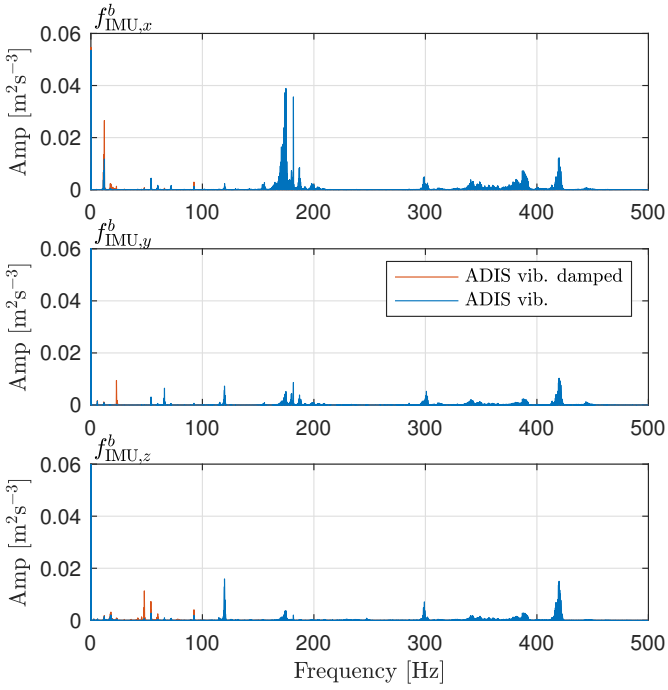

(a) Accelerometer.

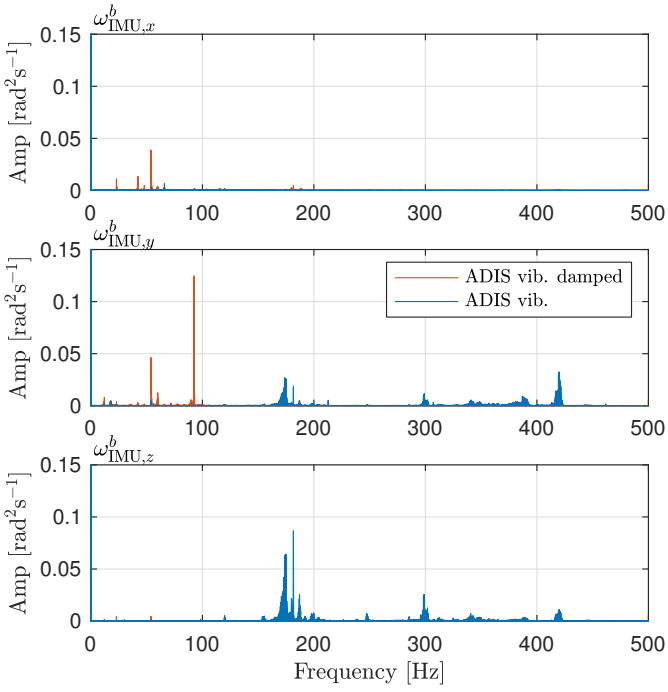

(b) Gyro.

Figure 4.14: Power spectral density estimate of IMU measurements, vibration isolated (red) and not (blue) in steaming.

4.10 Conclusion

A successful verification of two nonlinear observers was carried out, employing two different MEMS IMUs, namely the ADIS16485 and STIM300. The full-scale experimental data was collected on an offshore vessel operating outside the Norwegian coast. Comparing the observer output to industry standard VRUs and navigation software based on EKF showed that favorable performance could be achieved, and that for attitude estimation the method was more important than the IMU. The results also showed that estimating specific force in the navigation frame improves attitude estimates, in contrast to assuming that the vessel is not accelerating. Heave estimation was also compared, revealing more differences between the IMUs. Seemingly ADIS16485 had a better accelerometer than STIM300, which reflected upon the results. Dead reckoning for heading and position was also considered, where the heading case revealed the great qualities of the STIM300's angular rate sensors. For dead reckoning in position, the IMUs yielded comparable results with the STIM300 coming out on top, probably because of the better angular rate sensor.

A short discussion on the vibration and mechanical noise picked up by IMUs both with and without vibration isolation was undertaken, revealing that while using mechanical dampers are useful, one could consider mitigating the vibration-induced disturbances just in software instead, or including a non-isolated sensor. This would allow for keeping interesting information related to the ship's state embedded in the raw inertial measurements.

5

Redundant INS

This chapter is based on Rogne et al. (nda).

5.1 Introduction

Redundant IMUs have traditionally been applied in safety-critical systems such as aircraft and spacecraft. In the maritime domain, dynamic positioning vessels are required to have several gyrocompasses and vertical reference units (VRUs), a form of INS, on board. However, autonomous vehicles are on the horizon, not only in the air (Sukkarieh et al., 2000), but also on land and at sea. In order for these vehicles to operate safely and autonomously in areas potentially far from possible human intervention, they need functions for self-diagnostics and fault management. To be feasible and competitive in the nascent consumer and commercial markets, it is not viable to fit all these vehicles with expensive high-end gyroscopes and accelerometers. Therefore, an investigation on how to improve the FDI performance with MEMS sensors is of interest.

The main contribution of this chapter is providing and comparing methods for fusing redundant MEMS inertial measurements in the context of nonlinear attitude observers. Usage of redundant IMUs allow for both fault detection and automatic fault management. The latter is achieved by relying on the remaining sensors when experiencing inertial sensor faults in one of the available IMUs. Such capabilities have received little focus when applying NLOs for INSs.

Full-scale verification is performed, using data collected from three MEMS IMUs mounted on an anchor handling tug supply (AHTS) vessel. Artificial faults are added to the signals in order to trigger the FDI methods. The results are compared with the classical parity space method commonly used in high-grade redundant inertial systems.

5.1.1 Organization

The chapter is organized as follows: First the notation and models are presented, before the observers used throughout are introduced. Then, two alternative methods for fusing measurements and FDI are given. Thereafter, a full-scale verification is performed with a subsequent discussion. Finally, a conclusion is made.

5.2 Preliminaries

This section introduces the notation, coordinate frames and the strapdown equations that are the basis of this work.

5.2.1 Notation

The Euclidean vector norm and the induced matrix norm are denoted $\|\cdot\|_2$. The $n \times n$ identity matrix is denoted $\boldsymbol{I}_n$, while a block diagonal matrix is given by $\boldsymbol{M} = \text{blockdiag}(\boldsymbol{M}_1, \boldsymbol{M}_2, \ldots, \boldsymbol{M}_n)$ for square matrices $\boldsymbol{M}_j$. The transpose of a vector or a matrix is denoted with $(\cdot)^\intercal$. $\boldsymbol{S}(\cdot) \in SS(3)$ represents the skew symmetric matrix such that $\boldsymbol{S}(z_1)z_2 = z_1 \times z_2$ for two vectors $z_1, z_2 \in \mathbb{R}^3$. Moreover, $z = (z_1; z_2; \ldots; z_n)$ denotes a vector of stacked column vectors z_j.

$\boldsymbol{R}_a^b \in SO(3)$ denotes the rotation matrix from the given frame $\{a\}$ to the given frame $\{b\}$. $\boldsymbol{\omega}_{ab}^c \in \mathbb{R}^3$ is an angular velocity of $\{b\}$ relative $\{a\}$, decomposed in $\{c\}$. In addition to the rotation matrix, the rotation between $\{a\}$ to $\{b\}$ may be represented using the unit quaternion $\boldsymbol{q}_a^b \in Q$, for the set

$$Q = \left\{ \boldsymbol{q} \mid (\boldsymbol{q})^\intercal \boldsymbol{q} = 1,\ \boldsymbol{q} = (s, \boldsymbol{r}^\intercal)^\intercal,\ s \in \mathbb{R}^1,\ \boldsymbol{r} \in \mathbb{R}^3 \right\}, \tag{5.1}$$

where s and $\boldsymbol{r}$ denotes the real part and vector part of the unit quaternion, respectively. Moreover, $\otimes$ represents the Hamiltonian quaternion product. For a unit quaternion, $\boldsymbol{q}$, we define

$$\begin{aligned} \boldsymbol{T}(\boldsymbol{q}) &:= \begin{pmatrix} -\boldsymbol{r}^\intercal \\ s\boldsymbol{I}_3 + \boldsymbol{S}(\boldsymbol{r}) \end{pmatrix}, \\ \boldsymbol{\Xi}(\boldsymbol{q}) &:= \begin{pmatrix} -\boldsymbol{r}^\intercal \\ s\boldsymbol{I}_3 - \boldsymbol{S}(\boldsymbol{r}) \end{pmatrix}, \end{aligned} \tag{5.2}$$

such that the quaternion differential equation for $\boldsymbol{q}_a^b$ may be given as

$$\dot{\boldsymbol{q}}_a^b = \frac{1}{2}\boldsymbol{q}_a^b \otimes \begin{pmatrix} 0 \\ \boldsymbol{\omega}_{ca}^a \end{pmatrix} - \frac{1}{2}\begin{pmatrix} 0 \\ \boldsymbol{\omega}_{cb}^b \end{pmatrix} \otimes \boldsymbol{q}_a^b \tag{5.3}$$

$$= \frac{1}{2}\boldsymbol{T}(\boldsymbol{q}_a^b)\boldsymbol{\omega}_{ca}^a - \frac{1}{2}\boldsymbol{\Xi}(\boldsymbol{q}_a^b)\boldsymbol{\omega}_{cb}^b, \tag{5.4}$$

for some given coordinate frames $\{a\}$, $\{b\}$ and $\{c\}$. Furthermore, the unit quaternion conjugate of $\boldsymbol{q}_a^b$ is defined $\left(\boldsymbol{q}_a^b\right)^* := (s, -\boldsymbol{r}^\intercal)^\intercal$. The resulting error quaternion,

between two given unit quaternions, $\boldsymbol{q}_1$ and $\boldsymbol{q}_2$, can then be defined,

$$\tilde{\boldsymbol{q}} := \boldsymbol{q}_1 \otimes \boldsymbol{q}_2^* = \begin{pmatrix} \boldsymbol{q}_2 & \boldsymbol{\Xi}(\boldsymbol{q}_2) \end{pmatrix}^\mathsf{T} \boldsymbol{q}_1. \tag{5.5}$$

Roll, pitch and yaw are denoted ϕ, θ and ψ, respectively, in compliance with the SNAME notations (SNAME, 1950).

5.2.2 Coordinate reference frames

We use four reference frames: The earth-centered inertial (ECI) frame, the earth-centered, earth-fixed (ECEF) frame, a tangent frame equivalent to non-rotating north-east-down (NED), and the BODY reference frame, denoted $\{i\}$, $\{e\}$, $\{t\}$ and $\{b\}$, respectively (see Fig. 4.1). ECI is an assumed inertial frame following the Earth in space, where the x-axis points towards vernal equinox, the z-axis is pointing along the Earth's rotational axis and the y-axis completes the right hand frame. Regarding the ECEF, the x-axis points towards the zero meridian, the z-axis points along the Earth's rotational axis, while the y-axis completes the right hand frame. The Earth's rotation rate $\omega_{ie} = 7.292115 \cdot 10^{-5}$ rad/s is given by the WGS-84 datum. It is decomposed in the ECEF and NED frame as

$$\boldsymbol{\omega}_{ie}^e = \begin{pmatrix} 0 \\ 0 \\ 1 \end{pmatrix} \omega_{ie}, \quad \boldsymbol{\omega}_{ie}^t = \begin{pmatrix} \cos(\mu) \\ 0 \\ -\sin(\mu) \end{pmatrix} \omega_{ie}, \tag{5.6}$$

where μ is the latitude on the Earth. The longitude is denoted λ. The navigation frame is the local Earth-fixed tangent frame, $\{t\}$, where the x-axis points towards north, the y-axis points towards east, and the z-axis points downwards. The BODY frame is fixed to the vehicle, with its origin of $\{b\}$ is located at the vehicle's nominal center of gravity. The x-axis is directed from aft to fore, the y-axis is directed to starboard and the z-axis points downwards.

5.2.3 Kinematic strapdown equations

The most comprehensible attitude representation for a user is the attitude between BODY and the NED frame. This is also the most intuitive representation for control. For navigation of craft confined to a specific geographical area, taking into account the Earth's rotation, the tangent frame is a suitable navigation frame. Using the unit quaternion representation, the kinematic attitude strapdown equation between the BODY and the tangent frame becomes

$$\dot{\boldsymbol{q}}_b^t = \frac{1}{2} \boldsymbol{q}_b^t \otimes \begin{pmatrix} 0 \\ \boldsymbol{\omega}_{ib}^b \end{pmatrix} - \frac{1}{2} \begin{pmatrix} 0 \\ \boldsymbol{\omega}_{it}^t \end{pmatrix} \otimes \boldsymbol{q}_b^t, \tag{5.7}$$

using the unit quaternion attitude representation, where $\boldsymbol{\omega}_{in}^n$ is given as

$$\boldsymbol{\omega}_{it}^t = \boldsymbol{\omega}_{ie}^t + \boldsymbol{\omega}_{et}^t = \boldsymbol{\omega}_{ie}^t, \tag{5.8}$$

since a tangent frame representation of the strapdown equations is chosen, resulting in $\boldsymbol{\omega}_{et}^{t} = \mathbf{0}_{3\times1}$. $\boldsymbol{\omega}_{ib}^{b}$ is the angular rate of the navigating object relative the inertial frame, decomposed in $\{b\}$. From (Fossen, 2011, Eq. (2.56)) and reference therein, the rotation matrix $\boldsymbol{R}(\boldsymbol{q}_{b}^{t}) := \boldsymbol{R}_{b}^{t}$ is obtained from $\boldsymbol{q}_{b}^{t}$ using

$$\boldsymbol{R}(\boldsymbol{q}_{b}^{t}) = \boldsymbol{I}_3 + 2s\boldsymbol{S}(\boldsymbol{r}) + 2\boldsymbol{S}^2(\boldsymbol{r}). \tag{5.9}$$

When using the tangent frame as the navigation frame, the rotational and translational motion has the relation

$$\dot{\boldsymbol{p}}_{tb}^{t} = \boldsymbol{v}_{tb}^{t}, \tag{5.10}$$

$$\dot{\boldsymbol{v}}_{tb}^{t} = -2\boldsymbol{S}(\boldsymbol{\omega}_{ie}^{t})\boldsymbol{v}_{tb}^{t} + \boldsymbol{R}_{b}^{t}\boldsymbol{f}_{ib}^{b} + \boldsymbol{g}_{b}^{t}, \tag{5.11}$$

where $\boldsymbol{p}_{tb}^{t} \in \mathbb{R}^3$ is the position relative the origin of the tangent frame, $\mu(0)$ and $\lambda(0)$, and $\boldsymbol{v}_{tb}^{t} \in \mathbb{R}^3$ is the linear velocity. $\boldsymbol{g}_{b}^{t}(\mu, \lambda) \in \mathbb{R}^3$ is the local gravity vector dependent on the vehicle's latitude and longitude. $\boldsymbol{f}_{ib}^{b} = (\boldsymbol{R}_{b}^{t})^{\intercal}(\boldsymbol{a}_{ib}^{t} - \boldsymbol{g}_{b}^{t}) \in \mathbb{R}^3$ is the specific force, measured by the IMU, decomposed in $\{b\}$, where $\boldsymbol{a}_{ib}^{t}$ represents the accelerations decomposed in the tangent frame.

5.3 Inertial and Heading Sensors

In this section we present the IMU model, and discuss the consequences of employing redundant inertial measurement units.

5.3.1 IMU model

An IMU triad comprises sensors along three orthogonal axes, measuring angular rate (often called gyro measurements) or acceleration in some frame that may or may not be aligned with the body frame $\{b\}$. For our case though, we have that each accelerometer and gyro triad measures, in the ideal case,

$$\boldsymbol{f}_{\text{IMU}}^{b} = \left(f_x^b; f_y^b; f_z^b\right), \quad \boldsymbol{\omega}_{\text{IMU}}^{b} = \left(\omega_x^b; \omega_y^b; \omega_z^b\right),$$

where x, y and z are the forward, starboard and downward axes of the vehicle. In addition to these ideal case measurements, each of the measurements are polluted with noise, biases, other errors and potentially faults. Sensor errors include nonlinearity, scale factors, cross-coupling and g-sensitivity errors. External disturbances also affect the signals, and some sources may be electrical signals, magnetic fields or mechanical vibrations. (Groves, 2013, Ch. 4.4) and (Titterton and Weston, 2004, Ch. 4–8) provide more information on inertial sensors and inertial sensor errors. For the sensor outputs, we have the following model:

$$\boldsymbol{\omega}_{\text{IMU}}^{b} = \boldsymbol{\omega}_{ib}^{b} + \boldsymbol{b}_{\text{gyro}}^{b} + \boldsymbol{w}_{\text{gyro}}^{b} + \boldsymbol{d}_{\text{gyro}}^{b}, \tag{5.12}$$

$$\boldsymbol{f}_{\text{IMU}}^{b} = \boldsymbol{f}_{ib}^{b} + \boldsymbol{b}_{\text{acc}}^{b} + \boldsymbol{w}_{\text{acc}}^{b} + \boldsymbol{d}_{\text{acc}}^{b} \tag{5.13}$$

where $\boldsymbol{\omega}_{ib}^{b}$ and $\boldsymbol{f}_{ib}^{b}$ are the true angular rates and specific forces, $\boldsymbol{b}_{\text{gyro}}^{b}$ and $\boldsymbol{b}_{\text{acc}}^{b}$ are the angular rate sensor bias and accelerometer bias, while $\boldsymbol{w}_{\text{gyro}}^{b}$ and $\boldsymbol{w}_{\text{acc}}^{b}$ represent sensor noise and vibration induced noise in the sensors. $\boldsymbol{d}_{\star}^{b}$ denote the respective sensor fault, where

$$\boldsymbol{d}_{\star} = \begin{cases} \left(d_{\star,x}^{b},\, d_{\star,y}^{b},\, d_{\star,z}^{b}\right)^{\mathsf{T}} & \text{if fault has occured} \\ \mathbf{0}_{3\times 1} & \text{otherwise} \end{cases}. \tag{5.14}$$

Both the angular rate and accelerometer biases are assumed slowly time-varying,

$$\dot{\boldsymbol{b}}_{\text{gyro}}^{b} = \boldsymbol{w}_{b,\text{gyro}}^{b}, \quad \dot{\boldsymbol{b}}_{\text{acc}}^{b} = \boldsymbol{w}_{b,\text{acc}}^{b}, \tag{5.15}$$

where $\boldsymbol{w}_{b,\text{gyro}}^{b}$ and $\boldsymbol{w}_{b,\text{acc}}^{b}$ represent small variations in the biases (zero mean).

5.3.2 Heading reference

In addition to the MEMS IMU, we assume that there is a heading reference available, typically in the form of a gyrocompass providing the heading ψ_c, or derived from a magnetometer yielding a tri-axial measurement of the earth's magnetic field $\boldsymbol{m}_{tb}^{b}$ in the body frame, which can be related to the earth's magnetic field vector $\boldsymbol{m}_{tb}^{t}$ decomposed in the tangent frame at the vehicle's location, thus potentially providing a true-north heading.

5.3.3 Multiple IMUs

Combining multiple IMUs should in the ideal case reduce the noise levels and bias magnitudes. Indeed, for the combined inertial sensor output $\bar{x}$ from m independent measurements $\bar{x} = (y_1 + y_2 + \ldots + y_m)/m$, with equal standard deviation $\sigma_{y,j} = \sigma_y$ we have

$$\begin{aligned} \text{Var}(\bar{x}) &= \text{Var}\left(\frac{1}{m}\sum_{j=1}^{m} y_j\right) = \frac{1}{m^2}\sum_{j=1}^{m}\sigma_{y,j}^2 \\ \implies \sigma_{\bar{x}} &= \frac{\sigma_y}{\sqrt{m}} \end{aligned} \tag{5.16}$$

assuming the same zero-mean distribution for each of the measurement errors. However, when it comes to sensor noise, common mode noise like the external sources mentioned in the previous section could void the advantageous property of (5.16). Regardless, the bias magnitude in the aggregated measurement will be reduced compared to the magnitude of the of largest bias of the m measurements.

In Guerrier et al. (2012), it was found that for sensor triads, their relative orientation does not matter when it comes to optimality, but in the case of sensor failures a skewed configuration is preferred when using less than four sensor

triads. Later in this chapter we will use three sensor triads in an orthogonal configuration, arguably below the recommended number. However, as we will show, FDI results are attainable using this structure.

5.4 Nonlinear Observer Structure

This section presents the nonlinear observers employed for position, velocity and attitude estimation. The nominal observer structure with a single IMU is illustrated in Fig. 5.1

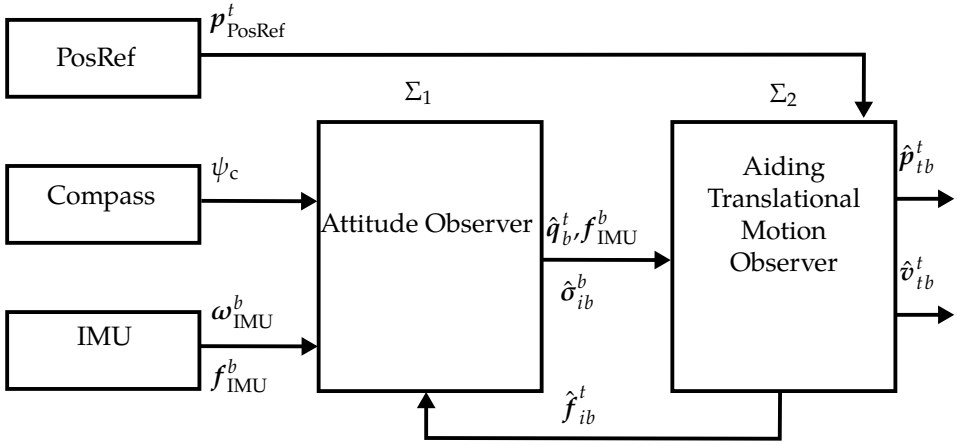

Figure 5.1: Nominal nonlinear observer structure for single IMU.

5.4.1 Attitude observer

The nonlinear attitude observer is the one found in Grip et al. (2013), which is based on Mahony et al. (2008):

$$\Sigma_{1,j}: \begin{cases} \dot{\hat{q}}^t_{b,j} = \frac{1}{2}\hat{q}^t_{b,j} \otimes \begin{pmatrix} 0 \\ \hat{\omega}^b_{ib,j} \end{pmatrix} - \frac{1}{2}\begin{pmatrix} 0 \\ \omega^t_{it} \end{pmatrix} \otimes \hat{q}^t_{b,j}, & (5.17a) \\ \hat{\omega}^b_{ib,j} = \omega^b_{\text{IMU},j} - \hat{b}^b_{\text{gyro},j} + \hat{\sigma}^b_{ib,j}, & (5.17b) \\ \dot{\hat{b}}^b_{\text{gyro},j} = \text{Proj}\left(\hat{b}^b_{\text{gyro},j}, -k_I \hat{\sigma}^b_{ib,j}\right), & (5.17c) \end{cases}$$

where

$$\hat{\sigma}^b_{ib,j} = k_1 \underline{v}^b_1 \times \boldsymbol{R}(\hat{q}^t_{b,j})^\intercal \underline{v}^t_1 + k_2 \underline{v}^b_2 \times \boldsymbol{R}(\hat{q}^t_{b,j})^\intercal \underline{v}^t_2. \tag{5.18}$$

$\text{Proj}(\cdot,\cdot)$ denotes the angular rate bias projection algorithm of Grip et al. (2012a) and the reference therein, imposing a bound on $\hat{b}^b_{\text{gyro},j}$ to a compact set. k_I is the gain associated with the angular rate bias estimation. The observers are implemented

with the injection terms, $\hat{\boldsymbol{\sigma}}^b_{ib,j}$, where the j^{th} observer uses its own attitude estimate $\hat{\boldsymbol{q}}^t_{b,j}$, and

$$\underline{\boldsymbol{v}}^b_1 = \underline{\boldsymbol{f}}^b, \quad \underline{\boldsymbol{v}}^b_2 = \underline{\boldsymbol{f}}^b \times \underline{\boldsymbol{c}}^b,$$
$$\underline{\boldsymbol{v}}^t_1 = \underline{\boldsymbol{f}}^t, \quad \underline{\boldsymbol{v}}^t_2 = \underline{\boldsymbol{f}}^t \times \underline{\boldsymbol{c}}^t.$$

The measurement and reference vectors are defined as

$$\underline{\boldsymbol{f}}^b = \frac{\bar{\boldsymbol{f}}^b_{\text{IMU}}}{\|\bar{\boldsymbol{f}}^b_{\text{IMU}}\|_2}, \tag{5.19}$$
$$\underline{\boldsymbol{c}}^b = \begin{pmatrix} \cos(\psi_c) & -\sin(\psi_c) & 0 \end{pmatrix}^\intercal, \tag{5.20}$$
$$\underline{\boldsymbol{f}}^t = \frac{\text{sat}_{M_f}(\hat{\boldsymbol{f}}^t_{ib})}{\|\text{sat}_{M_f}(\hat{\boldsymbol{f}}^t_{ib})\|_2}, \tag{5.21}$$
$$\underline{\boldsymbol{c}}^t = \begin{pmatrix} 1 & 0 & 0 \end{pmatrix}^\intercal \tag{5.22}$$

similar to the chosen measurement/reference vector realizations of Grip et al. (2013). $\bar{\boldsymbol{f}}^b_{\text{IMU}}$ is a fused accelerometer signal that we will get back to later. The measurement and reference vector pair $\underline{\boldsymbol{c}}^b$ and $\underline{\boldsymbol{c}}^t$ could easily be replaced with magnetometer equivalents described in Section 5.3.2, as is done in Grip et al. (2013).

Since the vectors are normalized, we can consider the gains k_1 and k_2 as the observer's complimentary filter cut-off frequencies, (Mahony et al., 2008; Hua et al., 2014). Therefore, for motions with frequencies higher than k_1 and k_2, the primary source of attitude information are angular rate measurements, while for lower frequency motions, the measurement vectors are the primary source of attitude information.

5.4.2 Translational motion observer

The translational motion observer (TMO) estimates position, linear velocity and specific forces $\hat{\boldsymbol{p}}^t_{tb} \in \mathbb{R}^3$, $\hat{\boldsymbol{v}}^t_{tb} \in \mathbb{R}^3$ and $\hat{\boldsymbol{f}}^t_{ib} \in \mathbb{R}^3$, in the given navigation frame $\{t\}$. The resulting TMO takes the form,

$$\Sigma_2 : \begin{cases} \dot{\hat{\boldsymbol{p}}}^t_{tb} = \hat{\boldsymbol{v}}^t_{tb} + \theta \boldsymbol{K}_{pp} \tilde{\boldsymbol{p}}^t_{tb} & \text{(5.23a)} \\ \dot{\hat{\boldsymbol{v}}}^t_{tb} = -2\boldsymbol{S}(\boldsymbol{\omega}^t_{ie})\hat{\boldsymbol{v}}^t_{tb} + \hat{\boldsymbol{f}}^t_{ib} + \boldsymbol{g}^t_b + \theta^2 \boldsymbol{K}_{vp} \tilde{\boldsymbol{p}}^t_{tb} & \text{(5.23b)} \\ \dot{\boldsymbol{\xi}}^t_{ib} = -\boldsymbol{R}\left(\bar{\boldsymbol{q}}^t_b\right) \boldsymbol{S}\left(\bar{\boldsymbol{\sigma}}^b_{ib}\right) \bar{\boldsymbol{f}}^b_{\text{IMU}} + \theta^3 \boldsymbol{K}_{\xi p} \tilde{\boldsymbol{p}}^t_{tb} & \text{(5.23c)} \\ \hat{\boldsymbol{f}}^t_{ib} = \boldsymbol{R}\left(\bar{\boldsymbol{q}}^t_b\right) \bar{\boldsymbol{f}}^b_{\text{IMU}} + \boldsymbol{\xi}^t_{ib}, & \text{(5.23d)} \end{cases}$$

equivalent to the design of Grip et al. (2013) except for use of the tangent frame $\{t\}$, instead of the ECEF frame $\{e\}$, as navigation frame and the use of fused signals $\bar{\boldsymbol{f}}^b_{\text{IMU}}$, $\bar{\boldsymbol{q}}^t_b$ and $\bar{\boldsymbol{\sigma}}^b_{ib}$ based on the signals $\boldsymbol{f}^b_{\text{IMU},j}$, $\hat{\boldsymbol{q}}^t_{b,j}$ and $\hat{\boldsymbol{\sigma}}^b_{ib,j}$ discussed in

Sec. 5.3.1 and 5.4.1. How $\bar{f}^b_{\text{IMU}}$, $\bar{q}^t_b$ and $\bar{\sigma}^b_{ib}$ are generated is presented in Sec. 5.5 and 5.6.

5.4.3 Observer structures for fusing redundant measurements

For exploiting the redundant measurements, we will employ two different structures. The first structure. Alternative 1, is shown in Fig. 5.2. Here the gyro and accelerometer outputs from the IMUs are combined into single measurements via the parity space method, before being fed into the observer. In this approach, no modification of the original observer structure of Grip et al. (2013) is necessary (only one Σ_1 is used) such that $\bar{q}^t_b = \hat{q}^t_b$ and $\bar{\omega}^b_{\text{IMU}}$ is utilized instead of $\omega^b_{\text{IMU},j}$ cf. Fig. 5.2. On the other hand, in alternative 2, portrayed in Fig. 5.3, only the accelerometer measurements are combined beforehand, while the angular rate measurements are sent to three different instances of the nonlinear attitude observer, (5.17). The outputs of these observers are then merged and forwarded to the aiding translational motion observer, (5.23a). The reason why the accelerometer measurements are not treated the same as the angular rate measurements in Alternative 2, is because of the feedback interconnection where the measured specific force enters the TMO directly through $\bar{f}^b_{\text{IMU}}$ and indirectly through $\bar{q}^t_b$ and $\bar{\sigma}^b_{\text{IMU}}$. Therefore if some faulty accelerometer measurements from IMU j enter the aiding TMO directly through both (5.23c) and (5.23d), the equilibrium of the feedback-interconnected system $\Sigma_j - \Sigma_2$ will be affected before the FDI algorithms of Section 5.6 have had time to react. If so this might further impair the unit quaternion weighting presented in Sec. 5.6.1. This can be understood from the fact that the stability properties of the feedback-interconnected NLO of Grip et al. (2013) only hold for fault-free measurements.

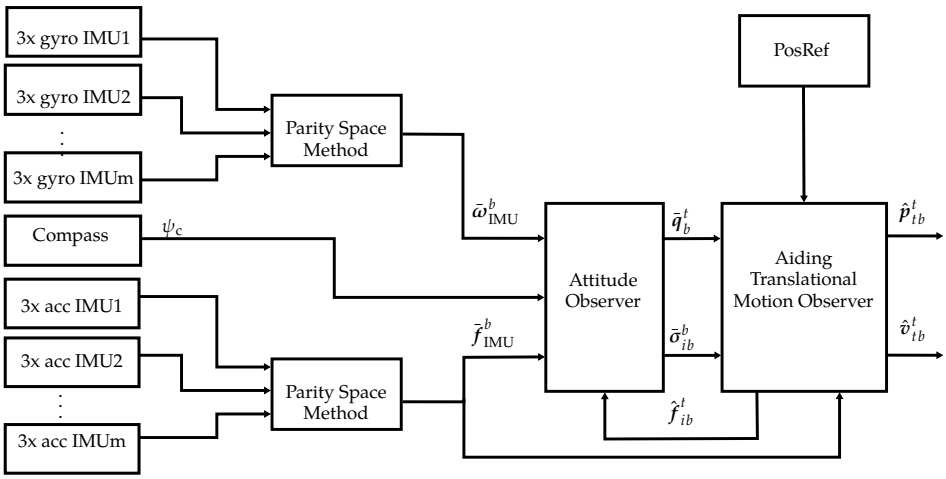

Figure 5.2: Redundant IMU alternative 1 – Observer structure.

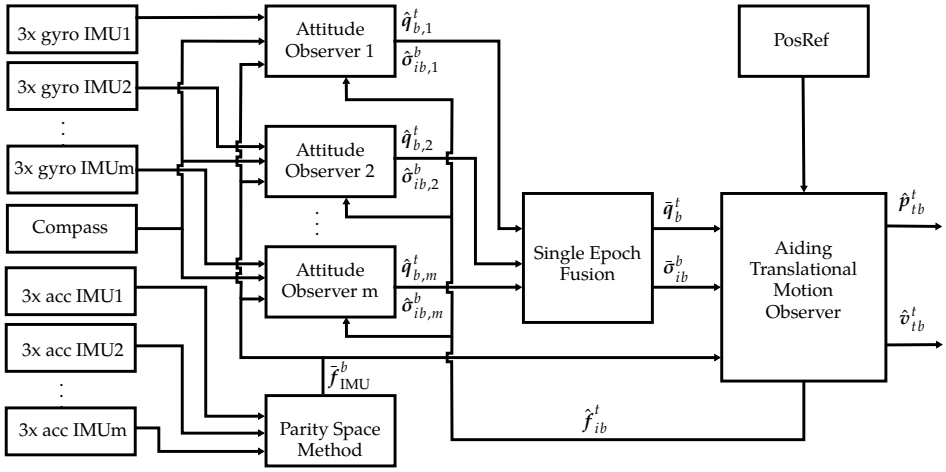

Figure 5.3: Redundant IMU alternative 2 – Observer structure.

5.5 Parity Space Method

In the parity space method, the detection of faults comes down to the choice between two hypotheses, either that an erroneous measurement has presented itself or not (Sturza, 1988). A statistical test is performed, based on a decision variable D_{det} obtained from separating the measurement space, i.e. all the redundant measurements, into two subspaces, namely the parity space and the dimensional state space, the latter of which is essentially the vehicle's body frame.

For $l = 3m$ measurements of a 3-dimensional state vector $\boldsymbol{x}$, we have the measurement model

$$\boldsymbol{y}^b_{\text{IMU}} = \boldsymbol{H}\boldsymbol{x}^b_{ib} + \boldsymbol{w}^b_\star + \boldsymbol{b}^b_\star + \boldsymbol{d}^b_\star \tag{5.24}$$

where $\boldsymbol{H}$ is the measurement matrix relating the state space to the measurement space, $\star$ represents either the accelerometers or the gyros, $\boldsymbol{w}^b_\star$ is a vector of white noise, $\boldsymbol{b}^b_\star$ is a vector of biases and $\boldsymbol{d}^b_\star$ is a vector of fault effects. $\boldsymbol{x}^b_{ib}$ is the state space value we are interested in, in our case either $\boldsymbol{\omega}^b_{ib}$ or $\boldsymbol{f}^b_{ib}$ as described in Section 5.3.1, and

$$\boldsymbol{H} = \begin{pmatrix} \boldsymbol{I}_3 & \boldsymbol{I}_3 & \dots & \boldsymbol{I}_3 \end{pmatrix}^\intercal . \tag{5.25}$$

To distinguish between faults and regular IMU biases, one should compensate as much as possible for the biases beforehand, such that the resultant bias $\boldsymbol{b}^b_\star$ is as close to zero as possible before applying the parity space method.

The least squares (LS) estimate of $\boldsymbol{x}^b_{ib}$ in (5.24) is

$$\bar{\boldsymbol{x}}^b_{ib} = (\boldsymbol{H}^\intercal \boldsymbol{H})^{-1}\boldsymbol{H}^\intercal \boldsymbol{y}^b_{\text{IMU}}, \tag{5.26}$$

while the residual (fault and noise) vector estimate

$$\boldsymbol{f}_r = \boldsymbol{S}_r \boldsymbol{y}^b_{\text{IMU}}, \tag{5.27}$$

where $\boldsymbol{S}_r$ is given by

$$\boldsymbol{S}_r = (\boldsymbol{I}_l - \boldsymbol{H}(\boldsymbol{H}^\intercal \boldsymbol{H})^{-1}\boldsymbol{H}^\intercal), \tag{5.28}$$

$l = 3m$, and the decision variable for detection can be computed as

$$\boldsymbol{D}_{\text{det}} = \boldsymbol{f}_r^\intercal \boldsymbol{f}_r. \tag{5.29}$$

Assuming that the measurement noises are Gaussian, uncorrelated and with equal variance, and that each of the sensors are equally likely to have measurement faults, the threshold T_{det}, to which D_{det} will be compared, is given as (Sturza, 1988)

$$T_{\text{det}}\left(p_{\text{FA}}, l-3, \sigma_n^2\right) = \sigma_n^2 F^{-1}\left(1 - p_{\text{FA}} | l-3\right), \tag{5.30}$$

where p_{FA} is the probability of false alarms, $l-3$ is the degree of freedom, σ_n^2 is the measurement noise variance, and $F^{-1}(p|v)$ is the inverse χ^2 cumulative distribution function, such that:

$$x = F^{-1}(p|v) = \{x : F(x|v) = p\}, \tag{5.31}$$

where

$$p = F(x|v) = \int_0^x \frac{t^{(v-2)/2} e^{-t/2}}{2^{v/2}\Gamma(v/2)}, \tag{5.32}$$

and $\Gamma(\cdot)$ is the Gamma function.

For fault isolation, the faulty sensor number k can be identified by

$$k = \arg\max_{j \in [1;l]} \frac{f_{r,j}^2}{s_{jj}} \tag{5.33}$$

where $f_{r,j}$ is the j^{th} element of $\boldsymbol{f}_r$ and s_{jj} is the j^{th} diagonal element of the matrix $\boldsymbol{S}_r$. The parity space method is summarized in Algorithm 1.

Algorithm 1 Parity Space Method.

Require: $\boldsymbol{H}$, $\boldsymbol{S}_r$, y^b_{IMU}, T_{det}
  b_dont_stop = true
  while b_dont_stop **do**
    $\boldsymbol{f}_r = \boldsymbol{S}_r \boldsymbol{y}^b_{\text{IMU}}$
    $D_{\text{det}} = \boldsymbol{f}_r^\intercal \boldsymbol{f}_r$
    if $D_{\text{det}} > T_{\text{det}}$ **then**
      $k = \arg\max_{j \in [1;l]} \frac{f_j^2}{s_{jj}}$
      Remove k^{th} measurement from $\boldsymbol{y}^b_{\text{IMU}}$, $\boldsymbol{H}$
      Recalculate $\boldsymbol{S}_r$
    else
      b_dont_stop = false
    end if
  end while
Output: $\bar{\boldsymbol{x}} = (\boldsymbol{H}^\intercal \boldsymbol{H})^{-1} \boldsymbol{H}^\intercal y^b_{\text{IMU}}$

5.6 Quaternion Averaging and FDI

5.6.1 Averaging quaternions

The estimated unit quaternions from Section 5.4.1 ($\hat{\boldsymbol{q}}^t_{b,1}, \hat{\boldsymbol{q}}^t_{b,2}, \ldots, \hat{\boldsymbol{q}}^t_{b,m}$) can be weighed optimally using a single epoch estimation algorithm solving the optimization problem

$$\bar{\boldsymbol{q}}^t_b := \underset{\boldsymbol{q}^t_b \in \mathcal{S}^3}{\arg\max} \sum_{j=1}^{m} w_j (\boldsymbol{q}^t_b)^\intercal \hat{\boldsymbol{q}}^t_{b,j} (\hat{\boldsymbol{q}}^t_{b,j})^\intercal \boldsymbol{q}^t_b, \tag{5.34}$$

equivalent to that posed in Markley (2007) with respect to the definition in (5.1). Equation (5.34) is a representation of the objective originally posed by Wahba Wahba (1965), where w_j are positive weights. Pure LS weighting is not applicable for unit quaternions since this procedure alone neither maintains the unity norm of the averaged quaternion nor can guarantee that the correct averaged quaternion is obtained regardless of the sign of the quaternions, $\hat{\boldsymbol{q}}^t_{b,j}$ with respect to the set Q from (5.1). This is a crucial property of a unit quaternion-based fusing algorithm due to the topology, and the inherit topological obstruction Bhat and Bernstein (2000), inferred by (5.1), where $\hat{\boldsymbol{q}}^t_{b,j}$ and $-\hat{\boldsymbol{q}}^t_{b,j}$ represents the same rotation.

Using scalar weighted quaternions, for each update of the m attitude observers the averaged/weighted quaternion, $\bar{\boldsymbol{q}}^t_b$, based on the m quaternion estimates $\hat{\boldsymbol{q}}^t_{b,1}, \hat{\boldsymbol{q}}^t_{b,2}, \ldots, \hat{\boldsymbol{q}}^t_{b,m}$, and the respective weights, $w_1, w_2, \ldots, w_m$, may be obtained using Algorithm 2 performing an eigenvalue/eigenvector decomposition of a matrix composed of the given quaternions and weights. Furthermore, in Algorithm 2, $\boldsymbol{E}$ is the matrix of eigenvectors of $\boldsymbol{K}_q$, $\boldsymbol{D}_{\text{eig}}$ is a diagonal matrix of the eigenvalues of

$\boldsymbol{K}_q$ and $i_{\max}$ is the column index associated with the maximum eigenvalue, $\lambda_{\max}$, of $\boldsymbol{D}_{\text{eig}}$. The algorithm results in a weighted quaternion $\bar{\boldsymbol{q}}_b^t$ providing a unique attitude representation, Markley (2007).

Algorithm 2 Quaternion Weighting with Scalar Weight

Input: Quaternion estimates $\hat{\boldsymbol{q}}_{b,j}^t$, weights w_j

1: $w_{\text{tot}} = \sum_{j=1}^{m} w_j$
2: $\boldsymbol{M} = \sum_{j=1}^{m} w_j \hat{\boldsymbol{q}}_{b,j}^t \left(\hat{\boldsymbol{q}}_{b,j}^t\right)^\intercal$
3: $\boldsymbol{K}_q = 4\boldsymbol{M} - w_{\text{tot}} \boldsymbol{I}_4$
4: $[\boldsymbol{E}, \boldsymbol{D}_{\text{eig}}] = \text{eig}(\boldsymbol{K}_q)$
5: $[\lambda_{\max}, j_{\max}] = \max(\text{diag}(\boldsymbol{D}_{\text{eig}}))$
6: $\bar{\boldsymbol{q}}_b^t = \boldsymbol{E}(:, j_{\max})$

Ensure: $\|\bar{\boldsymbol{q}}_b^t\| = 1 \implies \bar{\boldsymbol{q}}_b^t = \bar{\boldsymbol{q}}_b^t / \|\bar{\boldsymbol{q}}_b^t\|$
Output: $\bar{\boldsymbol{q}}_b^t$

According to Markley (2007), a computationally efficient alternative to Algorithm 2 is the QUaternion ESTtimation (QUEST) algorithm. A detailed study on QUEST is found in Shuster and Oh (1981). Alternatives to employing QUEST are presented in Markley and Mortari (2000).

5.6.2 FDI with quaternions

For the detection and isolation of faults in quaternions, we will employ the angle between orientations represented by the unit quaternions. Consider two unit quaternions $\boldsymbol{q}$ and $\boldsymbol{p}$, the error quaternion between them is described by (5.5). For unit quaternions, the scalar part of the error quaternion can be calculated by

$$\tilde{s} = q_1 p_1 + q_2 p_2 + q_3 p_3 + q_4 p_4, \tag{5.35}$$

which is equal to the dot product $\boldsymbol{q}^\intercal \boldsymbol{p}$. Now, consider that $\tilde{\beta}$ is the angle of rotation represented by the error quaternion around some axis, and consequently, a measure of the error's magnitude. Then, the relationship between the scalar part and the angle is given as Chou (1992)

$$\begin{aligned} \tilde{s} := \cos\left(\frac{\tilde{\beta}}{2}\right) &\implies \tilde{\beta} = 2\arccos\left(\tilde{s}\right) \\ \implies \tilde{\beta} &= 2\arccos\left(\boldsymbol{q}^\intercal \boldsymbol{p}\right). \end{aligned} \tag{5.36}$$

Equation (5.36) may serve as a useful metric for FDI. However, for $\rho \in [0, 1]$, due to

$$\beta = 2\arccos(\rho) = 2\pi - 2\arccos(-\rho), \tag{5.37}$$

and the fact that $\boldsymbol{q}$ and $-\boldsymbol{q}$ represents the same rotation, we can instead use the absolute value of the dot product to avoid calculating the absolute error angle. Therefore, we get

$$\tilde{\beta}_j = 2 \arccos\left(|(\hat{\boldsymbol{q}}_{b,j}^t)^\intercal \bar{\boldsymbol{q}}_b^t|\right), \tag{5.38}$$

is chosen to serve as basis for FDI. If any of the $\tilde{\beta}_j$ values are over a given threshold α_{det}, the corresponding quaternion is removed from the average, see Algorithm 3. The threshold α_{det} might be chosen as the maximum allowable angle difference between an attitude observer's output and the average output. The value should be as low as possible, but in order to minimise false alarms, a lower bound on α_{det} could be determined by empirical data from a fault-free case.

Algorithm 3 Quaternion FDI

Input: $\hat{\boldsymbol{q}}_{b,1}^t \dots \hat{\boldsymbol{q}}_{b,m}^t$, $w_1 \dots w_m$, α_{det}
b_dont_stop = true
while b_dont_stop **do**
  $\bar{q}_b^t$ = quat_avg($\hat{\boldsymbol{q}}_{b,j}^t \dots \hat{\boldsymbol{q}}_{b,m}^t, w_j \dots w_m$)
  for $j = 1 \dots m$ **do**
    $\tilde{\boldsymbol{\beta}}_j = 2 \arccos\left(|(\hat{\boldsymbol{q}}_{b,j}^t)^\intercal \bar{\boldsymbol{q}}_b^t|\right)$
  end for
  if any($\tilde{\boldsymbol{\beta}}_j$) $> \alpha_{\text{det}}$ **then**
    $k = \arg\max_{j \in [1;m]} \tilde{\boldsymbol{\beta}}_j$
    Remove k^{th} quaternion $\hat{\boldsymbol{q}}_{b,k}^t$
  else
    b_dont_stop = false
  end if
end while
Output: $\bar{\boldsymbol{q}}_b^t$

5.6.3 Fusing $\hat{\sigma}_{ib,j}^b$

In contrast to the unit quaternions, $\hat{\boldsymbol{q}}_{b,j}^t$, the injection terms from the respective attitude observers, $\hat{\boldsymbol{\sigma}}_{ib,j}^b \in \mathbb{R}^3$ may evolve freely on $\mathbb{R}^3$ with no topological constraints. Thus, the fused injection term, $\bar{\boldsymbol{\sigma}}_{ib}^b$, to be used in the TMO, is easily obtained with a LS-based weighting,

$$\bar{\boldsymbol{\sigma}}_{ib}^b = \left(\sum_{j=1}^m w_j\right)^{-1} \sum_{j=1}^m w_j \hat{\boldsymbol{\sigma}}_{ib,j}^b \tag{5.39}$$

$$= \left(\boldsymbol{H}_{\hat{\sigma}}^\intercal \boldsymbol{R}_{\hat{\sigma}}^{-1} \boldsymbol{H}_{\hat{\sigma}}\right)^{-1} \boldsymbol{H}_{\hat{\sigma}}^\intercal \boldsymbol{R}_{\hat{\sigma}}^{-1} \boldsymbol{y}_{\hat{\sigma}}. \tag{5.40}$$

where

$$\boldsymbol{y}_{\hat{o}} = \left(\hat{\boldsymbol{o}}^{b\mathsf{T}}_{ib,1};\quad \hat{\boldsymbol{o}}^{b\mathsf{T}}_{ib,2};\quad \ldots;\quad \hat{\boldsymbol{o}}^{b\mathsf{T}}_{ib,m}\right), \tag{5.41}$$

$$\boldsymbol{H}_{\hat{o}} = \begin{pmatrix}\boldsymbol{I}_3 & \boldsymbol{I}_3 & \ldots & \boldsymbol{I}_3\end{pmatrix}^{\mathsf{T}}. \tag{5.42}$$

The matrix $\boldsymbol{H}_{\hat{o}}$ and vector $y_{\hat{o}}$ are modified according to the output of the FDI method in Section 5.6.2, meaning that $\hat{o}^b_{ib,k}$ from faulty observer k is removed. Using the scalar weights, the matrix $\boldsymbol{R}_{\hat{o}}$ of (5.40), which can be considered as a covariance matrix, is easily obtained as

$$\boldsymbol{R}_{\hat{o}} = \text{blockdiag}\left(\frac{1}{w_1}\boldsymbol{I}_3, \frac{1}{w_2}\boldsymbol{I}_3, \ldots, \frac{1}{w_m}\boldsymbol{I}_3\right). \tag{5.43}$$

The weights of $\boldsymbol{R}_{\hat{o}}$ does not have to be diagonal, allowing for a block-diagonal structure for $\boldsymbol{R}_{\hat{o}}$

$$\boldsymbol{R}_{\hat{o}} = \text{blockdiag}\left(\boldsymbol{R}_1, \boldsymbol{R}_2, \ldots, \boldsymbol{R}_m\right), \tag{5.44}$$

based on some design criteria of positive definite matrices $\boldsymbol{R}_j$.

5.7 Case Study

In this section we present a case study for redundant IMUs onboard an AHTS vessel operation in the Norwegian sea. A modified version of the translational motion observer in Section 5.4.2 will be employed. This TMO is designed specifically for surface vessels, and is described in Sec. 5.7.1. Regarding the sensor configuration, three redundant MEMS IMUs of the same type were installed, in addition to one MEMS IMU with higher quality angular rate sensor for comparison. The details of these and other sensors installed are presented in Section 5.7.2. The vessel was doing a dynamic positioning operation at the time of data recording, and the north-east plot of its track is shown in Fig. 4.3a

5.7.1 TMO applicable for ship navigation

The strapdown equations (5.10)–(5.11) can be extended with the auxiliary variable $p^t_{tb,I}$, applicable for marine surface craft navigation. The augmentation, first applied in Bryne et al. (2014), follows from the wave-induced motion of the surface craft, by which the mean vertical position of the vessel is zero over time since the heave position oscillates about the mean sea surface. From Bryne et al. (2015b) and the references therein we may write:

$$p^t_{tb,I} = \lim_{T\to\infty}\frac{1}{T}\int_0^T p^t_z(t)\mathrm{d}t = 0. \tag{5.45}$$

Based on (5.45) we augment the strapdown equations (5.10)–(5.11) by introducing p^n_I as a state with

$$\dot{p}^t_{tb,I} = p^t_{tb,z}, \tag{5.46}$$

by integrating the vertical (down) position associated with the heave motion. This motivates the inclusion of a new measurement $p^t_{tb,I} = 0$, denoted virtual vertical reference (VVR) (Bryne et al., 2014, 2015b).

The resulting TMO takes the form,

$$
\Sigma_2 : \begin{cases}
\dot{\hat{p}}^t_{tb,I} = \hat{p}^t_{tb,z} + \vartheta K_{p_I p_I} \tilde{p}^t_{tb,I}, & \text{(5.47a)} \\
\dot{\hat{\boldsymbol{p}}}^t_{tb} = \hat{\boldsymbol{v}}^t_{tb} \\
\qquad + \vartheta^2 \begin{pmatrix} \boldsymbol{0}_{2\times 1} \\ K_{pp_I} \end{pmatrix} \tilde{p}^t_{tb,I} + \vartheta \begin{pmatrix} \boldsymbol{K}_{pp} \\ 0 \quad 0 \end{pmatrix} \tilde{\boldsymbol{p}}^t_{tb}, & \text{(5.47b)} \\
\dot{\hat{\boldsymbol{v}}}^t_{tb} = -2\boldsymbol{S}(\boldsymbol{\omega}^t_{ie}) \hat{\boldsymbol{v}}^t_{tb} + \hat{\boldsymbol{f}}^t_{ib} + \boldsymbol{g}^t_b \\
\qquad + \vartheta^3 \begin{pmatrix} \boldsymbol{0}_{2\times 1} \\ K_{vp_I} \end{pmatrix} \tilde{p}^t_{tb,I} + \vartheta^2 \begin{pmatrix} \boldsymbol{K}_{vp} \\ 0 \quad 0 \end{pmatrix} \tilde{\boldsymbol{p}}^t_{tb}, & \text{(5.47c)} \\
\dot{\boldsymbol{\xi}}^t_{ib} = -\boldsymbol{R}(\bar{\boldsymbol{q}}^t_b) \boldsymbol{S}(\bar{\boldsymbol{\sigma}}^b_{ib}) \bar{\boldsymbol{f}}^b_{\text{IMU}} \\
\qquad + \vartheta^4 \begin{pmatrix} \boldsymbol{0}_{2\times 1} \\ K_{\xi p_I} \end{pmatrix} \tilde{p}^t_{tb,I} + \vartheta^3 \begin{pmatrix} \boldsymbol{K}_{\xi p} \\ 0 \quad 0 \end{pmatrix} \tilde{\boldsymbol{p}}^t_{tb}, & \text{(5.47d)} \\
\hat{\boldsymbol{f}}^t_{ib} = \boldsymbol{R}(\bar{\boldsymbol{q}}^t_b) \bar{\boldsymbol{f}}^b_{\text{IMU}} + \boldsymbol{\xi}^t_{ib}, & \text{(5.47e)}
\end{cases}
$$

where $\tilde{p}^t_{tb,I} = p^t_{tb,I} - \hat{p}^t_{tb,I}$, $\tilde{\boldsymbol{p}}^t_{tb} = \boldsymbol{p}^t_{\text{GNSS}} - (\hat{p}^t_{tb,x}, \hat{p}^t_{tb,y})^\intercal$. $K_{[\cdot]p_I}$ and $\boldsymbol{K}_{[\cdot]p}$ are fixed gains, while $\vartheta \geq 1$ is a tuning gain. Since the VVR provides $p^t_{tb,I} = 0$ for all $t \geq 0$, the vertical estimates of Σ_2 are self contained regardless of GNSS precision and accuracy or GNSS position fix. The gains may be chosen such that the feedback interconnection $\Sigma_1 - \Sigma_2$ possesses uniform semiglobal exponential stability (Bryne et al., 2015b).

5.7.2 Ship sensor configuration

We installed several MEMS inertial sensors on an AHTS vessel in operation in the Norwegian sea. The ship had a Rolls-Royce DP system installed, with all the onboard sensors' output available to us, see Appendix A for more details. The sensor configuration used was:

- 1x differential GNSS position measurement, $\boldsymbol{p}^t_{\text{GNSS}} = (p^t_{tb,x}, p^t_{tb,y})^\intercal$ at 1 Hz (only horizontal position is used).
- VVR: $p^t_{tb,I} = 0$, for all $t \geq 0$ (see Section 5.7.1).
- 3x ADIS 16485 IMUs and 1x STIM300 IMU, each providing
  - Tri-axial angular rate measurements, $\boldsymbol{\omega}^b_{\text{IMU}}$
  - Tri-axial accelerometer-based specific force measurements, $\boldsymbol{f}^b_{\text{IMU}}$

  all interfaced at 1000 Hz.

- Yaw measurements from a triple-redundant gyrocompass (GC) solution, ψ_c, at 5 Hz.

For the performance and FDI evaluations, the IMU measurements are filtered with a 6th order low-pass Butterworth filter with a cutoff frequency of 5 Hz.

For comparison, a VRU providing roll (ϕ) and pitch (θ) signals at 5 Hz was used. See Tab. 4.1 for specifications from the manufacturer. The specifications of the IMUs installed are presented in Tab. 4.2.

5.7.3 Accelerometer bias estimation

In Bryne et al. (2016), it was found that the accelerometer biases were sufficiently in-run stable over several days for attitude estimation, and a constant accelerometer bias estimate $\bar{\boldsymbol{b}}^b_{\text{acc}}$ was used. We will use the same approach here, meaning that

$$\boldsymbol{f}^b_{\text{IMU,i}} = \boldsymbol{f}^b_{\text{IMU}^*,\text{i}} - \bar{\boldsymbol{b}}^b_{\text{acc,i}} \tag{5.48}$$

where $\boldsymbol{f}^b_{\text{IMU}^*,\text{i}}$ is the raw measurement from the IMU. Alternatively, the approach of Grip et al. (2016) could be applied, augmenting (5.23) (or (5.47)) with an accelerometer bias estimator subject to a persistent excitation requirement.

5.7.4 Full-scale testing: Noise reduction

To obtain some estimates for angular rate sensor and accelerometer noise, we perform *high-pass* filtering of the raw measurements with a 6th order Butterworth filter to remove bias and the vehicle motion, and calculate the standard deviation of the result. An example of the output is seen in Fig. 5.4. This will at least give us the possibility to compare the individual sensors to each other, and to the aggregated output based on several sensors. The results are presented in Tabs. 5.1–5.2, and show a slight reduction of noise. According to (5.16), we could have hoped for a reduction by the factor of $\sqrt{m} \approx 1.73$, but only for the z-axis angular rate sensor do we come close to that number. This is due to ship vibrations affecting the IMU noise reduction obtained by the LS weighting. Because of the noisy nature of the IMU measurements, we will employ the *low-pass* filter mentioned in Sec. 5.7.2 for the remainder of this chapter.

5.7.5 Full-scale testing: Attitude and heave performance evaluation

Both Alternatives 1 and 2 are compared with single-IMU solutions for attitude and heave estimation, and the onboard VRU serves as reference. The results are presented in Tabs. 5.3–5.4 in the form of mean error, root mean square error (RMSE) and cumulative estimation error (CAE), and show that for attitude there really is not much of a difference between the different alternatives and IMUs. This is in compliance with the findings of Chapter 4, where it was discovered that the choice

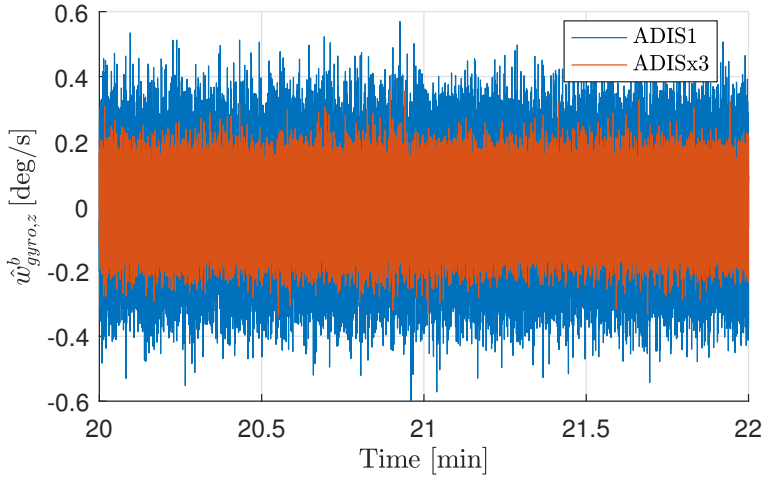

Figure 5.4: Noise estimates for z-axis angular rate sensor.

Table 5.1: Noise standard deviation estimates for angular rate sensors, in degrees/s.

	ADISx3	**ADIS1**	**ADIS2**	**ADIS3**	**STIM**
$\hat{\sigma}_{gyro,x}$	0.1162	0.1546	0.1545	0.1668	0.1252
$\hat{\sigma}_{gyro,y}$	0.1707	0.2101	0.2037	0.2073	0.1460
$\hat{\sigma}_{gyro,z}$	0.0776	0.1363	0.1194	0.1247	0.0881

Table 5.2: Noise standard deviation estimates for accelerometers, in m/s^2.

	ADISx3	**ADIS1**	**ADIS2**	**ADIS3**	**STIM**
$\hat{\sigma}_{acc,x}$	0.0557	0.0905	0.0400	0.0611	0.0432
$\hat{\sigma}_{acc,y}$	0.0441	0.0669	0.0343	0.0482	0.0485
$\hat{\sigma}_{acc,z}$	0.0696	0.0749	0.0750	0.0746	0.0616

of estimator had more impact than the choice of IMU. Even using a significantly more noisy signal yielded approximately the same estimation error compared to the VRU. When it comes to heave estimation, the results vary more, and apparently using a combined accelerometer input is favorable. Figs. 5.5–5.7 presents example output from Alternative 2 for attitude and heave, where the weighted result is denoted with w. Fig. 5.8 shows the fault-detection variables for both the parity space method and quaternion averaging in a fault-free case.

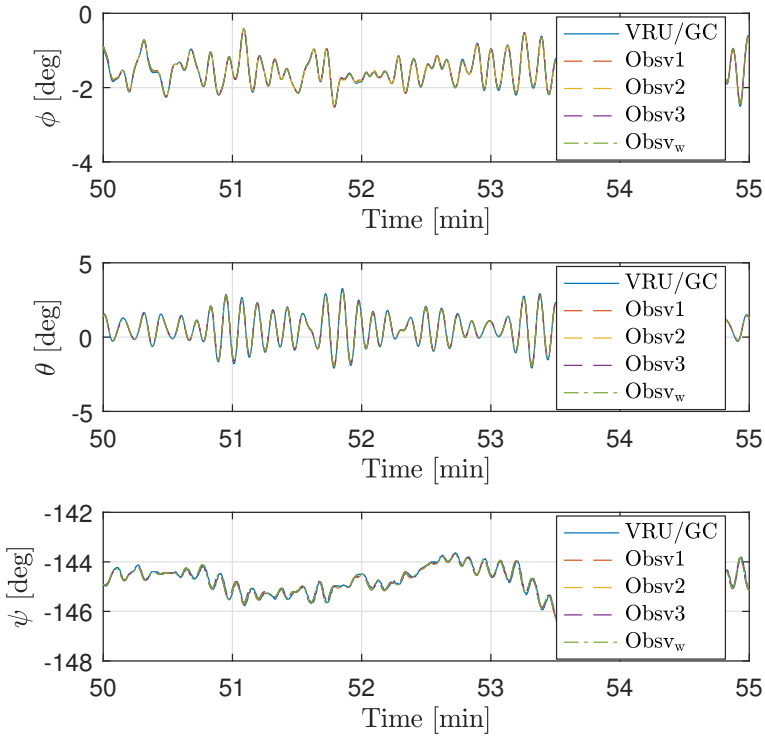

Figure 5.5: Attitude estimation with ADIS16485 quaternion averaging.

Table 5.3: Attitude estimation error compared to onboard VRU, in degrees.

	ADISx3 Alt. 1	**ADISx3 Alt. 2**	**ADIS2** (Tab. 4.6)	**STIM** (Tab. 4.6)
Roll mean error	0.0008	0.0011	-0.0007	-0.0044
Pitch mean error	0.0009	0.0009	0.0047	0.0016
Roll RMSE	0.0310	0.0328	0.0363	0.0299
Pitch RMSE	0.0653	0.0662	0.0670	0.0649
Roll CAE	648.28	687.92	759.80	628.99
Pitch CAE	1370.6	1389.1	1406.0	1357.5

5.7.6 Full-scale testing: Dead-reckoning performance evaluation

In Section 4.8, the dead-reckoning capabilities of the ADIS16485 and STIM300 IMUs were evaluated. It was found that they had similar potential, but with the specific units available the STIM300 was slightly better. Now, we will exploit our redundant ADIS16485 IMUs to see if there is any improve to be had in dead-reckoning. As in Section 4.8.2, to obtain statistically significant results we perform

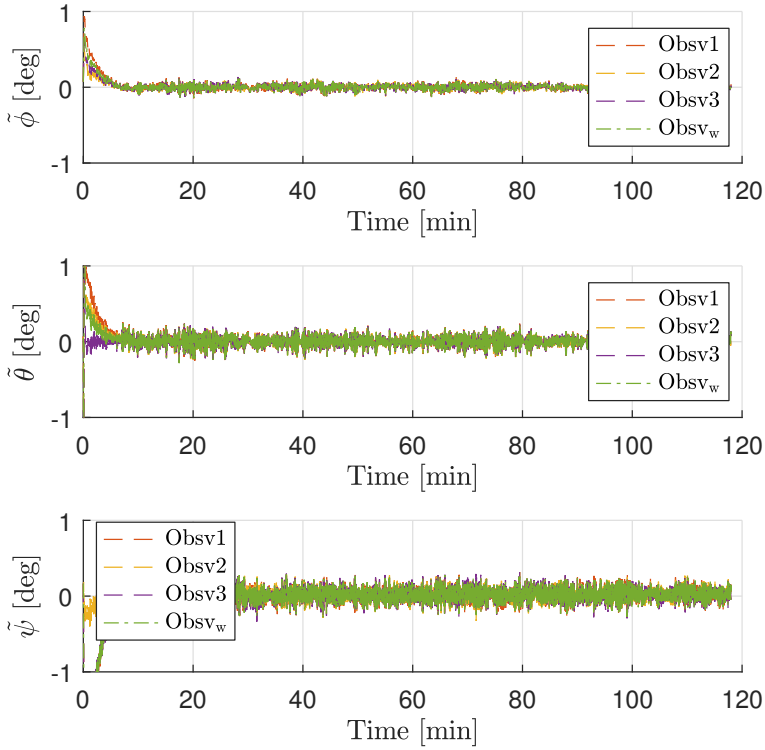

Figure 5.6: Attitude estimation error with triple-redundant ADIS16485 quaternion averaging.

Table 5.4: Heave estimation error compared to onboard VRU, in cm.

	ADISx3 Alt. 1	**ADISx3 Alt. 2**	**ADIS2** (Tab. 4.11)	**STIM** (Tab. 4.11)
Mean heave error	-0.6147	-0.6147	-0.6511	-0.6005
RMSE heave	4.0515	4.0515	5.7766	10.523
CAE heave	855.93	855.93	1215.0	2207.3

60 dead-reckoning runs (using different fragments of the dataset) by comparing the evolution of position errors after disabling GNSS feedback at selected intervals. The position evaluation metric is created by taking the norm of the difference between the horizontal components of $\boldsymbol{p}^t_{\text{GNSS}}$ and $\hat{\boldsymbol{p}}^t_{\text{GNSS}}$, defined as $\tilde{\boldsymbol{p}}^t_{\text{GNSS}} := \boldsymbol{p}^t_{\text{GNSS}} - \hat{\boldsymbol{p}}^t_{\text{GNSS}}$ where,

$$\hat{\boldsymbol{p}}^t_{\text{GNSS}} = \hat{\boldsymbol{p}}^t_{tb} + \boldsymbol{R}(\bar{\boldsymbol{q}}^t_b)\boldsymbol{r}^b_b, \tag{5.49}$$

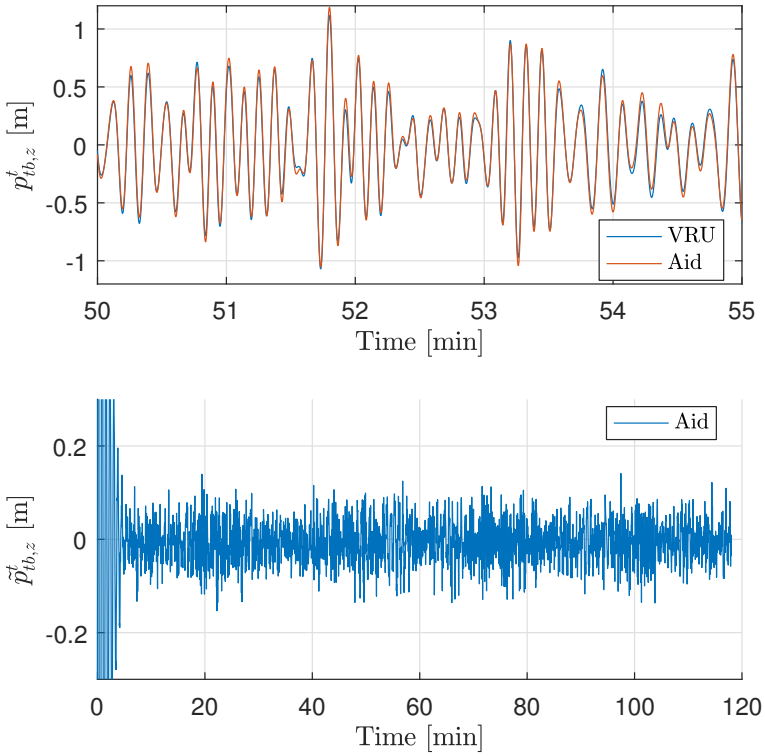

Figure 5.7: Heave estimation with triple-redundant ADIS16485 IMUs.

and where $\boldsymbol{r}^b_b$ is the lever arm from the IMU to the GNSS antenna position such that

$$\begin{aligned} \|\tilde{\boldsymbol{p}}^t_{\text{GNSS}}\|_2 &= \|\boldsymbol{p}^t_{tb} + \boldsymbol{R}^t_b \boldsymbol{r}^b_b - \hat{\boldsymbol{p}}^t_{tb} - \boldsymbol{R}(\bar{\boldsymbol{q}}^t_b)\boldsymbol{r}^b_b\|_2, \\ &= \|\tilde{\boldsymbol{p}}_{tb} + \left(\boldsymbol{R}^t_b - \boldsymbol{R}(\bar{\boldsymbol{q}}^t_b)\right)\boldsymbol{r}^b_b\|_2. \end{aligned} \tag{5.50}$$

For these tests, the exact same method as in Section 4.4.3 is used, employing another TMO in cascade with Σ_1, estimating a residual accelerometer bias. The feedback interconnection of (5.23d) containing the specific force estimate $\hat{\boldsymbol{f}}^t_{ib}$ is not used in this observer structure, as this arrangement collapses in the face of position reference outage. The outcome from the dead-reckoning test can be found in Tab. 5.5 where the results from Section 4.8.2 are included for comparison, and Figs. 5.9–5.10 (see also Fig. 4.10).

As we can see, using three IMUs does improve upon the dead-reckoning capabilities, especially for alternative 2 with quaternion averaging, approximately matching the use of a single STIM300.

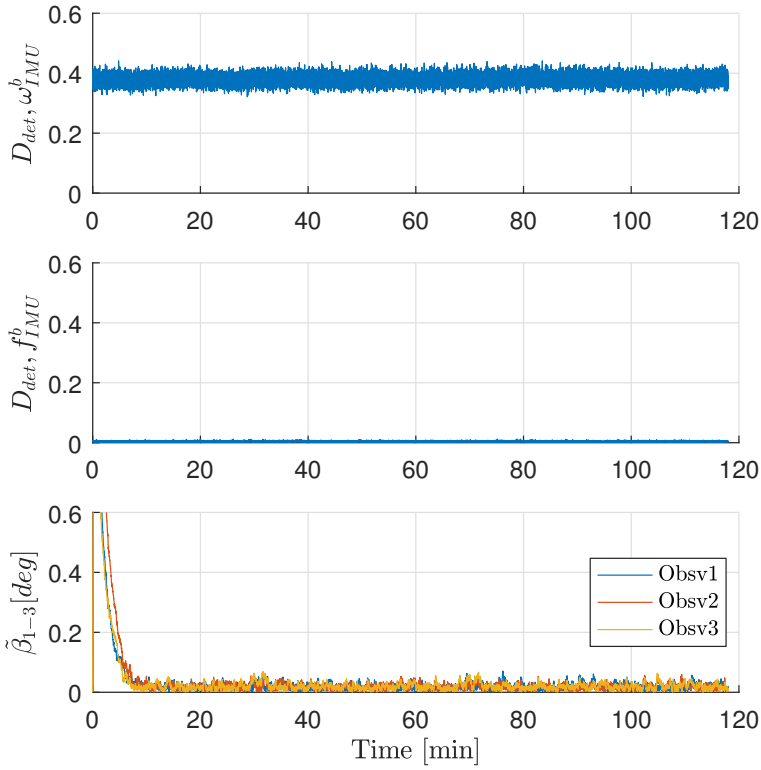

Figure 5.8: Fault detection variables in fault-free case. Top: Parity space method for angular rate sensor (Alternative 1). Middle: Parity space method for accelerometer (both Alternative 1 and 2). Bottom: Quaternion fault angles (Alternative 2).

5.7.7 Full-scale testing: FDI

In this section we will use the same dataset as in Section 5.7.4– 5.7.6, and add artificial faults to the accelerometer and angular rate sensor.

Accelerometer fault

An additional bias of 1 m/s^2 is added to the x-axis of ADIS2 at t = 20min. Since the accelerometer FDI for both alternatives is based on the exact same parity space method, the results are expected to be the same. Fig. 5.11 shows the fault detection variables and the fault status of the faulty accelerometer. The faulty sensor is removed in an orderly fashion, and practically no effect is seen on the estimates. Since the parity space method only removes one axis, the observers may still make use of the remaining eight axes to full effect.

Table 5.5: Dead-reckoning results in meters.

	ADISx3 Alt. 1	**ADISx3 Alt. 2**	**ADIS2** (Tab. 4.15)	**STIM** (Tab. 4.15)
Mean error 1 min	3.6617	3.6276	4.3014	3.2885
Mean error 5 min	29.674	27.054	35.125	25.762
Mean error 10 min	96.749	82.869	102.12	83.927
Min error 10 min	7.5878	13.040	11.639	3.0962
Max error 10 min	216.09	210.73	264.03	231.74
RMSE 10 min	110.88	94.810	115.74	96.141

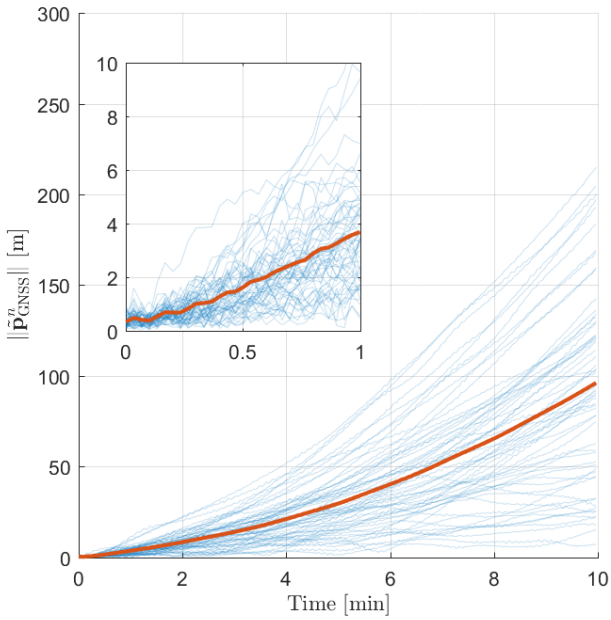

Figure 5.9: Dead-reckoning errors obtained with three ADIS16485, alt. 1. Red curve is mean error.

Angular rate sensor fault

For ADIS3, the gyro bias is increased by 1 deg/s on the y-axis at $t = 20$min. For Alternative 1, we observe from Fig. 5.12 that the attitude estimates deviate when the fault occurs, before converging back to its previous state. The reason can be seen in Fig. 5.13: When one the faulty angular rate sensor axis is removed, the bias balance of the combined sensor output is shifted, and the estimator needs some time to estimate the new bias level. From Fig. 5.14 we can see that the fault

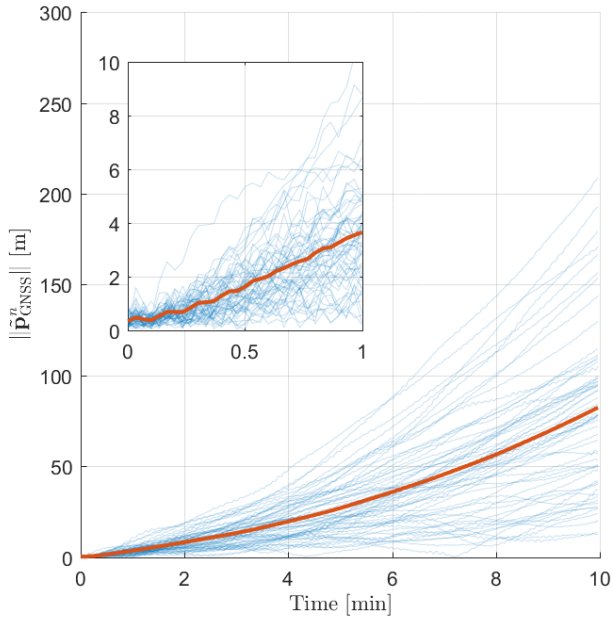

Figure 5.10: Dead-reckoning errors obtained with three ADIS16485, alt. 2. Red curve is mean error.

is detected and isolated sufficiently.

From Fig.5.15 we learn that the averaged attitude estimates of Alternative 2 are not significantly affected by the fault, while the one faulty estimator remains erroneous. Fig.5.16 shows the fault detection and isolation at work. After a transient period the first five minutes, the $\tilde{\beta}_j$ angles remain under the threshold α_{det}, before the fault occurs at t = 20min. The fault is then properly detected and isolated, and the faulty estimator output is removed from the quaternion average.

5.7.8 Discussion

For the noise reduction, we did not achieve the theoretical levels from (5.16). This is most likely because much of the noise is not independent from sensor to sensor, but rather common mechanical vibrations or electrical disturbances. For the z-axis of the accelerometer the reduction was only around 7%, strongly suggesting that the noise is correlated. The STIM300 we used for comparison had a slightly better noise characteristic than the individual ADIS16485s, but the combined output brought the latter to the same levels.

As far as performance goes, not much was achieved for the attitude estimation

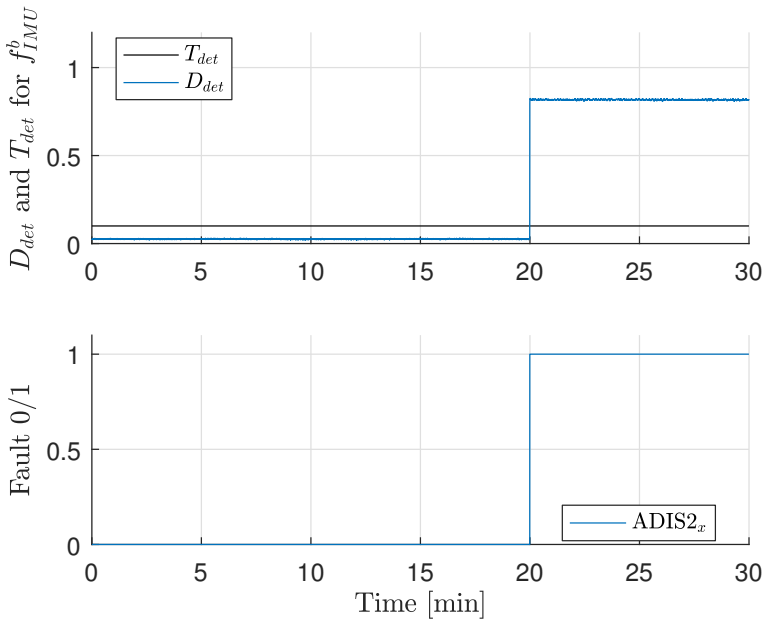

Figure 5.11: Fault detection for accelerometer fault. Parity space method.

by combining the IMUs, while heave estimation saw some improvement. The accelerometer plays a major role in this regard, so reducing the noise and bias before using it in (5.47) is evidently helpful. Even though the STIM300 had better noise characteristics according to Tab. 5.2, it proved worse than both the combining of three IMUs and a single IMU of type ADIS16485. This probably has something to do with the accelerometer bias in-run stability, which is a bit worse in specification for STIM300.

For dead-reckoning, improvements were seen by using three ADIS16485 instead of just one, with alternative 2 providing the best results. However, the redundant IMU solutions still did not surpass the single STIM300. This seems somewhat counter-intuitive, as the STIM300 apparently has an inferior accelerometer, and one would assume that the accelerometer is of great importance during position dead-reckoning. Seemingly, the angular rate sensor seems to be equally decisive in this matter.

Fault detection and isolation for the accelerometer with the parity space method proved successful. With much of the bias removed as per (5.48), the detection variable D_{det} clearly indicated a detected fault, while (5.33) found which sensor was misbehaving. For the angular rate sensors however, a problem arose as shown in Fig. 5.13. The bias estimates were disturbed, causing a perturbation in the attitude estimate. The quaternion-based FDI algorithm fared better in this concern, quickly voting out the erroneous estimator. After the estimate of

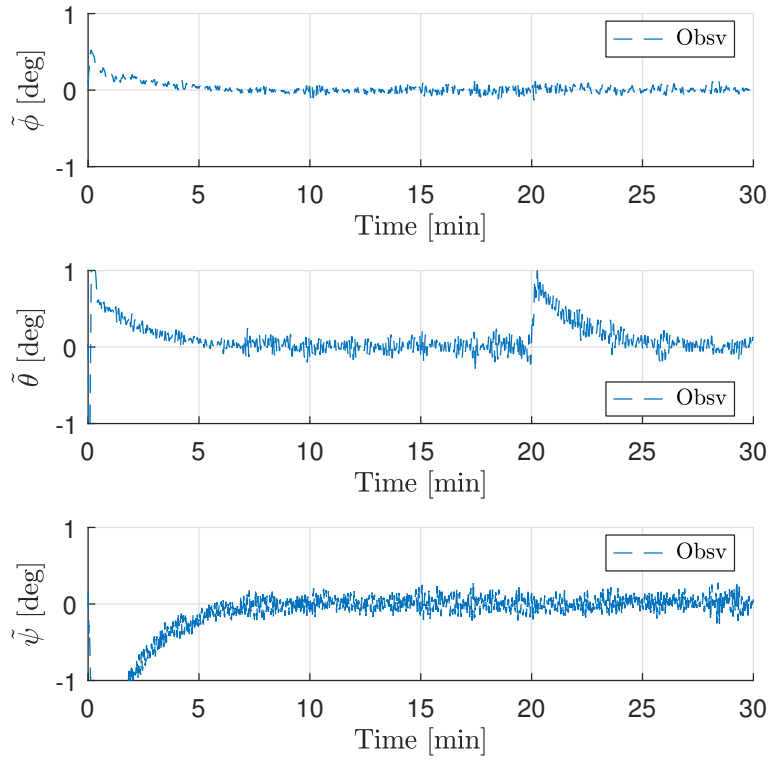

Figure 5.12: Attitude estimation error. Parity space method for angular rate sensor (Alternative 1).

Alternative 1 has converged again on the other hand, this method has the upper hand, seeing as eight gyro axes are still in play, versus only six in Alternative 2, since a whole gyro triad providing input to the faulty observer is removed.

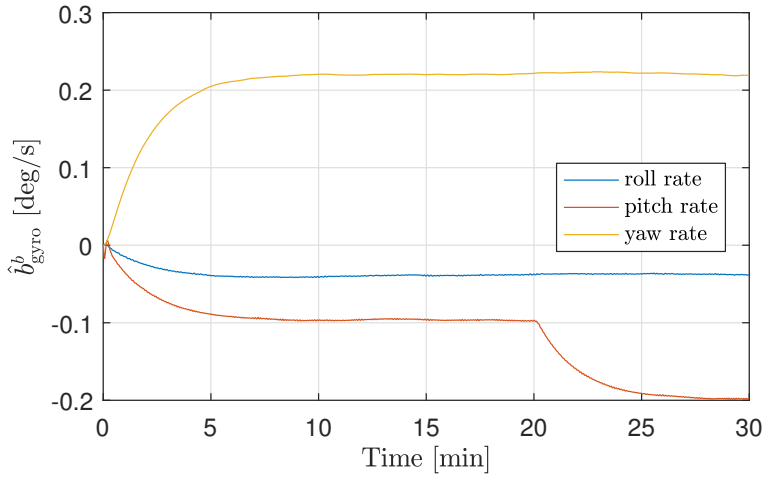

Figure 5.13: Gyro bias estimates. Parity space method for angular rate sensor (Alternative 1).

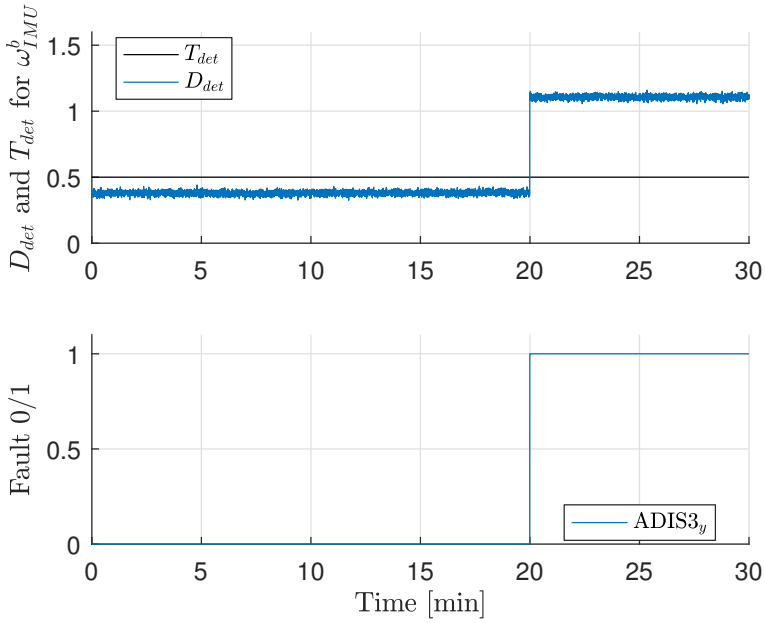

Figure 5.14: Fault detection for angular rate sensor fault. Parity space method (Alternative 1).

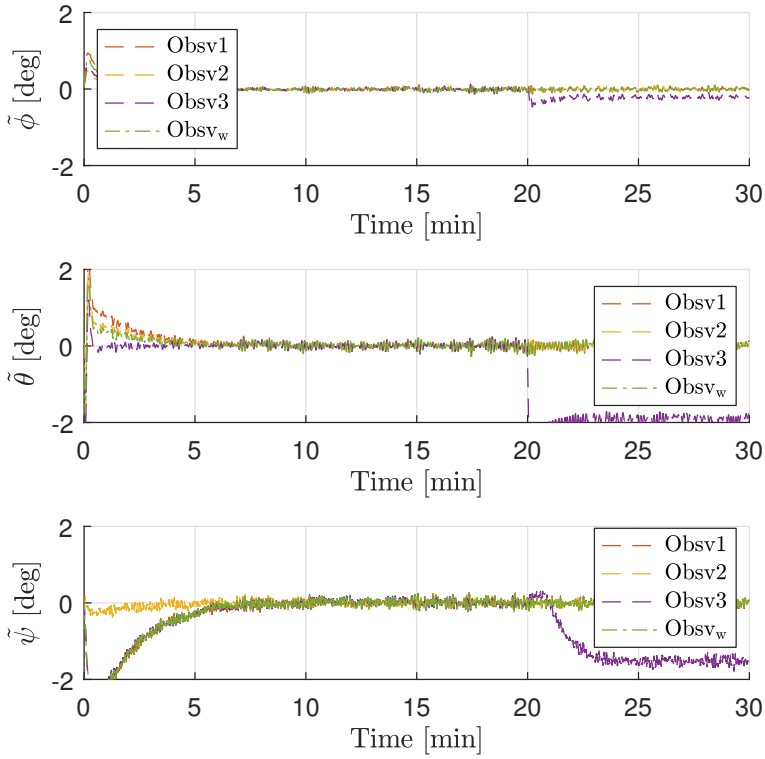

Figure 5.15: Attitude estimation error. Quaternion FDI method angular rate sensor (Alternative 2).

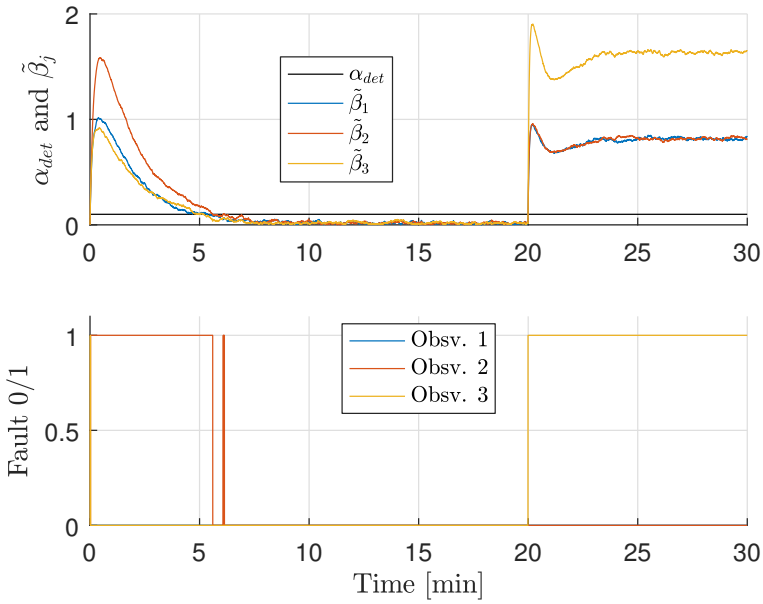

Figure 5.16: Fault detection for angular rate sensor fault. Quaternion FDI (Alternative 2).

5.8 Conclusion

Two alternatives for redundant MEMS IMUs using nonlinear observers has been presented. One alternative was based on the classic parity space method, while the other also employed a quaternion-based averaging, fault detection and fault isolation scheme. The structural differences between the alternatives were layed out, and we developed algorithms for both. The algorithms were validated on full-scale experimental data acquired from an offshore vessel, using three ADIS16485 IMUs. A STIM300, with a better angular rate sensor, was used for comparison. In addition, we also used the ship's industry-proven sensors for comparison, while the onboard gyrocompasses were used to aid the attitude observers. For attitude estimation, there was little to gain from redundant IMUs in this context, while for heave estimation and dead-reckoning there were some improvements.

Simulated faults were added to the signals for fault detection and isolation (FDI). In the accelerometer fault case, the fault was detected and isolated rapidly, and the FDI in this case was purely based on the parity space method in both alternatives. For the angular rate sensor fault, the parity space method implemented here showed some weaknesses compared to the quaternion-based method, but both methods successfully detected and isolated the fault.

For further work, one could consider finding ways of adding the accelerometer to the quaternion-based scheme as well. This was not done here because of the feedback-interconnection between the nonlinear attitude observer and the aiding translational motion observer, that is somewhat sensitive to accelerometer disturbances.

6

Position and Heading Reference Fault Detection and Isolation

This chapter is based on Rogne et al. (2015).

6.1 Introduction

In DP classes 2 and 3, there are currently requirements for triple redundancy in position reference systems and vessel sensors (see Chapter 8). However, as discussed in the first chapter, complete independence may be hard to achieve, with possibly only two different principles for position determination to lean on in deep waters. This chapter looks into the use of IMUs as a separate principle for position and heading information, in the context of nonlinear attitude observers.

In this chapter, three nonlinear state-of-the-art attitude estimators are compared, with the motivation for usage in a fault detection and isolation (FDI) setup. In Hua et al. (2014); Grip et al. (2013), the observers make use of magnetometer readings as one of the vector measurements, while we employ a gyrocompass instead. The contribution of this chapter is related to:

- Attitude observer characteristics and comparison
- Stability of a cascade comprising the nonlinear observers and a translational motion observer aided by GNSS
- Simulation of two FDI cases with posref system and gyrocompass fault.

6.1.1 Organization of the chapter

In Section 6.2 the system kinematics and the observer dynamics are presented. In Section 6.3 simulations are carried out in order to evaluate the capabilities of the observers in a DP scenario with one failing posref system or one failing gyrocompass.

6.2 Attitude observers

6.2.1 The concept for comparison and FDI

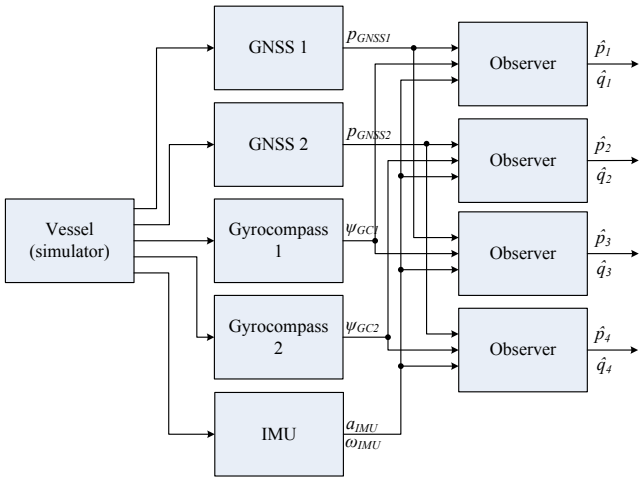

Figure 6.1: Four observers in parallel.

The three attitude estimators that will be compared are two variants of the nonlinear estimator of Grip et al. (2013), and the observer presented in Hua et al. (2014). One of them, as we shall see below, also provides estimates for position and velocity, but these will only be used internally by the observer to aid the attitude estimation. In order to compare them for FDI in position reference systems, a translational motion observer aided by GNSS from (Fossen, 2011, Ch. 11) will be added in cascade to all observers.

Fig. 6.1 shows the structure employed for detection and isolation of faults in either of the two posref systems, GNSS 1 and 2, or either of the two gyrocompasses. The notation is explained in Section 6.2.2. All the observers in Fig. 6.1 are identical, only the inputs differ between them. A fault can be easily be detected by comparing the measurements directly, since diverging values will indicate a fault. Isolation of the fault on the other hand will require some form of analysis of the observer outputs, and then tracing the fault back to the sensors feeding the observer.

For the simulation tests three such setups will be simulated in parallel, in order to compare the observers presented in later sections.

6.2.2 General assumptions and notation

The following assumptions and simplifications are made:

- Earth rotation is neglected and the north-east-down frame $\{n\}$ is assumed to be the inertial reference.

- IMU accelerometer biases are neglected, i.e. biases are assumed to be accounted for in calibration.
- No lever arms between measuring equipment and vessel origin.

Notation:

- $\boldsymbol{p}_{nb}^{n}$ - position of the origin of the body frame $\{b\}$ with respect to $\{n\}$ expressed in $\{n\}$
- $\boldsymbol{v}_{nb}^{n}$ - linear velocity of the origin of the body frame $\{b\}$ with respect to $\{n\}$ expressed in $\{n\}$
- ψ - yaw angle between between $\{b\}$ and $\{n\}$
- $\boldsymbol{\omega}_{nb}^{b}$ - body-fixed angular velocity
- $\boldsymbol{b}_{\text{gyro}}^{b}$ - gyro bias
- $\boldsymbol{q}_{b}^{n}$ - quaternion representation of rotation $\{b\}$ to $\{n\}$
- $\boldsymbol{R}_{b}^{n} = \boldsymbol{R}(\boldsymbol{q}_{b}^{n})$ and $\boldsymbol{R}_{n}^{b} = \boldsymbol{R}_{b}^{n\top}$ are the rotation matrices to $\{n\}$ from $\{b\}$ and vice versa, respectively
- $\boldsymbol{S}(\boldsymbol{x})$ - skew symmetric matrix:

$$\boldsymbol{S}(\boldsymbol{x}) = \begin{bmatrix} 0 & -x_3 & x_2 \\ x_3 & 0 & -x_1 \\ -x_2 & x_1 & 0 \end{bmatrix}, \ \boldsymbol{x} = \begin{bmatrix} x_1 \\ x_2 \\ x_3 \end{bmatrix}$$

- $\boldsymbol{g}_{b}^{n}$ - local gravity vector
- $\boldsymbol{f}_{\text{IMU}}^{b}$ - accelerometer specific force measurement in the body/vessel frame
- $\boldsymbol{\omega}_{\text{IMU}}^{b}$ - angular velocity measurement of the body
- $\boldsymbol{p}_{\text{GNSS}}^{n}$ - position measurement
- ψ_{c} - gyrocompass heading measurement

The kinematics of the system can be described as follows:

$$\dot{\boldsymbol{p}}_{nb}^{n} = \boldsymbol{v}_{nb}^{n} \tag{6.1a}$$
$$\dot{\boldsymbol{v}}_{nb}^{n} = \boldsymbol{R}(\boldsymbol{q}_{\boldsymbol{b}}^{\boldsymbol{n}})\boldsymbol{f}_{nb}^{b} + \boldsymbol{g}_{b}^{n} \tag{6.1b}$$
$$\dot{\boldsymbol{q}}_{\boldsymbol{b}}^{\boldsymbol{n}} = \frac{1}{2}\boldsymbol{\Omega}(\boldsymbol{\omega}_{nb}^{b})\boldsymbol{q}_{b}^{n} \tag{6.1c}$$
$$\boldsymbol{p}_{\text{GNSS}}^{n} = \boldsymbol{p}_{nb}^{n} + \boldsymbol{w}_{p} \tag{6.1d}$$
$$\psi_{\text{c}} = \psi + w_{\psi} \tag{6.1e}$$

where

$$\boldsymbol{\Omega}(\boldsymbol{x}) = \begin{bmatrix} \boldsymbol{0} & -\boldsymbol{x}^\top \\ \boldsymbol{x} & -\boldsymbol{S}(\boldsymbol{x}) \end{bmatrix} \tag{6.2}$$

where $\boldsymbol{w_p}$ and w_ψ represent disturbances or measurement faults on the position and heading, respectively. The disturbances will change according to various faults that might occur in the measuring equipment.

6.2.3 Nonlinear Observer 1

Nonlinear Observer 1a

This observer is a further development of the *Explicit complementary filter with bias correction* described in Mahony et al. (2008). Observer equations from Grip et al. (2013), sans GNSS velocity measurements and using gyrocompass heading instead of magnetometer for the second vector measurement:

$$\dot{\hat{\boldsymbol{p}}}^n_{nb} = \hat{\boldsymbol{v}}^n_{nb} + \vartheta \boldsymbol{K}_{pp}(\boldsymbol{p}^n_{\text{GNSS}} - \hat{\boldsymbol{p}}^n_{nb}) \tag{6.3a}$$

$$\dot{\hat{\boldsymbol{v}}}^n_{nb} = \hat{\boldsymbol{f}}^n_{nb} + \boldsymbol{g}^n_b + \vartheta^2 \boldsymbol{K}_{vp}(\boldsymbol{p}^n_{\text{GNSS}} - \hat{\boldsymbol{p}}^n_{nb}) \tag{6.3b}$$

$$\begin{aligned} \dot{\boldsymbol{\xi}}^n_{nb} = &-\boldsymbol{R}(\hat{\boldsymbol{q}}^n_b)\boldsymbol{S}(\hat{\boldsymbol{\sigma}}^b_{nb})\boldsymbol{f}^b_{\text{IMU}} + \\ &\vartheta^3 \boldsymbol{K}_{\xi p}(\boldsymbol{p}^n_{\text{GNSS}} - \hat{\boldsymbol{p}}^n_{nb}) \end{aligned} \tag{6.3c}$$

$$\dot{\hat{\boldsymbol{q}}}^n_b = \frac{1}{2}\boldsymbol{\Omega}(\hat{\boldsymbol{\omega}}^b_{nb})\hat{\boldsymbol{q}}^n_b \tag{6.3d}$$

$$\dot{\hat{\boldsymbol{b}}}^b_{\text{gyro}} = \text{Proj}(\hat{\boldsymbol{b}}^b_{\text{gyro}}, -k_I \hat{\boldsymbol{\sigma}}^b_{nb}) \tag{6.3e}$$

$$\hat{\boldsymbol{f}}^n_{nb} = \boldsymbol{R}(\hat{\boldsymbol{q}}^n_b)\boldsymbol{f}^b_{\text{IMU}} + \boldsymbol{\xi}^n_{nb} \tag{6.3f}$$

$$\hat{\boldsymbol{\sigma}}^b_{nb} = k_1 \boldsymbol{v}^b_1 \times \boldsymbol{R}^\top(\hat{\boldsymbol{q}}^n_b)\boldsymbol{v}^n_1 + k_2 \boldsymbol{v}^b_2 \times \boldsymbol{R}^\top(\hat{\boldsymbol{q}}^n_b)\boldsymbol{v}^n_2 \tag{6.3g}$$

$$\hat{\boldsymbol{\omega}}^b_{nb} = \boldsymbol{\omega}^b_{\text{IMU}} - \hat{\boldsymbol{b}}^b_{\text{gyro}} + \hat{\boldsymbol{\sigma}}^b_{nb} \tag{6.3h}$$

where $\boldsymbol{K}_{pp}$, $\boldsymbol{K}_{pp}$ and $\boldsymbol{K}_{\xi p}$ are gain matrices chosen such that $\boldsymbol{A} - \boldsymbol{KC}$ is Hurwitz, where

$$A = \begin{bmatrix} \boldsymbol{0} & \boldsymbol{I}_3 & \boldsymbol{0} \\ \boldsymbol{0} & \boldsymbol{0} & \boldsymbol{I}_3 \\ \boldsymbol{0} & \boldsymbol{0} & \boldsymbol{0} \end{bmatrix}, C = \begin{bmatrix} \boldsymbol{I}_3 & \boldsymbol{0} & \boldsymbol{0} \end{bmatrix} K = \begin{bmatrix} \boldsymbol{K}_{pp} \\ \boldsymbol{K}_{vp} \\ \boldsymbol{K}_{\xi p} \end{bmatrix}$$

Furthermore, ϑ is a tuning parameter larger than or equal to 1, used to guarantee stability, $k_I > 0$ is a gain, $\text{Proj}(\cdot, \cdot)$ is a parameter projection that puts a restriction on the estimate $\hat{\boldsymbol{b}}^b_{\text{gyro}}$, see Grip et al. (2012a) for details. k_1 and k_2 of the injection term $\hat{\boldsymbol{\sigma}}^b_{nb}$ are gains satisfying $k_1 \geq k_p$ and $k_2 \geq k_p$ for a $k_p > 0$. The other factors of

(6.3) are:

$$\boldsymbol{v}_1^b = \frac{\boldsymbol{f}_{\text{IMU}}^b}{||\boldsymbol{f}_{\text{IMU}}^b||},\ \boldsymbol{v}_2^b = \frac{\boldsymbol{f}_{\text{IMU}}^b \times \boldsymbol{c}_{nb}^b}{||\boldsymbol{f}_{\text{IMU}}^b \times \boldsymbol{c}_{nb}^b||}$$
$$\boldsymbol{v}_1^n = \frac{\hat{\boldsymbol{f}}_{nb}^n}{||\hat{\boldsymbol{f}}_{nb}^n||},\ \boldsymbol{v}_2^n = \frac{\hat{\boldsymbol{f}}_{nb}^n \times \boldsymbol{c}_{nb}^n}{||\hat{\boldsymbol{f}}_{nb}^n \times \boldsymbol{c}_{nb}^n||} \tag{6.4}$$

where

$$\boldsymbol{c}_{nb}^b = \begin{bmatrix} \cos(\psi_c) \\ -\sin(\psi_c) \\ 0 \end{bmatrix},\ \boldsymbol{c}_{nb}^n = \begin{bmatrix} 1 \\ 0 \\ 0 \end{bmatrix} \tag{6.5}$$

The position and velocity, and attitude estimators of Nonlinear Observer 1 form a feedback interconnection. In Grip et al. (2013), this feedback interconnection is proved to have a uniform semi-global exponentially stable (USGES) equilibrium point.

Nonlinear Observer 1b

From (6.3) we notice that p_{GNSS}^n is part of the observer equations of Nonlinear Observer 1. In the case of a GNSS fault, this signal cannot be trusted, and may cause errors in the attitude estimation and FDI. We therefore also test Nonlinear Observer 1a without the feedback interconnection, and call the resulting observer Nonlinear Observer 1b. In this case, the feedback from the position estimate is removed. This is achieved by instead of (6.4), using:

$$\boldsymbol{v}_1^b = -\frac{\boldsymbol{f}_{\text{IMU}}^b}{||\boldsymbol{g}_b^n||},\ \boldsymbol{v}_2^b = -\frac{\boldsymbol{f}_{\text{IMU}}^b \times \boldsymbol{c}_{nb}^b}{||\boldsymbol{g}_b^n \times \boldsymbol{c}_{nb}^n||}$$
$$\boldsymbol{v}_1^n = \frac{\boldsymbol{g}_b^n}{||\boldsymbol{g}_b^n||},\ \boldsymbol{v}_2^n = \frac{\boldsymbol{g}_b^n \times \boldsymbol{c}_{nb}^n}{||\boldsymbol{g}_b^n \times \boldsymbol{c}_{nb}^n||} \tag{6.6}$$

where $\boldsymbol{g}_b^n = [0\ 0\ g]^\top$.

6.2.4 Nonlinear Observer 2

This observer is also based on the *Explicit complementary filter with bias correction* described in Mahony et al. (2008). Observer equations from Hua et al. (2014), using

gyrocompass instead of magnetometer for the second vector measurement:

$$\dot{\hat{\boldsymbol{q}}}_b^n = \frac{1}{2}\boldsymbol{\Omega}(\hat{\boldsymbol{\omega}}_{nb}^b)\hat{\boldsymbol{q}}_b^n \tag{6.7a}$$

$$\dot{\hat{\boldsymbol{b}}}_{\text{gyro}}^b = -k_b\hat{\boldsymbol{b}}_{\text{gyro}}^b + k_b\text{sat}_\Delta(\hat{\boldsymbol{b}}_{\text{gyro}}^b) - \boldsymbol{\sigma_b} \tag{6.7b}$$

$$\boldsymbol{\sigma_R} = k_1\boldsymbol{v}_1^b \times \hat{\boldsymbol{v}}_1^b + k_2\hat{\boldsymbol{v}}_1^b\hat{\boldsymbol{v}}_1^{b\top}(\boldsymbol{v}_2^b \times \hat{\boldsymbol{v}}_2^b) \tag{6.7c}$$

$$\boldsymbol{\sigma_b} = k_3\boldsymbol{v}_1^b \times \hat{\boldsymbol{v}}_1^b + k_4\boldsymbol{v}_2^b \times \hat{\boldsymbol{v}}_2^b \tag{6.7d}$$

$$\hat{\boldsymbol{\omega}}_{nb}^b = \boldsymbol{\omega}_{\text{IMU}}^b - \hat{\boldsymbol{b}}_{\text{gyro}}^b + \boldsymbol{\sigma_R} \tag{6.7e}$$

where

$$\begin{gathered}
\boldsymbol{v}_1^b = -\frac{\boldsymbol{f}_{\text{IMU}}^b}{g},\ \boldsymbol{v}_2^b = \frac{\pi_{\boldsymbol{v}_1^b}\boldsymbol{c}^b}{||\pi_{\boldsymbol{v}_1^n}\boldsymbol{c}^n||} \\
\boldsymbol{v}_1^n = \begin{bmatrix}0\\0\\1\end{bmatrix},\ \boldsymbol{v}_2^n = \frac{\pi_{\boldsymbol{v}_1^n}\boldsymbol{c}^n}{||\pi_{\boldsymbol{v}_1^n}\boldsymbol{c}^n||} \\
\hat{\boldsymbol{v}}_1^b = \boldsymbol{R}^\top(\hat{\boldsymbol{q}}_b^n)\boldsymbol{v}_1^n,\ \hat{\boldsymbol{v}}_2^b = \boldsymbol{R}^\top(\hat{\boldsymbol{q}}_b^n)\boldsymbol{v}_2^n \\
\pi_{\boldsymbol{x}} = ||\boldsymbol{x}||^2\boldsymbol{I}_3 - \boldsymbol{x}\boldsymbol{x}^\top
\end{gathered} \tag{6.8}$$

Furthermore, k_1, k_2, k_3, k_4, k_b and Δ are positive numbers. $\text{sat}_\Delta(\cdot)$ denotes the saturation function $\text{sat}_\Delta(\boldsymbol{x}) = \boldsymbol{x}\min(1, \Delta/||\boldsymbol{x}||)$. k_3 must be chosen to be strictly larger than k_4.

In Hua et al. (2014), the observer (6.7) is proven to be "almost-globally stable" and locally exponentially stable, meaning that *"for almost all initial conditions (...) the trajectory* $(\hat{\boldsymbol{R}}_b^n(t), \hat{\boldsymbol{b}}_{\text{gyro}}^b(t))$ *converges to the trajectory* $(\boldsymbol{R}_b^n(t), \boldsymbol{b}_{\text{gyro}}^b(t))$*"*(Hua et al., 2014), where $\hat{\boldsymbol{R}}_b^n = \boldsymbol{R}(\hat{\boldsymbol{q}}_b^n)$ and $\boldsymbol{R}_b^n = \boldsymbol{R}(\boldsymbol{q}_b^n)$. In total there are three initial conditions from which the observer will not converge, each one an unstable equilibrium point.

6.2.5 Translational Motion Observer aided by GNSS

The observer presented is basically the same as one found in (Fossen, 2011, Ch. 11) sans accelerometer bias estimation:

$$\dot{\hat{\boldsymbol{p}}}_{nb}^n = \hat{\boldsymbol{v}}_{nb}^n + \boldsymbol{K}_1(\boldsymbol{p}_{\text{GNSS}}^n - \hat{\boldsymbol{p}}_{nb}^n) \tag{6.9a}$$

$$\dot{\hat{\boldsymbol{v}}}_{nb}^n = \boldsymbol{R}_b^n(\hat{\boldsymbol{q}}_b^n)\boldsymbol{f}_{\text{IMU}}^b + \boldsymbol{g}_b^n + \boldsymbol{K}_2(\boldsymbol{p}_{\text{GNSS}}^n - \hat{\boldsymbol{p}}_{nb}^n) \tag{6.9b}$$

This observer was also employed with success in Rogne et al. (2014) together with basic heading estimation, albeit under the assumption of known pitch and roll.

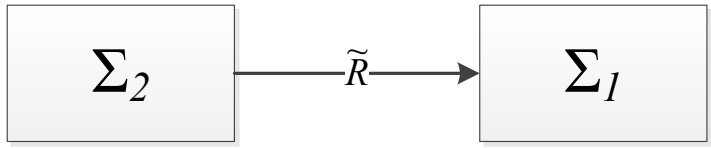

Figure 6.2: Cascade connection.

Stability of Nonlinear Observer and Translational Motion Observer in cascade

From (6.1) and (6.9), we obtain the following error dynamics for the Translational Motion Observer, without disturbances:

$$\dot{\tilde{\boldsymbol{p}}}^n_{nb} = \tilde{\boldsymbol{v}}^n_{nb} - \boldsymbol{K}_1 \tilde{\boldsymbol{p}}^n_{nb} \tag{6.10a}$$

$$\begin{aligned}\dot{\tilde{\boldsymbol{v}}}^n_{nb} &= (\boldsymbol{R}(\boldsymbol{q}^{\boldsymbol{n}}_{\boldsymbol{b}}) - \boldsymbol{R}(\hat{\boldsymbol{q}}^n_b))\boldsymbol{f}^b_{\text{IMU}} - \boldsymbol{K}_2 \tilde{\boldsymbol{p}}^n_{nb} \\ &= (\boldsymbol{I}_3 - \tilde{\boldsymbol{R}}^{n\top}_b)\boldsymbol{R}^n_b \boldsymbol{f}^b_{\text{IMU}} - \boldsymbol{K}_2 \tilde{\boldsymbol{p}}^n_{nb}\end{aligned} \tag{6.10b}$$

where $\tilde{\boldsymbol{p}}^n_{nb} = \boldsymbol{p}^n_{nb} - \hat{\boldsymbol{p}}^n_{nb}$, $\tilde{\boldsymbol{v}}^n_{nb} = \boldsymbol{v}^n_{nb} - \hat{\boldsymbol{v}}^n_{nb}$ and $\tilde{\boldsymbol{R}}^n_b = \boldsymbol{R}(\boldsymbol{q}^n_b)\boldsymbol{R}(\hat{\boldsymbol{q}}^n_b)^\top$ is the error rotation matrix .

Proposition 1. *Let* (6.10) *and the error dynamics of Nonlinear Observer 1 or 2 be connected like in Fig. 6.2, with* (6.10) *as* $\boldsymbol{\Sigma}_1$ *and the Nonlinear Observer error dynamics as* $\boldsymbol{\Sigma}_2$*, the tuning parameters* $\boldsymbol{K}_1$ *and* $\boldsymbol{K}_2$ *are chosen such that the matrix*

$$\boldsymbol{A}_{pv} := \begin{bmatrix} -\boldsymbol{K}_1 & \boldsymbol{I}_3 \\ -\boldsymbol{K}_2 & \boldsymbol{0} \end{bmatrix}$$

is Hurwitz, and the tuning parameters of the Nonlinear Observers satisfy the conditions found in Grip et al. (2013) or Hua et al. (2014). If all measured signals and biases are bounded, then the origin of the observer error dynamics for the cascade comprising $\boldsymbol{\Sigma}_1$ *and* $\boldsymbol{\Sigma}_2$ *retains the stability properties of* $\boldsymbol{\Sigma}_2$*.*

Proof. Define the interconnection between $\boldsymbol{\Sigma}_2$ and $\boldsymbol{\Sigma}_1$ as:

$$\boldsymbol{h}(t, \tilde{\boldsymbol{R}}^n_b) := (\boldsymbol{I}_3 - \tilde{\boldsymbol{R}}^{n\top}_b)\boldsymbol{R}^n_b(t)\boldsymbol{f}^b_{imu}(t). \tag{6.11}$$

Furthermore, it can be shown that

$$\begin{aligned}||\boldsymbol{h}(t, \tilde{\boldsymbol{R}}^n_b)|| &= ||(\boldsymbol{I}_3 - \tilde{\boldsymbol{R}}^{n\top}_b)\boldsymbol{R}^n_b \boldsymbol{f}^b_{\text{IMU}}|| \\ &= ||(\boldsymbol{I}_3 - \tilde{\boldsymbol{R}}^{n\top}_b)\boldsymbol{f}^b_{\text{IMU}}|| \\ &\leq 2 f_{\max} ||\tilde{\boldsymbol{\varepsilon}}||\end{aligned} \tag{6.12}$$

where $f_{\max} = \max(||\boldsymbol{f}^b_{\text{IMU}}||)$, $\tilde{\boldsymbol{\varepsilon}} = [\tilde{\varepsilon}_1 \ \tilde{\varepsilon}_2 \ \tilde{\varepsilon}_3]$ is the vector part of the quaternion $\tilde{\boldsymbol{q}}$ associated with $\tilde{\boldsymbol{R}}^n_b$, and $||\tilde{\boldsymbol{\varepsilon}}|| \to 0$ as $\tilde{\boldsymbol{R}}^n_b \to \boldsymbol{I}_3$. Above we have used the properties

that $||\boldsymbol{R}_b^n|| = 1$ and $||\boldsymbol{I}_3 - \tilde{\boldsymbol{R}}_b^{n\top}|| = ||\tilde{\eta}\boldsymbol{S}(\tilde{\boldsymbol{\varepsilon}}) - \boldsymbol{S}(\tilde{\boldsymbol{\varepsilon}})^2|| \leq 2||\tilde{\boldsymbol{\varepsilon}}||$ (Grip et al., 2013), where $\tilde{\eta}$ is the scalar part of $\tilde{\boldsymbol{q}}_b^n$. With the condition of (6.12), and making sure $\boldsymbol{A}_{pv}$ is Hurwitz, we now have a USGES subsystem in the case of Nonlinear Observer 1, or an "almost-globally stable" and locally exponentially stable subsystem in the case of Nonlinear Observer 2, connected to a globally exponentially stable linear system by a linearly bounded interconnection $\boldsymbol{h}(t, \tilde{\boldsymbol{R}}_b^n)$. According to cascade theory (Loria and Panteley, 2005), the cascade then retains the stability properties of $\boldsymbol{\Sigma}_2$. □

6.2.6 Implementation

The nonlinear attitude observers are implemented using the proposed implementation in Hua et al. (2014), using exact integration of (6.3d) and (6.7a):

$$\hat{\boldsymbol{q}}_{k+1} = \left(\cos\left(\frac{T||\hat{\boldsymbol{\omega}}_k||}{2}\right)\boldsymbol{I}_4 + \frac{T}{2}\text{sinc}\left(\frac{T||\hat{\boldsymbol{\omega}}_k||}{2}\right)\boldsymbol{\Omega}(\hat{\boldsymbol{\omega}}_k)\right)\hat{\boldsymbol{q}}_k$$

where $\text{sinc}(x) = \sin(x)/x$ and T is the time step.

6.2.7 Observer comparison

The attitude observers employ many of the same principles, such as fusing vector measurements with IMU gyro output, and putting a bound on the estimate of the gyro bias $\hat{\boldsymbol{b}}_{\text{gyro}}^b$ by using the saturation function or the projection algorithm. This is natural as they are all extensions of the work found in Mahony et al. (2008).

However, there are some major differences, the most important of which are the vectors chosen for $\boldsymbol{v}_1^b$ and $\boldsymbol{v}_1^n$. In Nonlinear Observer 2 (Hua et al., 2014), an assumption is made that $\boldsymbol{f}_{\text{IMU}}^b \approx -g\boldsymbol{R}_b^{n\top}\boldsymbol{e}_3$, where $\boldsymbol{e}_3 = [0\ 0\ 1]^\top$. This means that $\ddot{\boldsymbol{p}}_{nb}^n$, i.e. the vehicle's acceleration in the inertial frame n is considered negligible, and that the accelerometer measures mainly the gravity components. This is also the case for Nonlinear Observer 1b. In Nonlinear Observer 1a (Grip et al., 2013) on the other hand, an estimate $\hat{\boldsymbol{f}}_{nb}^n$ of $\ddot{\boldsymbol{p}}_{nb}^n$ is made with the help of position measurements, and the estimate is fed into the injection term $\hat{\boldsymbol{\sigma}}_{nb}^n$, ideally providing more accurate information. This will become apparent if the vehicle on which the observers are employed is faced with rotational motion or fast translational motion, inducing Coriolis acceleration. Only the former will be an issue in a DP scenario, where the vessel may be exposed to waves causing the vessel to oscillate in all six degrees of freedom.

Another difference between the observers is that Nonlinear Observer 2 provides a global decoupling of the roll and pitch estimations from the yaw estimations. Their motivation is the somewhat untrustworthy properties of the magnetometer used for yaw estimation, and the magnetometer's effect on roll and pitch without this decoupling (Hua et al., 2014; Martin and Salaün, 2010). We employ a gyrocompass instead, but still it gives the opportunity to tune the yaw estimation

Algorithm 4 GNSS fault detection by threshold

$x_1 = p_{\text{GNSS1},x}$, $y_1 = p_{\text{GNSS1},y}$
$x_2 = p_{\text{GNSS2},x}$, $y_2 = p_{\text{GNSS2},y}$
$r = \sqrt{(x_1 - x_2)^2 + (y_1 - y_2)^2}$

if $r > thld_{\text{det,GNSS}}$ **then**
    Fault detected.
end if

independently of roll and pitch. This could prove valuable for FDI in gyrocompasses.

6.2.8 Fault detection and isolation

Various methods for FDI can be found in for instance Blanke (2001), Blanke et al. (2006) and Gustafsson (2007). In this chapter however, since the main focus is on the comparison of the different nonlinear observers, we will base the FDI scheme on simple threshold values both for detection and identification. We will also limit ourselves to detecting and isolating faults that appear as a semi-slow signal drift, meaning here drifts that are slow enough to be difficult to detect and isolate immediately, but fast enough to put the operation at risk. In our DP scenario, we define this to be position and compass drifts below 1 m/s and 1 deg/s, respectively.

For detection of a fault, we will use the distance between the two measurements we have available. When the distance reaches a certain threshold $thld_{\text{det}}$, a fault will be indicated, see Algorithm 4 for a GNSS example. When choosing the threshold value, one must take into account normal sensor drifting, as to avoid false positives.

The next step is isolation. Rogne et al. (2014) provides a discussion on how sensor faults will affect the equilibrium points of the observer, and how the measurement error of the observer may be used for isolation. For example, if the GNSS is measuring values that differ too much from what the observer is estimating based on the IMU data, the measurement error $\tilde{\boldsymbol{p}}^n_{nb} = \boldsymbol{p}^n_{\text{GNSS}} - \hat{\boldsymbol{p}}^n_{nb}$ will have a transient response. Here we will monitor the outputs the Translational Motion Observers' position error for the GNSS, and the nonlinear attitude observers' yaw (or heading) error for the gyrocompasses, and check if the error passes a given threshold $thld_{\text{iso}}$, see Algorithm 5. The observers in the algorithm correspond to the ones in Fig. 6.1.

6.2.9 Observer tuning

The main objective of the observers is the detection and isolation of faults, so gains should be chosen with that in mind, while at the same time addressing the effects

Algorithm 5 GNSS fault isolation by threshold

for i = 1, i<=4, i++ **do**
  j = GNSS connected to observer i
  $\tilde{p}_{i,x} = p_{\text{GNSS}j,x} - \hat{p}_{i,x}$, $\tilde{p}_{i,y} = p_{\text{GNSS}j,y} - \hat{p}_{i,y}$
  $r_i = \sqrt{\tilde{p}_{i,x}^2 + \tilde{p}_{i,y}^2}$
  if $r_i > thld_{iso,GNSS}$ **then**
    Fault in GNSS j.
  end if
end for

of noise and other error sources. One should choose to have a not-so-aggressive feedback, to keep the transients lingering for a while, such that the feedback does not hide the fault. On the other hand, setting the gains too low could hamper the estimating qualities of the observer too much, introducing lag and possibly lowering the performance to the point where one would not be able to isolate faults at all.

With basis in the gains and parameters for the observers found in their respective papers Grip et al. (2013); Hua et al. (2014); Rogne et al. (2014), we performed a tuning process by trial and error. Nonlinear Observer 1a turned out to be somewhat more difficult to tune than the other observers. This is due to the feedback interconnection structure of the former, meaning that tuning the position estimation part is affecting the attitude estimation, and vice versa. In Nonlinear Observer 2, we also have a separation of yaw from roll and pitch, simplifying the tuning process since the gains can be tuned somewhat independently. After the tuning process, we opted for the following tuning parameters:

Nonlinear Observer 1a

$$k_1 = 0.5,\ k_2 = 0.5,\ k_I = 0.03$$
$$\theta = 3,\ \boldsymbol{K}_{pp} = 0.6\boldsymbol{I}_3,\ \boldsymbol{K}_{vp} = 0.11\boldsymbol{I}_3,\ \boldsymbol{K}_{\xi p} = 0.006\boldsymbol{I}_3$$

and a parameter projection $\text{Proj}(\cdot,\cdot)$ ensuring $||\hat{\boldsymbol{b}}^b|| \leq 0.51$ deg/s.

Nonlinear Observer 1b

$$k_1 = 0.1,\ k_2 = 0.5,\ k_I = 0.03$$

and a parameter projection $\text{Proj}(\cdot,\cdot)$ ensuring $||\hat{\boldsymbol{b}}^b|| \leq 0.51$ deg/s.

Nonlinear Observer 2

$$k_1 = 0.1,\ k_2 = 0.5,\ k_3 = 0.006,\ k_4 = 0.005$$
$$k_b = 8,\ \Delta = 0.03$$

Translational motion observer

$$\boldsymbol{K}_1 = 0.1\boldsymbol{I}_3,\ \boldsymbol{K}_2 = 0.001\boldsymbol{I}_3$$

6.3 Simulation

The simulations were carried out in MATLAB/Simulink R2013b using a dynamic ship simulator in full 6-DOF, with waves, vibration and measurement noise (Fossen and Perez, 2010). All measurements were set to have a zero mean normally distributed noise, except for the posref systems that have a Gauss-Markov process, see Table 6.1 for their parameters. The IMU had a sampling frequency of 100 Hz, the GNSS 5 Hz, and the gyrocompass 10 Hz. The observers were not part of the feedback loop for the simulated DP system, as it is only employed for fault detection and isolation.

Table 6.1: Measurement noises

Measurement	**Std. dev.**	**Markov time constant**
IMU acceleration	0.002 m/s^2	-
IMU gyro	0.08 deg/s	-
Position reference system x and y	1.1 m	4 min
Position reference system z	2.2 m	4 min
Gyrocompass	0.07 deg	-

6.3.1 Case 1: Attitude estimation test

In the first case, a simulation of fault free operation was carried out. No faults were simulated, as the goal of this test was to compare the performance of the estimators.

As we can see from Fig. 6.3 - 6.8, all attitude observers manage well, but Nonlinear Observer 1a seems to have the edge when it comes to bias, roll and pitch estimation. For Nonlinear Observer 1b and 2 in Fig. 6.7 some of the wave motion seems to pollute the bias estimates on roll and pitch, relating to one of the key points of Section 6.2.7, namely the assumptions on the vessel's acceleration.

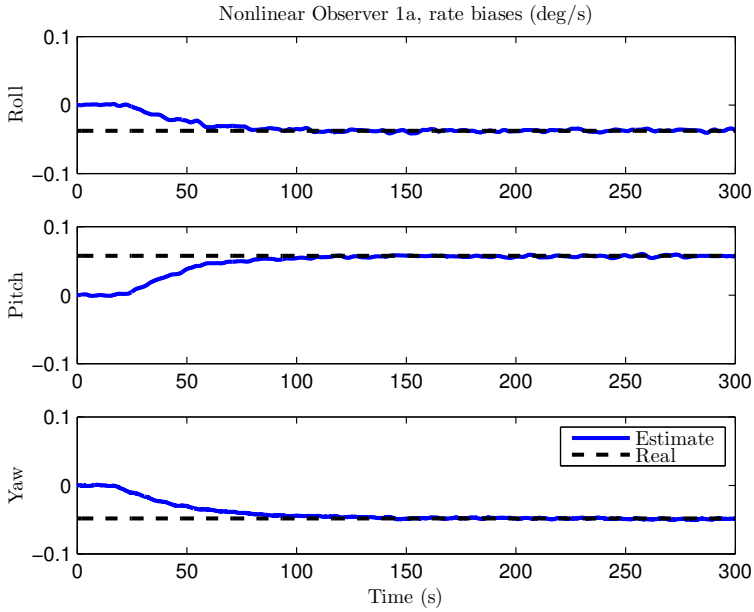

Figure 6.3: Case 1: Nonlinear Observer 1a IMU gyro bias estimates

6.3.2 Case 2: Position reference fault

In the second case, a position reference system was set to drift at a rate of 0.4 m/s up to a maximum fault of 20 meters. The fault was introduced at $t = 1000$ seconds. The vessel was keeping its position at the origin. The simulation results are shown in Figs. 6.9 and 6.10. The performance of the translational motion observer when it comes to estimating the position accurately is less than optimal, but our objective with this observer is solely to detect and isolate failures.

To detect the fault is trivial from Fig. 6.9 and since we have diverging estimates. A vertical dotted line in the figure marks the time when a fault has been the detected by comparing GNSS measurements. From Fig. 6.10 showing the position measurement errors of the translational motion observer, it is possible to isolate the faulty output from GNSS 1. A significant transient occurs for Observer 1b and 2 during the sensor drift-away. Translational Motion Observer 1a seems to cancel out the position error and keep it at lower level. This is likely due to the fact that it receives its attitude from Nonlinear Observer 1a, which we recall has the GNSS signal as part of the observer equations. When the attitude is estimated with the help of the faulty GNSS signal, the attitude estimate cannot be trusted for use in FDI of that same GNSS signal. However, the output of Observer 1a displays some smaller transients at $t = 1000$ when the position measurement drift starts and at $t = 1050$ when the drifting ends.

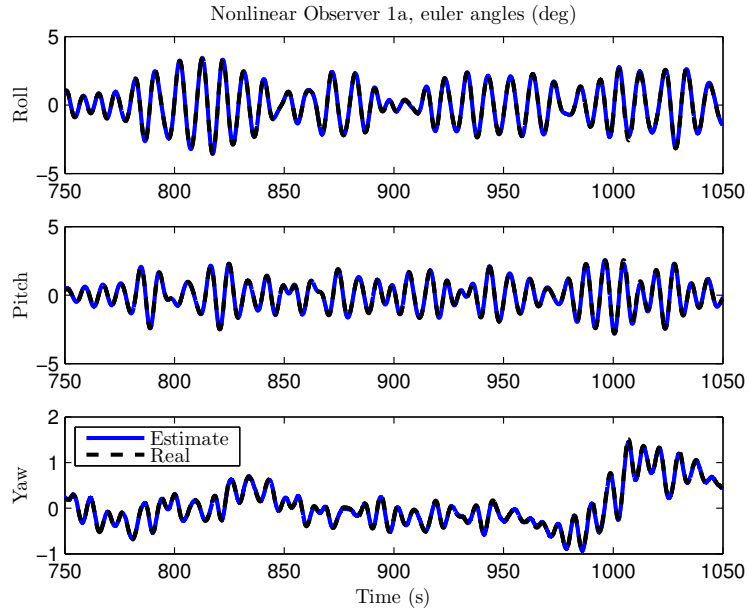

Figure 6.4: Case 1: Nonlinear Observer 1a attitude estimates

6.3.3 Case 3: Gyrocompass fault

In the third case, a gyrocompass was set to drift at a rate of 0.4 deg/s up to a maximum fault of 20 degrees. The fault was introduced at $t = 1000$ seconds. The vessel was as before keeping its position at the origin. The results can be seen in Figs. 6.11 and 6.12. As for the posref fault case, detecting a fault is trivial from looking at the estimates themselves (Fig. 6.11 as they diverge. By considering the heading estimation error (Fig. 6.12), we see that we may in this case use any of the observers to isolate the fault with the chosen thresholds.

6.3.4 Discussion

As the simulation results demonstrate, Nonlinear Observer 1a seems to have a slight edge on the others when it comes to fault free attitude estimation. This is most likely due to the fact that Nonlinear Observer 1a estimates the acceleration in the $\{n\}$-frame, while the others assumes that the acceleration is negligible. In our simulations, wave excitations impose motion on the vessel, especially in the heave direction, which will make significant contributions to the accelerometer measurement $\boldsymbol{f}^b_{\text{IMU}}$.

Nevertheless, all observers were able to isolate a faulty gyrocompass, and by using the attitude from the Nonlinear Observers 1b and 2 as input to a Translational Motion Observer aided by GNSS, we were able to detect and isolate a drift in GNSS

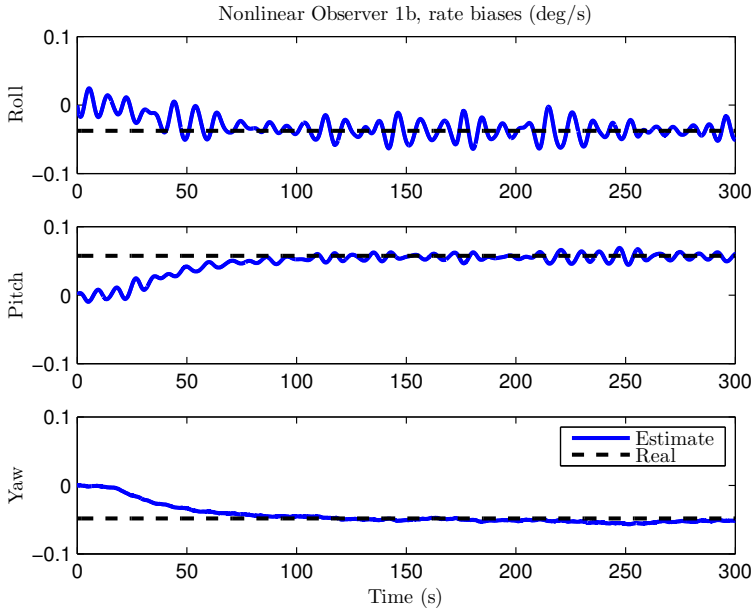

Figure 6.5: Case 1: Nonlinear Observer 1b IMU gyro bias estimates.

measurement. By doing some appropriate tuning, Nonlinear Observer 1a in the same cascade may be able to isolate the fault as well. However, that could impair the observer's performance and stability. In Blanke (2001), there are methods that describe applying a filter to the measurement error, in order to generate *residuals*. These filters should be designed so that noise and other error sources are masked out from the residual. Applying such a filter to the topmost output shown in Fig. 6.10, may yield good fault isolation results while keeping up performance.

In Rogne et al. (2014) results very similar to Figs. 6.9 - 6.12 were obtained. However, in this current work some of the restrictive assumptions in the previous work have been removed, due to the nonlinear observers that we employ. First, we now estimate roll and pitch alongside with yaw, instead of considering the two former as known external signals. Second, in Rogne et al. (2014) the IMU gyro bias was assumed to be accounted for beforehand, and was out of scope of the paper. The observers we use in this chapter estimate the gyro bias, while still being able to perform the FDI tasks completed in Rogne et al. (2014).

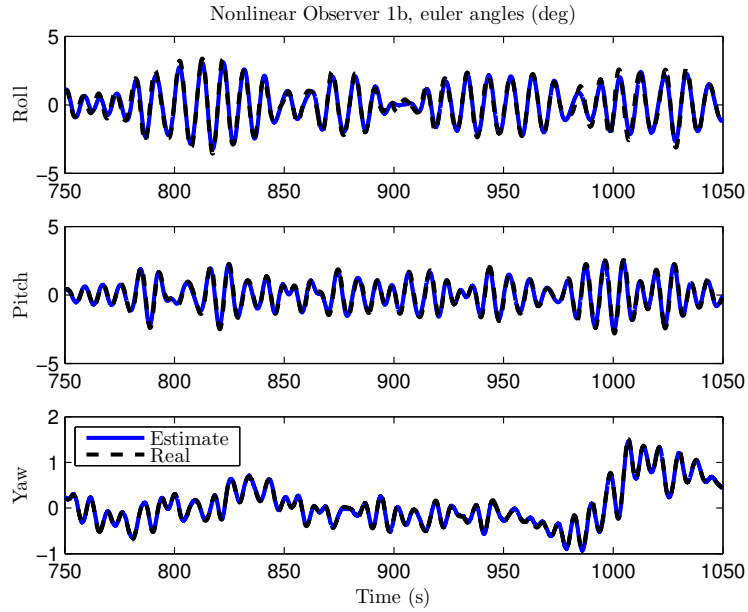

Figure 6.6: Case 1: Nonlinear Observer 1b attitude estimates.

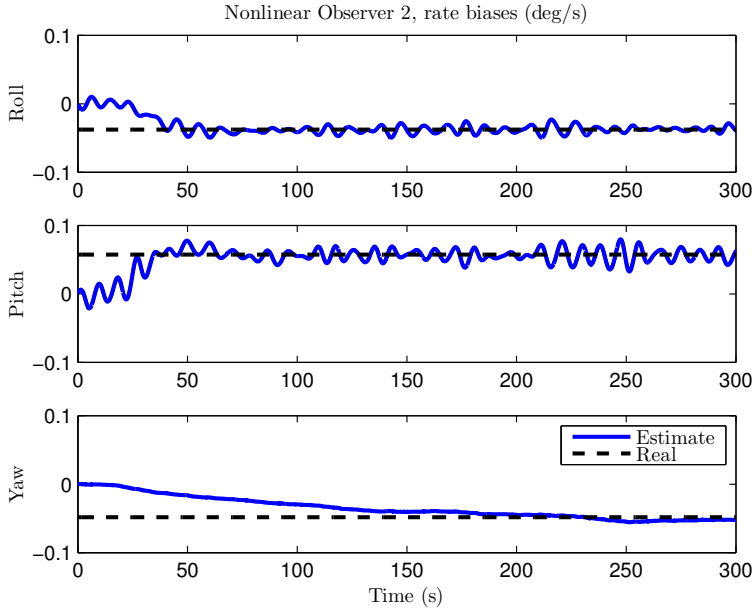

Figure 6.7: Case 1: Nonlinear Observer 2 IMU gyro bias estimates.

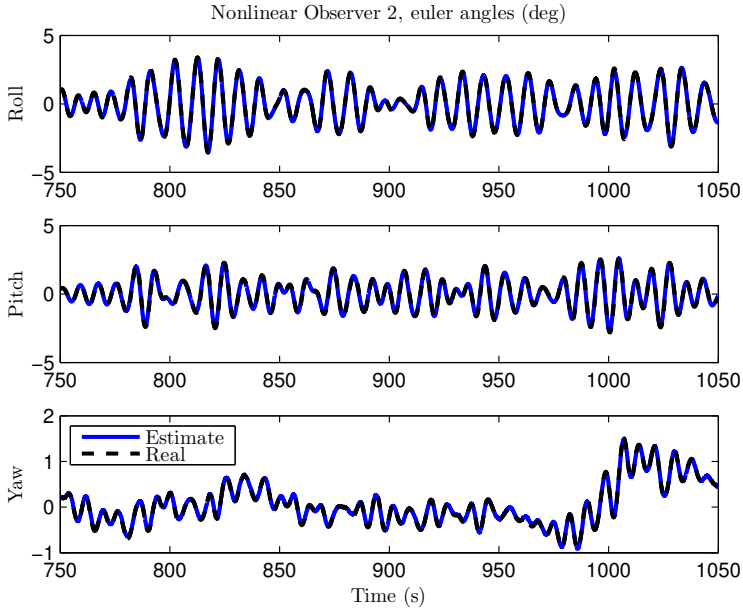

Figure 6.8: Case 1: Nonlinear Observer 2 attitude estimates.

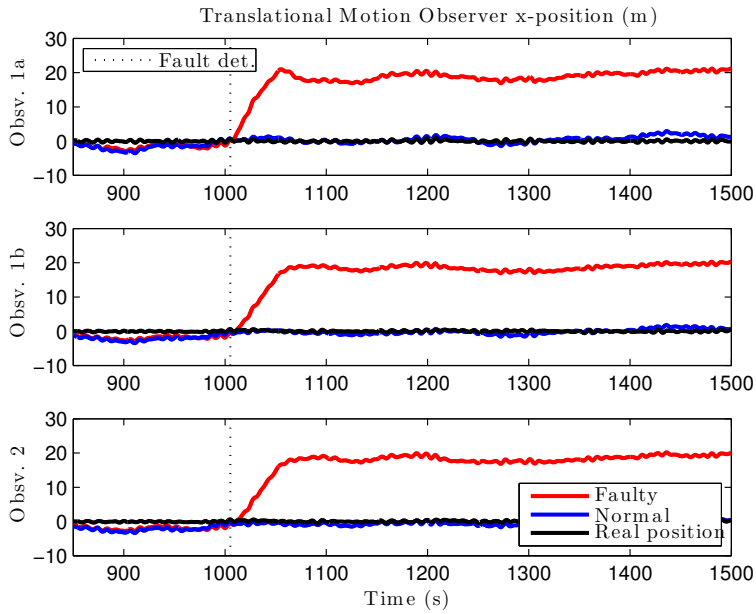

Figure 6.9: Case 2: Translational Motion Observer position estimates and true position during posref fault test.

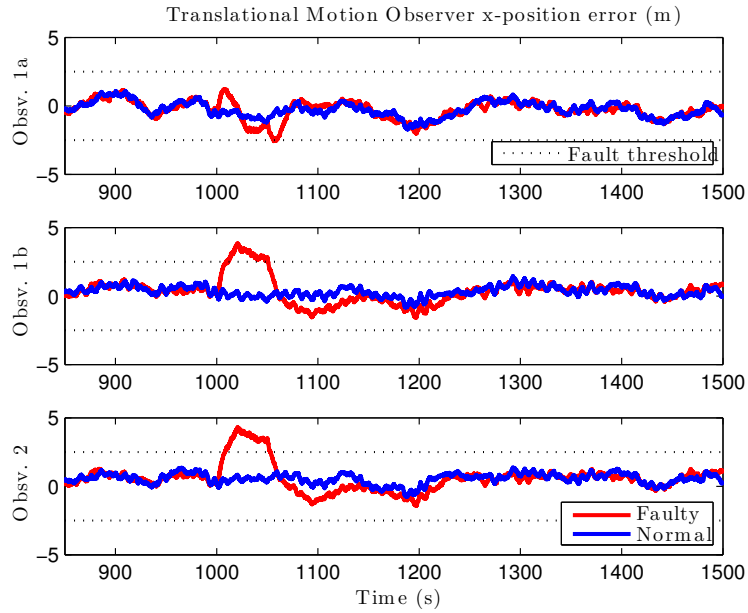

Figure 6.10: Case 2: Translational Motion Observer position errors during posref fault test, where the error is the difference between the measurement and estimate.

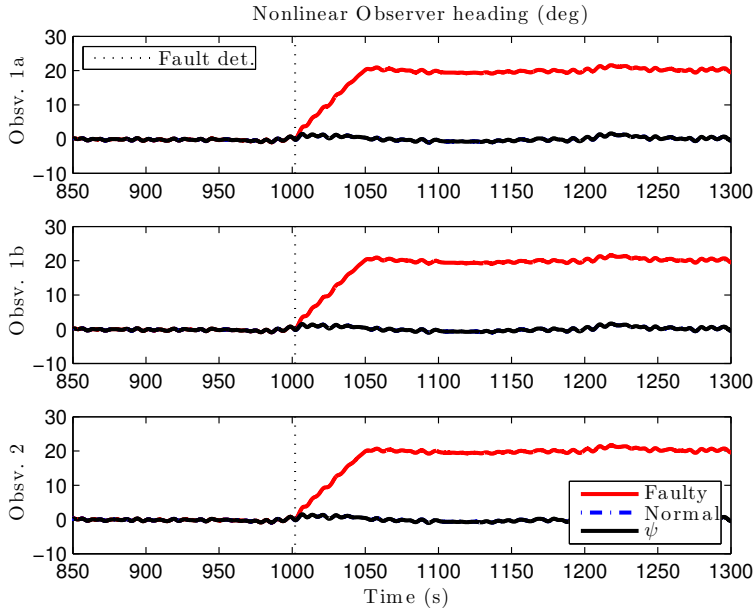

Figure 6.11: Case 3: Nonlinear Observer heading estimates and true heading during gyrocompass fault test.

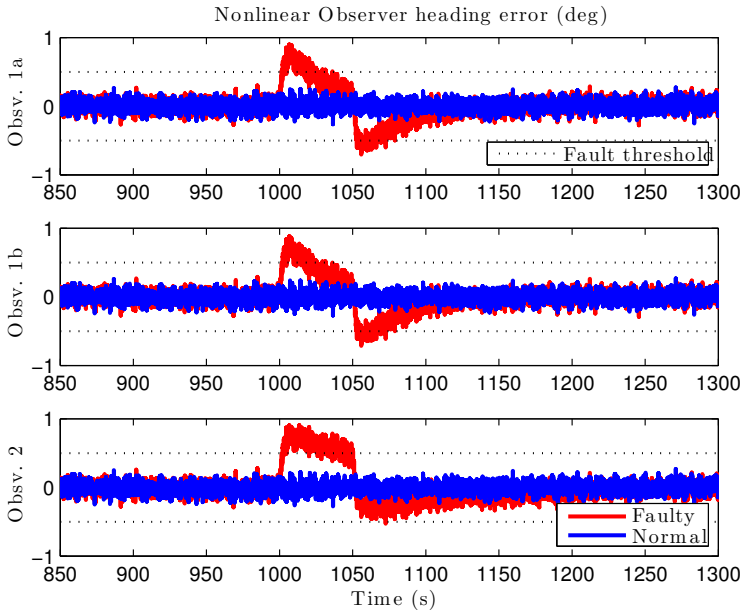

Figure 6.12: Case 3: Nonlinear Observer heading error during gyrocompass fault test, where the error is the difference between the measurement and estimate.

6.4 Conclusion

In this chapter we have compared three nonlinear attitude observers, in an attitude and bias estimation test, and in two FDI scenarios. Nonlinear Observer 1a was found to be slightly more suitable than Nonlinear Observer 1b and 2 when it came to fault free attitude and bias estimation. In the first FDI test case, the nonlinear observers were paired with a translational motion observer aided by GNSS to detect and isolate a position fault. Nonlinear Observer 1b and 2 performed well in this case, but Nonlinear Observer 1a fell a bit short, mainly because of its dependence on the position measurement itself. In the second FDI case, the attitude observers were used to detect and isolate a gyrocompass fault. In this case, all three observers managed to isolate the source of the fault.

7

Position Reference Fault Detection and Isolation with Lever-Arm Compensation and Heave Estimation

This chapter is based on Rogne et al. (2016b), except Section 7.7 which is new.

7.1 Introduction

This chapter picks up the thread from the previous chapter, where the conclusion was that attitude observers without dependence on position measurement is better at that detecting faults in said signal, than position aided attitude observers. This might seem simple enough, but the position aided observers have the benefit of estimating specific force in the inertial frame, making them superior in the fault-free case. Here we seek to combine these traits by employing virtual measurements instead of position reference systems.

Also, a sensor that is required for DP vessels is the vertical reference unit (VRU). Due to a DP vessel's design the respective PosRefs are located far from the nominal center of reference where the IMU may be located, as shown in Fig. 7.1. A distance between 30-50 meters is not uncommon. Therefore, the VRU is used to map the respective PosRefs' measurements from the measurement's location to a given point of interest utilizing roll and pitch readings provided by a VRU. Since the distance between the PosRef and the point of reference can be quite large, it is most important that the roll and pitch signals from the VRU is accurate. In this chapter there are no assumptions on the PosRef location on the craft, unlike the results of Vik and Fossen (2001); Grip et al. (2013); Bryne et al. (2014); Grip et al. (2015) where the position reference is implicitly assumed located in the same point as the IMU.

The main result presented in this chapter is twofold.

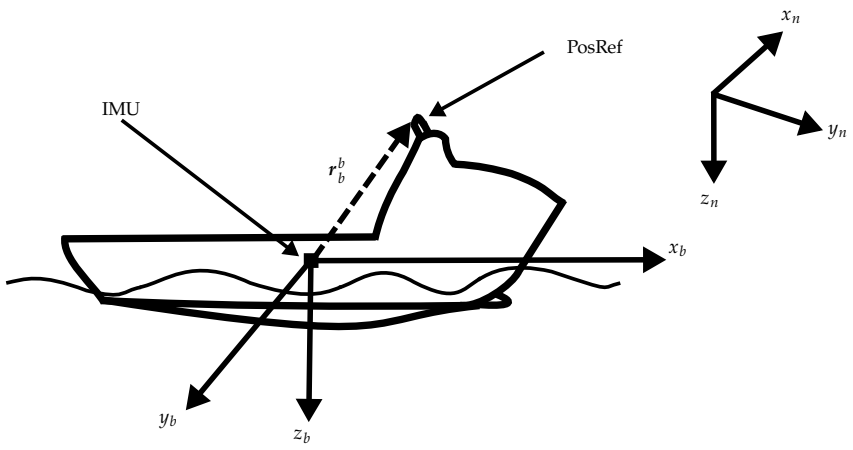

Figure 7.1: Platform support vessel: Frames definition and illustration of the lever arm from IMU to a GNSS PosRef

- Applying a three-stage observer design with uniform semiglobal exponential stability (USGES) properties to estimate position, velocity and attitude. The lever arm between the IMU and given position reference (PosRef) system is taken into account, in contrast to previous results on nonlinear observers with USGES. Hence, the VRU is functionally embedded in the observer design, using the IMU.
- Fault detection of PosRef position measurements with slowly emerging and varying faults using fault-diagnosis techniques and the observer structure posed.

7.2 Preliminaries

7.2.1 General assumptions and notation

We employ two coordinate frames, north-east-down (NED) and BODY, denoted $\{n\}$ and $\{b\}$, respectively as seen in Fig. 7.1. NED is a local Earth-fixed frame, while the BODY frame is fixed to the vessel. The origin of $\{b\}$ is defined at the nominal center of gravity of the vessel. The x-axis is directed from aft to fore, the y-axis is directed to starboard and the z-axis points downwards. A notation similar to the one in Fossen (2011) is used:

- $\boldsymbol{p}_{nb}^{n}$ - position of the vessel with respect to $\{n\}$ expressed in $\{n\}$
- $\boldsymbol{v}_{nb}^{n}$ - linear velocity of the vessel with respect to $\{n\}$ expressed in $\{n\}$

- ψ - yaw angle between between $\{b\}$ and $\{n\}$
- $\boldsymbol{\omega}_{nb}^{b}$ - body-fixed angular velocity
- $\boldsymbol{b}_{\text{gyro}}^{b}$ - gyro bias
- $\boldsymbol{q}_{b}^{n}$ - a unit quaternion representing the rotation between $\{b\}$ to $\{n\}$.
- $\boldsymbol{R}_{b}^{n} := \boldsymbol{R}(\boldsymbol{q}_{b}^{n})$ and $\boldsymbol{R}_{n}^{b} := \boldsymbol{R}(\boldsymbol{q}_{n}^{b})$ are the rotation matrices to $\{n\}$ from $\{b\}$ and vice versa, respectively. The argument $\boldsymbol{q}_{b}^{n}$ will be omitted for notational simplicity when suitable.
- $\boldsymbol{S}(\boldsymbol{x})$ - skew symmetric matrix:

$$\boldsymbol{S}(\boldsymbol{x}) = \begin{bmatrix} 0 & -x_3 & x_2 \\ x_3 & 0 & -x_1 \\ -x_2 & x_1 & 0 \end{bmatrix}, \ \boldsymbol{x} = \begin{bmatrix} x_1 \\ x_2 \\ x_3 \end{bmatrix}$$

- $\boldsymbol{g}_{b}^{n}$ - local gravity vector in $\{n\}$
- $\boldsymbol{f}_{\text{IMU}}^{b}$ - accelerometer specific force measurement in the body/vessel frame $\{b\}$
- $\boldsymbol{\omega}_{\text{IMU}}^{b} = \boldsymbol{\omega}_{nb}^{b} + \boldsymbol{b}_{\text{gyro}}^{b}$ - angular velocity measurement of the body
- $\boldsymbol{p}_{\text{PosRef}}^{n}$ - position measurement
- ψ_{c} - gyrocompass heading measurement
- $p_{nb,I}^{n}$ - integrated vertical position
- $\boldsymbol{c}_{nb}^{b} = [\cos(\psi_{\text{c}}), -\sin(\psi_{\text{c}}), 0]^{\intercal}$ - vectorized compass measurement
- $\boldsymbol{c}_{nb}^{n} = [1, 0, 0]^{\intercal}$ reference vector for compass

The following assumptions are made:

- IMU accelerometer biases are neglected, i.e. biases are assumed to be accounted for in calibration or by online estimation, utilizing e.g. (Grip et al., 2012a, Sec. IV).
- There exists a bound $f_{\max}$ on the magnitude of the specific force $\boldsymbol{f}_{\text{IMU}}^{b}$.
- $\boldsymbol{\omega}_{\text{IMU}}^{b}$ and $\dot{\boldsymbol{f}}_{\text{IMU}}^{b}$ are uniformly bounded.
- To guarantee uniform observability, there exists a constant $v_{\text{obs}} > 0$ such that $\|\boldsymbol{f}_{\text{IMU}}^{b} \times \boldsymbol{c}^{b}\| \geq v_{\text{obs}} \forall t \geq 0$
- We neglect measurement noise in the theoretical analysis, which is motivated by the possibility to account for noise during tuning of the observer parameters.

7.2.2 Concept

In Chapter 6 attitude estimation for use in PosRef fault detection was discussed. A main result was that a high quality attitude estimate is needed for successful IMU-based fault detection in PosRef systems. It was discovered that PosRef-aided attitude observers, such as the ones in Grip et al. (2013); Bryne et al. (2014); Grip et al. (2015) are excellent for fault free operation, but they are inherently vulnerable to PosRef faults. The attitude estimate should in this matter be independent from position measurements. Also, because of our intrinsic requirement that the position observer is as reliable as possible, while not filtering out information, we cannot employ observers using uncertain thrust measurements and applying wave filtering to their estimates, such as Fossen and Strand (1999); Fossen and Perez (2009). Velocity measurements from PosRefs are in this design neglected since without any in-depth knowledge of how the measurement is generated, one cannot guarantee that the velocity information is independent of position. An example of such PosRefs where this might be the case is (d)GNSS.

PosRef fault detection, including lever-arm compensation, is thus done with three main components:

1. Estimating the attitude independent of the translational motion such that the innovation from a given erroneous PosRef is not attenuated by a feedback interconnection, but still aided by a virtual reference.

2. Lever-arm-compensated translational motion estimation — mapping the PosRef measurement to the IMU's location.

3. Monitoring of the innovation signal by use of an established algorithm for detecting change in mean value.

7.2.3 System equations

The NED position of a PosRef relative a given position on the vessel is given as

$$\boldsymbol{p}^n_{nb} = \boldsymbol{p}^n_{\text{PosRef}} - \boldsymbol{R}^n_b \boldsymbol{r}^b_b \tag{7.1}$$

where $\boldsymbol{r}^b_b$ is the lever arm between the origin of $\{b\}$ and the PosRef as in (Fossen, 2011, Ch. 11.5). The kinematics of the system can be described as follows:

$$\dot{\boldsymbol{p}}^n_{nb} = \boldsymbol{v}^n_{nb} \tag{7.2a}$$

$$\dot{\boldsymbol{v}}^n_{nb} = \boldsymbol{R}^n_b \boldsymbol{f}^b + \boldsymbol{g}^n_b \tag{7.2b}$$

$$\dot{\boldsymbol{q}}^n_b = \frac{1}{2}\boldsymbol{\Omega}(\boldsymbol{\omega}^b_{nb})\boldsymbol{q}^n_b \tag{7.2c}$$

$$\boldsymbol{y}_p = \boldsymbol{p}^n_{\text{PosRef}} = \boldsymbol{p}^n_{nb} + \boldsymbol{R}^n_b \boldsymbol{r}^b_b + \boldsymbol{d}_p \tag{7.2d}$$

$$y_\psi = \psi_{\text{c}} = \psi + w_\psi \tag{7.2e}$$

where

$$\boldsymbol{\Omega}(\boldsymbol{x}) = \begin{bmatrix} \mathbf{0} & -\boldsymbol{x}^\intercal \\ \boldsymbol{x} & -\boldsymbol{S}(\boldsymbol{x}) \end{bmatrix} \tag{7.3}$$

where $\boldsymbol{d}_p$ are noise and faults on the position measurement, and w_ψ is measurement noise and faults on the gyrocompass.

7.3 Attitude and Heading Reference System

The methods of Grip et al. (2013); Bryne et al. (2014); Grip et al. (2015) estimate the position, linear velocity and attitude where the position measurements affect the attitude estimates in a feedback-interconnected structure. In the observer presented below, the attitude is estimated independently of position measurements such that any PosRef error is prevented from propagating to the attitude estimates. The Attitude and Heading Reference System (AHRS) is however still based on the feedback-interconnected structure of Grip et al. (2013); Bryne et al. (2014) consisting of an attitude observer, Σ_1, and an aiding translational motion observer (TMO), Σ_2 as illustrated in Fig. 7.2.

7.3.1 Observer equations

The attitude observer of Grip et al. (2013), extended from Mahony et al. (2008); Grip et al. (2012a) is given as:

$$\Sigma_1 : \begin{cases} \dot{\hat{\boldsymbol{q}}}_b^n = \frac{1}{2}\boldsymbol{\Omega}(\hat{\boldsymbol{\omega}}_{nb}^b)\hat{\boldsymbol{q}}_b^n & \text{(7.4a)} \\ \dot{\hat{\boldsymbol{b}}}_{\text{gyro}}^b = \text{Proj}(\hat{\boldsymbol{b}}_{\text{gyro}}^b, -k_I(t)\hat{\boldsymbol{\sigma}}_{nb}^b) & \text{(7.4b)} \end{cases}$$

with

$$\hat{\boldsymbol{\sigma}}_{nb}^b = k_1 \boldsymbol{v}_1^b \times \boldsymbol{R}(\hat{\boldsymbol{q}}_b^n)^\intercal \boldsymbol{v}_1^n + k_2 \boldsymbol{v}_2^b \times \boldsymbol{R}(\hat{\boldsymbol{q}}_b^n)^\intercal \boldsymbol{v}_2^n \tag{7.5}$$

where

$$\boldsymbol{v}_1^b = \frac{\boldsymbol{f}_{\text{IMU}}^b}{||\boldsymbol{f}_{\text{IMU}}^b||}, \ \boldsymbol{v}_2^b = \frac{\boldsymbol{f}_{\text{IMU}}^b \times \boldsymbol{c}_{nb}^b}{||\boldsymbol{f}_{\text{IMU}}^b \times \boldsymbol{c}_{nb}^b||} \tag{7.6a}$$

$$\boldsymbol{v}_1^n = \frac{\hat{\boldsymbol{f}}_{nb}^n}{||\hat{\boldsymbol{f}}_{nb}^n||}, \ \boldsymbol{v}_2^n = \frac{\hat{\boldsymbol{f}}_{nb}^n \times \boldsymbol{c}_{nb}^n}{||\hat{\boldsymbol{f}}_{nb}^n \times \boldsymbol{c}_{nb}^n||} \tag{7.6b}$$

and $\hat{\boldsymbol{\omega}}_{nb}^b = \boldsymbol{\omega}_{\text{IMU}}^b - \hat{\boldsymbol{b}}_{\text{gyro}}^b + \hat{\boldsymbol{\sigma}}_{nb}^b$, and $\text{Proj}(\cdot,\cdot)$ is a parameter projection that restrict the estimate $\hat{\boldsymbol{b}}_{\text{gyro}}^b$, see Grip et al. (2012a) and references therein for details.

The estimate reference vector $\hat{\boldsymbol{f}}_{nb}^n = \boldsymbol{R}(\hat{\boldsymbol{q}}_b^n)\boldsymbol{f}_{\text{IMU}}^b + \boldsymbol{\xi}_{nb}^n$ is obtained by utilizing the state $\boldsymbol{\xi}_{nb}^n$ from a translational motion observer Σ_2 based on these kinematic

equations:

$$\dot{p}^n_{nb,I} = p^n_{nb,z} \tag{7.7}$$
$$\dot{p}^n_{nb,z} = v^n_{nb,z} \tag{7.8}$$
$$\dot{\boldsymbol{v}}^n_{nb} = \boldsymbol{R}^n_b \boldsymbol{f}^b_{\text{IMU}} + \boldsymbol{g}^n_b \tag{7.9}$$

Furthermore, this results in the following TMO aiding the attitude observer through a feedback interconnection:

$$\Sigma_2 : \begin{cases} \dot{\hat{p}}^n_{nb,I} = \hat{p}^n_{nb,z} + \vartheta K_{p_I p_I} \tilde{p}^n_{nb,I} & \text{(7.10a)} \\ \dot{\hat{p}}^n_{nb,z} = \hat{v}^n_{nb,z} + \vartheta^2 K_{p p_I} \tilde{p}^n_{nb,I} & \text{(7.10b)} \\ \dot{\hat{\boldsymbol{v}}}^n_{nb} = \hat{\boldsymbol{f}}^n_{nb} + \boldsymbol{g}^n_b + \vartheta^3 \begin{bmatrix} 0 \\ 0 \\ K_{v p_I} \end{bmatrix} \tilde{p}^n_{nb,I} + \\ \qquad \vartheta \begin{bmatrix} K_{v v_x} & 0 & 0 \\ 0 & K_{v v_y} & 0 \\ 0 & 0 & 0 \end{bmatrix} \tilde{\boldsymbol{v}}^n_{nb} & \text{(7.10c)} \\ \dot{\hat{\boldsymbol{\xi}}}^n_{nb} = -\boldsymbol{R}(\hat{\boldsymbol{q}}^n_b) \boldsymbol{S}(\hat{\boldsymbol{\sigma}}) \boldsymbol{f}^b_{\text{IMU}} + \vartheta^4 \begin{bmatrix} 0 \\ 0 \\ K_{\xi p_I} \end{bmatrix} \tilde{p}^n_{nb,I} + \\ \qquad \vartheta^2 \begin{bmatrix} K_{\xi v_x} & 0 & 0 \\ 0 & K_{\xi v_y} & 0 \\ 0 & 0 & 0 \end{bmatrix} \tilde{\boldsymbol{v}}^n_{nb} & \text{(7.10d)} \\ \hat{\boldsymbol{f}}^n_{nb} = \boldsymbol{R}(\hat{\boldsymbol{q}}^n_b) \boldsymbol{f}^b_{\text{IMU}} + \boldsymbol{\xi}^n_{nb} & \text{(7.10e)} \end{cases}$$

with $p^n_{nb,I} = 0$, and $\boldsymbol{v}^n_{\text{vir}} = \boldsymbol{0}$ such that $\tilde{p}^n_{nb,I} = 0 - \hat{p}^n_{nb,I}$ and $\tilde{\boldsymbol{v}}^n_{nb} = \boldsymbol{v}^n_{\text{vir}} - \hat{\boldsymbol{v}}^n_{nb}$. The virtual vertical reference (VVR) measurement, $p^n_{nb,I}$, applied in Bryne et al. (2014, 2015b), is motivated by the average vertical position relative the mean sea surface is zero.

The virtual zero-velocity measurement, $\boldsymbol{v}^n_{\text{vir}}$, is a natural choice since the vessel is in stationkeeping mode where the velocity is small. In transit, the virtual velocity signals can e.g. be chosen from the desired speed s_d, obtained from the auto pilot, and the measured heading ψ_{c} utilizing the mapping $\boldsymbol{v}^n_{\text{vir}} = [s_d \cos(\psi_{\text{c}}),\ s_d \sin(\psi_{\text{c}}),\ 0]^\intercal$ or velocity signals from reference models such as (Fossen, 2011, Ch. 10) applied in DP when the vessel changes heading and position.

7.3.2 Stability of the AHRS

In Proposition 7.1, a USGES stability results of the AHRS is obtained by exploiting that $\Sigma_1 - \Sigma_2$ is structurally similar to the $\Sigma_1 - \Sigma_2$ of Bryne et al. (2014).

Proposition 7.1. *The error dynamics of the observer $\Sigma_1 - \Sigma_2$ is USGES if the gain $\vartheta \geq 1$ is chosen sufficiently large, the gains k_1 and k_2 satisfy $k_1 \geq k_P$ and $k_2 \geq k_P$ for some $k_P > 0$, and measurements $\boldsymbol{f}^b_{\text{IMU}}$ and $\boldsymbol{\omega}^b_{\text{IMU}}$ satisfy the assumptions in Sec. 7.2.1*

Proof. By defining $\tilde{p}^n_{nb,z} := p^n_{nb,z} - \hat{p}^n_{nb,z}$ and $\boldsymbol{f}^{\tilde{n}}_{nb} := \boldsymbol{f}^n_{nb} - \hat{\boldsymbol{f}}^n_{nb}$, we use that $\tilde{\boldsymbol{x}}_a := [\tilde{\boldsymbol{p}}^n_{nb,I}, \tilde{p}^n_{nb,z}, \tilde{\boldsymbol{v}}^n_{nb}{}^\intercal, \tilde{\boldsymbol{f}}^n_{nb}{}^\intercal]^\intercal$, such that the error dynamics of (7.10) may be written

$$\dot{\tilde{\boldsymbol{x}}}_a = (\boldsymbol{A}_a - \boldsymbol{K}_a \boldsymbol{C}_a)\, \tilde{\boldsymbol{x}}_a + \boldsymbol{B}_a \tilde{\boldsymbol{u}}_a \tag{7.11}$$

where

$$\begin{aligned} \tilde{\boldsymbol{u}}_a := \; & (\boldsymbol{I}_3 - \tilde{\boldsymbol{R}}^\intercal)\boldsymbol{R}(\boldsymbol{q}^n_b)\left(\boldsymbol{S}(\boldsymbol{\omega}^b_{nb}) + \dot{\boldsymbol{f}}^b_{nb}\right) - \\ & \tilde{\boldsymbol{R}}^\intercal \boldsymbol{R}(\boldsymbol{q}^n_b)\boldsymbol{S}(\tilde{\boldsymbol{b}})\boldsymbol{f}^b_{nb} \end{aligned} \tag{7.12}$$

with $\tilde{\boldsymbol{b}}^b_{\text{gyro}} := \boldsymbol{b}^b_{\text{gyro}} - \hat{\boldsymbol{b}}^b_{\text{gyro}}$ and the matrices are given

$$\begin{aligned} \boldsymbol{A}_a &= \begin{bmatrix} 0 & 1 & 0 & 0 & 0 & \\ 0 & 0 & 0 & 0 & 1 & \boldsymbol{0}_{2\times 3} \\ \boldsymbol{0}_{3\times 2} & & \boldsymbol{0}_{3\times 3} & & \boldsymbol{I}_3 & \\ \boldsymbol{0}_{3\times 2} & & \boldsymbol{0}_{3\times 3} & & \boldsymbol{0}_{3\times 3} & \end{bmatrix}, \\ \boldsymbol{B}_a &= \begin{bmatrix} \boldsymbol{0}_{2\times 3} \\ \boldsymbol{0}_{3\times 3} \\ \boldsymbol{I}_3 \end{bmatrix}, \quad \boldsymbol{C}_a = \begin{bmatrix} 1 & 0 & 0 & 0 & \dots & 0 \\ 0 & 0 & 1 & 0 & \dots & 0 \\ 0 & 0 & 0 & 1 & \dots & 0 \end{bmatrix}, \\ \boldsymbol{K}_a &= \vartheta \boldsymbol{L}_\vartheta^{-1} \boldsymbol{K}_0 \boldsymbol{E}_\vartheta, \end{aligned} \tag{7.13}$$

where

$$\begin{aligned} \boldsymbol{K}_0 &= \begin{bmatrix} K_{p_I p_I} & \boldsymbol{0}_{1\times 2} \\ K_{p p_I} & \boldsymbol{0}_{1\times 2} \\ \boldsymbol{0}_{2\times 1} & \boldsymbol{K}_{a,v} \\ K_{v p_I} & \\ \boldsymbol{0}_{2\times 1} & \boldsymbol{K}_{a,\xi} \\ K_{\xi p_I} & \end{bmatrix} \\ \boldsymbol{K}_{a,v} &= \text{blockdiag}\left(K_{v v_x}, K_{v v_y}, 0\right), \\ \boldsymbol{K}_{a,\xi} &= \text{blockdiag}\left(K_{v \xi_x}, K_{v \xi_y}, 0\right), \end{aligned} \tag{7.14}$$

and

$$\boldsymbol{L}_\vartheta = \text{blockdiag}\left(1, \frac{1}{\vartheta}, \frac{1}{\vartheta^2}\boldsymbol{I}_3, \frac{1}{\vartheta^3}\boldsymbol{I}_3\right) \tag{7.15}$$

such that $\boldsymbol{E}_\vartheta$ satisfies $\boldsymbol{E}_\vartheta \boldsymbol{C}_a = \boldsymbol{C}_a \boldsymbol{L}_\vartheta$ and $\tilde{\boldsymbol{u}}_a$ is the perturbing term from the error dynamics of Σ_1. Since the $\boldsymbol{C}_a$ the matrix is time-invariant, its pseudoinverse $\boldsymbol{C}^\dagger$, where † denotes the Moore–Penrose pseudoinverse, always has full rank. $\boldsymbol{E}_\vartheta$ can

then be calculated as $\boldsymbol{E}_\vartheta = \boldsymbol{C}_a \boldsymbol{L}_\vartheta \boldsymbol{C}_a^\dagger$. From the results of Grip et al. (2013), extended to incorporate the VVR by Bryne et al. (2014), the feedback interconnected system of (7.4)–(7.10) requires that the matrix $(\boldsymbol{A}_a - \boldsymbol{K}_0 \boldsymbol{C}_a)$ is Hurwitz and that $\vartheta \geq 1$ is utilized to suppress any perturbing terms from Σ_1. By defining $\boldsymbol{\eta} = \boldsymbol{L}_\vartheta \tilde{\boldsymbol{x}}_a$ the transformed error dynamics becomes

$$\frac{1}{\vartheta}\dot{\boldsymbol{\eta}} = (\boldsymbol{A}_a - \boldsymbol{K}_0 \boldsymbol{C}_a)\boldsymbol{\eta} + \frac{1}{\vartheta^4}\boldsymbol{B}_a \tilde{\boldsymbol{u}}_a. \tag{7.16}$$

Since the error dynamics of (7.16) is equal to the corresponding error dynamics in (Bryne et al., 2014, Eqs. (14)), the stability proof of Bryne et al. (2014), based on the conditions of Grip et al. (2013), is applicable to prove that the origin of the error dynamics of the feedback interconnected system $\Sigma_1 - \Sigma_2$ is USGES. The proof in Bryne et al. (2014) involves compounded Lyapunov function candidates (LFC) for (7.16) and the error dynamics of (7.4), and dominating any indefinite terms relating the attitude and translational motion error dynamics in the compounded LFC's derivatives, using k_1, k_2 and the high-gain-like parameter ϑ. □

7.4 Lever-arm-compensated Translational Motion Observer

7.4.1 Observer equations

We employ the observer found in (Fossen, 2011, Ch. 11) sans accelerometer bias estimation, but with the lever arm for the position measurement:

$$\Sigma_3 : \begin{cases} \dot{\hat{\boldsymbol{p}}}^n_{nb} = \hat{\boldsymbol{v}}^n_{nb} + \boldsymbol{K}_p \tilde{\boldsymbol{y}}_p & \text{(7.17a)} \\ \dot{\hat{\boldsymbol{v}}}^n_{nb} = \hat{\boldsymbol{R}}^n_b \boldsymbol{f}^b_{\text{IMU}} + \boldsymbol{g}^n_b + \boldsymbol{K}_v \tilde{\boldsymbol{y}}_p & \text{(7.17b)} \\ \hat{\boldsymbol{p}}^n_{\text{PosRef}} = \hat{\boldsymbol{p}}^n_{nb} + \hat{\boldsymbol{R}}^n_b \boldsymbol{r}^b_b & \text{(7.17c)} \end{cases}$$

where

$$\tilde{\boldsymbol{y}}_p = \boldsymbol{p}^n_{\text{PosRef}} - \hat{\boldsymbol{p}}^n_{\text{PosRef}} \tag{7.18}$$

and $\hat{\boldsymbol{R}}^n_b := \boldsymbol{R}\left(\hat{\boldsymbol{q}}^n_b\right)$. With $\hat{\boldsymbol{x}} = [\hat{\boldsymbol{p}}^{n\,\intercal}_{nb}, \hat{\boldsymbol{v}}^{n\,\intercal}_{nb}]^\intercal$, the observer (7.17)-(7.18) can be written as:

$$\dot{\hat{\boldsymbol{x}}} = \boldsymbol{A}\hat{\boldsymbol{x}} + \boldsymbol{B}\hat{\boldsymbol{u}} + \boldsymbol{K}(\boldsymbol{y}_p - \boldsymbol{C}\hat{\boldsymbol{x}} - \boldsymbol{D}\hat{\boldsymbol{u}}) \tag{7.19}$$

where

$$\boldsymbol{A} = \begin{bmatrix} \boldsymbol{0} & \boldsymbol{I} \\ \boldsymbol{0} & \boldsymbol{0} \end{bmatrix}, \boldsymbol{B} = \begin{bmatrix} \boldsymbol{0} & \boldsymbol{0} \\ \boldsymbol{0} & \boldsymbol{I} \end{bmatrix}, \boldsymbol{C} = \begin{bmatrix} \boldsymbol{I} & \boldsymbol{0} \end{bmatrix}, \boldsymbol{D} = \begin{bmatrix} \boldsymbol{I} & \boldsymbol{0} \end{bmatrix}$$

and

$$\hat{\boldsymbol{u}} = \begin{bmatrix} \hat{\boldsymbol{R}}^n_b \boldsymbol{r}^b_b \\ \hat{\boldsymbol{R}}^n_b \boldsymbol{f}^b_{\text{IMU}} + \boldsymbol{g}^n_b \end{bmatrix}$$

and the gain $\boldsymbol{K} = [\boldsymbol{K}_p^\intercal, \boldsymbol{K}_v^\intercal]^\intercal$ is chosen such that $\boldsymbol{A} - \boldsymbol{K}\boldsymbol{C}$ becomes Hurwitz. The terms $\boldsymbol{B}\hat{\boldsymbol{u}}$ and $\boldsymbol{D}\hat{\boldsymbol{u}}$ represent cascaded interconnections between $\Sigma_1 - \Sigma_2$ and Σ_3. The overall observer structure is found in Fig. 7.2

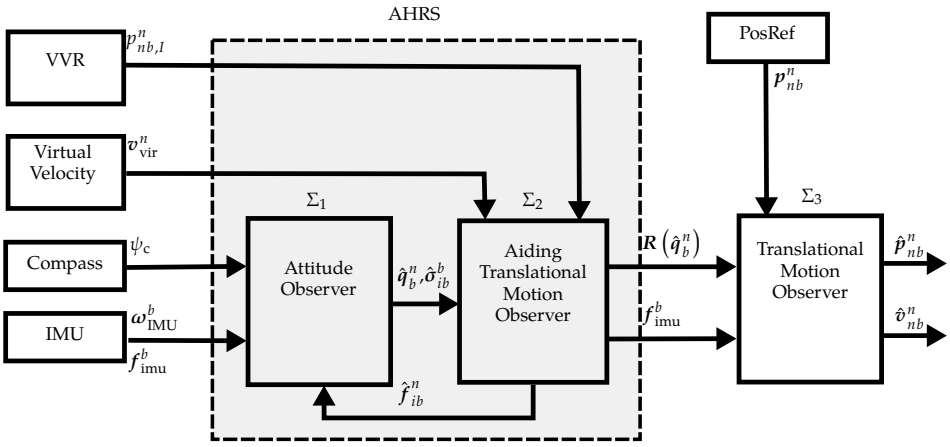

Figure 7.2: Feedback-interconnected and cascaded observer structure.

7.4.2 Stability of the Cascaded Interconnection Between the AHRS $\Sigma_1 - \Sigma_2$ and TMO Σ_3

Using (7.2), we put the translational motion system model in the state-space representation

$$\dot{\boldsymbol{x}} = \boldsymbol{A}\boldsymbol{x} + \boldsymbol{B}\boldsymbol{u} \tag{7.20a}$$

$$\boldsymbol{y}_p = \boldsymbol{C}\boldsymbol{x} + \boldsymbol{D}\boldsymbol{u} + \boldsymbol{d}_p \tag{7.20b}$$

where

$$\boldsymbol{u} = \begin{bmatrix} \boldsymbol{R}^n_b \boldsymbol{r}^b_b \\ \boldsymbol{R}^n_b \boldsymbol{f}^b_{\text{IMU}} + \boldsymbol{g}^n_b \end{bmatrix}.$$

From (7.20) and (7.17)-(7.19), we can derive the error dynamics for the TMO

$$\dot{\tilde{\boldsymbol{x}}} = (\boldsymbol{A} - \boldsymbol{K}\boldsymbol{C})\tilde{\boldsymbol{x}} + (\boldsymbol{B} - \boldsymbol{K}\boldsymbol{D})\tilde{\boldsymbol{u}} - \boldsymbol{K}\boldsymbol{d}_p \tag{7.21}$$

where $\tilde{\boldsymbol{x}} = \boldsymbol{x} - \hat{\boldsymbol{x}}$ and $\tilde{\boldsymbol{u}} = \boldsymbol{u} - \hat{\boldsymbol{u}}$.

From (7.21) we see that the sensor noise and faults $\boldsymbol{d}_p$ will influence the estimates, and this will be exploited in Section 7.5 to detect faults. However, for this method to be successful the nominal estimator without faults needs to be able to estimate the states in a consistent manner, so for now $\boldsymbol{d}_p$ will be neglected in order to evaluate the estimator stability.

Proposition 2. *Let the gain matrix $\boldsymbol{K}$ be chosen such that $\boldsymbol{A} - \boldsymbol{K}\boldsymbol{C}$ is Hurwitz, and the conditions of Proposition 7.1 be satisfied. If $\boldsymbol{d}_p = \boldsymbol{0}$, the origin of the error dynamics of $\Sigma_1 - \Sigma_2 - \Sigma_3$ is USGES.*

Proof. Consider the nominal linear error dynamics of (7.21),

$$\dot{\tilde{\boldsymbol{x}}} = (\boldsymbol{A} - \boldsymbol{K}\boldsymbol{C})\tilde{\boldsymbol{x}} \tag{7.22}$$

where the origin is GES since $(\boldsymbol{A} - \boldsymbol{KC})$ is Hurwitz. The error dynamics of (7.21) is perturbed by $(\boldsymbol{B} - \boldsymbol{KD})\tilde{\boldsymbol{u}}$ where the input $\tilde{\boldsymbol{u}}$ can be written as:

$$\begin{aligned}\tilde{\boldsymbol{u}} &= \begin{bmatrix} \boldsymbol{R}_b^n \boldsymbol{r}_b^b - \hat{\boldsymbol{R}}_b^n \boldsymbol{r}_b^b \\ \boldsymbol{R}_b^n \boldsymbol{f}_{\text{IMU}}^b + \boldsymbol{g}_b^n - \hat{\boldsymbol{R}}_b^n \boldsymbol{f}_{\text{IMU}}^b - \boldsymbol{g}_b^n \end{bmatrix} \\ &= \begin{bmatrix} \left(\boldsymbol{R}_b^n - \hat{\boldsymbol{R}}_b^n\right) \boldsymbol{r}_b^b \\ \left(\boldsymbol{R}_b^n - \hat{\boldsymbol{R}}_b^n\right) \boldsymbol{f}_{\text{IMU}}^b \end{bmatrix} \\ &= \begin{bmatrix} \left(\boldsymbol{I}_3 - \tilde{\boldsymbol{R}}^\intercal\right) \boldsymbol{R}_b^n \boldsymbol{r}_b^b \\ \left(\boldsymbol{I}_3 - \tilde{\boldsymbol{R}}^\intercal\right) \boldsymbol{R}_b^n \boldsymbol{f}_{\text{IMU}}^b \end{bmatrix} = \begin{bmatrix} \tilde{\boldsymbol{u}}_1 \\ \tilde{\boldsymbol{u}}_2 \end{bmatrix} \end{aligned} \tag{7.23}$$

where $\tilde{\boldsymbol{R}} = \boldsymbol{R}_b^n \left(\hat{\boldsymbol{R}}_b^n\right)^\intercal$. Taking the norm of $\tilde{\boldsymbol{u}}_1$ and $\tilde{\boldsymbol{u}}_2$ and applying that $\left\|\boldsymbol{R}_b^n\right\| = 1$, $\|\boldsymbol{I}_3 - \tilde{\boldsymbol{R}}^\intercal\| = \left\|\tilde{\eta}\boldsymbol{S}(\tilde{\boldsymbol{\varepsilon}}) - \boldsymbol{S}(\tilde{\boldsymbol{\varepsilon}})^2\right\| \leq 2\|\tilde{\boldsymbol{\varepsilon}}\|$, where $\tilde{\eta}$ is the scalar part of $\tilde{\boldsymbol{q}}$, yields:

$$\begin{aligned} \|\tilde{\boldsymbol{u}}_1\| &= \left\| \left(\boldsymbol{I}_3 - \tilde{\boldsymbol{R}}^\intercal\right) \boldsymbol{R}_b^n \boldsymbol{r}_b^b \right\| \\ \|\tilde{\boldsymbol{u}}_1\| &\leq 2l\|\tilde{\boldsymbol{\varepsilon}}\| \end{aligned} \tag{7.24}$$

$$\begin{aligned} \|\tilde{\boldsymbol{u}}_2\| &= \left\| \left(\boldsymbol{I}_3 - \tilde{\boldsymbol{R}}^\intercal\right) \boldsymbol{R}_b^n \boldsymbol{f}_{\text{IMU}}^b \right\| \\ \|\tilde{\boldsymbol{u}}_2\| &\leq 2f_{\max}\|\tilde{\boldsymbol{\varepsilon}}\| \end{aligned} \tag{7.25}$$

where $l = \|\boldsymbol{r}_b^b\|$, $f_{\max} = \max(||\boldsymbol{f}_{\text{IMU}}^b||)$, $\tilde{\boldsymbol{\varepsilon}} = [\tilde{\varepsilon}_1 \ \tilde{\varepsilon}_2 \ \tilde{\varepsilon}_3]$ is the vector part of the error quaternion $\tilde{\boldsymbol{q}}$ associated with $\tilde{\boldsymbol{R}}$, such that if $||\tilde{\boldsymbol{\varepsilon}}|| \to 0$ then, $\tilde{\boldsymbol{R}} \to \boldsymbol{I}_3$. While satisfying the conditions of (7.24)-(7.25), Proposition 7.1, and adhering to $(\boldsymbol{A} - \boldsymbol{KC})$ being Hurwitz, the GES error dynamics (7.22) is perturbed by the USGES error dynamics of $\Sigma_1 - \Sigma_2$ via a linearly bounded cascade connection. Then, according to Loria and Panteley (2005), the error dynamics of the total system $\Sigma_1 - \Sigma_2 - \Sigma_3$ is USGES. □

7.5 Fault Detection

There exist numerous PosRefs available for DP. In this work we have chosen to focus on dGNSS faults, in particular non abrupt errors which in general are difficult to detect.

We have a selected a method from Blanke et al. (2006) to detect the fault itself, see below.

7.5.1 Types of faults

There are several GNSS errors that manifests themselves as faults on the GNSS receivers' outputs, like ephemeris, troposphere, satellite clock, multipath, ionosphere and receiver errors (Grewal et al., 2013, Ch. 7). Some of these may be alleviated by employing differential GNSS (Grewal et al., 2013), but there are

still cases where error causes faults in the receiver outputs leading to potentially dangerous situations. Chen et al. (2009); Johansen et al. (2005) describes three manifestations as such:

- Position jump
- Slow drift
- Rapid drift

The focus will be on drifts, as detection of jumps or wild points is relatively easy and well established, see e.g. (Gustafsson, 2012, Ch. 7.6).

7.5.2 Drift detection

For detecting position drifts, we will monitor the innovation signal $\tilde{\boldsymbol{y}}_p$ for any discrepancies or transients caused by $\boldsymbol{d}_p$, in a similar way as in Rogne et al. (2014) and Rogne et al. (2015) (see Section 6.2.8. In those papers, the TMOs were tuned so that the fault could literally be spotted by monitoring the $\tilde{\boldsymbol{y}}_p$ directly, but this caused the accuracy of the position measurement to suffer.

However, in contrast to those rather basic methods, a well established fault detection technique will be used in this chapter. (Blanke et al., 2006, Ch. 6.7) provides the algorithm *"CUSUM algorithm for detection of a change in the mean of a Gaussian sequence"*. The motivation for applying this algorithm is that one could reliably detect faults, while at the same time tune the observer to maintain a reasonably accurate position estimate, because of the algorithm's more sophisticated analysis of the innovation signal. Transient changes in the innovation signal as described in Rogne et al. (2014, 2015), should be detected adequately by the CUSUM algorithm.

The steps in the algorithm involves:

- Initialization:
  - Assess mean and standard deviation $\tilde{\boldsymbol{y}}_p$ in fault free operation by statistical analysis of the signal.
  - Specify change of mean to be detected, as well as mean time for detection and false alarm
  - Tune the algorithm parameters to make the output comply with the detection requirements
- While running:
  - Acquire new data $\tilde{\boldsymbol{y}}_p$
  - Input new data to decision function
  - If decision function output is larger than a threshold based on the initialization, i.e. the mean has changed enough, raise an alarm.

– Estimate time of fault occurrence

For slowly emerging PosRef faults, even minor errors in bias compensation, both for rate gyros and accelerometers, will affect the fault-detection ability since larger PosRef injection is needed if such errors sources is not compensated for sufficiently well. Also, the signal-to-noise ratio of a given PosRef measurement will affect how the decision function of the CUSUM algorithm is tuned. The algorithm must be able to distinguish between normal sensor output variation, and the rarer faults and drifts that may occur. A natural consequence of this is that the fault detecting abilities are limited by the noise in the nominal case.

This chapter presents a fault detection strategy applicable for loosely coupled GNSS/INS integration. For tightly coupled integration strategies, other and perhaps better performing methods might be used, such as Receiver Autonomous Integrity Monitoring, known as RAIM, presented in e.g. (Groves, 2013, Ch. 17.4) combined with an inertial measurement unit.

7.6 Simulation Case Study

The simulations were performed in MATLAB/Simulink R2013b, making use of a dynamic ship simulator in full 6-DOF with waves (Fossen and Perez, 2010), a simulated DP controller and added measurement noise. All measurements were set to have a zero mean normally distributed noise, except for the position reference system noise which was modeled as a Gauss-Markov process Mohleji and Wang (2010), see Table 7.1 for their parameters. The IMU had a sampling frequency of 100 Hz, the GNSS 1 Hz, and the gyrocompass 5 Hz. The observers were not part of the feedback loop for the DP controller. The chosen lever arm was $\boldsymbol{r}_b^b = [30,\ 0,\ -20]^\top$ corresponding to the PosRef providing measurements in a point 30 meters in front of and 20 over the IMU.

Table 7.1: Measurement noises

Measurement	**Std. dev.**	**Markov time constant**
IMU acceleration	0.002 m/s^2	-
IMU gyro	0.08 deg/s	-
Position reference system x and y	1.2 m	8 min
Position reference system z	2.4 m	8 min
Gyrocompass	0.07 deg	-

7.6.1 Observer tuning

For Σ_1 we used the gains $k_1 = 1.0, k_2 = 1.5, k_I = 0.03$. The high-gain like parameter for Σ_2 was chosen $\theta = 1$. For the gains $\boldsymbol{K}_0$ and $\boldsymbol{K}$ for Σ_2 and Σ_3, respectively, we

employed the continous-time steady-state Riccati equation, similar to the Kalman-Bucy filter Kalman and Bucy (1961), with the following covariance matrices:

$$\begin{aligned}
\boldsymbol{Q}_{\Sigma_2} &= \text{blockdiag}(0.1^2\boldsymbol{I}_3, 0.15^2\boldsymbol{I}_3) \\
\boldsymbol{R}_{\Sigma_2} &= \text{diag}(75^2, 5^2, 5^2) \\
\boldsymbol{Q}_{\Sigma_3} &= \text{blockdiag}(\boldsymbol{0}_{3\times3}, 0.1^2\boldsymbol{I}_3) \\
\boldsymbol{R}_{\Sigma_3} &= \text{diag}(4.8^2, 4.8^2, 9.6^2)
\end{aligned}$$

For the CUSUM algorithm we set $h = 15$ and $\mu_1 = \pm 1$, where h is a tuning parameter for the algorithm sensitivity, and μ_1 is the change we want to detect. We refer to (Blanke et al., 2006, Ch. 6.7, pp. 245-247) for the details of these parameters.

7.6.2 Fault free position, velocity and attitude estimation

In the first case we did a basic simulation of estimating bias, attitude, position and velocity. The results can be seen in Figs. 7.3 - 7.5. As can be witnessed, the observers managed fairly well in this task.

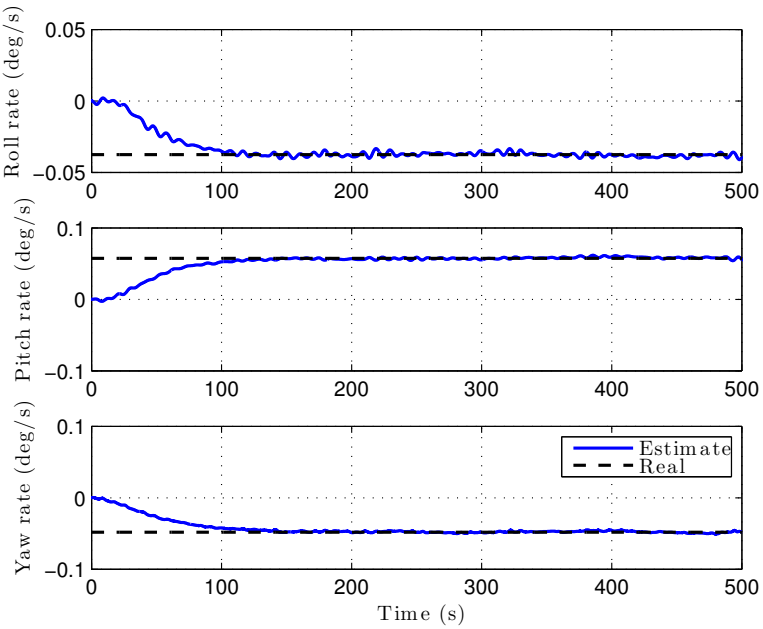

Figure 7.3: Case 1 (no fault): Bias estimates.

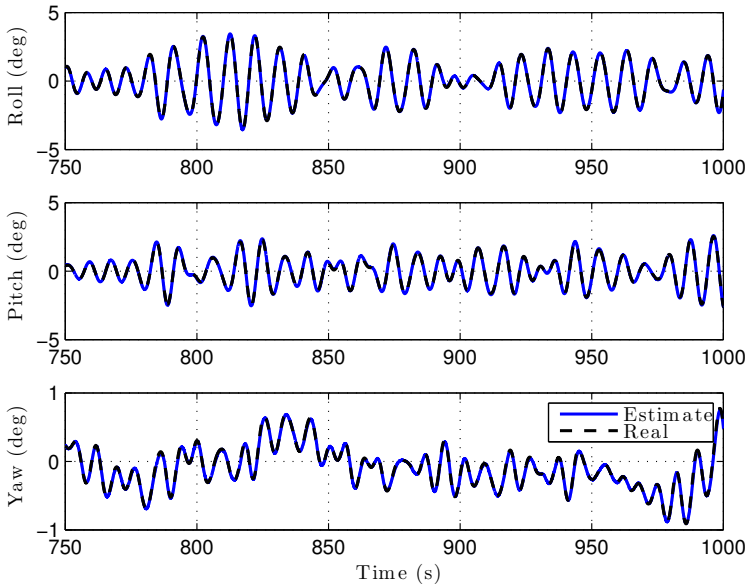

Figure 7.4: Case 1 (no fault): Attitude estimates.

7.6.3 Drift detection

In the second case, the position reference system was set to drift at $t = 1000s$ in the North direction with the drift shown in Fig. 7.6. The results are laid out in Fig. 7.7. As the topmost plot reveals, the position estimate followed the faulty measurement trustingly. However, the graph in the middle shows the estimation error $\tilde{\boldsymbol{y}}_{p,\text{north}}$, from which we can faintly see some spikes just after $t = 1000s$ when the drift started, and at $t = 1100s$, around the time the drift stopped. The bottom plot shows the alarm output of the CUSUM algorithm. The first alarm were raised at about $t = 1014s$, at which point the drift profile has just not yet reached 1.5 meters. The algorithm also raised an alarm at the end of the drift profile, indicating another change of mean. Furthermore, no false alarms were raised during the simulation run.

7.6.4 Discussion

The results of simulation Case 1 and 2 tell us that the proposed observer and fault detection scheme manages well in both disciplines — both accurate estimation and fault detection. This is in contrast to the methods in Rogne et al. (2014, 2015), which had to tune their equivalent of Σ_3 very relaxed in order to catch the fault. In opposition to Rogne et al. (2014, 2015), the proposed detection scheme is based on a CUSUM algorithm. To ensure that the innovation $\tilde{\boldsymbol{y}}_p$ resembles a

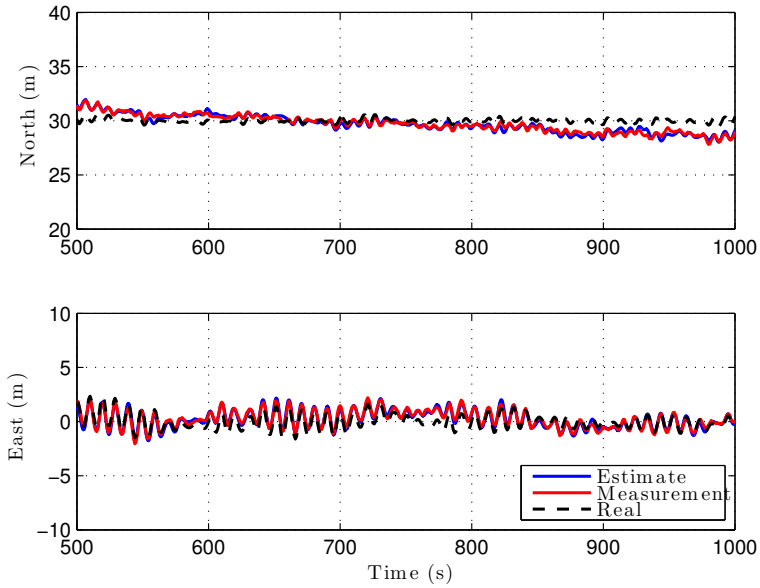

Figure 7.5: Case 1 (no fault): Position estimates.

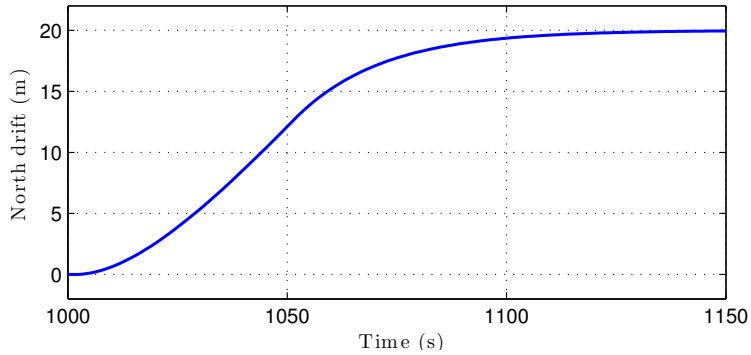

Figure 7.6: Case 2: GNSS measurement drift.

gaussian sequence over shorter sampling intervals, the tuning is chosen to have larger feedback compared to the results Rogne et al. (2014, 2015). With a more relaxed tuning, $\tilde{\boldsymbol{y}}_p$ will resemble a Gauss-Markov process due to the simulated noise characteristics of the dGNSS. It this case, the chance of false positives might increase. Nevertheless, in a practical system, the tuning might still have to be more relaxed for robustness and sensitivity to a wider range of drift rates.

With an alarm being raised for drifting before reaching 1.5 meters, this proves that the system is a viable way of detecting faults early in the drift's progress even

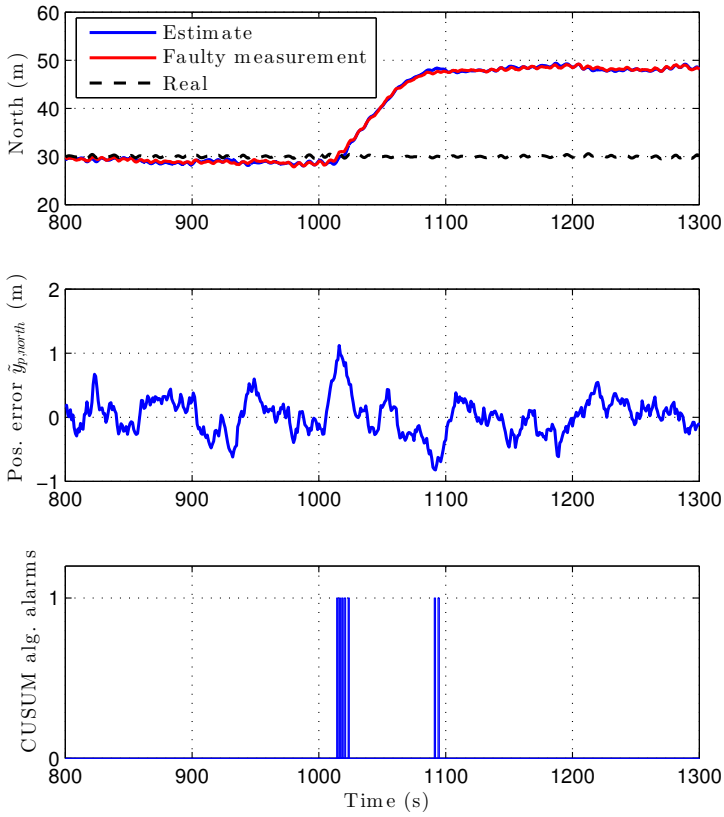

Figure 7.7: Case 2: Top: Position estimate, GNSS measurement and real GNSS position. Middle: position estimate error. Bottom: CUSUM algorithm alarm output.

tough the drift scenario here is seemingly more difficult, compared to those in Rogne et al. (2014, 2015), since the drift is smooth, as seen in Fig 7.6, as opposed to a ramp shape (see Section 6.3.2).

7.7 Full-Scale Verification

The drift detection of Section 7.6.3 has, after the completion of Rogne et al. (2016b) upon which this chapter is based, been applied to the same DP dataset as in Chapter 4 (Fig. 4.3a), with the added drift of Fig. 7.6. The sensor used was the STIM300. The results can be seen in Fig. 7.8, corresponding to the simulated results of Fig. 7.7. As we can see, the CUSUM algorithm successfully detected the

position drift also in this test.

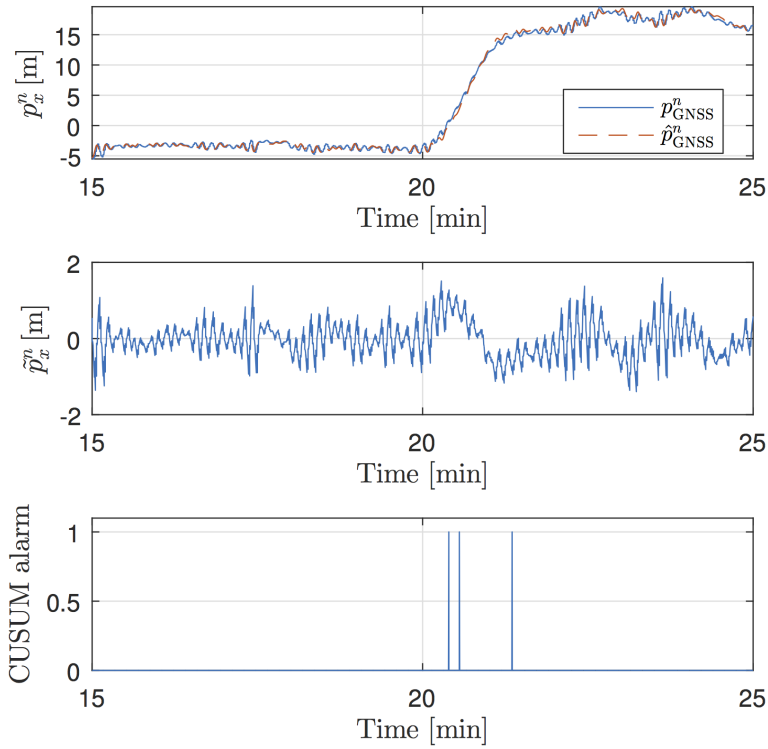

Figure 7.8: Case 2: Top: GNSS measurement and position estimate. Middle: position estimate error. Bottom: CUSUM algorithm alarm output

7.8 Conclusion

We proposed a three-stage nonlinear observer based on IMUs aided by a position reference system. The position reference system was assumed to be placed at a distance from the IMU, necessitating the need for lever arm compensation. Connecting a feedback interconnected AHRS to a translational motion observer in cascade, USGES properties were proven for the three stage observer. The observer was put in tandem with an established algorithm for fault detection, and simulations demonstrated that scheme has the capacity to detect slow drifts within a position reference system. A simple full-scale verification of the same result displayed similar capabilites.

8

INS in Fault-Tolerant Dynamic Positioning

This chapter is based on Bryne et al. (2017b).

8.1 Introduction

The International Maritime Organization (IMO) have issued guidelines for vessels with dynamic positioning (DP) systems (International Maritime Organization, 1994) to reduce the risk of loss of position during DP operations. Classification societies have defined class notations based on these guidelines. The DP classifications are dependent on vessel type, operation and the potential consequences in the event of loss of position. These range from equipment class 1 to 3, while some societies also operate with equipment class 0.

The general functional requirement is that single failure in an active component should not result in loss of position. This is handled by redundancy in all active components, where redundancy, according to DNV GL (2013), is defined:

> *Redundancy*. The ability of a component or system to maintain its function when one failure has occurred. Redundancy can be achieved, for instance, by installation of multiple components, systems or alternative means of performing a function.

For equipment class 2 and 3, the following main rules are given by MSC/Circ. 645, International Maritime Organization (1994):

- Equipment class 2: Redundancy in all active components.
- Equipment class 3: Redundancy in all active components and physical separation (A.60) of the components.

Equipment class 1 (and 0) allow for loss of position in the event of a single failure. Therefore, these classes will not be dealt with further. A more detailed description

is given in Tab. 8.1, where class notations from DNV GL, American Bureau of Shipping (ABS) and Lloyds Register (LR) are given. Concerning the sensors system on

Table 8.1: DP Classifications

Description	**IMO**	**Class notations**		
Related to automatic and manual position and heading control	**DP Class**	**DNV GL**	**ABS**	**LR**
In case of single fault excluding loss of a compartment. Two independent computer systems. Specified maximum environmental conditions.	Class 2	DPS 2 DYNPOS-AUTR	DPS-2	DP (AA)
Single fault including loss of a compartment due to fire or flood. Two (or more) independent computer systems. Extra back-up system separated by A60 class division). Specified maximum environmental conditions.	Class 3	DPS 3 DYNPOS–AUTRO	DPS-3	DP (AAA)

a DP vessel, both DP notations related to equipment class 2 and 3 often implement the redundancy requirement by enforcing a triple-redundancy sensor related installation. In the authors' opinion, this practice has so far not taken advantage of the full potential of MEMS inertial sensors, obtained from recent developments, and the knowledge of upside and downsides with the different standard onboard sensors. The triple-redundancy requirements may also in certain circumstances impair robustness and safety since the potential downsides outweighs the potential upsides. Especially so related to the wind sensor where the conclusions from Stephens (2011), state that using the wind sensor is not essential for maintaining positing and, in fact, that using wind-feed-forward control can be detrimental in stationkeeping.

This chapter proposes an alternative sensor configuration to that of today's state-of-the-art class notations. The configuration has low-cost redundant MEMS IMUs at its center. With this structure, the redundant IMUs, with appropriate software, have the potential to replace existing sensor solutions. In addition, dual-redundant PosRefs and gyrocompasses are deemed sufficient to maintain position and heading. The latter is due to fault detection and identification (FDI) of the PosRefs and gyrocompases obtained by exploiting the redundant IMUs and estimators. Moreover, the sensor structure is compliant with the main principle

of both equipment class 2 and 3; no single point of failure in an active (sensor) component shall results in loss of position. With IMUs, all accelerations, induced by forces affecting the vessel, are measured directly by accelerometers. Therefore, the wind sensors can be circumvented without impeding the DP control performance. Furthermore, the industry-standard VRU solutions can also be replaced since the vessel motions are obtained using the same redundant-IMU configuration and sensor fusion. All in all, the proposed sensor configuration has the potential to significantly reduce the cost of dynamic positioning systems without compromising safety.

8.1.1 Nomenclature

- $\{b\}$ - BODY coordinate frame
- $\{t\}$ - tangent frame equivalent to north-east-down (NED) where $\{t\}$ is Earth fixed and rotates with the Earth rate
- $\{i\}$ - inertial coordinate frame
- $\boldsymbol{p}_{tb}^{t} \in \mathbb{R}^3$ - position in $\{t\}$ frame
- $\boldsymbol{v}_{tb}^{t} \in \mathbb{R}^3$ - linear velocity in NED frame
- $\boldsymbol{\omega}_{ib}^{b} \in \mathbb{R}^3$ - angular rate of the vessel($\{b\}$ frame) relative the inertial frame in the BODY frame, given in the BODY frame
- $\boldsymbol{f}_{ib}^{b} \in \mathbb{R}^3$ - specific force of the vessel($\{b\}$ frame) relative the inertial frame in the BODY frame, given in the BODY frame
- ϕ, θ, ψ - euler angles: Roll, pitch, yaw
- $\boldsymbol{R}(\psi) \in SO(3)$ - rotation matrix: For rotating the BODY z-axis to the NED frame
- $\boldsymbol{R}_{b}^{t} \in SO(3)$ - full rotation matrix
- $\boldsymbol{r}_{b}^{b} \in \mathbb{R}^3$ - leverarm from vessel CO to given position reference system (PosRef)
- p_{x}^{t} - north position components given in $\{t\}$ (similar to NED)
- p_{y}^{t} - east position components given in $\{t\}$ (similar to NED)
- u_{tb}^{b}, v_{tb}^{b} - surge and sway velocity
- r - yaw rate
- $\tau_{\star}$ - generalized force vector
- $\boldsymbol{M}$ - mass matrix. $M > 0 \in \mathbb{R}^{3\times3}$.
- $\boldsymbol{D}$ - linear damping matrix. $D > 0 \in \mathbb{R}^{3\times3}$.

8.2 Sensor and Control Systems

8.2.1 DP sensor systems

Several types of sensors are applied on a DP vessel. IMO and the classification societies differentiate between position references (PosRef) systems and (external) vessel sensors. PosRefs provide localization of the vessel, local position relative some known point or global positioning, and can be based on differential global navigation satellite systems (dGNSS), e.g. dGPS, dGLONASS, dBeiDou, hydroacoustic position reference (HPR), optical (e.g. Fanbeam, CyScan) and microwave (RadaScan, Radius). The other vessels sensors consist of three main types:

- **Gyrocompasses**: Providing heading measurements, ψ.
- **Wind sensors**: Providing measurements of wind speed and direction. With these signals, wind forces and moments are calculated using wind coefficients and a model of the wind projection area.
- **VRUs/vertical reference sensors(VRSs)**: Provide roll (ϕ), pitch (θ) and sometimes heave. These signals are primarily utilized for leverarm compensation of PosRefs to a given point of the vessel/center of orientation (CO);

$$\boldsymbol{p}^t_{\text{CO}} = \boldsymbol{p}^t_{\text{PosRef}} - \boldsymbol{R}^t_b(\phi, \theta, \psi)\boldsymbol{r}^b_b. \tag{8.1}$$

8.2.2 DP control system

The sensors are related to the control problem illustrated with the simplified vessel model, Fossen (2011),

$$\dot{\boldsymbol{\eta}} = \boldsymbol{R}(\psi)\boldsymbol{\nu} \tag{8.2}$$

$$\boldsymbol{M}\dot{\boldsymbol{\nu}} = -\boldsymbol{D}\boldsymbol{\nu} + \boldsymbol{\tau}_{\text{envir}} + \boldsymbol{\tau}_{\text{DPc}} \tag{8.3}$$

where $\boldsymbol{\eta} := (p^n_{\text{CO},x}, p^n_{\text{CO},y}, \psi)^\intercal$ and $\boldsymbol{\nu} = (u^b, v^b, r)^\intercal$ are vessel's horizontal generalized position and velocity, respectively. Furthermore, the generalized environmental forces on the vessel are represented by

$$\boldsymbol{\tau}_{\text{envir}} = \boldsymbol{\tau}_{\text{current}} + \boldsymbol{\tau}_{\text{waves}} + \boldsymbol{\tau}_{\text{wind}} + \boldsymbol{\tau}_{\text{ice}}, \tag{8.4}$$

where $\boldsymbol{\tau}_{\text{DPc}} = -\hat{\boldsymbol{\tau}}_{\text{wind}} + \boldsymbol{\tau}_{\text{DP}}$ is the vessel controller induced force. The forces obtained from the wind sensors, $\hat{\boldsymbol{\tau}}_{\text{wind}}$, can be utilized in wind-feed-forward control. In addition, the DP controller signal, $\boldsymbol{\tau}_{\text{DP}}$, is used to compensate for current, wave drift and possibly ice forces and moments.

8.2.3 Inertial measurement units (IMUs)

An IMU provides measurements of tri-axial angular rate and specific force, provided by rate gyros and accelerometers, respectively, corrupted with noise and other error sources such as biases:

$$\boldsymbol{\omega}^b_{\text{IMU}} = \boldsymbol{\omega}^b_{ib} + \boldsymbol{b}^b_{\text{gyro}} + \boldsymbol{\varepsilon}_{\text{gyro}} \tag{8.5}$$

$$\boldsymbol{f}^b_{\text{IMU}} = \boldsymbol{f}^b_{ib} + \boldsymbol{b}^b_{\text{acc}} + \boldsymbol{\varepsilon}_{\text{acc}}. \tag{8.6}$$

Both type of error sources are mitigated with estimators and observers which are well established (Titterton and Weston, 2004; Farrell, 2008; Groves, 2013) in the literature.

8.2.4 Inertial navigation system (INS)

An inertial navigation system can be utilized to estimate the vessel's position, velocity and attitude (PVA). In addition, the inertial sensor biases are estimated by utilizing aided INS. Aided INS is implemented with some sensor fusion software based on e.g. extended Kalman filters (EKF), (Farrell, 2008; Groves, 2013) or nonlinear observers (NLOs), Bryne et al. (2016); Rogne et al. (2016a) and the references therein.

The INS can be realized by mechanizing the strapdown equations based on the IMU measurements; see e.g. Farrell (2008). For DP, this can be done be e.g. choosing a tangent representation of the NED frame, taking the form

$$\dot{\boldsymbol{p}}^t_{tb} = \boldsymbol{v}^t_{tb}, \tag{8.7}$$

$$\dot{\boldsymbol{v}}^t_{tb} = -2\boldsymbol{S}(\boldsymbol{\omega}^e_{ie})\boldsymbol{v}^t_{tb} + \boldsymbol{R}^t_b \boldsymbol{f}^b_{ib} + \boldsymbol{g}^t_b, \tag{8.8}$$

$$\dot{\boldsymbol{R}}^t_b = \boldsymbol{R}^t_b \boldsymbol{S}(\boldsymbol{\omega}^b_{ib}) - \boldsymbol{R}^t_b \boldsymbol{S}(\boldsymbol{\omega}^t_{ie}). \tag{8.9}$$

8.3 Current DP Sensor Configurations and Classifications

The current DP sensors classification are based upon MSC/Circ. 645, International Maritime Organization (1994). Related to PosRef, MSC/Circ. 645 states:

1. Position reference systems should be selected with due consideration to operational requirements, both with regard to restrictions caused by the manner of deployment and expected performance in working situation.

2. For equipment classes 2 and 3, at least three position reference systems should be installed and simultaneously available to the DP-control system during operation.

3. When two or more position reference systems are required, they should not all be of the same type, but based on different principles and suitable for the operating conditions.

4. The position reference systems should produce data with adequate accuracy for the intended DP-operation

5. The performance of position reference systems should be monitored and warnings provided when the signals from the position reference systems are either incorrect or substantially degraded.

6. For equipment class 3, at least one of the position reference systems should be connected directly to the back-up control system and separated by A.60 class division from the other position reference systems.

Furthermore, the IMO guidelines have put fourth the following guidelines related to the remaining vessel sensors:

1. Vessel sensors should at least measure vessel heading, vessel motions, and wind speed and direction.

2. When an equipment class 2 or 3 DP-control system is fully dependent on correct signals from vessel sensors, then these signals should be based on three systems serving the same purpose (i.e. this will result in at least three gyrocompasses being installed).

3. Sensors for the same purpose, connected to redundant systems should be arranged independently so that failure of one will not affect the others.

4. For equipment class 3, one of each type of sensors should be connected directly to the back-up control system and separated by A.60 class division from the other sensors.

DNV GL has, based on these guidelines, created classifications related to the necessary amount of sensors as presented in Tab. 8.2. The resulting sensors structure is illustrated in Fig. 8.1. This structure has the benefit of being intuitive where consequent triple redundancy makes it easy to perform FDI if one sensor fails, since the two remaining exclude the erroneous one with majority voting. However, this is not optimal since the specific force and angular rate inertial sensors contained in the VRUs are not exploited in the FDI of the PosRefs and gyrocompasses. Moreover, usage of the wind sensors is non-optimal and potentiality detrimental for stationkeeping capabilities, Stephens (2011). Here, taking advantage of contemporary high-quality MEMS sensors, with a relatively low cost, can serve as an alternative in the force calculations, (DNV GL, 2013, Appendix B), currently done by the wind sensor. The benefit of the inertial sensors are that regardless of the wind speed, direction and distribution, the induced vessel's accelerations

Table 8.2: Current Sensor configuration classifications required by DNV GL (2013)

Sensors		**Class 2**	**Class 3**
PosRef		3	3
External sensors	Wind	3(2)[a]	3(2)[a]
	Gyro compass	3	3
	VRS/VRU	3(2)[b]	3

[a] Three for DYNPOS–AUTR and AUTRO. Two for DPS 2 and DPS 3.
[b] Three for DYNPOS–AUTR. Where necessary for the correct functioning of position reference systems, at least three vertical reference sensors are to be provided for notation DPS 2

and angular velocities are measured directly, whereas for the wind sensors, the respective locations are important to obtain the correct forces. The wind force calculations are also sensitive to errors in the wind coefficients, projection area in addition to the speeds and directions measured. Moreover, the triple-redundant sensor requirement is also a cost driver of DP systems.

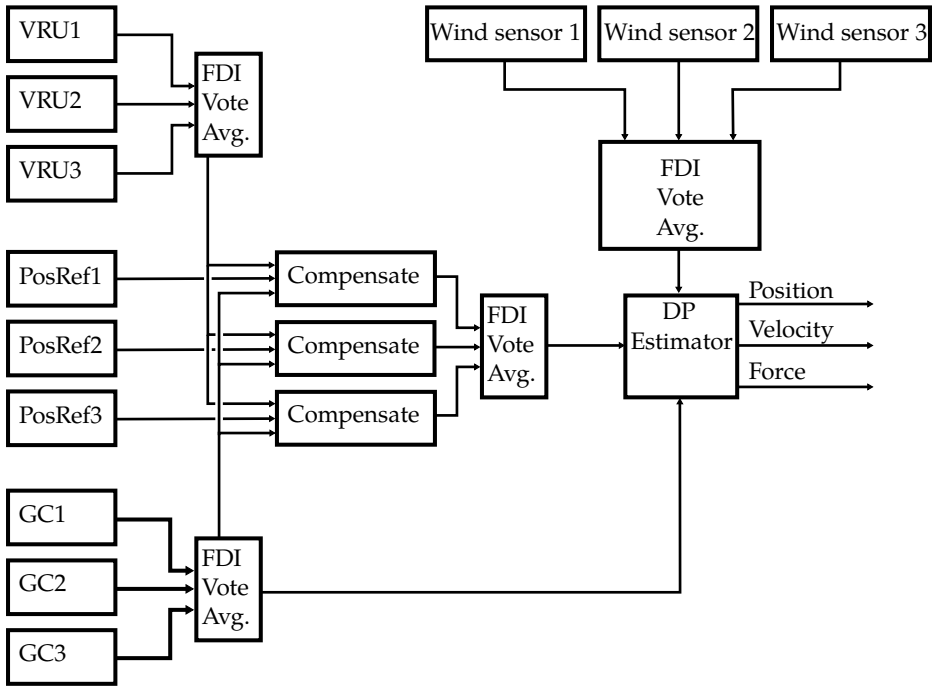

Figure 8.1: Current sensor structure of PosRefs, gyrocompasses (GC), VRUs and wind sensors. It is also common to use VRU*i* to motion compensate PosRef*i* and not use the averaged roll and pitch signals .

8.4 Proposed Sensor Configuration

The proposed sensor configuration, based on triple-redundant IMU measurements and dual-redundant PosRefs and gyrocompasses, is given in Tab. 8.3 and depicted

Table 8.3: Proposed sensor structure for DP

Sensors	**Class 2**	**Class 3**
PosRef	2	2[a]
Gyrocompass	2	2[a]
MEMS IMU	3	3[a]
Wind[b]	0	0

[a] Minimum 1 is subjected to A.60 class division for fire and flooding protection.

[b] Zero for positioning (wind-feed-forward control). One for weather predication and satisfying IMO Circ. 465. is applicable.

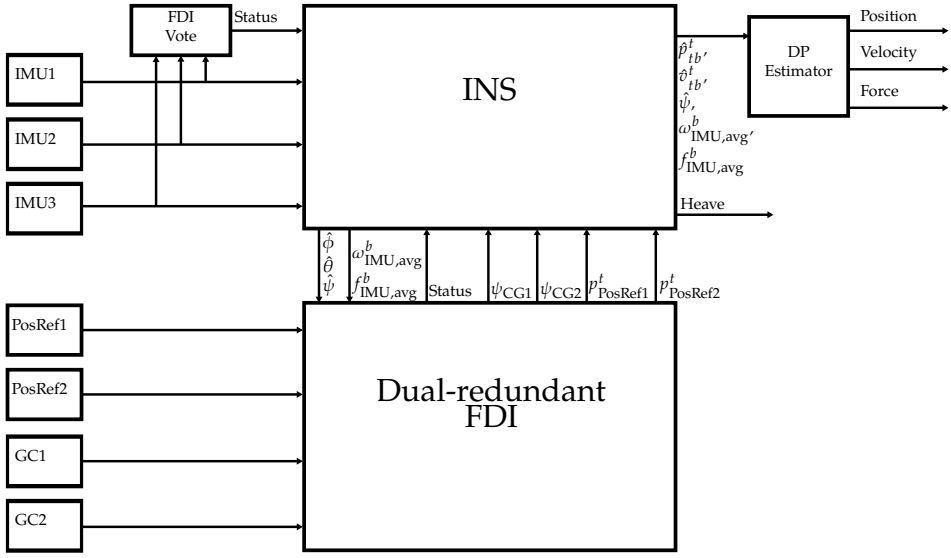

Figure 8.2: Proposed sensor structure. Detailed overview of the dual-redundant FDI is presented in Fig 8.3.

in Fig. 8.2. In contrast to the current class notations, the wind sensors are removed. This design is based upon applying sufficiently many inertial sensors such that any single fault in any of the IMUs' axis measurements are detectable and identifiable.

Inertial measurements that are deemed fault-free are weighted/averaged and then utilized in an FDI framework used to validate PosRefs and gyrocompasses. In addition to the inertial sensors and dual PosRefs and gyrocompasses, the FDI framework is based on redundant estimators. The weighted/averaged IMU measurements also form the basis for obtaining the inherit VRU solution, by estimating roll, pitch and heave, without any use of distinct VRUs. In addition, since specific force and angular rate measurements are available, an INS can be sufficient as DP estimator, and vessel-model-based DP estimator is not necessary. This claim is supported by developments of INS-based wave filters (Bryne et al., 2015a), where wave filters are utilized to prevent the oscillatory wave-induced motions to be considered by the control system, Fossen and Perez (2009).

8.4.1 Redundant IMUs instead of VRUs

State-of-the-art redundant-VRU FDI is based on signal processing of the respective roll and pitch outputs (ϕ_1, ϕ_2, ϕ_3 and $\theta_1, \theta_2, \theta_3$) before providing the DP system with averaged roll and pitch estimates (ϕ_{avg} and θ_{avg}). These, together with the averaged gyrocompass measurements are utilized for leverarm compensation of PosRefs. The VRUs are based on some type of inertial sensors, MEMS or other type of inertial sensing technology. Therefore, we propose that the averaging is

performed at the IMU level (as in Chapter 5) before estimating the VRU solution, providing roll, pitch and heave estimates, still based on redundant sensing. However, now only one set of VRU-output estimates are provided. The VRU solution is obtained from the INS, depicted in Fig. 8.3. The VRU solution can be carried out with or without aiding from PosRefs, and the former is done in Bryne et al. (2016).

In order to ensure that IMU faults are detection and identified, a parity-based FDI can be applied (Section 5.5), which is well established for redundant inertial sensing (Sturza, 1988). Redundancy in just the inertial sensors at the input level and in both inertial sensing and attitude estimation output can be applied in order to achieve appropriate FDI. The result of Section 5.7.5 also indicate that averaged accelerometers are beneficial for heave estimation performance.

8.4.2 Dual vs. triple-redundant PosRefs and gyrocompass

The idea behind triple redundancy in PosRef systems and vessel sensors is that if one of them fails, it is straightforward to identity the faulty sensor by voting algorithms. Also, for performance, the combined, weighted output of three systems surpasses that of a single system. However, especially for PosRefs, common mode faults and disturbances reduce the advantages that may be reaped from such configurations if identical systems are used. The average of three false outputs is still false.

For position reference systems in DP, there are cases where one might not be able to utilize three separate systems operating by different principles. In deep waters, it is conceivable that only GNSS and HPR are available. Adding a third position reference then means adding a second one of the existing types, potentially leaving the navigation system more vulnerable than was the intention of the triple-redundancy requirement. This is where an INS could be useful, providing position information that is independent from the position reference systems, and even from any external factors like satellites for GNSS and seabed transponders for HPR.

Usage of INS in a DP context is not new. As several papers (Vickery, 1999; Faugstadmo and Jacobsen, 2003; Paturel, 2004; Stephens et al., 2008; Carter, 2011; Russell, 2012) discuss, INS might be used in DP for enhancing position reference systems by filtering noise, increasing update rates, removing outliers, and providing position through dead reckoning (DR) during PosRef outages. While testifying the great effects and upsides the deployment of an INS may have, these references primarily suggest using one or two IMUs per position reference system for performance, and not fully integrate a redundant IMU solution in the DP system. Bryne et al. (2015a) and Rogne et al. (2015) demonstrated the potential for using IMUs as a mean for fault detection and isolation in triple and dual position reference systems, and Rogne et al. (2016b) for fault detection in the case of having a single position reference. Granted, INS based on MEMS might not be

satisfactory as a separate position reference, as in the purported purpose of such systems. An unaided MEMS INS tends to drift quite a lot after a while, staying within 5 meters in 1 minute (Rogne et al., 2016a), but for fault-tolerance usage, w.r.t. to PosRef fault detection, this might still be acceptable performance-wise. For PosRef errors develops slower that this ($\sim$ 10 cm per second) other information might be necessary for FDI. However, in such situations, the DP operator also have more time to make a decision regarding the ongoing DP operation. Using the zero velocity measurement applied in Rogne et al. (2016b), could improve cited results, but that remains to be investigated. With the help of a fiber optic gyro (FOG) or ring laser gyro (RLG) angular rate sensors, such a system may fare even better. In Paturel (2004), an unaided INS was demonstrated to stay within GPS accuracy for over 2.5 minutes. Another option is to use tightly coupled integration of GNSS/HPR and IMU such that integrity monitoring of each of the individually measured (pseudo)ranges, from the respective satellites/transponders to the receiver/transducer on vessel, can be carried out. This might improve FDI in the event of slowly evolving PosRef errors or faults.

For gyrocompasses, the concern of non-independence does not carry the same burden, as one gyrocompass is inherently independent from another. The argument for reducing the number of these vessel sensors rather comes down to cost and performance. Compared to even the highest quality MEMS angular rate sensor available for purchase, a gyrocompass is quite expensive. Addtionally, in situations where the vessel is subject to relatively high-dynamic yaw rates, the traditional gyrocompass, atleast the mechanical ones, might lag behind the output of a MEMS-based INS. In Rogne et al. (2016a), a MEMS-based INS running unaided from gyrocompasses, stayed within one degree on average for an hour over 12 runs compared to the reference. Rogne et al. (2014, 2015) investigates using IMUs for FDI in gyrocompasses, discovering that this is easier than for position because there is only one integrator between the IMU measurement (angular rate) and state (heading), as opposed to two integrators for position (from acceleration to position). For the reasons above, one could easily imagine replacing a gyrocompass with a triple-redundant MEMS IMUs configuration, as the latter is also useful in other parts of the DP system. State of the art within MEMS angular rate sensors also allows for a single IMU to be utilized as a heading reference for a limited amount of time if both gyrocompasses are unavailable.

8.4.3 Using IMUs instead of wind sensors in force and moment calculations

A ship can be exposed to environmental forces and moments as indicated in (8.2)–(8.3). The forces and moments may stem from current, waves, wind and is some cases ice loads. Wind sensors, measuring wind speeds and directions, together with using models including wind coefficients related to the wind projection area,

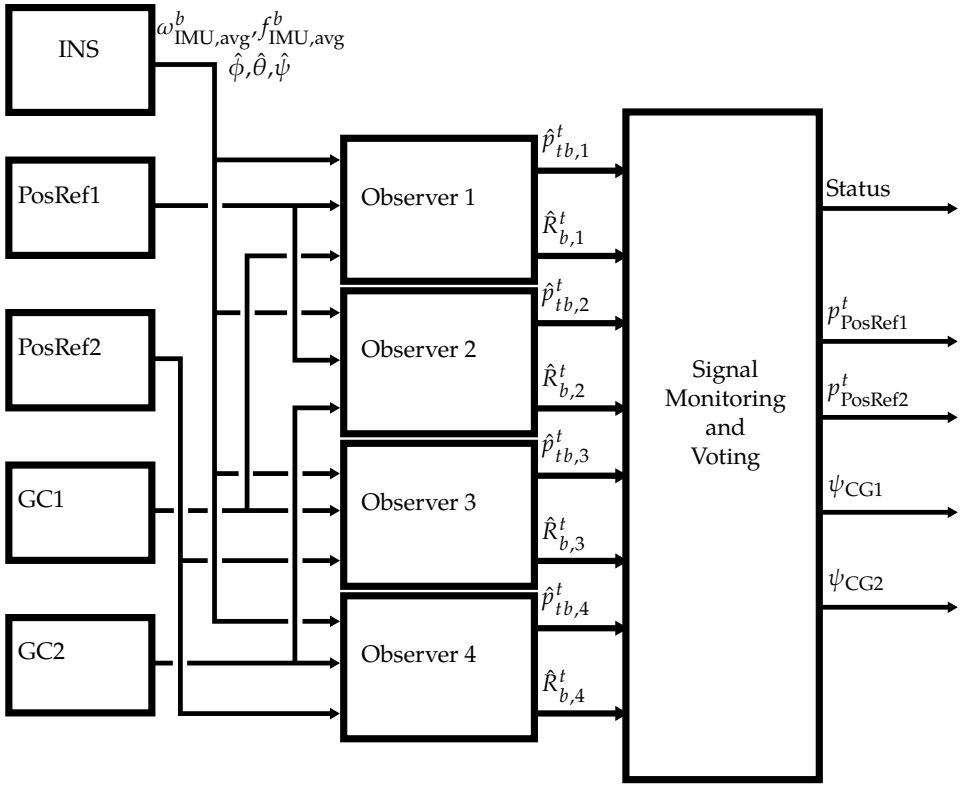

Figure 8.3: Dual-redundant FDI concept using observers and signal processing based on observer-innovation monitoring.

are utilized in order to calculate the wind forces and moments. These calculations are prone to errors in measurement of wind speed, direction and projection area. The wind is not necessarily uniform such that the location of the wind sensors of the ship also can influence these calculations (sheltering effects due to sensor location, structure-induced turbulence etc.), Stephens (2011). In addition, the wind force also must be lowpass filtered such that force from wind gusts is prevented to enter the control loop, Fossen (2011).

Reliable environmental force estimates can be obtained by exploiting the IMU measurements, since the inertial sensors measure vessel motions induced by the environment and the control system. Reliable accelerations and angular velocity responses, due to wind (or other environmental forces), are obtained regardless of wind type and wind sensor location with the redundant IMU configuration presented above. Based on this and the other estimates from the INS, the unknown aggregated environmental forces can be obtained by augmenting the vessel model (8.2)–(8.3), with the non-physical quantity $\boldsymbol{b} \in \mathbb{R}^3$. This quantity represents unmodeled forces and moments, in our case forces and moments due to wind, waves,

current and possibly ice, without using the wind sensor, even for wind loads with moderate and faster dynamics. The resulting model can take the form:

$$\dot{\boldsymbol{\eta}} = R(\psi)\boldsymbol{\nu}, \tag{8.10}$$

$$\dot{\boldsymbol{\nu}} = \boldsymbol{M}^{-1}\left(-D\nu + \boldsymbol{b} + \boldsymbol{\tau}_{\mathrm{DP}},\right) \tag{8.11}$$

$$\dot{\boldsymbol{b}} = -\boldsymbol{T}^{-1}\boldsymbol{b}. \tag{8.12}$$

The matrix $\boldsymbol{T} \in \mathbb{R}^{3\times 3}$ can be chosen as a diagonal matrix consisting of the axes' time constants, which are considered as tuning variables. For control purposes one can design an estimator or observer for the vessel model (8.10)–(8.12), to estimate $\boldsymbol{b}$ using the measurements

$$\boldsymbol{y} = \begin{pmatrix} p^n_{\mathrm{INS},x} \\ p^n_{\mathrm{INS},y} \\ \psi_{\mathrm{INS}} \\ v^n_{\mathrm{INS},x} \\ v^n_{\mathrm{INS},y} \\ \omega^b_{\mathrm{IMU,avg},z} \\ f^b_{\mathrm{IMU,avg},x} \\ f^b_{\mathrm{IMU,avg},y} \end{pmatrix}, \tag{8.13}$$

obtained from the INS and the averaged redundant inertial sensors. By putting the system on a general dynamic form,

$$\dot{\boldsymbol{x}} = \boldsymbol{f}(\boldsymbol{x}, \boldsymbol{u}), \tag{8.14}$$

$$\boldsymbol{y} = \boldsymbol{h}(\boldsymbol{x}, \boldsymbol{u}), \tag{8.15}$$

where $\boldsymbol{x} = (\boldsymbol{\eta}; \boldsymbol{\nu}; \boldsymbol{b})$ and $\boldsymbol{u} = \boldsymbol{\tau}_{\mathrm{DP}}$ and

$$\boldsymbol{h}(\boldsymbol{x}, \boldsymbol{u}) = \begin{pmatrix} \boldsymbol{\eta} \\ \boldsymbol{R}^t_b(\psi)\boldsymbol{\nu} \\ \boldsymbol{C}_{\mathrm{acc}}\boldsymbol{M}^{-1}\left(-\boldsymbol{D}\boldsymbol{\nu} + \boldsymbol{b} + \boldsymbol{\tau}_{\mathrm{DP}}\right) \end{pmatrix}, \boldsymbol{C}_{\mathrm{acc}} = \begin{pmatrix} 1 & 0 & 0 \\ 0 & 1 & 0 \end{pmatrix}. \tag{8.16}$$

The residual generalized force $\boldsymbol{b}$ is easily estimated with e.g. an extended Kalman filter without utilizing the wind sensors since $\boldsymbol{b}$ is the only state that is not measured. In addition, the two upper components of the left-hand side of (8.11) is measured by the weighted accelerometer measurements. This facilitates a highly responsive estimate of $\boldsymbol{b}$. Other examples of such strategies centered towards DP in managed ice is Kjerstad and Skjetne (2014). Since accelerometer measurements are available, acceleration feedback in harsh weather conditions is also possible (Lindegaard and Fossen, 2001).

8.5 Discussions

8.5.1 Cost vs. robustness

It can be argued that dual-redundant PosRefs and gyrocompasses are less robust than triple redundancy. Cost-wise dual-redundancy is favorable especially since both the wind sensors and VRU can be replaced with IMUs. Also saving one PosRef and gyrocompass contributes to reduce cost. In order to increase reliability further, one can spend money on more modern gyrocompass products, based on FOG, hemispherical resonator gyro (HRG) or RLG technology, Armenise et al. (2010), instead of traditional mechanical gyrocompasses in need of more frequent maintenance. In a life-cycle perspective modern gyrocompasses may be cost-effective and while being more reliable than traditional mechanical products.

The case was made earlier that common mode failures reduce the benefits of having two references of the same type. Regarding GNSS however, having two antennas and systems on board is still beneficial, as a separate heading reference could be obtained for free from the vector between them if the GNSS antennas are located sufficiently apart from each other, Rinnan et al. (2012); Gade (2016). Because of physical separation principles, partly due to class A.60 division requirements, and partly to protect one self from GNSS shadowing, one should in any case place one system at a distance from the other.

The economical argument may on the contrary also be used against having only dual redundancy in sensors and position references. Triple redundancy may facilitate increased uptime in the event of a failed sensor, resulting in that ongoing operations may be continued until a replacement unit can be acquired. If an INS is employed as in our proposed sensor configuration, one would still have the means to detect faults and stay in Class 2 or 3.

8.5.2 Testing of DP system with proposed structure

Testing of DP systems is currently carried out with Failure Mode and Effects Analysis (FMEA) (DNV GL, 2012), a qualitative methodology for systemically analyzing reliability and redundancy by investigating each possible failure mode, followed by sea-trials in which certain aspects of the FMEA tests are verified. Within today's DP system architecture, FMEA is an effective tool to verify how sensor errors and faults propagate, and if fault barriers are functioning properly, but it is not without its weaknesses (Spouge, 2004). While DP FMEA is geared towards hardware, components and tangible systems, a more recent advancement in testing is hardware-in-the-loop (HIL) testing (Johansen et al., 2005) where DP control computers are verified in a simulation environment. In this regime, it is possible to scrutinize the software of control systems not only as a single failed/not failed component, but also how they respond to different inputs, possibly leading the system to danger later on. HIL is receiving more and more attention, where

Karlsen and Ruud (2010) presents an optional enhanced reliability classification notation based on this DP system testing framework. Rokseth et al. (2016) goes even further, beyond the realm of software and hardware, including human operators and organizations together with traditional components in a system-theoretic process analysis (STPA) scheme. Rokseth et al. (2016) argues that the current focus on redundancy and component failure is too narrow, and that a broader strategy such as STPA could be applied to complement current testing programs.

With a new system- and risk-based approach for design DP control systems, and perhaps even with current systems, more sophisticated testing beyond today's FMEA should be considered. Because of ever more sophisticated software and hardware arrangements, sensor faults and failures are not guaranteed to propagate predictably, but ultimately depends on a system that is more than the sum of its parts.

8.5.3 In case of loss of all PosRefs: Vessel-model-based dead reckoning (DR)

Results have shown that the position estimates of MEMS-bases INS drift fast in the event of loss of aiding, Rogne et al. (2016a), Section 4.8.2 and Section 5.7.6. Therefore, in the event of loss of all PosRefs, usage of vessel-model-based DR using the DP estimator is advised since this has better natural stability properties due to the damping term, $-\boldsymbol{D}\boldsymbol{\nu}$, in contrast to the kinematic model of (8.7)–(8.8) based on pure integration, which is utilized by the INS. The DR performance of the model-based DR may also be improved by still using both the averaged accelerometer and rate gyro measurements, in addition to the heading measurements from the gyrocompass in the event of PosRef loss.

8.6 Conclusion

We have presented a new structure for dynamic positioning vessel sensors and position reference systems. The case was made that much of current DP redundancy requirement may not improve the safety of operation as intended. Employing low-cost triple-redundant IMUs, we described many advantages that follows from using such technology: First, a vertical reference unit inherently follows from the inclusion of IMUs. Second, fault-tolerance is improved, in some cases, because of independent measurement principles. Third, the wind sensor can be expelled from DP control, by measuring environmental forces directly with the IMUs, instead of through uncertain wind measurements and models.

A dual redundancy in both gyrocompasses and position references was proposed. For gyrocompasses, we argued that two sensors for redundancy are enough, and that fault detection and isolation could be carried with the help of MEMS IMUs. For position reference, two GNSSs and an independent system

was recommended, as in deep water operation generally only two types of systems are available (GNSS and HPR). Two GNSSs with a sufficient baseline between them would allow for position reference based heading. In case of loss of both position reference systems, we suggested falling back on a vessel-model-based estimator. Some faults could be detected and isolated by MEMS IMUs, but for slowly emerging faults more information is need, for instance from integrity monitoring of the position reference system through tight integration.

We noted that new methods for testing beyond FMEA should be applied when moving towards risk- and system-based design, but remarked that new methods are already being investigated and to some extent applied.

All in all, the inclusion of MEMS IMUs is arguably profitable. With low cost, but high value, both performance and fault tolerance is potentially increased.

9

Concluding Remarks

This dissertation set out to investigate the use of nonlinear observers (NLOs) and MEMS inertial measurement units (IMUs) for navigation. In an illustration of platform independence, two widely different vehicles were studied in experiments: an unmanned aerial vehicle (UAV), and an anchor handling tug supply (AHTS) dynamic positioning (DP) vessel.

For the UAV, loosely and tightly coupled integration of an IMU with a global navigation satellite system (GNSS) were explored. Using a real time kinematic GNSS solution as reference, the tight integration was naturally favored, being a more elaborate scheme for sensor fusion.

For the AHTS DP vessel, an extensive array of tests and analyses were conducted: Attitude and heave estimation, dead reckoning in heading and position, fault detection and isolation (FDI), comparison of NLO variations and of two different MEMS IMUs: ADIS16485 and STIM300. The tests were executed using either one MEMS IMU or a redundant configuration of IMUs. Results in all categories were favorable, showing that in attitude and heave estimation the NLOs were on par with classic methods such as the extended Kalman filter. The ADIS16485 was better for heave estimation, while STIM300 was the preferred choice for unaided heading estimation and position dead reckoning. Using three ADIS16485 in a triple-redundant configuration improved heave estimation and dead reckoning compared to employing a single one, while for attitude estimation any improvement was negligible.

Simulation studies comparing NLO variations in a position and heading reference FDI context were provided, showing that NLOs for attitude estimation should be completely independent of position references for detection of fault in such systems. Consequently, an NLO with virtual aiding for use in DP was proposed. Further, an established method for FDI was employed in a novel way to detect slow drifts.

An attempt to paint a broader picture was done in the final chapter. Based

on the newfound knowledge of this thesis, a case was made to create a new DP sensory structure and review current DP classification. New ideas in system- and risk-based thinking were promoted, to allow for integrated INSs to become a natural part of a DP system.

After seeing nonlinear observers engage MEMS based inertial sensors in such a fruitful relationship, the conclusion is that these methods and sensors have a strong potential and promise for navigational use, in dynamic positioning and other areas such as UAVs. The NLOs are computationally efficient, the MEMS IMUs are small and relatively low-cost, and the equations are model-free and thus platform independent, meaning that any navigation system can reap the benefits in performance and fault tolerance portrayed in this work.

Future Work

Standing at the end of this dissertation and looking ahead, there are several topics for research that could be interesting to look into. First and foremost, performing studies with experimental data from more sensors than was presented should be considered, especially for the chapters covering ships. We only used the horizontal position measurements from the GNSS, whereas horizontal velocity was also available. With access to more detailed information from the receiver such as pseudoranges and range-rates, we could also have performed studies with tightly coupled integration to further improve results in redundancy and position reference FDI. Additionally, as mentioned in the last chapter, dead reckoning with vessel model is compelling, but requires the control forces from the DP system acting on the vessel. A comparison beckons, between pure unaided INS and vessel-model-based navigation to back up the claim that the latter is superior in dead reckoning.

All of the estimators presented were implemented offline, so to implement a real-time version running off of live data would be intriguing. Following that, a full-scale closed loop verification of both performance and fault tolerance with the control system is also in order, as an ultimate way to assert the results.

A

Full-Scale Experiments

In cooperation with Rolls-Rolls Marine AS, a hardware setup consisting of several MEMS IMUs and computers was deployed on an anchor handling tug supply vessel owned by Farstad Shipping. The vessel was similar to the one depicted in Fig. A.1a, and the path of the ship during the experiments can be seen in Fig. A.1b.

(a) AHTS vessel. Courtesy of Rolls-Royce Marine AS.

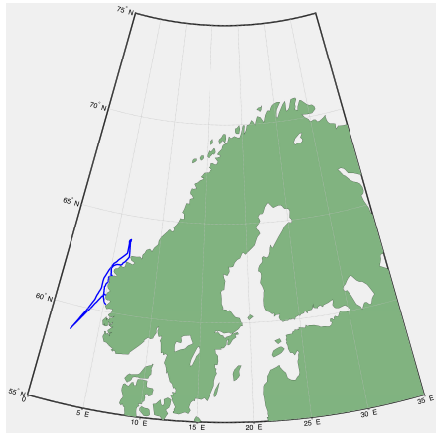

(b) The ship's path.

Figure A.1: An AHTS vessel and its path during experiments.

The sensor payload can be seen in Fig. A.2a, and contains:

- Vibration isolated sensors:
  - 1xSTIM300 IMU
  - 3xADIS16485 IMU
- Non-isolated sensor:

  - 1xADIS16485 IMU

- 2x BeagleBone Black for collecting data from the ADIS16485 IMUs via SPI
- Intel NUC for communcating with STIM300 IMU via RS422
- Network switch
- 5V and 12V power supply

The payload was installed next to the vessel's VRUs, Fig. A.2b, while a server responsible for saving data coming in at 1000 Hz was placed in the instrument room, Fig. A.2c.

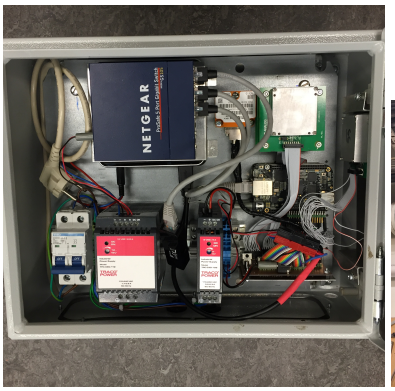

(a) Payload interior.

(b) Payload location.

(c) Server saving data.

Figure A.2: IMU sensor payload and server installed on AHTS vessel.

Data gathering and synchronization

There were some challenges related to the collection of data, the main one being that our IMU data and the traditional DP sensor data from the ship was logged at two different systems. This caused some synchronization issues between the datastreams, which had to be manually corrected offline. The IMU logging was done with our own software and hardware, while the DP data was collected with a solution provided by the DP vendor. Admittedly, there were also some internal synchronization problems in our payload. While all the IMUs were logged at approximately 1000 Hz, none of them were perfectly in sync. This was because of a decision to make do with commodity hardware like BeagleBone Blacks and an Intel NUC. With more focus on real-time properties, for instance by employing a field-programmable gate array, we could have had more accurate timestamping and simultaneity internally. However, this was not a problem in practice as we could do any time corrections offline. For a real-time implementation this might have an effect, but the dynamics are relatively slow compared to the sample rate of the IMUs, and there are ways to deal with asynchronous inputs as described in Chapter 3.

References

American Bureau of Shipping (2013). Guide for dynamic positioning systems.

Armenise, M. N., Ciminelli, C., Dell'Olio, F., and Passaro, V. M. N. (2010). *Advances in Gyroscope Technologies*. Springer-Verlag, Berlin Heidelberg.

Barbour, N., Hopkins, R., and Kourepenis, A. (2011). Inertial MEMS system applications. Technical report, NATO Lecture series RTO-EN-SET-116 Low-Cost Navigation Sensors and Integration Technology.

Batista, P., Silvestre, C., and Oliveira, P. (2010). A sensor-based long baseline position and velocity navigation filter for underwater vehicles. In *Proc. of NOLCOS 2010 - 8th IFAC Symposium on Nonlinear Control Systems*, Bologna, Italy.

Batista, P., Silvestre, C., and Oliveira, P. (2011). GES attitude observers - Part I: Multiple general vector observations. In *Proc. IFAC World Congress*, pp. 2985–2990, Milan. doi: 10.3182/20110828-6-IT-1002.01112.

Batista, P., Silvestre, C., and Oliveira, P. (2012a). A GES attitude observer with single vector observations. *Automatica*, 48(2): 388–39. doi: 10.1016/j.automatica.2011.07.005.

Batista, P., Silvestre, C., and Oliveira, P. (2012b). Globally exponentially stable cascade observers for attitude estimation. *Control Engineering Practice*, 20(2): 148–155. doi: 10.1016/j.conengprac.2011.10.005.

Batista, P., Silvestre, C., and Oliveira, P. (2012c). Sensor-based globally asymptotically stable filters for attitude estimation: Analysis, design, and performance evaluation. *IEEE Transactions on Automatic Control*, 57(8): 2095–2100. doi: 10.1109/TAC.2012.2187142.

Batista, P., Silvestre, C., and Oliveira, P. (2013). Gas tightly coupled lbl/usbl position and velocity filter for underwater vehicles. In *Proc. of the European Control Conference (ECC)*, pp. 2982–2987.

Batista, P., Silvestre, C., and Oliveira, P. (2014). Sensor-based long baseline navigation: observability analysis and filter design. *Asian J. Control*, 16(974–994).

Beard, R. W. and McLain, T. W. (2012). *Small Unmanned Aircraft: Theory and Practice*. Princeton University Press.

Berntsen, M. (2007). Hydroacoustic aided inertial navigation system – HAIN a new reference for DP. In *Proc. of the Dynamic Positioning Conference*, Houston, TX.

Bhat, S. and Bernstein, D. (2000). A topological obstruction to continuous global stabilization of rotational motion and the unwinding phenomenon. *Systems & Control Letters*, 39(1): 63–70. doi: 10.1016/S0167-6911(99)00090-0.

Black, H. D. (1964). A passive system for determining the attitude of a satellite. *AIAA Journal*, 2(7): 1350–1351. doi: 10.2514/3.2555.

Blanke, M. (2001). Enhanced maritime safety through diagnosis and fault tolerant control. In *Control Applications in Marine Systems 2001 (CAMS 2001) Proceedings volume from the IFAC Conference*, pp. 1 – 19, Kidlington, UK.

Blanke, M. (2005). Diagnosis and fault-tolerant control for ship station keeping. In *Intelligent Control, 2005. Proceedings of the 2005 IEEE International Symposium on, Mediterrean Conference on Control and Automation*, pp. 1379–1384. IEEE.

Blanke, M., Kinnaert, M., Lunze, J., and Staroswiecki, M. (2006). *Diagnosis and Fault-Tolerant Control*. Springer-Verlag Berlin Heidelberg, 2 edition.

Britting, K. R. (1971). *Inertial Navigation Systems Analysis*. John Wiley & Sons Ltd.

Brown, R. G. and Hwang, P. Y. C. (2012). *Introduction to Random Signals and Applied Kalman Filtering*. John Wiley & Sons, Inc., Hoboken, New Jersey, fourth edition.

Bryne, T. H., Fossen, T. I., and Johansen, T. A. (2014). Nonlinear observer with time-varying gains for inertial navigation aided by satellite reference systems in dynamic positioning. In *Proc. of the IEEE Mediterranean Conference on Control and Automation*, pp. 1353–1360, Palermo, Italy. doi: 10.1109/MED.2014.6961564.

Bryne, T. H., Fossen, T. I., and Johansen, T. A. (2015a). Design of inertial navigation systems for marine craft with adaptive wave filtering aided by triple-redundant sensor packages. *International Journal of Adaptive Control and Signal Processing*, pp. 1–23. doi: 10.1002/acs.2645.

Bryne, T. H., Fossen, T. I., and Johansen, T. A. (2015b). A virtual vertical reference concept for GNSS/INS applications at the sea surface. In *Proc. of the 10th IFAC Conference on Manoeuvring and Control of Marine Craft*, pp. 127–133, Copenhagen, Denmark. doi: j.ifacol.2015.10.269.

Bryne, T. H., Hansen, J. M., Rogne, R. H., Sokolova, N., Fossen, T. I., and Johansen, T. A. (2017a). Nonlinear observers for integrated INS/GNSS navigation – implementation aspects. *IEEE Control Systems Magazine*. To Appear.

Bryne, T. H., Rogne, R. H., Fossen, T. I., and Johansen, T. A. (2016). Attitude and heave estimation for ships using mems-based inertial measurements using MEMS-based inertial measurements. In *Proc. of the 10th IFAC Conference on Control Applications in Marine Systems*, pp. 568–575, Trondheim, Norway. doi: 10.1016/j.ifacol.2016.10.496.

Bryne, T. H., Rogne, R. H., Fossen, T. I., and Johansen, T. A. (2017b). Inertial sensors for risk-based redundancy in dynamic positioning. In *Proc. of the 36th International Conference on Ocean, Offshore and Arctic Engineering*, Trondheim, Norway. To Appear.

Bryne, T. H., Rogne, R. H., Fossen, T. I., and Johansen, T. A. (n.d.). A virtual vertical reference concept for integrated inertial navigation at the sea surface. *Control Engineering Practice*. Submitted for publication.

Carter, M. (2011). DP INS – a paradigm shift? In *Proc. of the Dynamic Positioning Conference*, Houston, TX.

Chen, H. and Moan, T. (2005). DP incidents on mobile offshore drilling units on the Norwegian Continental Shelf. In *Advances in Safety and Reliability - Proceedings of the European Safety and Reliability Conference, ESREL 2005*, volume 1, pp. 337–344.

Chen, H., Moan, T., and Verhoeven, H. (2008). Safety of dynamic positioning operations on mobile offshore drilling units. *Reliability Engineering & System Safety*, 93(7): 1072 – 1090.

Chen, H., Moan, T., and Verhoeven, H. (2009). Effect of dGPS failures on dynamic positioning of mobile drilling units in the North Sea. *Accident Analysis and Prevention*, 41(6): 1164–1171.

Chou, J. C. (1992). Quaternion kinematic and dynamic differential equations. *IEEE Transactions on robotics and automation*, 8(1): 53–64.

Daly, K. C., Gai, E., and Harrison, J. V. (1979). Generalized likelihood test for FDI in redundant sensor configurations. *Journal of Guidance, Control, and Dynamics*, 2(1): 9–17. doi: 10.2514/3.55825.

Djuric, P. M., Kotecha, J. H., Zhang, J., Huang, Y., Ghirmai, T., Bugallo, M. F., and Miguez, J. (2003). Particle filtering. *IEEE Signal Processing Magazine*, 20(5): 19–38. doi: 10.1109/MSP.2003.1236770.

DNV GL (2012). Failure mode and effect analysis (FMEA) of redundant systems DNV-RP-D102.

DNV GL (2013). Newbuilding - special equipment and systems - additional class - Dynamic Positioning Systems. Rules for Classification of Ships, Part 6 Chapter 7.

Farrell, J. A. (2008). *Aided Navigation: GPS with High Rate Sensors*. McGraw-Hill.

Faugstadmo, J. E. and Jacobsen, H. P. (2003). An integrated acoustic positioning and inertial navigation system. In *Proc. of the Dynamic Positioning Conference*, Houston, TX.

Fossen, T. I. (2011). *Handbook of Marine Craft Hydrodynamics and Motion Control*. John Wiley & Sons, Ltd.

Fossen, T. I. and Perez, T. (2009). Kalman filtering for positioning and heading control of ships and offshore rigs. *IEEE Control Systems Magazine*, 29(6): 32–46. doi: 10.1109/MCS.2009.934408.

Fossen, T. I. and Perez, T. (2010). Marine Systems Simulator (MSS). Viewed 01.08.2014, www.marinecontrol.org.

Fossen, T. I. and Strand, J. P. (1999). Passive nonlinear observer design for ships using lyapunov methods: full-scale experiments with a supply vessel. *Automatica*, 35(1): 3 – 16. doi: 10.1016/S0005-1098(98)00121-6.

Gade, K. (2004). Navlab, a generic simulation and post-processing tool for navigation. *European Journal of Navigation*, 2(4): 51–59.
URL: *http://www.navlab.net/Publications/*

Gade, K. (2016). The seven ways to find heading. *The Journal of Navigation*, 69(05): 955–970.

Godhavn, J.-M. (1998). Adaptive tuning of heave filter in motion sensor. In *OCEANS '98 Conf. Proc.*, volume 1, pp. 174–178, Nice, France.

Grewal, M., Andrews, A. P., and Bartone, C. G. (2013). *Global navigation satellite systems, inertial navigation, and integration*. John Wiley & Sons, Inc., Hoboken, New Jersey, 3rd edition.

Grip, H. F., Fossen, T. I., Johansen, T. A., and Saberi, A. (2012a). Attitude estimation using biased gyro and vector measurements with time-varying reference vectors. *IEEE Transactions on Automatic Control*, 57(5): 1332—1338. doi: 10.1109/TAC.2011.2173415.

Grip, H. F., Fossen, T. I., Johansen, T. A., and Saberi, A. (2013). Nonlinear observer for GNSS-aided inertial navigation with quaternion-based attitude estimation. In *Proc. of the American Contr. Conf.*, pp. 272–279, Washington, DC. doi: 10.1109/ACC.2013.6579849.

Grip, H. F., Fossen, T. I., Johansen, T. A., and Saberi, A. (2015). Globally exponentially stable attitude and gyro bias estimation with application to GNSS/INS integration. *Automatica*, 51: 158—166. doi: 10.1016/j.automatica.2014.10.076.

Grip, H. F., Fossen, T. I., Johansen, T. A., and Saberi, A. (2016). Nonlinear observer for attitude, position, and velocity: Theory and experiments. In Fourati, H. and Belkhia, D. C., editors, *Multisensor Attitude Estimation*, chapter 17, pp. 291–313. CRC Press (Taylor & Francis Group).

Grip, H. F., Saberi, A., and Johansen, T. A. (2012b). Observers for interconnected nonlinear and linear systems. *Automatica*, 48(7): 1339–1346. doi: 10.1016/j.automatica.2012.04.008.

Groves, P. D. (2013). *Principles of GNSS, Inertial, and Multisensor Integrated Navigation Systems*. Artech House, 2nd edition.

Guerrier, S., Waegli, A., Skaloud, J., and Victoria-Feser, M.-P. (2012). Fault detection and isolation in multiple mems-imus configurations. *IEEE Transactions on Aerospace and Electronic Systems*, 48(3): 2015–2031. doi: 10.1109/TAES.2012.6237576.

Gustafsson, F. (2007). Statistical signal processing approaches to fault detection. *Annual Reviews in Control*, 31(1): 41–54.

Gustafsson, F. (2012). *Statistical Sensor Fusion*. Studentlitteratur, 2nd edition.

Hansen, J. M., Fossen, T. I., and Johansen, T. A. (2015). Nonlinear observer for INS aided by time-delayed GNSS measuements: Implementation and UAV experiments. In *Proc. International Conference Unmanned Aircraft Systems (ICUAS)*, pp. 157–166, Denver, Colorado. doi: 10.1109/ICUAS.2015.7152287.

Hansen, J. M., Johansen, T. A., and Fossen, T. I. (2016). Tightly coupled integrated inertial and real-time-kinematic positioning approach using nonlinear observer. In *Proc. of the American Contr. Conf.*, pp. 5511–5518, Boston, Ma. doi: 10.1109/ACC.2016.7526534.

Hua, M.-D. (2010). Attitude estimation for accelerated vehicles using GPS/INS measurements. *Control Engineering Practice*, 18(7): 723–732. doi: 10.1016/j.conengprac.2010.01.016.

Hua, M.-D., Ducard, G., Hamel, T., Mahony, R., and Rudin, K. (2014). Implementation of a nonlinear attitude estimator for aerial robotic vehicles. *IEEE Transactions On Control System Technology*, 22(1): 201–212. doi: 10.1109/TCST.2013.2251635.

Hua, M.-D., Martin, P., and Hamel, T. (2016). Stability analysis of velocity-aided attitude observers for accelerated vehicles. *Automatica*, 63: 11–15. doi: 10.1016/j.automatica.2015.10.014.

Ingram, M. J., Tyce, R. C., and Allen, R. G. (1996). Dynamic testing of state of the art vertical reference units. In *Proc. Oceans 96 MTS/IEEE*, pp. 1533–1538.

International Maritime Organization (1994). Guidelines for vessels with dynamic positioning systems. Maritime Safety Committee, Circular 645.

Johansen, T. A. and Fossen, T. I. (2015). Nonlinear observer for inertial navigation aided by pseudo-range and range-rate measurements. In *Proc. of the European Contr. Conf.*, pp. 1673–1680, Linz, Austria. doi: 10.1109/ECC.2015.7330778.

Johansen, T. A., Fossen, T. I., and Vik, B. (2005). Hardware-in-the-loop testing of dp systems. In *MTS Dynamic Positioning Conference*, Houston, TX.

Julier, S. J. and Uhlmann, J. K. (2004). Unscented filtering and nonlinear estimation. *Proceedings of the IEEE*, 92(3): 401–422. doi: 10.1109/JPROC.2003.823141.

Kalman, R. and Bucy, R. (1961). New results in linear filtering and prediction theory. *American Society of Mechanical Engineers – Transactions – Journal of Basic Engineering Series D*, 83(1): 95–108.

Karlsen, A. and Ruud, S. (2010). New initiatives related to classification of dp systems. In *Proc. of the Dynamic Positioning Conference*, Houston, TX.

Khosravian, A., Trumpf, J., Mahony, R., and Hamel, T. (2014). Velocity aided attitude estimation on SO(3) with sensor delay. In *Proc. IEEE Conf. Decision and Control*, pp. 114–120, Los Angeles, CA. doi: 10.1109/CDC.2014.7039368.

Khosravian, A., Trumpf, J., Mahony, R., and Hamel, T. (2015). Recursive attitude estimation in the presence of multi-rate and multi-delay vector measurements. In *Proc. American Control Conference*, pp. 3199–3205, Chicago, IL. doi: 10.1109/ACC.2015.7171825.

Kjerstad, O. K. and Skjetne, R. (2014). Modeling and control for dynamic positioned marine vessels in drifting managed sea ice. *Modeling, Identification and Control*, 35(4): 249—262. doi: 10.4173/mic.2014.4.3 â*f*c 2014 Norwegian Society of Automatic Control.

Küchler, S., Eberharter, J. K., Langer, K., Schneider, K., and Sawodny, O. (2011). Heave motion estimation of a vessel using acceleration measurements. In *Proc. of the 18th IFAC World Congress*, pp. 14742–14747, MIlan, Italy.

Lindegaard, K. P. and Fossen, T. I. (2001). A model based wave filter for surface vessels using position, velocity and partial acceleration feedback. In *Proc of the 40th IEEE Conference on Decision and Control*, pp. 946–951.

Loria, A. and Panteley, E. (2005). Cascaded nonlinear time-varying systems: Analysis and design. In Lamnabhi-Lagarrigue, F., Loria, A., and Panteley, E., editors, *Adv. Top. in Cntrl. Sys. Theory*, volume 311 of *LNCIS*, chapter 2, pp. 23–64. Springer-Verlag. doi: 10.1007/11334774_2.

Mahony, R., Hamel, T., and Pflimlin, J. M. (2008). Nonlinear complementary filters on the special orthogonal group. *IEEE Transactions on Automatic Control*, 53(5): 1203–2018. doi: 10.1109/TAC.2008.923738.

Markley, F. L. (2003). Attitude error representation for kalman filtering. *Journal of Guidance, Control and Dynamics*, 26(2): 311–317.

Markley, F. L. (2007). Averaging quaternions. *Journal of Guidance, Control and Dynamics*, 30(4): 1193–1196.

Markley, F. L. and Mortari, D. (2000). Quaternion attitude estimation using vector observations. *Journal of the Astronautical Sciences*, 48(2—3): 359—380.

Martin, P. and Salaün, E. (2010). Design and implementation of a low-cost observer-based attitude and heading reference system. *Control Engineering Practice*, 18(7): 712—722. doi: 10.1016/j.conengprac.2010.01.012.

Maybeck, P. (1979). Stochastic models, estimation, and control, volume 1. In *Mathematics in Science and Engineering*, volume 141. Academic Press.

Medvedev, A. (1995). Fault detection and isolation by a continuous parity space method. *Automatica*, 31(7): 1039–1044. doi: 10.1016/0005-1098(95)00008-K.

Mohleji, S. C. and Wang, G. (2010). Modeling ADS-B position and velocity errors for airborne merging and spacing in interval management application. https://www.mitre.org/sites/default/files/pdf/10_3026.pdf, The MITRE Corporation, 7515 Colshire Drive, McLean VA 22102.

Morgado, M., Batista, P., Oliveira, P., and Silvestre, C. (2011). Position and velocity USBL/IMU sensor-based navigation filter. *IFAC Proceedings Volumes*, 44(1): 13642 – 13647. 18th {IFAC} World Congress. doi: http://dx.doi.org/10.3182/20110828-6-IT-1002.01127.

Paturel, Y. (2004). PHINS, an all-in-one sensor for DP applications. In *Proc. of the Dynamic Positioning Conference*, Houston, TX.

Rankin, J. (1994). GPS and differential GPS: An error model for sensor simulation. In *IEEE Position Location and Navigation Symposium*, pp. 260–266, Las Vegas, NV.

Richter, M., Schneider, K., Walser, D., and Sawodny, O. (2014). Real-time heave motion estimation using adaptive filtering techniques. In *Proc. of the 19th IFAC World Congress*, pp. 10119–10125, Cape Town, South Africa.

Rinnan, A., Gundersen, N., Bratberg, S., and Sigmond, M. E. (2012). Including GNSS based heading in inertial aided GNSS DP reference system. In *Proc. of the Dynamic Positioning Conference*, Houston, TX.

Rogne, R. H., Bryne, T. H., Fossen, T. I., and Johansen, T. A. (2016a). MEMS-based inertial navigation on dynamically positioned ships: Dead reckoning. In *Proc. of the 10th IFAC Conference on Control Applications in Marine Systems*, pp. 139—146, Trondheim. doi: 10.1016/j.ifacol.2016.10.334.

Rogne, R. H., Bryne, T. H., Fossen, T. I., and Johansen, T. A. (n.d.a). Redudant MEMS-based inertial navigation using nonlinear observers. *ASME Journal of Dynamic Systems, Measurement and Control*. Submitted for publication.

Rogne, R. H., Bryne, T. H., Fossen, T. I., and Johansen, T. A. (n.d.b). Strapdown inertial navigation on ships using mems sensors and nonlinear observers. *IEEE Transactions On Control System Technology*. Submitted for publication.

Rogne, R. H., Bryne, T. H., Johansen, T. A., and Fossen, T. I. (2016b). Fault detection in lever-arm-compensated position reference systems based on nonlinear attitude observers and inertial measurements in dynamic positioning. In *Proc. of the American Contr. Conf.*, pp. 985–992, Boston, Ma. doi: 10.1109/ACC.2016.7525043.

Rogne, R. H., Johansen, T. A., and Fossen, T. I. (2014). Observer and IMU-based detection of faults in position reference systems and gyrocompasses with dual redundancy in dynamic positioning. In *Proc of the IEEE Conference on Control Applications (CCA)*, pp. 83–88, Antibes, France.

Rogne, R. H., Johansen, T. A., and Fossen, T. I. (2015). On attitude observers and inertial navigation for reference system fault detection and isolation in dynamic positioning. In *Proc. European Control Conference (ECC)*, pp. 3665–3672, Linz, Austria.

Rokseth, B., Utne, I. B., and Vinnem, J. E. (2016). A systems approach to risk analysis of maritime operations. *Proceedings of the Institution of Mechanical Engineers, Part O: Journal of Risk and Reliability*.

RTKLIB (Last updated: 29.04.2013). Available online at http://www.rtklib.com. Version 2.4.2.

Russell, D. (2012). Integrating INS and GNSS sensors to provide reliable surface positioning. In *Proc. of the Dynamic Positioning Conference*, Houston, TX.

Salcudean, S. (1991). A globally convergent angular velocity observer for rigid body motion. *IEEE Trans. Automat. Contr.*, 36(12): 1493 – 1497.

Shuster, M. D. and Oh, S. D. (1981). Three-axis attitude determination from vector observations. *Journal of Guidance Control and Dynamics*, 4(1).

SNAME (1950). Nomenclature for treating the motion of a submerged body through a fluid. In *Technical and Research Bulletin No. 1—5*, pp. 1–15, New York. The Society of Naval Architects and Marine Engineers.

Spouge, J. (2004). Review of methods for demonstrating redundancy in dynamic positioning systems for the offshore industry - research report 195. Health and Safety Executive.

Stephens, R., Crétollier, F., Morvan, P.-Y., and Chamberlain, A. (2008). Integration of an inertial navigation system and DP. In *Proc. of the Dynamic Positioning Conference*, Houston, TX.

Stephens, R. I. (2011). Wind feedforward: blowing away the myths. In *Proc. of the Dynamic Positioning Conference*, Houston, TX.

Sturza, M. A. (1988). Navigation system integrity monitoring using redundant measurements. *Navigation*, 35(4): 483–501. doi: 10.1002/j.2161-4296.1988.tb00975.x.

Sukkarieh, S., Gibbens, P., Grocholsky, B., Willis, K., and Durrant-Whyte, H. F. (2000). A low-cost, redundant inertial measurement unit for unmanned air vehicles. *The International Journal of Robotics Research*, 19(11): 1089–1103.

Titterton, D. H. and Weston, J. L. (2004). *Strapdown inertial navigation technology*. Institution of Electrical Engineers and American Institute of Aeronautics and Astronautics, 2nd edition.

van Loan, C. F. (1978). Computing integrals involving the matrix exponential. *IEEE Trans. Automatic Control*, AC–23(3): 395–404. doi: 10.1109/TAC.1978.1101743.

Vermeille, H. (2004). Computing geodetic coordinates from geocentric coordinates. *Journal of Geodesy*, 78: 94—95.

Vickery, K. (1999). The development and use of an inertial navigation system as a DP position reference sensor (IPRS). In *Proc. of the Dynamic Positioning Conference*, Houston, TX.

Vik, B. and Fossen, T. (2001). A nonlinear observer for GPS and INS integration. In *Proc. IEEE Conf. Dec. Cont*, volume 3, pp. 2956–61, Orlando, FL. doi: 10.1109/.2001.980726.

Waegli, A., Guerrier, S., and Skaloud, J. (2008). Redundant MEMS-IMU integrated with GPS for performance assessment in sports. In *2008 IEEE/ION Position, Location and Navigation Symposium*, pp. 1260–1268. IEEE. doi: 10.1109/PLANS.2008.4570079.

Wahba, G. (1965). A least squares estimate of spacecraft attitude. *SIAM Review*, 7(3): 409—409.

Willsky, A. and Jones, H. (1976). A generalized likelihood ratio approach to the detection and estimation of jumps in linear systems. *IEEE Transactions on Automatic control*, 21(1): 108–112. doi: 10.1109/TAC.1976.1101146.

Zamani, M., Trumpf, J., and Mahony, R. (2013). Minimum-energy filtering for attitude estimation. *IEEE Transactions on Automatic Control*, 58: 2917–2921. doi: 10.1109/TAC.2013.2259092.

Zhao, B. and Skjetne, R. (2014). A unified framework for fault detection and diagnosis using particle filter. *Modeling, Identification and Control*, 35(4): 303—315.